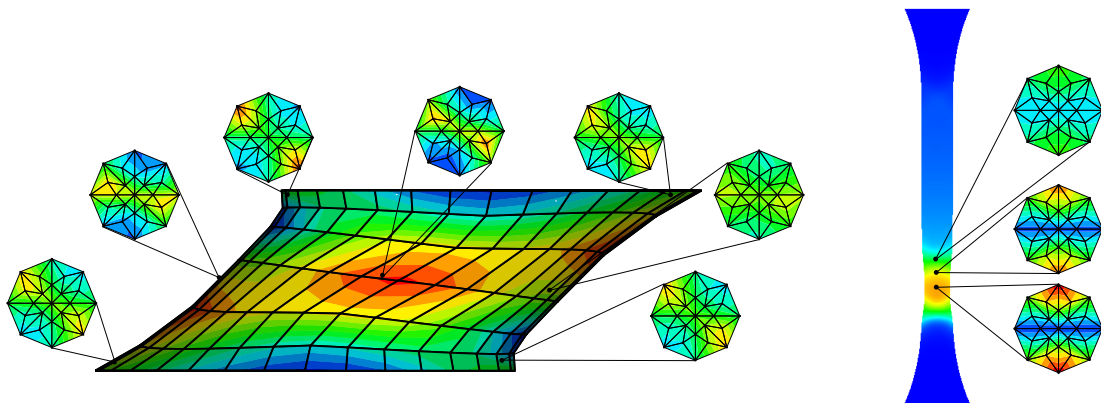


Micro-Macro Approaches to Rubbery and Glassy Polymers: Predictive Micromechanically-Based Models and Simulations

Serdar Göktepe



$$\lambda_{chain} \rightarrow \lambda_{network} = \left(\frac{1}{|\mathcal{S}|} \int_{\mathcal{S}} |\mathbf{F}\mathbf{r}|^p dA \right)^{1/p}$$

Bericht Nr.: I-20 (2007)
Institut für Mechanik (Bauwesen), Lehrstuhl I
Professor Dr.-Ing. C. Miehe
Stuttgart 2007

Micro-Macro Approaches to Rubbery and Glassy Polymers: Predictive Micromechanically-Based Models and Simulations

Von der Fakultät Bau- und Umweltingenieurwissenschaften
der Universität Stuttgart zur Erlangung der Würde
eines Doktor-Ingenieurs (Dr.-Ing.)
genehmigte Abhandlung

vorgelegt von

Serdar Göktepe

aus Fethiye (Türkei)

Hauptberichter : Prof. Dr.-Ing. C. Miehe

Mitberichter : Prof. Dr.-Ing. A. Lion

Tag der mündlichen Prüfung: 22. Oktober 2007

Institut für Mechanik (Bauwesen) der Universität Stuttgart

2007

Herausgeber:

Prof. Dr.-Ing. habil. C. Miehe

Organisation und Verwaltung:

Institut für Mechanik (Bauwesen)

Lehrstuhl I

Universität Stuttgart

Pfaffenwaldring 7

70550 Stuttgart

Tel.: ++49(0)711/685-66378

Fax: ++49(0)711/685-66347

© Serdar Göktepe
Institut für Mechanik (Bauwesen)
Lehrstuhl I
Universität Stuttgart
Pfaffenwaldring 7
70550 Stuttgart
Tel.: ++49(0)711/685-66377
Fax: ++49(0)711/685-66347

Alle Rechte, insbesondere das der Übersetzung in fremde Sprachen, vorbehalten. Ohne Genehmigung des Autors ist es nicht gestattet, dieses Heft ganz oder teilweise auf fotomechanischem Wege (Fotokopie, Mikrokopie) zu vervielfältigen.

ISBN 3-937859-08-X (D 93 Stuttgart)

Zusammenfassung

Die vorliegende Arbeit befasst sich mit der Entwicklung von physikalisch motivierten Modellen für die Beschreibung des Materialverhaltens von gummi- und glasartigen Polymeren. Ein besonderer Fokus dieser Arbeit liegt auf der Elastizität, finiten Viskoelastizität, deformationsinduzierten Mullins-Typ Schädigung in gummiartigen Polymeren sowie auf der Viskoplastizität amorpher glasartiger Polymere bei finiten Deformationen. Die entwickelten Modelle besitzen intrinsische mikro-makro Übergangseigenschaften die uns erlauben Mechanismen der Mikrostruktur zu berücksichtigen. Physikalisch motivierte Materialparameter folgen aus der geometrischen Betrachtung diese Mechanismen. Vorgeschlagen wird eine Mikrostruktur, die durch eine sogenannte Mikrokugel charakterisiert ist. Die Oberfläche der Mikrokugel stellt die stetige Verteilung der räumlichen Orientierung der Polymerketten dar. Die Hauptidee des vorgeschlagenen konstitutiven Rahmens beruht auf zwei Schritten: der Entwicklung eines mikromechanisch motivierten konstitutiven Modells einer einzelnen Polymerkette und der Definition der makroskopischen Spannungen die aus einem Homogenisierungsverfahren der Zustandsvariablen folgen. Die Verteilung und die räumliche Orientierung der mikroskopischen Zustandsvariablen werden in diskreter Weise auf der Mikrokugel definiert. Die diskutierten Modelle werden weiter mit den zugehörigen algorithmischen Verfahren ausgestattet, die einerseits die Aktualisierung der internen Variablen durchführt und andererseits die Berechnung von Spannungen und konsistenten Tangentenmodulen bereitstellt. Die Leistungsfähigkeit der Modelle wird anhand zahlreicher Vergleiche homogener und inhomogener Experimente mit den entsprechenden Simulationen gezeigt.

Abstract

This work is concerned with the development of physically motivated constitutive models for the description of the material behavior of rubbery and glassy polymers. The particular focus of the thesis is placed on elasticity, finite viscoelasticity, deformation-induced Mullins-type damage in rubbery polymers, and finite viscoplasticity of amorphous glassy polymers. The models developed possess the intrinsic character of a micro-macro transition that, in turn, allows us to incorporate the physical mechanisms stemming from a micro-structure of the material through geometrically well defined kinematic measures and in terms of physically motivated material parameters. The proposed approaches make use of a micro-structure that is symbolized by a unit sphere, the so-called micro-sphere. The surface of the micro-sphere represents a continuous distribution of chain orientations in space. A key idea of the proposed constitutive framework may be considered as a two-step procedure that incorporates the set up of micromechanically-based constitutive models for a single chain orientation and the definition of the macroscopic stress response through a directly evaluated homogenization of state variables. The distribution of micro-state variables are defined on the micro-sphere of space orientations in a discrete manner. The proposed models are further furnished with the associated algorithmic procedures that perform the update of internal variables and computation of stresses and tangent moduli in a way consistent with the employed integration scheme. The modeling performance of the models is tested against broad range of homogeneous and inhomogeneous experimental data with particular regard to their predictive simulation capabilities.

Acknowledgements

The work presented in this thesis was carried out between the years 2002 and 2007, during which I was employed as a research associate at the Institute of Applied Mechanics (CEE) at the University of Stuttgart. I would like to take this opportunity to thank the people who supported me in different ways and made this endeavor enjoyable.

First, I wish to express my heartfelt gratitude to my advisor Professor Christian Miehe for his strong support and constructive criticism. The academic freedom that he provided and his confidence in my work encouraged me to take on challenges during my thesis. It has definitely been his patient guidance and invaluable advice that have made this dissertation possible. I would also like to thank Professor Alexander Lion for accepting to serve as the co-referee of this thesis and for his interest in the work. My deep thanks also go to Professor Erman Tekkaya who not only encouraged me to come to Germany for my graduate studies, but also has continuously supported me throughout this period.

I would like to express my most grateful thanks to my very close friend and my roommate Ercan Gürses for our long-lasting friendship. Many stimulating scientific discussions, which were not restricted to working time at the institute but also continued during dinner time after work, have greatly furthered my knowledge on computational mechanics.

Furthermore, I am truly indebted to my colleague and friend Joel Méndez Diez for his generous friendship and for our fruitful collaborative research on mechanics of polymers. His experimental results undoubtedly enriched the material presented in this thesis.

I would like to thank all colleagues at the institute for the friendly and peaceful working atmosphere. Among them, I am especially thankful to two former colleagues, Dr. Matthias Lambrecht and Dr. Nikolas Apel, and also their families, for the cordial friendship, hospitality and strong help with many personal issues.

In addition, I thank Arun Balasubramanian, Joel Méndez Diez, Hüsnü Dal, Aruna Prakash, Harish Iyer, Shaofei Qu and Dirk Liefeth. They were involved in the research during their master/diploma theses for which I had the pleasure to serve as an advisor. Our stimulating discussions and their results definitely contributed to this dissertation.

Last but not least, I would like to take this opportunity also to thank my parents, Serpil and Nail Göktepe, for their unconditional love, everlasting support and constant encouragement. My grateful thanks also go to my sister Serap Şimşek, my brother-in-law Aydın Şimşek and my nephews Yağız Toprak and Yalın Deniz Şimşek.

Stuttgart, October 2007

Serdar Göktepe

Contents

1. Introduction	1
1.1. Motivation and State of the Art	1
1.1.1. Finite Elasticity and Inelasticity of Rubber-like Materials	1
1.1.2. Finite Viscoplasticity of Amorphous Glassy Polymers	8
1.2. Scope and Outline	13
2. Fundamentals of Continuum Mechanics	15
2.1. The Motion, Fundamental Geometric Maps and Deformation Measures	15
2.2. Cauchy's Stress Theorem and the Fundamental Stress Measures	20
2.3. Balance Principles of Continuum Thermomechanics	22
2.4. Dissipation and Thermomechanics with Internal Variables	26
3. The Non-Affine Micro-Sphere Model of Rubber Elasticity	29
3.1. Macroscopic Spatial Elasticity of a Polymer Network	31
3.2. Micromechanics of a Single Polymer Chain in a Tube	32
3.2.1. Definition of Micro-Kinematic Variables of the Chain	32
3.2.2. Free Energy of a Single Chain	34
3.2.3. The Free Energy of an Unconstrained Single Chain	34
3.2.4. Free Energy Due to the Tube-Like Constraint of the Chain	36
3.3. Network Models for Affine and Non-Affine Stretches	36
3.3.1. Split of the Macroscopic Free Energy of the Network	36
3.3.2. The Affine Full Network Model for Unconstrained Chains	37
3.3.3. A Non-Affine Network Model for Unconstrained Chains	40
3.3.4. A Non-Affine Network Model for the Tube Constraint	42
3.4. Algorithmic Setting of the Constitutive Model	43
3.4.1. Summary of the Effective Material Parameters	43
3.4.2. Discretization of Fields on the Micro-Sphere	44
3.5. Assessment of the Modeling Capacity of the Model	47
3.5.1. Performance of the Proposed Algorithmic Implementation	49
3.5.2. Comparison of Affine Network Models with the Eight-Chain Model	49
3.5.3. Characteristics of the Proposed Non-Affine Micro-Sphere Model	53
3.5.4. Modeling Capacity of the Non-Affine Micro-Sphere Model	55
3.5.5. Three-Dimensional Analysis of a Non-Homogeneous Shear Test	58
4. The Micro-Sphere Model of Finite Rubber Viscoelasticity	63
4.1. Macroscopic Spatial Viscoelasticity of a Polymer Network	64
4.2. Micromechanics of Chains in a Constrained Environment	66
4.2.1. Definition of Micro-Kinematic Variables of the Chain	66
4.2.2. Free Energy of the Elastic Ground State Response	66
4.2.3. Free Energy and Dissipation of Viscoelastic Overstress Response	66
4.2.4. Algorithmic Representation of the Overstress Response	68

4.3.	Network Model for Finite Rubber Viscoelasticity	69
4.3.1.	Definition of Macroscopic Stretch and Area Deformation	69
4.3.2.	Non-Affine Network Model for Elastic Equilibrium Response	70
4.3.3.	Affine Network Model for Viscoelastic Overstress Response	71
4.3.4.	Discretization of Fields on the Micro-Sphere	72
4.4.	Numerical Examples	73
4.4.1.	Simulation of Homogeneous Experiments	73
4.4.2.	3-D Analyses of a Non-Homogeneous Shear Test	78
5.	The Micro-Sphere Model of Anisotropic Mullins-Type Damage	81
5.1.	Macroscopic Finite Elasticity with Damage	82
5.2.	Micromechanics of Chains in a Constrained Environment	83
5.2.1.	Free Energy of the Crosslink-to-Crosslink Response	83
5.2.2.	Free Energy and Dissipation of the Particle-to-Particle Response	84
5.2.3.	Algorithmic Representation of the PP Micro-Stresses	86
5.3.	Anisotropic Network Model of Mullins-Type Damage	87
5.3.1.	Definition of Macro-Kinematic Variables of the Continuum	87
5.3.2.	Non-Affine Network Model for Crosslink-to-Crosslink Response	87
5.3.3.	Affine Network Model for Particle-to-Particle Response	88
5.3.4.	Discretization of Fields on the Micro-Sphere	89
5.4.	Representative Numerical Examples	89
5.4.1.	Numerical Investigations on Homogeneous Tests	90
5.4.2.	A Cube Subjected to Combined Tension and Shear	93
6.	Finite Viscoplasticity of Amorphous Glassy Polymers	95
6.1.	Additive Finite Plasticity in the Logarithmic Strain Space	95
6.1.1.	Additive Kinematic Approach Based on Logarithmic Strains	96
6.1.2.	Modular Structure of the Constitutive Equations	97
6.2.	Constitutive Model for Viscoplasticity of Glassy Polymers	101
6.2.1.	Overall Constitutive Structure	101
6.2.2.	Specific Forms of the Constitutive Equations	101
6.2.3.	Algorithmic Setting of the Model	106
6.3.	Illustrative Numerical Examples	109
6.3.1.	Investigations on Homogeneous Deformation States	109
6.3.2.	Cold Drawing of a Dumbbell-Shaped PC Specimen	112
7.	Concluding Remarks	117
A.	Spectral Representation of the Right Cauchy-Green Tensor	119
B.	Decoupled Volumetric-Isochoric Finite Elasticity	123
C.	Statistics of the Freely Jointed Chain	127

1. Introduction

The goal of this thesis is to develop new physically motivated constitutive models for the description of material behavior of rubbery and glassy polymers. The particular emphases are laid on the finite elasticity, finite viscoelasticity, deformation-induced Mullins-type damage in rubbery polymers, and the finite viscoplasticity of amorphous glassy polymers. The developed models possess the intrinsic character of micro-macro transition that allows us to incorporate the physical mechanisms stemming from a micro-structure of the material through geometrically clear deformation measures and in terms of physically motivated material parameters. The proposed models furnished with associated algorithmic settings are tested against broad range of homogeneous and inhomogeneous experimental data with particular regard to their predictive simulation capabilities.

1.1. Motivation and State of the Art

1.1.1. Finite Elasticity and Inelasticity of Rubber-like Materials. Since the beginning of the last century the mechanics of rubber-like materials has been a very active field of research due to their wide range of industrial applications. Recently developed production techniques have led to a broad use of rubbery polymer products in diverse industrial applications, which include tire technology, automotive industry, conveyor belts, membranes, base isolations, seals, to name a few. The predictive three-dimensional analyses of the rubbery products that possess complex geometry and are subjected to various loading conditions are of great importance for their efficient use and functional design. This can only be achieved by the sound constitutive models accounting for the time-dependent inelastic material behavior at finite deformations. The various effects observed in the material response are prevailed by its chemical and structural composition as well as the loading program to which the material is subjected. The dominating highly non-linear elasticity, characterized by the typical S-shaped uniaxial nominal stress-stretch curve, Figure 3.14, is generally accompanied by complicated inelastic effects such as visco-elastic-plastic phenomena coupled with the so-called Mullins effect of strain-softening, see Figure 1.2. The combined inelastic effects may be accounted for through their superposition onto a non-linear ground-elastic response, see e.g. MIEHE & KECK [150].

Elasticity of Rubber-like Materials. The elastic response of rubber-like materials is characterized by its extreme deformability and an almost full recovery upon unloading, see for example TRELOAR [196] or MARK & ERMAN [129] for an introduction. Rubbery polymer networks are formed by vulcanization of their basic constituents, the long chain molecules. Rubber-like elasticity can be achieved through two fundamental microstructural requirements. These demand the existence of very flexible and mobile (thermally agitated) chain molecules and a three-dimensional network structure that is formed by sparsely separated cross-links where chains are connected. Although rubber is commonly classified as a solid material, it resembles the three states –solid, liquid and gas– of a matter with regard to different aspects. Its ability to undergo elastic deformations, i.e. almost full recovery of its initial shape upon unloading, indicates that it has a certain structure that is commonly observed in conventional solid materials. Practically rubbery polymers are incompressible materials possessing the volumetric stiffness nearly four orders of ten larger than the shear modulus while they are readily deformable in shear. This is a typical property of a liquid material. Their striking thermoelastic properties resemble a gaseous material whose pressure is also chiefly entropically derived. That is,

the internal energy practically does not change under isothermal deformations. Therefore, it is widely accepted that the dominant contribution to the high elastic response of rubber-like materials is due to changes in conformations of network constituents commonly referred to as the entropy elasticity theory. Entropic elasticity of chain molecules is well established in the context of statistical mechanics, see e.g. KUHN [112], KUHN & GRÜN [114], JAMES & GUTH [101], TRELOAR [196], FLORY [64] and references therein. The key challenge in the micromechanically-based modeling of rubber-like materials, however, is the construction of a *micro-macro transition* that provides a bridge between microscopic kinematic variables of a single chain and macroscopic deformation measures of a continuum.

There is a large body of literature on the constitutive modeling of macroscopic elastic response of rubbery polymers. These models can roughly be classified into two types: *purely phenomenological models* and *micromechanically-based models*. For an excellent overview, the reader is referred to the recent papers of BOYCE & ARRUDA [25] and MARCKMANN & VERRON [127]. The latter critically compares twenty hyperelasticity models of rubber-like materials and provides a ranking list based chiefly on the two sets of celebrated experimental data reported by TRELOAR [193] and KAWABATA ET AL. [107].

Traditionally the elasticity of rubber-like materials has been considered as an ideal area of application of isotropic elasticity theory. This has apparently given rise to the *phenomenological models* that are formulated in the form of polynomial strain energy functions in terms of principal invariants or principal stretches. These phenomenological constitutive models generally lack a connection to the molecular structure of the material. Owing to their polynomial form, these models may result in unrealistic results beyond the deformation range within which their material parameters are determined. The Mooney-Rivlin model, which has originally been proposed by MOONEY [153], can be considered as one of the simplest form of the invariant-based models. It is generally recalled with a straight line representation of its uniaxial response in the so-called *Mooney plot*, i.e. $f^* := P_{11}/(\lambda - \lambda^{-2}) = 2(C_{10} + C_{01}/\lambda)$ vs $1/\lambda$. Its generalized form $\Psi(I_1, I_2) = \sum_{i,j=0}^{\infty} C_{ij}(I_1-3)^i(I_2-3)^j$ was introduced by RIVLIN & SAUNDERS [175]. One of the well-known models belonging to this class has been suggested by YEOH [210] in the form of a third-order polynomial of the first invariant I_1 of the right Cauchy-Green tensor. The Ogden model proposed in OGDEN [160, 161] is probably the best known example for the principal stretch-based constitutive formulations consistent with the Valanis-Landel hypothesis. Its free energy is of the form $\Psi(\lambda_1, \lambda_2, \lambda_3) = \sum_n \frac{\mu_n}{\alpha_n} (\lambda_1^{\alpha_n} + \lambda_2^{\alpha_n} + \lambda_3^{\alpha_n})$. Apparently, all the invariant-based free energy functions can readily be recast into the forms in terms of principal stretches. The reverse, however, generally does not hold. As mentioned above, rubber-like materials deform under nearly constant volume, i.e. incompressible with $J = \sqrt{I_3} = \lambda_1\lambda_2\lambda_3 \approx 1$. For this reason, a general deformation state at a material point can completely be described in terms of two independent measures of deformation such as $\{\lambda_1, \lambda_2\}$ or $\{I_1, I_2\}$. For a plane-stress biaxial deformation, for instance, the derivatives of a free energy function $\partial_{I_1}\Psi(I_1, I_2)$, $\partial_{I_2}\Psi(I_1, I_2)$ can be acquired in terms of the nominal stresses and stretches measured during an experiment. This set of experimental curves can then be used as guidelines for estimating the functional form of these derivatives, see e.g. JONES & TRELOAR [102], KAWABATA ET AL. [107].

Besides the purely phenomenological models, there have been various *micromechanically-based idealized network models* proposed in the literature. These include the three-chain,

the four-chain, the eight-chain and the full network models. The *three-chain model* of JAMES & GUTH [101] and WANG & GUTH [203] assumes that the polymer network can be represented by three sets of chains oriented in the principal directions of deformation. The macroscopic free energy of the network is assumed to be determined by multiplication of the number of chains in the network with the arithmetic mean of the non-Gaussian chain free energies consistently computed through the *affinity assumption* in principal directions; that is, $\Psi(\lambda_1, \lambda_2, \lambda_3) = \frac{n}{3} \sum_{i=1}^3 \psi_{\mathcal{L}}(\lambda_i)$ where n denotes the network chain density. The *four-chain model* of FLORY & REHNER [66], TRELOAR [194] simplifies the complex polymer network with four chains, which are connected to the corners of a tetrahedron. The tetrahedron deforms in accordance with the macroscopic deformation while the displacement of the central junction point of chains is iteratively determined through an equilibrium condition. In this sense, the chain deformations are *non-affine*. The *eight-chain model*, proposed by ARRUDA & BOYCE [8], defines a *single non-affine network stretch* $\lambda := ((\lambda_1^2 + \lambda_2^2 + \lambda_3^2)/3)^{1/2}$ that is assumed to be representative for all chains constituting the network. The macroscopic free energy of the network is simply given by $\Psi(\lambda) = n\psi_{\mathcal{L}}(\lambda)$. Recently, BOYCE [24] compared the eight-chain model to the first invariant-based Gent model, GENT [68], and demonstrated the almost equivalence of these two models in the sense of their set-up and fitting qualities of test data. The *affine full network model* has been originally proposed by TRELOAR [195] only for the uniaxial deformation case. In this model, the chain orientations are assumed to be equally distributed in space. Later, TRELOAR & RIDING [197] advanced the affine full network model to the biaxial deformation and provided a numerical implementation. Its generalized three-dimensional form applicable to complex non-homogeneous deformations was recently formulated by WU & VAN DER GIESSEN [206]. In addition, LULEI & MIEHE [125] suggested an efficient algorithmic setting for the affine full network model. However, it is a well-known fact that the affinity assumption yields model response that is not completely in agreement with experimental observations, especially in the range of large deformations. Owing to this fact, it was argued in BOYCE & ARRUDA [25] and WU & VAN DER GIESSEN [206] that the eight-chain model yields more realistic results than the seemingly more precise affine full network models.

The above mentioned micromechanically-based models consider idealized polymer networks to be composed of chains which are assumed to pass through each other freely and no intermolecular forces among them are taken into account. In real networks, however, topological constraint effects arise due to entanglement-like formations. Molecular-based statistical approaches that incorporate these effects can be classified into two main groups: the *constrained junction theories* which formulate the topological constraints around the junctions and the *constrained segment theories* which define interaction effects along the chain length. The former approach has been independently proposed by RONCA & ALLEGRA [177] and FLORY [62] and further developed in a series of papers by FLORY [63], ERMAN & FLORY [56] and FLORY & ERMAN [65]. The constraint part of the model proposed by Flory and Erman was already considered as a remedy to improve the performance of the eight-chain model in BOYCE & ARRUDA [25]. The constraint segment approach is consistent with the so-called *tube model* of rubber elasticity, see for example DEAM & EDWARDS [40], EDWARDS & VILGIS [53], HEINRICH & STRAUBE [93, 94] and references cited therein. Agreement between the *tube model* approach and small-angle neutron scattering (SANS) patterns in the two-dimensional detector plane was reported by STRAUBE ET AL. [188, 189]. The *extended tube model* proposed by KALISKE &

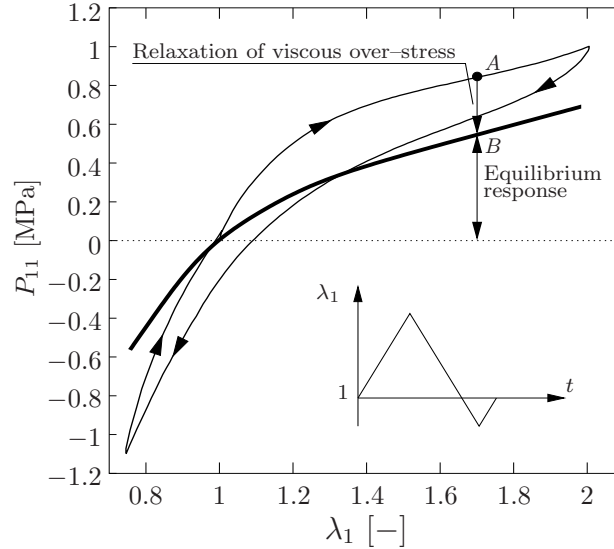


Figure 1.1: Nominal stress-stretch response of a viscoelastic HNBR50 material subjected to a uniaxial cyclic deformation at constant stretch-rate (thin line). A full relaxation from a non-equilibrium point A to an equilibrium point B identifies an *elastic equilibrium curve without hysteresis* (thick line). The two experimentally obtained curves justify a separate constitutive modeling of the elastic equilibrium and viscous overstress response.

HEINRICH [104] can be looked upon as the successful three-dimensional extension of the constrained segment ideas. Furthermore, similarities of the physics employed in the constrained junction and constrained segment approaches have been shown by VILGIS & ERMAN [200], albeit the different viewpoints in the treatment of topological constraints.

Finite Viscoelasticity of Rubber-like Materials. In context of the phenomenological material modeling on a macroscopic continuum level, dissipative inelastic phenomena observed in rubbery polymers are generally referred to as finite elasto-visco-plasticity coupled with deformation-induced softening. The overall behavior of rubbery polymer aggregates exhibits highly non-linear finite elasticity combined with time-dependent inelastic effects. The uniaxial nominal stress-stretch response a cylindrical hydrogenated nitrile butadiene rubber HNBR50 specimen under cyclic loading at room temperature is shown in Figure 1.1. In order to exclude the Mullins effect due to a partial breakdown of the microstructure, a *pre-conditioning* (deformation-induced pre-damaging) was performed as described for example in JAMES & GREEN [99], LION [118], BERGSTRÖM & BOYCE [14], MIEHE & KECK [150] and MÉNDEZ [135]. Following HAUPT [86], the dissipative hysteresis in Figure 1.1 can be explained either by elasto-visco-plasticity (response with equilibrium hysteresis) or by viscoelasticity (response without equilibrium hysteresis). In order to investigate the existence of a possible equilibrium hysteresis, pre-conditioned specimens were subjected to cyclic uniaxial tests including holding periods of relaxation, as depicted in Figure 4.6. A convergence of the relaxation processes to the same stress value at the same stretch value and at the end of a long holding period was observed as shown in Figure 1.1, indicating that the pre-conditioned material exhibits almost *no equilibrium hysteresis*, see also MÉNDEZ [135] and ZECHA [211]. This observation is in accord with the experimental results reported by BERGSTRÖM & BOYCE [14] and HAUPT & SEDLAN [88] on similar materials. In the light of this investigation, we consider the inelastic behavior of the pre-conditioned material to be *viscoelastic*.

The challenges faced in the modeling of finite rubber viscoelasticity have been tackled

by many researchers from different disciplines. Approaches of the engineering community possess a more macroscopic viewpoint, while the scientists from physical chemistry have addressed the problem on a molecular level. Comprehensive reviews are outlined in the textbooks FERRY [58], TANNER [191], DOI & EDWARDS [45], FINDLEY, LAI & ONARAN [59] and DROZDOV [49]. Purely phenomenological approaches to finite viscoelasticity usually introduce *tensorial* stress- or strain-like internal variables. The formulations proposed, for example, in SIMÓ [183], GOVINDJEE & SIMÓ [73], HOLZAPFEL & SIMÓ [97], LION [118] and KALISKE & ROTHERT [106] use internal variables of the *stress-type*. Most of them exploit the structure of linear viscoelastic standard solids and can be looked upon as special cases of the general theory of simple materials with fading memory as outlined in TRUESDELL & NOLL [198] and COLEMAN & NOLL [36]. In addition, the celebrated K-BKZ model of KAYE [108] and BERNSTEIN, KEARSLEY & ZAPAS [17] represents a class of optimal single-integral models of viscoelasticity. Besides the theories employing stress-like internal variables in the form of convolution integrals, the formulations of SIDOROFF [181], LUBLINER [122], LION [119], KECK & MIEHE [109], BERGSTRÖM & BOYCE [14], REESE & GOVINDJEE [171], HAUPT & SEDLAN [88] and REESE [170] use the multiplicative *split of the deformation gradient* into elastic and inelastic parts. The inelastic part enters the formulation as a *strain-like* tensorial internal state variable in the sense of COLEMAN & GURTIN [35]. An alternate kinematic approach to viscoelasticity based on the introduction of evolving *viscous metric tensors* as internal variables was outlined by MIEHE & KECK [150]. This framework a priori avoids difficulties of the above mentioned intermediate configuration theories, in particular doubts concerning a separate modeling of viscous rotations.

Some of the above mentioned approaches are purely phenomenological while some others are motivated from micromechanical considerations. Several molecular theories for the modeling of viscous behavior of molten polymers and physically cross-linked concentrated polymer networks were proposed in the last decades. Following WIJNTJES ET AL. [204], these molecular approaches can roughly be classified in three groups. The first group consists of *bead-spring models* conceptually in line with ROUSE [178] and ZIMM [212], see BIRD ET AL. [19] for a review. The *reptation-type tube models* proposed by DE GENNES [41] and DOI & EDWARDS [45] can be considered to define a second group of more advanced versions of bead-spring models. Ideas of the reptation model has already been utilized in the above mentioned macroscopic model of BERGSTRÖM & BOYCE [14], see also LULEI & MIEHE [125]. The *transient network model* was originally proposed by GREEN & TOBOLSKY [76] and further developed and revised by LODGE [120], TANAKA & EDWARDS [190]. In this third group of micromechanical approaches, polymer segments located between junction points are assumed to be reformed and destroyed during the deformation process. The effect of the chain breakage and formation on the network distribution was investigated in SCOTT & STEIN [180] and FURUKAWA [67]. Basic ideas of transient network models have been employed in the macroscopic models of LUBLINER [122], DROZDOV & DORFMANN [51], REESE [170], among others.

Deformation-Induced Softening in Rubbery Polymers. Investigations on the effect of stress softening in cyclic tensile stretching of rubber specimens can be traced back to the beginning of the last century starting with the works of BOUASSE & CARRIÈRE [20] and HOLT [96]. The observed deformation-induced softening phenomenon has often been referred to as the *Mullins effect* due to his detailed investigations starting from the late 1940s. MULLINS [155, 156] reported the following basic phenomenological observations:

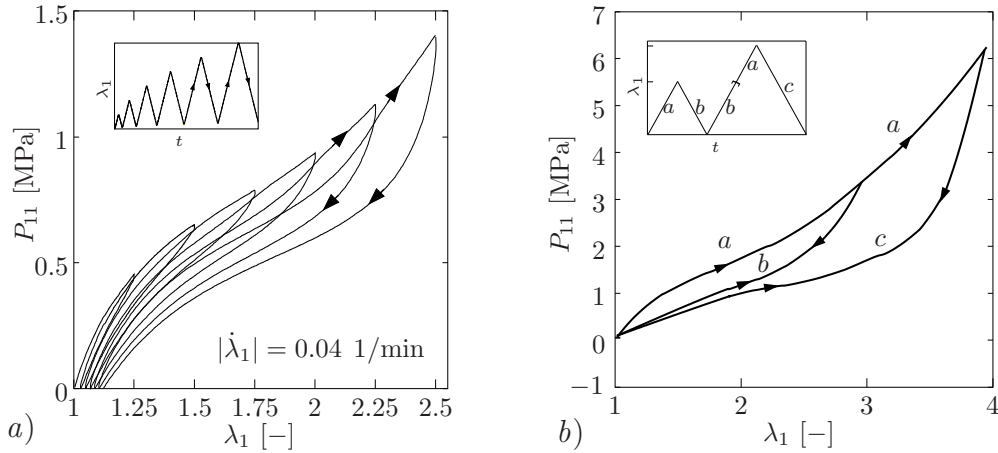


Figure 1.2: The Mullins effect. *a)* Cyclic uniaxial experiment on a fresh cylindrical rubber specimen HNBR50 at room temperature, MÉNDEZ [135]. Six cycles at progressively increasing stretch values $\lambda \in [1, 2.5]$ were applied at very slow loading rate $|\dot{\lambda}| = 4 \times 10^{-2}$ 1/min. The unloading-reloading curves do not coincide due to the rate dependency of the material. The stress-free state is recovered at a permanent set of non-vanishing strain. *b)* An idealized description considers the Mullins effect as a rate-independent phenomenon by neglecting the hystereses of unloading-reloading curves as well as the permanent set.

i) A substantial softening only occurs in rubbers at stretch values greater than a maximum obtained in the previous deformation history. *ii)* The degree of softening increases with the initial volume fraction of the filler, characterizing the softening effect as the breakdown of the stiffening microstructure due to fillers. *iii)* An anisotropic directional dependence of the softening was observed and supported by swelling experiments. *iv)* The healing of softening observed was very slow and complete recovery was never achieved. *v)* A softening behavior was also observed in compression tests, as also reported by BERGSTRÖM & BOYCE [14]. An *idealized description* of the Mullins effect in a quasi-static cyclic uniaxial tensile test with successively increasing stretches is schematically shown in Figure 1.2b. This idealization neglects viscous hystereses of the unloading-reloading curves depicted in Figure 1.2a. A common procedure is to interpret either retraction or reloading curves in Figure 1.2a as the idealized softened response of Figure 1.2b, see for example MULLINS & TOBIN [157], JAMES & GREEN [99] or MARCKMANN ET AL. [128] for recent treatment. Furthermore, it was observed that the retraction curves attain zero stress value at non-zero strain levels. It has commonly been attributed to intrinsic plasticity in the material behavior. This *permanent set phenomenon*, however, can also be considered as a basic indication of a *characteristic anisotropy* due to the strain-induced softening response. It has often been eliminated in context of isotropic damage models as shown in Figure 1.2b by shifting the unloading curves to the left by the amount of the permanent set, see for example the procedure explained in MULLINS & TOBIN [157].

A typical microstructure of a carbon-black filled rubber is depicted in Figure 5.1. The complex inelastic overall response of the material may be explained through various micromechanical mechanisms which simultaneously take place between the polymer matrix and the filler particles, see for example the reviews AKSEL & HÜBNER [2], DROZDOV & DORFMANN [50] and DANNENBERG [39]. However, there is no common agreement in the literature on a unique micromechanical mechanism leading to the Mullins-type stress softening. A rather phenomenological approach to the description of softening behavior of filled vulcanizates was proposed by MULLINS & TOBIN [157]. They considered the ma-

terial to be composed of *soft and hard regions* of rubber where most of the straining takes place in the soft regions. During deformation, the *fraction of the hard regions decreases* continuously and is transformed into the soft phase. In unloading-reloading up to a previous maximum deformation, the fractions of the individual phases are assumed to remain constant and upon extension beyond the previous maximum, the micro-stretch transformation continues. In a follow-up work, MULLINS & TOBIN [158] employed a *strain amplification factor* in order to describe the homogenized overall response of the two-phase composite. A similar approach was recently elaborated by KLÜPPEL & SCHRAMM [110]. A comparison of different approaches involving strain amplifications was carried out by GOVINDJEE [71] and BERGSTRÖM & BOYCE [15].

A rather molecular approach was suggested by BUECHE [31]. His theory of softening is based on the *breaking of bonds between chains and the fillers*. Considering three different chains of different contour lengths as depicted in Figure 5.1c, he argued that for appreciable amount of stretching, the shortest chain must rupture. Subsequently, the chain of intermediate length might rupture when it is subjected to moderate stretch values. Very large extension values are required for a breakdown of the longest chain. Owing to the different lengths of chains, the breakdown of chains takes place at any level of maximum extension. The chains torn off from the particles are considered as *elastically inactive*, because they do not contribute to entropy alteration of the network due to an externally imposed deformation. Hence, in case of reloading after retraction, the behavior of the rubber will be softer. He also explained the softening in the unfilled network at very large deformations on the basis of a *non-affine deformation* of the chains. As discussed in [149], short chains start to carry large forces at moderate deformations. At larger deformations a redistribution takes place and these chains elongate smaller than values dictated by an affine deformation. As a consequence, the network will not fail until such large deformations where redistributions are no longer possible. Hence, at small and moderate deformations relative to the limiting stretch values of the chains, the softening observed in pure gum vulcanizates is much smaller than in filled vulcanizates.

The explanation of the softening of unfilled rubbers by BUECHE [31] has been experimentally approved in a series of papers by HARWOOD ET AL. [81, 82, 83]. They contended that the softening should take place not at the interface between rubber and particles but solely in the rubber matrix. Possible mechanisms involving *breaking and reforming of crosslinks* during extension, residual local orientations after retraction and breaking of constituent chains were proposed. However, their conclusions that were drawn based on a normalization of data by using strain amplification factors were severely criticized by RIGBI [173], p.31 and MEDALIA [134]. Especially the claim that softening mechanisms should take place solely in the rubber matrix did not find common acceptance.

As mentioned above, a microstructural alteration scenario based on the destruction and reformation of the junction points, known as the transient network theory, was originally proposed by GREEN & TOBOLSKY [76] to account for the rate-dependent viscoelastic behavior of the polymeric networks. This idea was further exploited by RAJAGOPAL & WINEMAN [169] in their so-called *two network theory*. The activation conditions for the new junction points are formulated similar to the yield criterion in plasticity theory but evolution of the activation surface was not allowed. Further studies within this framework were conducted by BEATTY & KRISHNASWAMMY [12, 11] and MARKMANN ET AL. [128].

In addition to the above mentioned mechanisms, the *molecular slippage mechanism* discussed in the review papers DANNENBERG [39] and RIGBI [173] may be considered as generalizations of the breakage scenario of Bueche. It accounts for both viscoelastic and stress softening effects. Upon loading, chains slip relative to filler particles without rupturing. During this slippage a stress redistribution takes place and upon unloading the network attains a random distribution with chains of longer contour length. More advanced ideas in this direction as discussed in HAMED & HATFIELD [80] involve de-tangling mechanisms based on a bound layer and its interaction to the rubber phase. Even the healing phenomenon can be connected to a bound rubber layer formed on the particle surface. GOVINDJEE & SIMÓ [72] advanced the molecular ideas of BUECHE [31] to three-dimensional deformations by an averaging approach in a statistically representative sample volume. An important feature of their theory is the additive split of the free energy into CC- and PP-contributions motivated by the micromechanical structure, shown also in Figure 5.1. They were able to simulate large hysteresis effects very well. In their follow-up work, GOVINDJEE & SIMÓ [74] recast their former approach into a rather phenomenological framework based on the introduction of a *normalized stress function* which governs the unloading-reloading paths at a given level of stress softening.

Besides the micromechanically motivated theories mentioned above, many purely macroscopic models have been developed in the context of classical continuum damage mechanics. We refer to the works GURTIN & FRANCIS [79], SIMÓ [183], DE SOUZA NETO, PERIĆ & OWEN [43], MIEHE [139], LION [118, 119], MIEHE & KECK [150], KALISKE, NASDALA & ROTHERT [105] which model macroscopically *isotropic damage* in line with general treatments of KACHANOV [103] and LEMAITRE [116]. Furthermore, the *notion of pseudo elasticity* was employed for the modeling of the Mullins effect by OGDEN & ROXBURG [162]. Very recently, DORFMANN & OGDEN [46, 47] investigated the behavior of rubber for unloading-reloading and permanent set effects.

1.1.2. Finite Viscoplasticity of Amorphous Glassy Polymers. Amorphous glassy polymers have widely been employed in various practical application areas that cover automotive and construction industry, electronics, optical devices and medical technology, to mention a few. The broad spectrum of application is due to their good processing features, high energy absorption capacity under impact loadings, lower weight relative to glass, excellent optical properties. Geometry of the products used in the above mentioned practical applications is generally three-dimensional and has varying aspect ratios. Apart from the geometrical challenge, amorphous glassy polymers exhibit rate-dependent finite elastic-plastic material behavior. The elasto-viscoplastic response stems from the inherent disordered micro-structure of the material that is formed by linear polymer chains existing in the “*frozen-in*” state below the glass transition temperature. That is, in contrast to the chains constituting the rubber-like materials, the macromolecules of glassy polymers are not thermally agitated. Furthermore, being different from rubber-like materials and thermosets, they are generally not cross-linked by chemical bonds but their network structure is rather formed by physical junctions, the so-called *entanglements*. This intrinsic micro-structure gives rise to the rate and temperature effects prevailing in the material behavior. The finite elasto-viscoplastic behavior is not specific only to tough glassy polymers but is also observed in brittle glassy polymers on a much smaller scale, especially in the course of crazing. For this reason, both a sound three-dimensional constitutive model accounting for the complicated material behavior and an associated effective numerical algorithm for finite element simulations are of great importance.

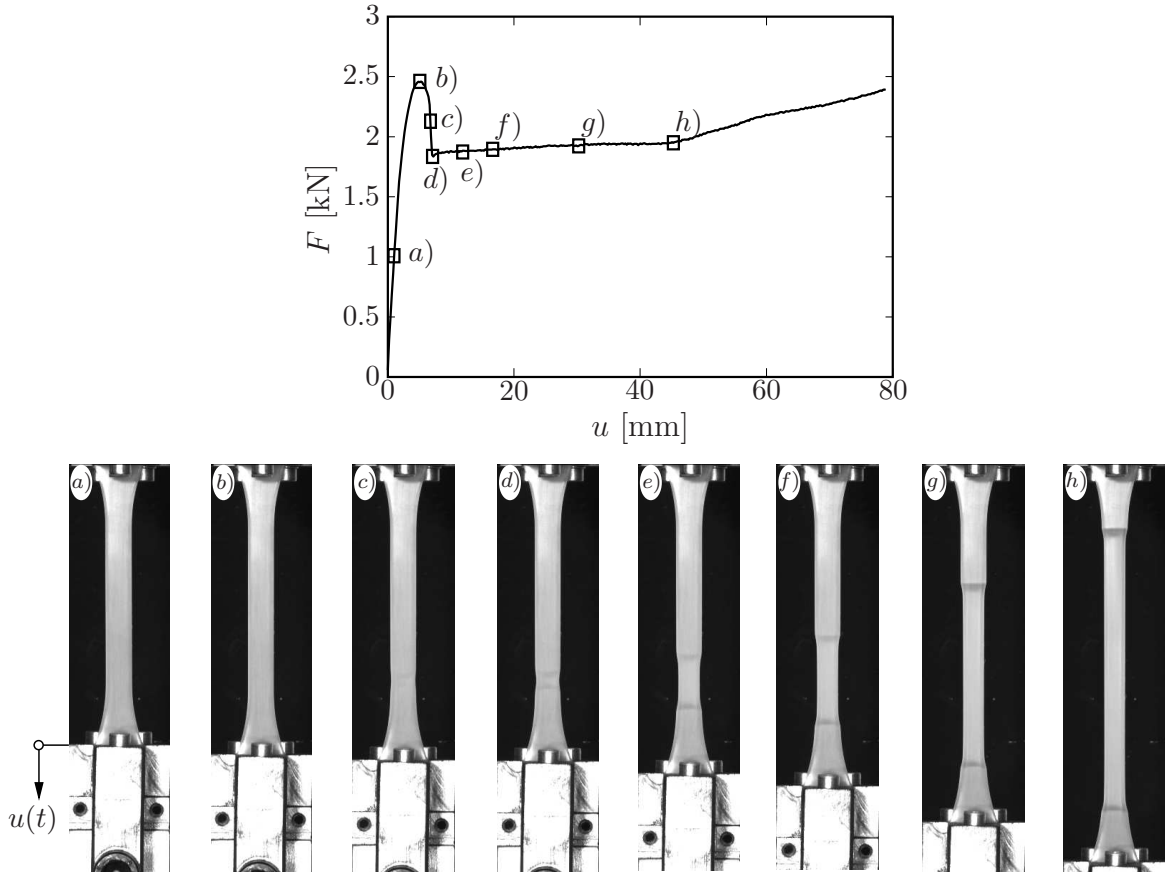


Figure 1.3: Load-displacement diagram and the snapshots of a dumbbell-shaped polycarbonate (PC) specimen subjected to extension at a constant cross-head speed $\dot{u}=2$ mm/min and room temperature. The selected stages of deformation labeled from *a)* to *h)* depict the process of initiation, stabilization and propagation (cold drawing) of neck.

Probably the most illustrative example for the finite viscoplastic behavior of ductile glassy polymers is the *cold drawing* process. A tensile load-displacement curve of a dumbbell-shaped polycarbonate (Makrolon 2607) test piece (ISO 527-Type 1B) undergoing cold drawing is depicted in Figure 1.3. The experiment was conducted at a constant cross-head speed $\dot{u}=2$ mm/min and room temperature. The representative stages of the deformation are labeled from *a)* to *h)* on both the load-displacement diagram and the snapshots of the deformed specimen in Figure 1.3. Combined the load-displacement diagram with the associated images shows the initiation, stabilization and propagation of the neck. Apart from these images, the quantitative principal stretch contours corresponding to the stages *a)*-*f)* of the experiment are presented in Figure 1.4. The contours were obtained by post-processing the recognized part of each associated image whose periphery is highlighted with the solid line in Figure 1.4. The commercial application ARAMIS was used to capture the three-dimensional strain field evolving on the surface of the dumbbell-shaped specimens during deformation, see also MÉNDEZ, GÖKTEPE & MIEHE [136].

In Figure 1.3, the initial linearly elastic part of the load-displacement curve bounded by the level *a)* falls into the range of small deformations. In the succeeding interval, between the stages *a)* and *b)*, the curve becomes gradually non-linear and exhibits viscoelastic characteristics as shown in Figure 1.3. At these stages of the extension, the strain field along the specimen is measured to be uniform, see Figures 1.4a and 1.4b. The highest

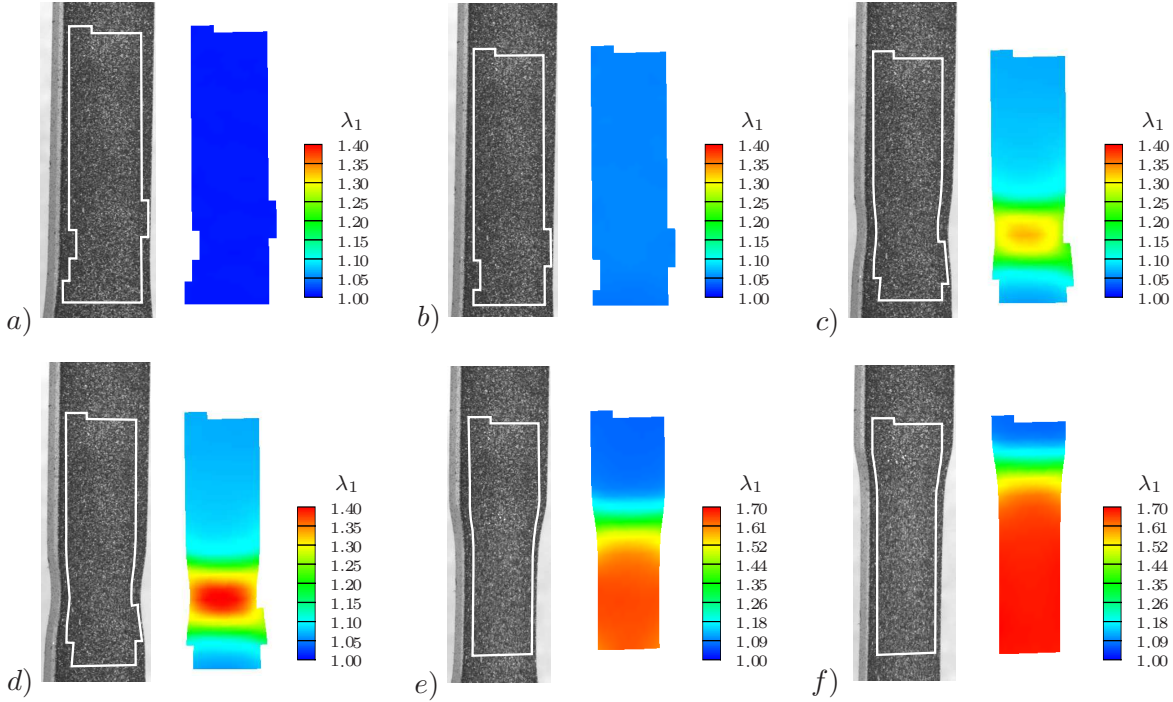


Figure 1.4: Major principal stretch measurements carried out by means of the optical measurement facility during the extension of the dumbbell-shaped of polycarbonate specimen described in Figure 1.3. Each set of a speckled snapshot of the specimen and a corresponding principal stretch contour plot labeled from a) to f) corresponds to a deformation state labeled with the same letter in Figure 1.3. The solid line drawn on the speckled specimen denotes the periphery of the active measurement region.

load level *b*) attained at the end of the non-linear viscoelastic part is generally called the *macro yield point*. Any unloading below this point does not result in significant hystereses or permanent strains, see also LU & RAVI-CHANDAR [123]. It has been shown that the pre-yield viscoelastic behavior is essential to elucidate the non-linear unloading and creep response of the material. For more detailed discussions concerning the phenomenon, the reader is referred to the recent works of HASAN & BOYCE [84] and ANAND & AMES [3]. Further extension beyond the yield point *b*) leads to inelastic strain localization regions that generally appear in the form of micro shear bands causing a softening in the load-displacement response, see also [123]. These bands then very rapidly multiply and combine between the load levels *b*) and *d*) initiating a macroscopic plastic localization zone, commonly called *necking*, compare Figures 1.3d and 1.4d. The contour plot in Figure 1.4c corresponding to an intermediate step during the process of neck stabilization clearly exhibits the nature of this process. As depicted in Figure 1.3, the thickness of the neck reaches an almost stationary state and stabilizes around the lowest post-yield load level at the stage *d*). This is the point where the chains in the active necking zone start to align plastically along the extension direction. The alignment of the molecules gives rise to the *local strain hardening* and causes the neck front to propagate through the test piece at an almost constant load level between the stages *d*) and *h*). This process is commonly called *cold drawing* and yields a highly anisotropic deformed state as a result of large inelastic alignment of chains. During this process, the contour plots corresponding to the stages *d*)-*f*) indicate some further extension in the already plasticized regions. This is also reflected in the gradual hardening in the load-displacement diagram, albeit its slight slope. As the neck shoulders reach the grip zone about point *h*), the curve starts to stiffen

again and climbs up till the ultimate failure.

In the above described cold drawing experiment, as the contour plots in Figure 1.4 clearly illustrate, beyond the macroscopic yield point *b*) the stress/strain field along the specimen is not homogeneous anymore. Besides, the rate of deformation at different material points considerably differs from each other. Since the material response is rate-dependent, any stress-strain relation obtained from such type of experiment without special measuring techniques equipped with specific control devices would not reflect the true local material response, see for example HOPE, WARD & GIBSON [98], G'SELL & JONAS [78] and G'SELL ET AL. [77]. In order to circumvent the difficulties associated with the inhomogeneous strain distribution in tensile experiments, uniaxial and plane strain compression experiments have been carried out to investigate the local stress-strain response. In these compressive tests a macroscopically homogeneous strain state can be achieved provided that the friction between the specimen and platens is eliminated by employing an appropriate lubrication technique. For instance, BOWDEN & RAHA [23, 168] reported the results of plane strain compression tests on polymethylmethacrylate (PMMA) and polystyrene (PS). The uniaxial and plane strain compression stress-strain data of PMMA and PC up to the true strain value $\ln \lambda \approx -1$ have been presented in ARRUDA & BOYCE [7], BOYCE, ARRUDA & JAYACHANDRAN [26]. In Figure 6.4b the true stress-true strain response of PC under uniaxial and plane strain compression is depicted. As can be immediately noticed, the stress-strain response exhibits a *true strain softening* followed by *strain hardening* at large deformations. The softening is believed to be resulted from a localized shear band formation accompanied by the evolution of local free-volume, see ARGON [5], HASAN ET AL. [85], HASAN & BOYCE [84] and ANAND & GURTIN [4]. It has also been observed in Figure 6.4b that the yield stress in glassy polymers exhibits both the deformation state and the pressure dependency, see SPITZIG & RICHMOND [187].

During the transition from a rubbery to a glassy state, the random micro-structure of the material is generally conserved, see TRELOAR [196]. The mobility of the chains, however, is greatly affected by a decrease in temperature. At temperatures well below the glass transition temperature, the mobility of the molecules declines substantially and they exist in a “frozen-in” state. As commonly accepted, two types of physical resistance govern the energy barrier that must be overcome to yield the material and to deform it up to large plastic strains. These are associated with the *intermolecular* and *intramolecular* mechanisms, respectively. The plastic flow of glassy polymers is a thermally activated, statistical process whose rate is proportional to the celebrated Boltzmann factor $\exp(-\Delta G/k\theta)$, where ΔG , k , θ are the energy barrier to be surmounted, the Boltzmann constant, and the absolute temperature, respectively. To achieve the macroscopic yielding, the stress state in the material must be brought to a level at which the necessary thermal energy state for the segment rotation can be attained. This barrier is proven to be closely related to the *intermolecular resistance*, and thus depends on the pressure, which increases the degree of packing in the material micro-structure. After yielding, the material flows and molecules align in the flow direction. During the orientation of chains, conformational entropy of chains decreases. Similar to the elasticity of rubbery polymers, finite plastic deformations accompanied by strain hardening can only be attained by overcoming the *entropic resistance*, see HAWARD & THACKRAY [91], ARGON [5] and references therein.

Early theories on glassy polymers, e.g. MARSHALL & THOMPSON [132], endeavored to account for the plastic deformation through an increase in chain mobility due to either a

deformation-induced dissipative heating leading to higher temperature or a deformation-induced increase in *free volume* providing more room for the motion. Although these factors facilitate the plastic flow below the glass transition temperature, they cannot be justified as the sole reasons yielding the active motion of molecules, see VINCENT [201]. Owing to the above arguments, first, viscoelasticity theories have been employed for the description of the phenomena. These theories, being essentially based on Eyring-type [57] rate equations, are restricted to limited range of temperature and deformation rates. Besides, the physical significance of the phenomenological parameters appearing in the theory remains dubious, see BOWDEN [21], CRIST [38] for a review. These theories have been followed by physically-based plasticity models motivated from the experimentally observed permanent residual deformation remaining after unloading. Probably the most significant molecular theories for the rate-dependent inelastic behavior of amorphous polymers have been proposed by ROBERTSON [176] and ARGON [5]. In the Robertson model, plasticity is attributed to a thermally activated transition of molecular chains from flexed to extended configurations by rotation of its segments. This scenario is based on the overcoming of only the *intramolecular* resistance by externally applied stress. The celebrated *double-kink* theory of ARGON [5] is also based on the thermally activated process but the resistance to the flow is primarily attributed to the *intermolecular* interactions via the so-called wedge disclinations, see LI & GILMAN [117]. Compared to the former, the latter yields better agreement with the experiments conducted at temperatures well below the glass transition temperature θ_g . This indicates the importance of intermolecular interactions in the yield mechanism of glassy polymers. On the other hand, the former has been shown to be relatively better at temperatures close to θ_g , see ARGON & BESSONOV [6].

Over the past decades, considerable effort was made to develop three-dimensional constitutive models that account for the finite viscoplastic behavior of glassy polymers. The pioneering works of BOYCE, ARGON, PARKS and co-workers [28, 8, 9, 84] have been followed, for instance, by WU & VAN DER GIESSEN [206, 207, 208], TOMITA & TANAKA [192], GOVAERT, TIMMERMANS & BREKELMANS [70] and ANAND & GURTIN [4]. The molecular double-kink theory [5] was extended to the three-dimensional formulation by BOYCE, PARKS & ARGON [28] where they also incorporated the strain softening by a phenomenological evolution equation for the athermal shear strength. In this work, they applied the double-kink theory to the rate-dependent evolution of finite plastic flow. Kinematics of the plastic deformation is based on the multiplicative split of the deformation gradient into elastic and plastic parts. The immediate outgrowth of this multiplicative split is the hypothetical intermediate configuration, in contrast to metals, the rotation of which is not unique and is not well understood in the case of amorphous materials. Therefore, in this context one needs to make an additional assumption concerning the rotation tensor or the plastic spin. Motivating from the results of BOYCE, WEBER & PARKS [29], they assumed that the elastic part of the deformation gradient is symmetric. For modeling the strain hardening in the post-yield regime, the entropic network models borrowed from the statistical rubber elasticity theories have been employed. As the temperature of a plastically deformed material is risen above the glass transition temperature without any restraint, it is observed to regain its original shape as well as isotropic molecular structure, see HAWARD & MANN [89], HAWARD, MURPHY & WHITE [90]. Therefore, the recovery of the original shape at $\theta > \theta_g$ suggests the existence of internal forces, commonly referred to as back stresses at $\theta < \theta_g$. These may be considered as external forces at $\theta > \theta_g$ required to keep the material in the deformed state. Moreover, the

existence of memory effect necessitates an sparsely connected network structure. In the case of linear glassy polymers possessing high molecular weight, this network structure is provided by entanglements. Owing to the similarity between rubber-like and plastic post-yield response, as originally suggested by HAWARD & THACKRAY [91], the post-yield strain hardening response has conventionally been modeled by the network models proposed in [101, 203, 8, 206].

1.2. Scope and Outline

Chapter 2 is devoted to the principal kinematic and balance relations of continuum thermomechanics. These involve the fundamental geometric mappings, basic deformation and stress measures, and balance equations of a solid body undergoing finite deformations. Apart from the reiteration of the basic relations, it is also aimed to introduce the nomenclature employed in the subsequent chapters. This chapter is further supplemented by **Appendix A** where the spectral representation of the right Cauchy-Green tensor along with the derivatives of its eigenvalues and eigenvectors is addressed.

In **Chapter 3**, we develop a micro-mechanically based non-affine network model incorporating topological constraints on a single chain. The proposed approach to rubber-like elasticity is based on a micro-structure symbolized by a *micro-sphere* whose surface represents a continuous distribution of chain orientations in space. Core of the model is a new two-dimensional constitutive setting of the micro-mechanical response of a *single polymer chain in a constrained environment* defined by two micro-kinematic variables: the stretch of the chain and the contraction of the cross-section of a micro-tube surrounding the chain under consideration. The second key feature is a new *non-affine micro-macro transition* that defines the three-dimensional overall response of the polymer network based on a characteristic homogenization procedure of micro-variables defined on the micro-sphere of space orientations. The micro-macro procedure determines a stretch fluctuation field on the micro-sphere through a variational principle of minimum averaged free energy and links the two micro-kinematic variables in a non-affine manner to the line-stretch and the area-stretch of the macro-continuum. Therefore, the model describes two superimposed contributions resulting from free chain motions and their topological constraints in an attractive dual geometric structure on both the micro- and the macro-level. Averaging operations on the micro-sphere are directly evaluated through an efficient numerical integration scheme. The overall model contains five effective material parameters obtained from the single chain statistics and properties of the network with clearly identifiable relationships to characteristic phenomena observed in homogeneous experiments. The proposed approach substantially advances features of the *affine full network* and the *eight-chain* models with regard to their modeling capability. The excellent quantitative performance of the model is illustrated through comparative studies with previously developed network models and by fitting experimental benchmark data acquired from homogeneous and non-homogeneous tests. Complementary **Appendices B** and **C** provide details of the employed decoupled volumetric-isochoric framework and the Gaussian and non-Gaussian statistics of the freely jointed chain, respectively.

Chapter 4 is concerned with an extension of the non-affine micro-sphere model towards the description of time-dependent finite viscoelastic effects. The viscoelastic network model is constructed through an additive split of the overall response into elastic equilibrium-stress and viscous overstress contributions. The equilibrium response of the

network is understood to be related to results obtained from an infinite relaxation process and modeled via the elasticity formulation outlined in Chapter 3. Inspiring from our elastic network model, the rate-dependent overstress response is assumed to be driven by *two micro-kinematical mechanisms* related to the stretch and the area contraction of a tube containing a prototype chain. Firstly, a *retraction of fictitiously unconstrained dangling chains* is described by diffusive reptile motions. Secondly, a *release of constraint effects* due to surrounding chains is modeled by a time-dependent alteration of tube cross-section area. The latter contribution is considered to be a result of the retraction of constraining forest chains. We outline a distinct micromechanically-based model for the viscous overstress in terms of the above outlined two micro-kinematic mechanisms and discuss its numerical implementation in context of an *affine homogenization procedure* of space orientations. The characteristics and modeling capabilities of the proposed micro-sphere model of finite rubber viscoelasticity are reported for a broad spectrum of experimentally-based benchmark simulations, which involve rate and hysteresis effects of rubbery polymers.

Chapter 5 provides a further extension of the micro-sphere network model towards to the deformation-induced softening commonly referred to as the Mullins effect. To this end, a continuum formulation is constructed by a superimposed modeling of a crosslink-to-crosslink (CC) and a particle-to-particle (PP) network. The former is described by the non-affine elastic network model outlined in Chapter 3. The Mullins-type damage phenomenon is embedded into the PP network and micromechanically motivated by a breakdown of bonds between chains and filler particles. Key idea of the constitutive approach is a two-step procedure that includes *i)* the set up of micromechanically-based constitutive models for a *single chain orientation* and *ii)* the definition of the macroscopic stress response by a *directly evaluated homogenization* of state variables defined on a micro-sphere of space orientations. In contrast to previous works on the Mullins effect, our formulation inherently describes a *deformation-induced anisotropy* of the damage as observed in experiments. We show that the experimentally observed *permanent set* in stress-strain diagrams is automatically attained by the proposed model as a natural outgrowth of the anisotropic distribution of damage. The performance of the model is demonstrated by means of several numerical experiments.

Chapter 6 addresses the constitutive modeling of rate-dependent finite elastic-plastic behavior of amorphous glassy polymers. The kinematical formulation of the present model is based on the framework in the logarithmic strain space. In contrast to the existing kinematical approaches to the finite viscoplasticity of glassy polymers, the modular kinematic setting of the proposed framework is based on the *a priori* six-dimensional plastic metric. Therefore, it avoids inherent difficulties concerning the uniqueness of plastic rotation in the intermediate space. The analogy between the formulation of finite plasticity in the logarithmic strain space and the geometrically linear theory of plasticity makes this framework very attractive, in particular regarding the algorithmic implementation. The micromechanically motivated flow rule for viscoplastic strains in the logarithmic strain space is adopted from the celebrated *double-kink* theory. The post-yield kinematic hardening response is modeled through the eight-chain model and our non-affine micro-sphere model. The models are compared against homogeneous experimental data acquired from uniaxial and plane strain compression tests on polycarbonate. Besides the simulation of the true stress-strain curves obtained from homogeneous experiments, a load-displacement diagram of a dumbbell-shaped polycarbonate specimen undergoing cold-drawing along with three-dimensional optical measurements of the surface strain fields is simulated.

2. Fundamentals of Continuum Mechanics

This chapter outlines the principal equations of non-linear continuum mechanics that describe the fundamental geometric mappings, basic stress measures, balance equations of a solid body undergoing finite, possibly inelastic, deformations. Apart from the reiteration of the basic relations in continuum mechanics, it is also aimed to introduce the notation used in the forthcoming chapters. Most of the material treated here is based on the lecture notes of MIEHE [143, 145] and also well documented in the literature. For more comprehensive treatment the reader is referred to the monographs and books, for example, by ERINGEN [54], TRUESDELL & NOLL [198], CHADWICK [33], MARSDEN & HUGHES [131], OGDEN [161], HAUPT [87], MIEHE [141, 142] among others.

2.1. The Motion, Fundamental Geometric Maps and Deformation Measures

A *material body* B is composed of infinitely many *material points* $P \in B$ that are identified with geometrical points in the three-dimensional Euclidean metric space \mathbb{R}^3 . The configuration of the body B in \mathbb{R}^3 at time t is described by a one-to-one relation

$$\chi_t := \begin{cases} B & \rightarrow \mathcal{B}_t \in \mathbb{R}^3, \\ P \in B & \mapsto \mathbf{x}_t = \chi_t(P) \in \mathcal{B}_t. \end{cases} \quad (2.1)$$

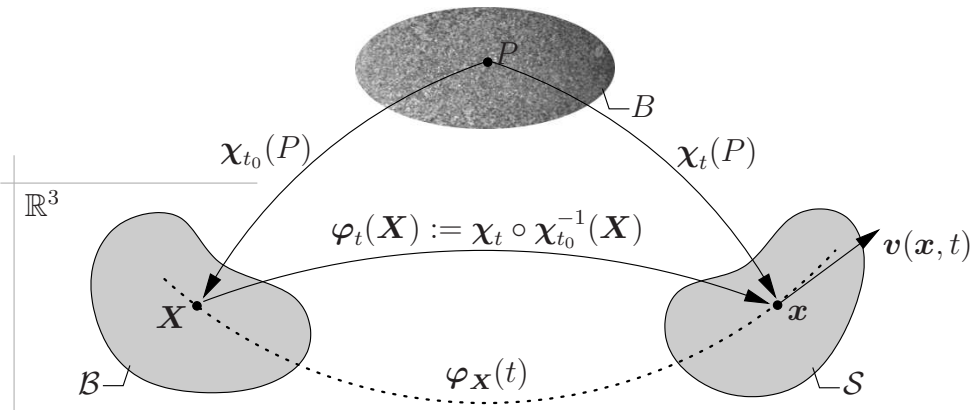


Figure 2.1: Mathematical description of the motion of a solid body in \mathbb{R}^3 .

While describing the motion of a solid body, it is common practice to name its placement at time t_0 as the *reference configuration* that generally possesses an undistorted stress-free state and is henceforth denoted as $\mathcal{B} \equiv \chi_{t_0}(B)$. Likewise, the configuration of the body at current time t is hereafter denoted as $\mathcal{S} \equiv \chi_t(B)$. The reference and the spatial positions occupied by a material point P within the Euclidean space are labeled by the *reference coordinates* $\mathbf{X} := \chi_{t_0}(P) \in \mathcal{B}$ and the *spatial coordinates* $\mathbf{x} := \chi_t(P) \in \mathcal{S}$, respectively. In order to describe the *motion* of the solid body in the Euclidean space, we introduce a non-linear *deformation map* $\varphi_t(\mathbf{X})$ between $\chi_{t_0}(P)$ and $\chi_t(P)$

$$\varphi_t(\mathbf{X}) := \begin{cases} \mathcal{B} & \rightarrow \mathcal{S}, \\ \mathbf{X} & \mapsto \mathbf{x} = \varphi_t(\mathbf{X}) := \chi_t \circ \chi_{t_0}^{-1}(\mathbf{X}) \end{cases} \quad (2.2)$$

that maps the material points $\mathbf{X} \in \mathcal{B}$ onto their deformed *spatial* positions $\mathbf{x} = \varphi_t(\mathbf{X}) \in \mathcal{S}$ at time $t \in \mathbb{R}_+$, see Figure 2.1.

Having the motion (2.2) defined, we are now in a position to introduce the *material velocity*

$$\mathbf{V}_t(\mathbf{X}) := \partial_t \boldsymbol{\varphi}(\mathbf{X}, t) = \frac{d}{dt} \boldsymbol{\varphi}_{\mathbf{X}}(t), \quad (2.3)$$

and the *material acceleration* of the motion

$$\mathbf{A}_t(\mathbf{X}) := \partial_t \mathbf{V}(\mathbf{X}, t) = \frac{d}{dt} \mathbf{V}_{\mathbf{X}}(t). \quad (2.4)$$

The *spatial velocity* is then expressed as

$$\mathbf{v}_t(\mathbf{x}, t) := \mathbf{V}_t(\mathbf{X}) \circ \boldsymbol{\varphi}_t^{-1}(\mathbf{x}), \quad (2.5)$$

and the *spatial acceleration* is defined as the *material time derivative* of the spatial velocity

$$\mathbf{a}_t(\mathbf{x}, t) := \mathbf{A}_t(\mathbf{X}) \circ \boldsymbol{\varphi}_t^{-1}(\mathbf{x}) = \partial_t \mathbf{v} + \nabla_x \mathbf{v} \cdot \mathbf{v}. \quad (2.6)$$

where $\nabla_x \mathbf{v} =: \mathbf{l}$ stands for the *spatial velocity gradient*. The *path* $\boldsymbol{\varphi}_{\mathbf{X}}(t)$ is then called the *integral curve* of \mathbf{v} as shown in Figure 2.1.

The reference \mathcal{B} and spatial \mathcal{S} configurations of a body can be considered as continuous three-dimensional manifolds which are locally furnished by charts in the neighborhoods \mathcal{N}_X and \mathcal{N}_x of the reference coordinates $\{X^A\}_{A=1,2,3}$ and spatial coordinates $\{x^a\}_{a=1,2,3}$, respectively. For the computation of norm quantities such as scalar products, length measures, invariants, these local coordinate systems are further equipped with the covariant reference $\mathbf{G} = G_{AB}$ and spatial $\mathbf{g} = g_{ab}$ metrics, respectively. The both metric tensors, however, reduce to the Kronecker deltas, $\mathbf{G} = \delta_{AB}$ and $\mathbf{g} = \delta_{ab}$, in the case of Cartesian coordinate systems, which we devise in the subsequent treatment. It is important to note that both metrics are symmetric and positive definite due to their basic function.

Probably the most fundamental deformation measure used in kinematics of finite deformation is the *deformation gradient*. It can be considered as a linear map of the referential tangent vectors onto the spatial counterparts. To this end, let $\mathfrak{C}(\Theta)$ and $\mathfrak{c}(\Theta)$ be the material and spatial curves parameterized by a common variable $\Theta \in \mathbb{R}$ on \mathcal{B} and \mathcal{S} , respectively. Furthermore, we consider that the spatial curve is related to the reference curve by the non-linear deformation map $\mathfrak{c}(\Theta) = \boldsymbol{\varphi}_t(\mathfrak{C}(\Theta))$ due to (2.2). Tangents of the curves belonging to the respective tangent spaces defined as the derivatives $\mathbf{T} := d\mathfrak{C}(\Theta)/d\Theta \in T_X \mathcal{B}$ and $\mathbf{t} := d\mathfrak{c}(\Theta)/d\Theta \in T_x \mathcal{S}$ as depicted in Figure 2.2. Through the chain rule, the spatial tangent \mathbf{t} can be expressed in terms of the material tangent \mathbf{T}

$$\mathbf{t} = \frac{d}{d\Theta} \mathfrak{c}(\Theta) = \nabla_X \boldsymbol{\varphi}_t(\mathbf{X}) \frac{d}{d\Theta} \mathfrak{C}(\Theta) = \mathbf{F} \mathbf{T} \quad \text{with} \quad t^a = F^a_A T^A. \quad (2.7)$$

This already introduces the deformation gradient $\mathbf{F} := \nabla_X \boldsymbol{\varphi}_t(\mathbf{X})$ with components $F^a_A := \partial \varphi^a / \partial X^A$ as the *tangent map*

$$\mathbf{F}_t := \begin{cases} T_X \mathcal{B} & \rightarrow T_x \mathcal{S}, \\ \mathbf{T} & \mapsto \mathbf{t} = \mathbf{F}_t \mathbf{T}, \end{cases} \quad (2.8)$$

between the tangent spaces $T_X \mathcal{B}$ and $T_x \mathcal{S}$ of the manifolds \mathcal{B} and \mathcal{S} , respectively.

Once the deformation gradient has been defined, we can proceed with the other two fundamental maps. For this purpose, let dV and dv denote the infinitesimal volumes of parallelepipeds

$$dV := d\mathbf{X}_1 \cdot (d\mathbf{X}_2 \times d\mathbf{X}_3) \quad \text{and} \quad dv := d\mathbf{x}_1 \cdot (d\mathbf{x}_2 \times d\mathbf{x}_3) \quad (2.9)$$

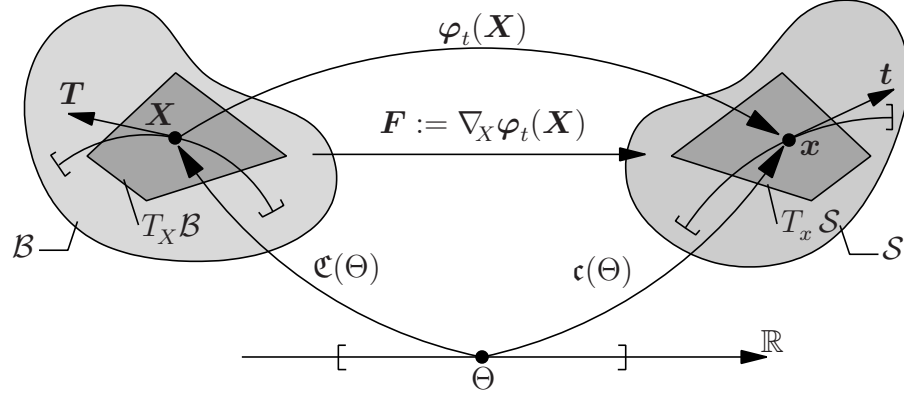


Figure 2.2: The deformation gradient \mathbf{F} defined as a *tangent map* linearly transforming the material vector $\mathbf{T} \in T_X \mathcal{B}$ tangent to the material curve $\mathfrak{C}(\Theta)$ at \mathbf{X} onto the the spatial vector $\mathbf{t} \in T_x \mathcal{S}$ tangent to the spatial curve $\mathfrak{c}(\Theta)$ at \mathbf{x} .

defined as the scalar triple product of vectors $d\mathbf{X}_{i=1,2,3} \in T_X \mathcal{B}$ and $d\mathbf{x}_{i=1,2,3} \in T_x \mathcal{S}$, respectively. Each spatial tangent vector $d\mathbf{x}_i$ is defined as a tangential map of its material counterpart, i.e. $d\mathbf{x}_i := \mathbf{F}d\mathbf{X}_i$ for $i = 1, 2, 3$. This then leads to the definition of the *volume map*

$$dv = (\mathbf{F}d\mathbf{X}_1) \cdot ((\mathbf{F}d\mathbf{X}_2) \times (\mathbf{F}d\mathbf{X}_3)) = \det \mathbf{F} dV =: J dV \quad (2.10)$$

following the conventional coordinate-free definition of the determinant of a second order tensor, see e.g. ŠILHAVÝ [182]. The value of the Jacobian J is restricted to positive real numbers \mathbb{R}_+ , i.e. $J > 0$, in order to ensure the one-to-one relation between \mathbf{x} and \mathbf{X} and the impenetrability of a material. Then, we say that the volume map, $\det \mathbf{F}$, maps the reference volume elements onto their spatial counterparts

$$J = \det \mathbf{F} := \begin{cases} \mathbb{R}_+ & \rightarrow \mathbb{R}_+, \\ dV & \mapsto dv = \det \mathbf{F} dV. \end{cases} \quad (2.11)$$

The *co-factor* of the deformation gradient $\text{cof } \mathbf{F}$ is defined as the derivative of the volume map $J := \det \mathbf{F}$ with respect to deformation gradient \mathbf{F} . In order to derive the explicit form of $\text{cof } \mathbf{F}$, we begin by taking the derivative of both sides of (2.10) with respect to \mathbf{F}

$$\partial_{\mathbf{F}} dv = \partial_{\mathbf{F}} \det \mathbf{F} dV = (d\mathbf{x}_2 \times d\mathbf{x}_3) \otimes d\mathbf{X}_1 + (d\mathbf{x}_3 \times d\mathbf{x}_1) \otimes d\mathbf{X}_2 + (d\mathbf{x}_1 \times d\mathbf{x}_2) \otimes d\mathbf{X}_3.$$

Contraction of the both sides of this equality from left by one of the spatial tangent vectors $d\mathbf{x}_i$ and division of the result by dV lead us to

$$(\mathbf{F}d\mathbf{X}_i) \cdot \partial_{\mathbf{F}} \det \mathbf{F} = \det \mathbf{F} d\mathbf{X}_i, \quad (2.12)$$

where the orthogonality condition $d\mathbf{x}_i \cdot (d\mathbf{x}_i \times d\mathbf{x}_j) = d\mathbf{x}_i \cdot (d\mathbf{x}_j \times d\mathbf{x}_i) = 0$ (no sum over i) and the definition (2.11) have been incorporated. Finally, the solution of (2.12) for $\partial_{\mathbf{F}} \det \mathbf{F}$ by eliminating $d\mathbf{X}_i$ yields the sought explicit form the co-factor

$$\text{cof } \mathbf{F} := \partial_{\mathbf{F}} \det \mathbf{F} = (\det \mathbf{F}) \mathbf{F}^{-T}. \quad (2.13)$$

In order to make the geometrical meaning of $\text{cof } \mathbf{F}$ more transparent, let us define the reference and spatial *area co-vectors* $\mathbf{N}dA := d\mathbf{X}_2 \times d\mathbf{X}_3$ and $\mathbf{n}da := d\mathbf{x}_2 \times d\mathbf{x}_3$, respectively. With these definitions at hand, we can recast (2.11) into the following from

$$d\mathbf{x}_1 \cdot \mathbf{n}da = J d\mathbf{X}_1 \cdot \mathbf{N}dA. \quad (2.14)$$

If we incorporate the identity $d\mathbf{x}_1 = \mathbf{F}d\mathbf{X}_1$ in (2.14) and solve this equality for $\mathbf{n}da$ for an arbitrary tangent vector $d\mathbf{X}_1$, we end up with the interpretation of co-factor as the *area map*

$$\mathbf{n}da = J\mathbf{F}^{-T}\mathbf{N}dA = (\text{cof } \mathbf{F})\mathbf{N}dA \quad (2.15)$$

transforming the co-vectors (one-forms) of the material surfaces onto the normal vectors of spatial surfaces. Furthermore, we observe that the tensorial quantity carrying out the mapping operation in (2.15) is none other than \mathbf{F}^{-T} . Thus, we consider \mathbf{F}^{-T} as the *normal map* transforming the reference co-vectors \mathbf{N} onto the spatial co-vectors \mathbf{n} belonging to the respective *co-tangent* spaces $T_X^*\mathcal{B}$ and $T_x^*\mathcal{S}$. The *normal map* is then defined as

$$\mathbf{F}^{-T} := \begin{cases} T_X^*\mathcal{B} & \rightarrow T_x^*\mathcal{S}, \\ \mathbf{N} & \mapsto \mathbf{n} = \mathbf{F}^{-T}\mathbf{N}. \end{cases} \quad (2.16)$$

Having the tangent and the co-tangent spaces defined, we can now interpret the covariant reference \mathbf{G} and the spatial \mathbf{g} metrics

$$\mathbf{G}: T_X\mathcal{B} \rightarrow T_X^*\mathcal{B} \quad , \quad \mathbf{g}: T_x\mathcal{S} \rightarrow T_x^*\mathcal{S} \quad , \quad (2.17)$$

as the mappings from the tangent spaces $T_X\mathcal{B}$ and $T_x\mathcal{S}$ to the co-tangent spaces $T_X^*\mathcal{B}$ and $T_x^*\mathcal{S}$, respectively. That is, \mathbf{G} and \mathbf{g} map tangents onto co-vectors by the *index lowering* operation

$$\begin{aligned} \mathbf{T}^b &= \mathbf{G}\mathbf{T} & , & & T_A &= G_{AB}T^B, \\ \mathbf{t}^b &= \mathbf{g}\mathbf{t} & , & & t_a &= g_{ab}t^b. \end{aligned} \quad (2.18)$$

Analogously, we can further consider the inverse metrics \mathbf{G}^{-1} and \mathbf{g}^{-1}

$$\begin{aligned} \mathbf{T} &= \mathbf{G}^{-1}\mathbf{T}^b & , & & T^A &= G^{AB}T_B, \\ \mathbf{t} &= \mathbf{g}^{-1}\mathbf{t}^b & , & & t^a &= g^{ab}t_b, \end{aligned} \quad (2.19)$$

as the mappings from the co-tangent spaces $T_X^*\mathcal{B}$ and $T_x^*\mathcal{S}$ to the tangent spaces $T_X\mathcal{B}$ and $T_x\mathcal{S}$ through the *index raising*. With the definitions (2.17)-(2.19) at hand, we are ready to construct the commutative diagrams, Figure 2.3, illustrating the *pull-back* and the *push-forward* operations on \mathbf{G} and \mathbf{g} and their contravariant inverse metrics \mathbf{G}^{-1} and \mathbf{g}^{-1} , separately. As shown in Figure 2.3a, the push-forward of the inverse of the reference metric $\mathbf{b} := \varphi_*(\mathbf{G}^{-1})$ and itself $\mathbf{c} := \varphi_*(\mathbf{G})$ are defined by

$$\begin{aligned} \mathbf{b} &:= \varphi_*(\mathbf{G}^{-1}) = \mathbf{F}\mathbf{G}^{-1}\mathbf{F}^T & , & & b^{ab} &= F^a_A G^{AB} F^b_B, \\ \mathbf{c} = \mathbf{b}^{-1} &:= \varphi_*(\mathbf{G}) = \mathbf{F}^{-T}\mathbf{G}\mathbf{F}^{-1} & , & & c_{ab} &= (F^{-1})^A_a G_{AB} (F^{-1})^B_b \end{aligned} \quad (2.20)$$

and called the *left Cauchy-Green tensor (Finger deformation tensor)* and the *inverse left Cauchy-Green tensor*, respectively. Similarly, based on the commutative diagram depicted in Figure 2.20b, the pull-back of the spatial metric $\mathbf{C} := \varphi^*(\mathbf{g})$ and its inverse $\mathbf{C}^{-1} := \varphi^*(\mathbf{g}^{-1})$ are defined by

$$\begin{aligned} \mathbf{C} &:= \varphi^*(\mathbf{g}) = \mathbf{F}^T\mathbf{g}\mathbf{F} & , & & C_{AB} &= F^a_A g_{ab} F^b_B, \\ \mathbf{C}^{-1} &:= \varphi^*(\mathbf{g}^{-1}) = \mathbf{F}^{-1}\mathbf{g}^{-1}\mathbf{F}^{-T} & , & & (C^{-1})^{AB} &= (F^{-1})^A_a g^{ab} (F^{-1})^B_b \end{aligned} \quad (2.21)$$

and denoted as the *right Cauchy-Green tensor (convected spatial metric)* and the *inverse right Cauchy-Green tensor*, respectively.

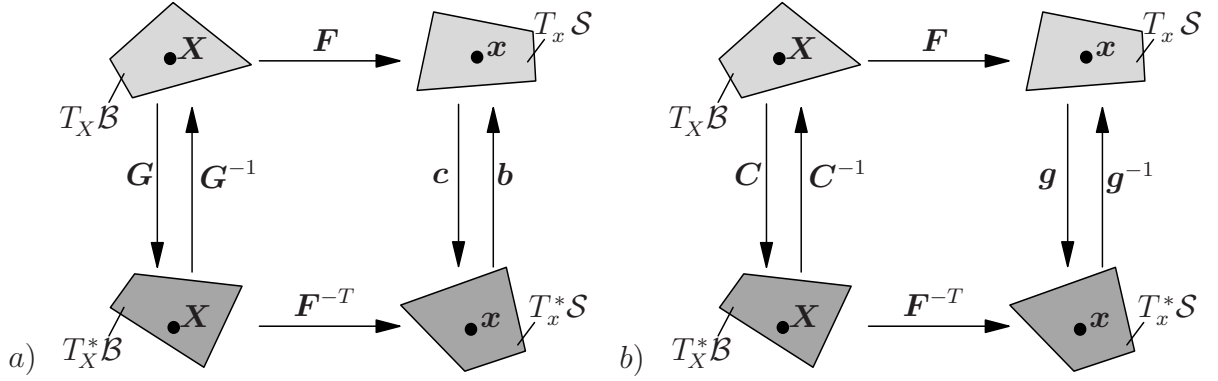


Figure 2.3: The *push-forward* and *pull-back* of the reference G and spatial g metrics and their contravariant inverse forms G^{-1} and g^{-1} , separately.

As mentioned above, the both metric tensors and their inverse tensors are symmetric and positive definite and therefore so do their respective push-forwards (2.20) and pull-backs (2.21). The above introduced deformation tensors play a fundamental role in measuring the basic deformations. To illustrate this, let us consider tangent vectors $\mathbf{T} \in T_X \mathcal{B}$ and $\mathbf{t} := \mathbf{F}\mathbf{T} \in T_x \mathcal{S}$, and define the *stretch*, $\bar{\lambda}$, as the ratio of the length of the deformed tangent vector \mathbf{t} to the length of the reference tangent vector \mathbf{T} , i.e. $\bar{\lambda} := |\mathbf{t}|_g / |\mathbf{T}|_G = \sqrt{\mathbf{t} \cdot \mathbf{g}\mathbf{t}} / \sqrt{\mathbf{T} \cdot \mathbf{G}\mathbf{T}} > 0$. Setting $|\mathbf{T}|_G = 1$ as the *reference* value, the stretch can be expressed as

$$\bar{\lambda} = \sqrt{\mathbf{t} \cdot \mathbf{g}\mathbf{t}} = \sqrt{\mathbf{F}\mathbf{T} \cdot \mathbf{g}\mathbf{F}\mathbf{T}} = \sqrt{\mathbf{T} \cdot \mathbf{F}^T \mathbf{g}\mathbf{F}\mathbf{T}} = \sqrt{\mathbf{T} \cdot \mathbf{C}\mathbf{T}} =: |\mathbf{T}|_C$$

in the so-called *Lagrangian* (material) description of the length deformation, compare with (3.30). This justifies the name *convected spatial metric* coined to the right Cauchy-Green tensor \mathbf{C} . On the other hand, we can also set $|\mathbf{t}|_g = 1$ in the so-called *Eulerian* (spatial) description of the deformation and express the inverse stretch

$$\bar{\lambda}^{-1} = \sqrt{\mathbf{T} \cdot \mathbf{G}\mathbf{T}} = \sqrt{\mathbf{F}^{-1}\mathbf{t} \cdot \mathbf{G}\mathbf{F}^{-1}\mathbf{t}} = \sqrt{\mathbf{t} \cdot \mathbf{F}^{-T} \mathbf{G}\mathbf{F}^{-1}\mathbf{t}} = \sqrt{\mathbf{t} \cdot \mathbf{c}\mathbf{t}} =: |\mathbf{t}|_c$$

in terms of the inverse left Cauchy-Green tensor $\mathbf{c} = \mathbf{b}^{-1}$. We observe that \mathbf{C} and \mathbf{c} act as metric tensors in the respective Lagrangian and Eulerian description of the length deformation. Analogous to the length stretch $\bar{\lambda}$, we can also introduce the *area stretch*, $\bar{\nu}$, as the ratio of the length of the deformed normal $\mathbf{n} = \mathbf{F}^{-T}\mathbf{N} \in T_x^* \mathcal{S}$ to the length of the reference normal $\mathbf{N} \in T_X^* \mathcal{B}$; that is, $\bar{\nu} := |\mathbf{n}|_{g^{-1}} / |\mathbf{N}|_{G^{-1}} = \sqrt{\mathbf{n} \cdot \mathbf{g}^{-1}\mathbf{n}} / \sqrt{\mathbf{N} \cdot \mathbf{G}^{-1}\mathbf{N}} > 0$. Fixing the value $|\mathbf{N}|_{G^{-1}} = 1$, we obtain the Lagrangian description of the area stretch

$$\bar{\nu} = \sqrt{\mathbf{n} \cdot \mathbf{g}^{-1}\mathbf{n}} = \sqrt{\mathbf{F}^{-T}\mathbf{N} \cdot \mathbf{g}^{-1}\mathbf{F}^{-T}\mathbf{N}} = \sqrt{\mathbf{N} \cdot \mathbf{F}^{-1} \mathbf{g}^{-1} \mathbf{F}^{-T} \mathbf{N}} =: |\mathbf{N}|_{C^{-1}}$$

as a norm of the material normal \mathbf{N} with respect to the inverse right Cauchy-Green tensor \mathbf{C}^{-1} , compare with (3.55). In the spatial description, we set $|\mathbf{n}|_{g^{-1}} = 1$ and express the inverse area stretch $\bar{\nu}^{-1}$ in terms of the Finger tensor

$$\bar{\nu}^{-1} = \sqrt{\mathbf{N} \cdot \mathbf{G}^{-1}\mathbf{N}} = \sqrt{\mathbf{F}^T \mathbf{n} \cdot \mathbf{G}^{-1} \mathbf{F}^T \mathbf{n}} = \sqrt{\mathbf{n} \cdot \mathbf{F}\mathbf{G}^{-1} \mathbf{F}^T \mathbf{n}} = \sqrt{\mathbf{n} \cdot \mathbf{b}\mathbf{n}} =: |\mathbf{n}|_b.$$

The foregoing examples concerning the elongation and area changes give a clear geometrical interpretation of the fundamental deformation tensors introduced by the pull-back and

push-forward operations of the metrics. These deformation measures enter the various constitutive formulations of non-linear material theories. The isotropic finite elasticity theory, especially in modeling of rubber-like materials, is conceivably the most fundamental class of these theories where the invariants and the principal values of these deformation tensors are widely employed. The models formulated in terms of the principal stretches necessitate the knowledge of eigenvalues, eigenvectors and their derivatives with respect to an associated deformation tensor. Appendix A is, therefore, dedicated to the spectral representation of the right Cauchy-Green tensor as a representative example.

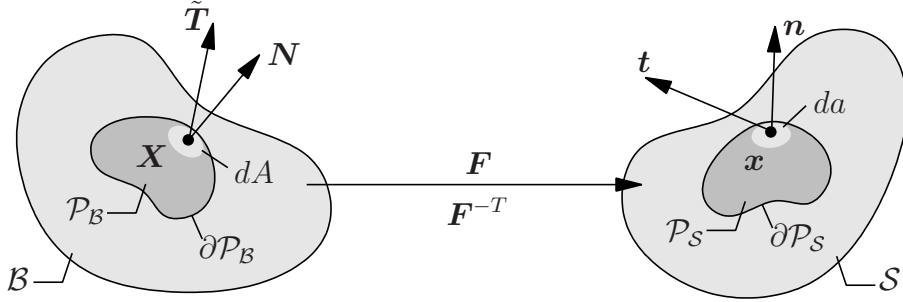


Figure 2.4: The material $\tilde{\mathbf{T}}(\mathbf{X}, t; \mathbf{N}) \in T_{\mathbf{X}}\mathcal{B}$ and spatial $\mathbf{t}(\mathbf{x}, t; \mathbf{n}) \in T_{\mathbf{x}}\mathcal{S}$ traction (stress) vectors representing the force action of the rest of the body at the vicinity, on the surfaces of the cut parts $\partial\mathcal{P}_B$ and $\partial\mathcal{P}_S$, respectively.

2.2. Cauchy's Stress Theorem and the Fundamental Stress Measures

Consider a part $\mathcal{P}_B \subset \mathcal{B}$ cut off from the reference body \mathcal{B} and its spatial counterpart $\mathcal{P}_S \subset \mathcal{S}$ closed by the respective boundaries $\partial\mathcal{P}_B$ and $\partial\mathcal{P}_S$ as depicted in Figure 2.4. In the deformed configuration, we introduce the *stress vector* \mathbf{t} that acts on the surface element da of $\partial\mathcal{P}_S$ and represents the force action of the rest of the body at the vicinity $\mathcal{P}_S \setminus \mathcal{S}$ on $\partial\mathcal{P}_S$. The *Cauchy stress theorem* states that the spatial traction vector $\mathbf{t} \in T_{\mathbf{x}}\mathcal{S}$ linearly depends on the spatial normal $\mathbf{n} \in T_{\mathbf{x}}^*\mathcal{S}$ of the surface $\partial\mathcal{P}_S$, i.e.

$$\mathbf{t}(\mathbf{x}, t; \mathbf{n}) := \boldsymbol{\sigma}(\mathbf{x}, t) \mathbf{n} , \quad (2.22)$$

through the *Cauchy (true) stress tensor* $\boldsymbol{\sigma}$. Cauchy's stress theorem can be proven based on the force equilibrium on a tetrahedron, see e.g. HAUPT [87], p.91. In the geometrical framework outlined so far, the Cauchy stress tensor can be understood as a contravariant mapping transforming normals $\mathbf{n} \in T_{\mathbf{x}}^*\mathcal{S}$ onto tangent vectors $\mathbf{t} \in T_{\mathbf{x}}\mathcal{S}$

$$\boldsymbol{\sigma} := \begin{cases} T_{\mathbf{x}}^*\mathcal{S} & \rightarrow T_{\mathbf{x}}\mathcal{S} , \\ \mathbf{n} & \mapsto \mathbf{t} = \boldsymbol{\sigma} \mathbf{n} . \end{cases} \quad (2.23)$$

Another spatial stress measure, the *Kirchhoff stress tensor*, also known as the *weighted Cauchy stress tensor*, is defined as

$$\boldsymbol{\tau} := J \boldsymbol{\sigma} \quad (2.24)$$

and widely used in the spatial description of stress power terms in the reference volume. Owing to the scalar scaling by the Jacobian J , the Kirchhoff stresses retain the geometrical transformation characteristics of the Cauchy stress, i.e. $\boldsymbol{\tau} : T_{\mathbf{x}}^*\mathcal{S} \rightarrow T_{\mathbf{x}}\mathcal{S}$. Now let us consider another spatial traction vector $\mathbf{T} \in T_{\mathbf{x}}\mathcal{S}$ defined through the force equality $\mathbf{T} dA := \mathbf{t} da$ by scaling the spatial force term ($\mathbf{t} da$) through the reference area element dA . Based on this definition, we introduce the *first Piola-Kirchhoff stress tensor* by the

reference Cauchy theorem $\mathbf{T} := \mathbf{P}\mathbf{N}$ leading to $\mathbf{P}\mathbf{N} dA = \boldsymbol{\sigma}\mathbf{n} da$. Using the area map (2.15), we obtain the relation $\mathbf{P} = \boldsymbol{\tau}\mathbf{F}^{-T} = J\boldsymbol{\sigma}\mathbf{F}^{-T}$ between the first Piola-Kirchhoff stress tensor and the spatial stress measures introduced in (2.23) and (2.24). Notice that \mathbf{P} is a two-point tensor possessing the geometrical mapping properties

$$\mathbf{P} := \begin{cases} T_X^* \mathcal{B} & \rightarrow T_x \mathcal{S}, \\ \mathbf{N} & \mapsto \mathbf{T} = \mathbf{P} \mathbf{N}. \end{cases} \quad (2.25)$$

The transformation $(\blacksquare) = J(\bullet)\mathbf{F}^{-T}$ devised in obtaining the first Piola-Kirchhoff stress tensor from the Cauchy stress tensor is called the *Piola transformation*. It is widely employed in transforming the objects acting on a *spatial surface* onto their material counterparts. The immediate outcome of the Piola transformation is the *Piola Identity*

$$J \operatorname{div}(\bullet) = \operatorname{DIV}(\blacksquare) = \operatorname{DIV}(J(\bullet)\mathbf{F}^{-T}) \quad (2.26)$$

that also implies the equality $\operatorname{DIV}(J\mathbf{F}^{-T}) = \mathbf{0}$. In order to show this identity, we consider a spatial vector field \mathbf{t} . The surface integral of its scalar product with a spatial normal \mathbf{n} over a sufficiently smooth spatial surface $\partial\mathcal{P}_S$ can be converted to the volume integral through the *Gauss integral theorem*, i.e.

$$\int_{\partial\mathcal{P}_S} \mathbf{t} \cdot \mathbf{n} da = \int_{\mathcal{P}_S} \operatorname{div}(\mathbf{t}) dv. \quad (2.27)$$

The domain of the surface integral in (2.27) can be changed to the material surface $\partial\mathcal{P}_B$ by the area map (2.15) and then again converted to the volume integral in the reference volume \mathcal{P}_B by the Gauss integral theorem in material coordinates; that is,

$$\int_{\partial\mathcal{P}_B} \mathbf{t} \cdot J\mathbf{F}^{-T} \mathbf{N} dA = \int_{\mathcal{P}_B} \operatorname{DIV}(J\mathbf{t}\mathbf{F}^{-T}) dV = \int_{\mathcal{P}_S} \operatorname{div}(\mathbf{t}) dv + \int_{\mathcal{P}_B} \mathbf{t} \cdot \operatorname{DIV}(J\mathbf{F}^{-T}) dV. \quad (2.28)$$

Comparison of (2.27) and (2.28) necessitates $\int_{\mathcal{P}_B} \mathbf{t} \cdot \operatorname{DIV}(J\mathbf{F}^{-T}) dV = 0$ that in turn leads us to the Piola Identity

$$\operatorname{DIV}(J\mathbf{F}^{-T}) = \mathbf{0}$$

for infinitely small \mathcal{P}_B and an arbitrary spatial vector field \mathbf{t} . For a sufficiently smooth surface $\partial\mathcal{P}_B$ this result of the Piola identity also implies that

$$\int_{\mathcal{P}_B} \operatorname{DIV}(J\mathbf{F}^{-T}) dV = \int_{\partial\mathcal{P}_B} J\mathbf{F}^{-T} \mathbf{N} dA = \int_{\partial\mathcal{P}_S} \mathbf{n} da = \mathbf{0}.$$

Following analogous steps, it can also be readily shown that

$$\operatorname{div}(J\mathbf{F}^T) = \mathbf{0} \quad \text{and} \quad \int_{\partial\mathcal{P}_B} \mathbf{N} dA = \mathbf{0}.$$

The Lagrangean stress vector $\tilde{\mathbf{T}} \in T_X \mathcal{B}$ may be defined through the pull-back of the spatial stress vector $\mathbf{T} \in T_x \mathcal{S}$

$$\tilde{\mathbf{T}} = \boldsymbol{\varphi}^*(\mathbf{t}) = \mathbf{F}^{-1} \mathbf{T} \in T_X \mathcal{B}, \quad \tilde{T}^A = (F^{-1})^A_a T^a,$$

as depicted in Figure 2.4. The third fundamental stress measure, the *second Piola-Kirchhoff stress tensor* \mathbf{S} , is then defined by $\tilde{\mathbf{T}} := \mathbf{S}\mathbf{N}$ yielding

$$\mathbf{S} := \begin{cases} T_X^*\mathcal{B} & \rightarrow T_X\mathcal{B}, \\ \mathbf{N} & \mapsto \tilde{\mathbf{T}} = \mathbf{S}\mathbf{N}. \end{cases} \quad (2.29)$$

Incorporating the definitions (2.23)-(2.25) in (2.29), we can express the second Piola-Kirchhoff stress tensor in terms of the other stress tensors

$$\begin{aligned} \mathbf{S} &:= \varphi^*(\mathbf{P}) = \mathbf{F}^{-1}\mathbf{P} & , & \quad S^{AB} = (F^{-1})^A{}_a P^{aB}, \\ \mathbf{S} &:= \varphi^*(\boldsymbol{\tau}) = \mathbf{F}^{-1}\boldsymbol{\tau}\mathbf{F}^{-T} & , & \quad S^{AB} = (F^{-1})^A{}_a \tau^{ab} (F^{-1})^B{}_b \end{aligned}$$

as the pull-back of the contravariant two-point and spatial objects. Apparently the converse push-forward relations do also hold for the spatial stress tensors

$$\boldsymbol{\tau} = J\boldsymbol{\sigma} = \varphi_*(\mathbf{P}) = \mathbf{P}\mathbf{F}^T \quad \text{and} \quad \boldsymbol{\tau} = \varphi_*(\mathbf{S}) = \mathbf{F}\mathbf{S}\mathbf{F}^T,$$

as shown in the commutative diagram, Figure 2.5.

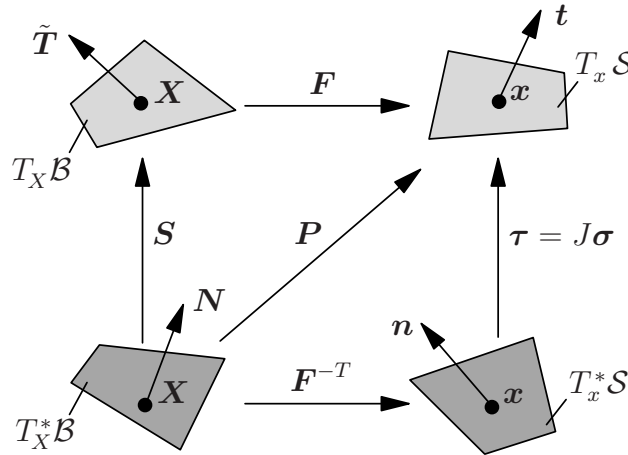


Figure 2.5: Commutative diagram illustrating the *push-forward* and *pull-back* operations among the stress measures.

2.3. Balance Principles of Continuum Thermomechanics

The balance laws of continuum mechanics serve as a basic set of equations required to solve an initial boundary value problem of thermomechanics for the primary variables. This section is devoted to derivation of the fundamental balance laws of continuum thermomechanics. In what follows, we consider a certain spatial volume \mathcal{P}_S closed by the boundary $\partial\mathcal{P}_S$ as shown in Figure 2.4. For this part of the body, we write a balance equation where we will often have the volumetric source and the surface flux terms contributing a temporal change of the quantity for which the balance principle is constructed. In order to derive the local forms of the balance laws, we follow the following basic steps. First, we carry the surface flux terms into the body through the Gauss integral theorem (2.27). Once the balance equation is completely recast into a volume integral, the expression can be localized to its local form by stating that integrand must also fulfill the equality for an infinitely small part \mathcal{P}_S provided that the continuity conditions are met. This spatial balance equation is then recast into its reference form.

Balance of Mass. Total mass of a closed system, the part of a body \mathcal{P}_S under consideration, remains constant; that is, the system is free of agencies that produce or destroy mass within the volume \mathcal{P}_S or is not subjected to flux terms that transfer mass over the surface $\partial\mathcal{P}_S$. To this end, we define the *spatial mass density* $\rho(\mathbf{x}, t)$ and its material counterpart the *reference mass density* $\rho_0(\mathbf{X})$ and require

$$\frac{d}{dt}\mathcal{M} := \frac{d}{dt} \int_{\mathcal{P}_S} \rho(\mathbf{x}, t) dv = \frac{d}{dt} \int_{\mathcal{P}_B} J\rho(\mathbf{x}, t) dV = \frac{d}{dt} \int_{\mathcal{P}_B} \rho_0(\mathbf{X}) dV = 0. \quad (2.30)$$

Making use of the identity $\dot{J} := dJ/dt = \text{cof } \mathbf{F} : \dot{\mathbf{F}} = J \text{tr}(\mathbf{l}) = J \text{div}(\mathbf{v})$ in (2.30)₃ and equating the integrands of (2.30)₂ and (2.30)₃, we end up with the spatial and material forms of the *local mass balance* equations

$$\dot{\rho} + \rho \text{div}(\mathbf{v}) = 0 \quad \text{and} \quad J\rho(\mathbf{x}, t) = \rho_0(\mathbf{X}). \quad (2.31)$$

Balance of Linear Momentum. Being analogous to classical discrete mechanics, the time rate of linear momentum of the volume \mathcal{P}_S is equal to the sum of the forces acting on the body. Two types of forces are considered: the mass specific body forces $\boldsymbol{\gamma}(\mathbf{x}, t)$ due to the action of other bodies at a distance and the surface forces (stress vectors) \mathbf{t} due to the action at a vicinity. These can also be regarded as a momentum source and a momentum flux terms, respectively. The *balance of linear momentum* then requires

$$\frac{d}{dt}\mathcal{L} := \frac{d}{dt} \int_{\mathcal{P}_S} \rho\mathbf{v}(\mathbf{x}, t) dv = \int_{\mathcal{P}_S} \rho\boldsymbol{\gamma}(\mathbf{x}, t) dv + \int_{\partial\mathcal{P}_S} \mathbf{t}(\mathbf{x}, t; \mathbf{n}) da. \quad (2.32)$$

Incorporation of the mass balance (2.31) in the time derivative and the Cauchy stress theorem (2.22) through the integral theorem (2.27) in the surface integral, we obtain the local form of the spatial linear momentum balance

$$\rho\mathbf{a} = \rho\boldsymbol{\gamma} + \text{div}(\boldsymbol{\sigma}). \quad (2.33)$$

Multiplication of the spatial form (2.33) with the Jacobian J , and incorporation of the mass balance (2.31)₁ and the Piola identity (2.26) yields the material form of the local linear momentum balance

$$\rho_0\mathbf{A} = \rho_0\boldsymbol{\Gamma} + \text{DIV}(\mathbf{P}) \quad (2.34)$$

where $\mathbf{A}(\mathbf{X}, t)$ denotes the material acceleration defined in (2.4) and $\boldsymbol{\Gamma}(\mathbf{X}, t) := \boldsymbol{\gamma}(\mathbf{x}, t) \circ \boldsymbol{\varphi}_t(\mathbf{X})$ stands for the material body force defined per unit mass.

It is believed to be illustrative that the integration of the product of spatial linear momentum balance (2.33) with the spatial velocity co-vector $\mathbf{v}^b = \mathbf{g}\mathbf{v}$ over the body \mathcal{P}_S yields

$$\frac{d}{dt} \int_{\mathcal{P}_S} \frac{1}{2} \rho \mathbf{v} \cdot \mathbf{v}^b dv = \int_{\mathcal{P}_S} \rho \boldsymbol{\gamma} \cdot \mathbf{v}^b dv + \int_{\mathcal{P}_S} \text{div}(\boldsymbol{\sigma}) \cdot \mathbf{v}^b dv.$$

Insertion of the equality $\int_{\mathcal{P}_S} \text{div}(\boldsymbol{\sigma}) \cdot \mathbf{v}^b dv = \int_{\partial\mathcal{P}_S} (\boldsymbol{\sigma}\mathbf{n}) \cdot \mathbf{v}^b da - \int_{\mathcal{P}_S} \boldsymbol{\sigma} : (\mathbf{g}\mathbf{l}) dv$ for the last term yields the so-called *theorem of expended power*

$$\left. \begin{aligned} \dot{\mathcal{K}} &+ \dot{\mathcal{W}} &= &\mathcal{P} \\ \frac{d}{dt} \int_{\mathcal{P}_S} \frac{1}{2} \rho \mathbf{v} \cdot \mathbf{v}^b dv &+ \int_{\mathcal{P}_S} \boldsymbol{\sigma} : (\mathbf{g}\mathbf{l}) dv &= &\int_{\mathcal{P}_S} \rho \boldsymbol{\gamma} \cdot \mathbf{v}^b dv + \int_{\partial\mathcal{P}_S} \mathbf{t} \cdot \mathbf{v}^b da \end{aligned} \right\} \quad (2.35)$$

stating that the total power due to the externally applied forces \mathcal{P} is equal to the summation of the temporal change of the kinetic energy \mathcal{K} and the internal stress power $\dot{\mathcal{W}}$.

Balance of Angular Momentum. The time derivative of the moment of linear momentum of \mathcal{P}_S is required to be equal to the sum of the moments of the forces acting on the body with respect to the same point. Without loss of generality, taking the moment with respect to the origin yields

$$\frac{d}{dt} \int_{\mathcal{P}_S} \mathbf{x} \times \rho \mathbf{v} dv = \int_{\mathcal{P}_S} \mathbf{x} \times \rho \boldsymbol{\gamma} dv + \int_{\partial \mathcal{P}_S} \mathbf{x} \times \mathbf{t} da. \quad (2.36)$$

Exploiting the mass balance (2.31), the equality $\mathbf{v} \times \mathbf{v} = \mathbf{0}$ in (2.36)₁ and the Cauchy stress theorem (2.22) through the integral theorem (2.27) in the surface integral (2.36)₃, we obtain

$$\int_{\mathcal{P}_S} \mathbf{x} \times (\rho \mathbf{a} - \rho \boldsymbol{\gamma} - \operatorname{div}(\boldsymbol{\sigma})) dv = \int_{\mathcal{P}_S} \boldsymbol{\iota} dv = \mathbf{0} \quad (2.37)$$

where we demand $\iota_a := \epsilon_{abc} \sigma^{cb} = 0$. Since the *permutation symbol* ϵ_{abc} is skew symmetric with respect to two indices, e.g. $\epsilon_{abc} = -\epsilon_{acb}$, the equality (2.37) is fulfilled only for the symmetric Cauchy stresses. Thus, the balance of angular momentum results in

$$\boldsymbol{\sigma} = \boldsymbol{\sigma}^T, \quad \sigma^{ab} = \sigma^{ba}. \quad (2.38)$$

Owing to the push-forward and pull-back relations derived in Section 2.2, the other two stress measures $\boldsymbol{\tau}$ and \mathbf{S} are required to satisfy the following symmetry relations

$$\boldsymbol{\tau} = \boldsymbol{\tau}^T, \quad \mathbf{P}\mathbf{F}^T = \mathbf{F}\mathbf{P}^T, \quad \mathbf{S} = \mathbf{S}^T \quad (2.39)$$

as well. Observe that the first Piola-Kirchhoff stresses are generally non-symmetric.

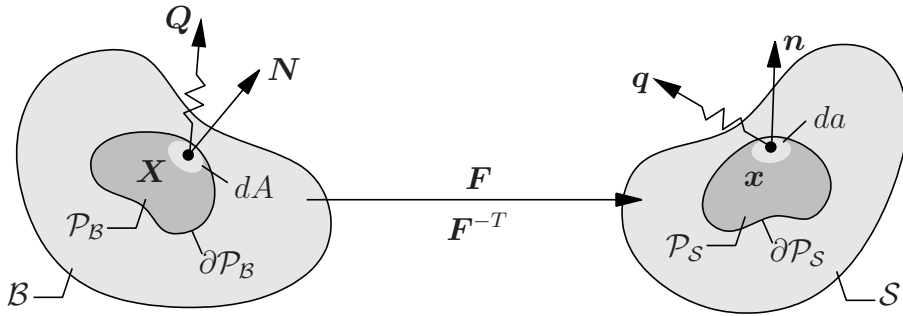


Figure 2.6: The material $\mathbf{Q}(\mathbf{X}, t) \in T_X \mathcal{B}$ and spatial $\mathbf{q}(\mathbf{x}, t) \in T_x \mathcal{S}$ heat flux vectors representing the conduction of heat through the rest of the body over the surfaces of the cut parts $\partial \mathcal{P}_B$ and $\partial \mathcal{P}_S$, respectively.

Balance of Energy (The First Law of Thermodynamics). The *first law of thermodynamics* states that temporal change of total energy is equal to the sum of the mechanical and thermal power. The total energy is defined as a summation of the kinetic energy \mathcal{K} , see (2.35), and the internal energy $\mathcal{E} := \int_{\mathcal{P}_S} \rho e(\mathbf{x}, t) dv$ where $e(\mathbf{x}, t)$ denotes the mass specific *internal energy density*. The external mechanical power \mathcal{P} has already been introduced in (2.35). The *thermal power* $\mathcal{Q} = \int_{\mathcal{P}_S} \rho r dv - \int_{\partial \mathcal{P}_S} \mathbf{q} \cdot \mathbf{n} da$ is composed of the specific heat source $r(\mathbf{x}, t)$ and the surface heat flux vector $\mathbf{q}(\mathbf{x}, t)$, see Figure 2.6. The balance of energy has then the following global form

$$\frac{d}{dt} (\mathcal{K} + \mathcal{E}) = \mathcal{P} + \mathcal{Q} \quad (2.40)$$

where we immediately observe that $\dot{\mathcal{K}} - \mathcal{P} = -\dot{\mathcal{W}}$ due to the *theorem of power expended* introduced in (2.35). Incorporating this result in (2.40), we obtain $\dot{\mathcal{E}} = \dot{\mathcal{W}} + \mathcal{Q}$, localization of which through the integral theorem leads us to the spatial local form

$$\rho \dot{e} = \boldsymbol{\sigma} : (\mathbf{g}\mathbf{l}) + \rho r - \operatorname{div}(\mathbf{q}) . \quad (2.41)$$

Analogous to the definition of the first Piola-Kirchhoff stress tensor, we introduce the *reference heat flux vector* \mathbf{Q} that fulfills the equality $\mathbf{q} \cdot \mathbf{n} da = \mathbf{Q} \cdot \mathbf{N} dA$ through the area map $\mathbf{Q} := J\mathbf{q}\mathbf{F}^{-T}$ as introduced in (2.15) and depicted in Figure 2.6. This immediately implies that \mathbf{Q} is none other than the Piola transform of the spatial heat flux vector \mathbf{q} and therefore the equality $J \operatorname{div}(\mathbf{q}) = \operatorname{DIV}(\mathbf{Q})$ is satisfied identically. Having defined the reference heat flux vector \mathbf{Q} , the spatial energy balance equation (2.41) can be recast into the reference local form by following the obvious steps

$$\rho_0 \dot{e} = \boldsymbol{\tau} : (\mathbf{g}\mathbf{l}) + \rho_0 R - \operatorname{DIV}(\mathbf{Q}) \quad (2.42)$$

with $R(\mathbf{X}, t) := r(\mathbf{x}, t) \circ \boldsymbol{\varphi}_t(\mathbf{X})$.

For the forthcoming developments, it is important to note that the volume specific stress power term $\mathcal{P} := J\boldsymbol{\sigma} : (\mathbf{g}\mathbf{l}) = \boldsymbol{\tau} : (\mathbf{g}\mathbf{l})$ appears as a scalar product the stress measures and their *work conjugate* variable the spatial velocity gradient $\mathbf{g}\mathbf{l}$. Since $\boldsymbol{\tau}$ or $\boldsymbol{\sigma}$ is symmetric, the stress power term \mathcal{P} can be rewritten as $\mathcal{P} = \boldsymbol{\tau} : \mathbf{d}$ with $\mathbf{d} := \operatorname{sym}(\mathbf{g}\mathbf{l}) = \frac{1}{2}(\mathbf{g}\mathbf{l} + \mathbf{l}^T \mathbf{g})$ denoting the *rate of deformation tensor*, which is equivalent to the half of the *Lie derivative* of the spatial metric \mathbf{g} . The Lie derivative of a spatial object is geometrically defined as the push-forward of the material time derivative of its pull-back; that is,

$$\mathcal{L}_v(\bullet) := \boldsymbol{\varphi}_* \left(\frac{d}{dt} \boldsymbol{\varphi}^*(\bullet) \right) . \quad (2.43)$$

With this definition at hand, the *rate of deformation gradient* \mathbf{d} can be obtained as

$$\frac{1}{2} \mathcal{L}_v(\mathbf{g}) = \frac{1}{2} \boldsymbol{\varphi}_* \left(\frac{d}{dt} \boldsymbol{\varphi}^*(\mathbf{g}) \right) = \frac{1}{2} \boldsymbol{\varphi}_* \left(\frac{d}{dt} \mathbf{C} \right) = \frac{1}{2} \mathbf{F}^{-T} \dot{\mathbf{C}} \mathbf{F}^{-1} = \frac{1}{2} (\mathbf{g}\mathbf{l} + \mathbf{l}^T \mathbf{g}) , \quad (2.44)$$

where $\mathbf{l} := \nabla_x \mathbf{v} = \dot{\mathbf{F}} \mathbf{F}^{-1}$ denotes the spatial velocity gradient. Therefore, the analogous representations of the stress power \mathcal{P} can also be derived in terms of \mathbf{P}

$$\mathcal{P} := \boldsymbol{\tau} : (\mathbf{g}\mathbf{l}) = \mathbf{P} \mathbf{F}^T : \mathbf{g} \dot{\mathbf{F}} \mathbf{F}^{-1} = \mathbf{g} \mathbf{P} : \dot{\mathbf{F}} \quad (2.45)$$

and also for \mathbf{S}

$$\mathcal{P} := \boldsymbol{\tau} : \mathbf{d} = \boldsymbol{\tau} : \frac{1}{2} \mathcal{L}_v(\mathbf{g}) = \mathbf{F} \mathbf{S} \mathbf{F}^T : \frac{1}{2} \mathbf{F}^{-T} \dot{\mathbf{C}} \mathbf{F}^{-1} = \mathbf{S} : \frac{1}{2} \dot{\mathbf{C}} . \quad (2.46)$$

The alternative representations of the stress power $\mathcal{P} = \boldsymbol{\tau} : \mathbf{d} = \mathbf{g} \mathbf{P} : \dot{\mathbf{F}} = \mathbf{S} : \frac{1}{2} \dot{\mathbf{C}}$ manifest the distinct work conjugate couples

$$(\boldsymbol{\tau}; \mathbf{d}) \quad , \quad (\mathbf{g} \mathbf{P}; \dot{\mathbf{F}}) \quad \text{and} \quad (\mathbf{S}; \frac{1}{2} \dot{\mathbf{C}}) . \quad (2.47)$$

Balance of Entropy (*The Second Law of Thermodynamics*). The second law of thermodynamics, which is in fact an inequality unlike the other balance principles, serves as a major mathematical restriction on the constitutive equations governing, for instance, heat conduction or evolution of internal variables describing an internal dissipative mechanism. The concept of *entropy* may be conceived as a *measure of disorder* providing a bridge between thermomechanics with the treatments of statistical mechanics. For the part of the body \mathcal{P}_S under consideration, we define the *total entropy* \mathcal{H} by integrating the *specific entropy* η over the volume, i.e. $\mathcal{H} := \int_{\mathcal{P}_S} \rho\eta(\mathbf{x}, t)dv$. The temporal change of the entropy has two contributions, namely the *reversible* and the *irreversible* parts, see e.g. DE GROOT & MAZUR [42]. The reversible change of the entropy is due to external heat sources. The irreversible part of the entropy change, however, stems from internal dissipative mechanisms such as plastic deformations, damage etc. The second law of thermodynamics states that the irreversible part of the entropy rate is always positive. For this purpose, we introduce the *specific rate of entropy production* $\gamma(\mathbf{x}, t)$ whose integration over the volume leads us to the *total rate of entropy production* $\Gamma = \int_{\mathcal{P}_S} \rho\gamma(\mathbf{x}, t)dv \geq 0$.¹ The balance of entropy can then be expressed as

$$\int_{\mathcal{P}_S} \rho\gamma dv := \frac{d}{dt} \int_{\mathcal{P}_S} \rho\eta dv - \left(\int_{\mathcal{P}_S} \frac{\rho r}{\theta} dv - \int_{\partial\mathcal{P}_S} \frac{\mathbf{q} \cdot \mathbf{n}}{\theta} da \right) \geq 0 \quad (2.48)$$

where θ stands for the *absolute temperature* restricted to the positive values $\theta > 0$. Following the conventional steps, we end up with the local spatial entropy balance

$$\rho\gamma = \rho\dot{\eta} - \rho\frac{r}{\theta} + \operatorname{div}\left(\frac{\mathbf{q}}{\theta}\right) = \rho\dot{\eta} - \rho\frac{r}{\theta} + \frac{1}{\theta}\operatorname{div}(\mathbf{q}) - \frac{1}{\theta^2}\mathbf{q} \cdot \nabla_x \theta \geq 0. \quad (2.49)$$

Apparently the inequality (2.49)₃ can also be written in the form commonly referred to as the *Clausius-Duhem inequality*

$$\rho\dot{\eta} \geq \rho\frac{r}{\theta} - \frac{1}{\theta}\operatorname{div}(\mathbf{q}) + \frac{1}{\theta^2}\mathbf{q} \cdot \nabla_x \theta. \quad (2.50)$$

The material version of (2.50) then reads as

$$\rho_0\dot{\eta} \geq \rho_0\frac{R}{\theta} - \frac{1}{\theta}\operatorname{DIV}(\mathbf{Q}) + \frac{1}{\theta^2}\mathbf{Q} \cdot \nabla_X \theta. \quad (2.51)$$

2.4. Dissipation and Thermomechanics with Internal Variables

The *spatial dissipation* is defined as the product of the rate of entropy production in (2.49) with the absolute temperature θ , i.e. $\mathcal{D} := \rho\gamma\theta \geq 0$. Owing to the nature of the terms in (2.49), it is common practice to additively split the dissipation into the *local (intrinsic)* \mathcal{D}_{loc} and the *conductive (thermal)* \mathcal{D}_{con} parts, $\mathcal{D} = \mathcal{D}_{loc} + \mathcal{D}_{con}$. We then require a more strict condition than (2.49) by demanding the positiveness of the both terms \mathcal{D}_{loc} and \mathcal{D}_{con} separately. To this end, we introduce the *Clausius-Planck inequality*

$$\mathcal{D}_{loc} := \rho\dot{\eta}\theta - (\rho r - \operatorname{div}(\mathbf{q})) \geq 0, \quad (2.52)$$

¹The Greek letters $\gamma(\mathbf{x}, t)$ and $\Gamma(\mathbf{X}, t)$ standing for the rate of entropy production should not be confused with $\boldsymbol{\gamma}(\mathbf{x}, t)$ and $\boldsymbol{\Gamma}(\mathbf{X}, t)$ printed in bold to denote the specific body forces in the preceding sections.

and the *Fourier inequality*

$$\mathcal{D}_{con} := -\frac{1}{\theta} \mathbf{q} \cdot \nabla_x \theta \geq 0 \quad (2.53)$$

that can also be expressed in the following Lagrangean form

$$J\mathcal{D}_{con} := -\frac{1}{\theta} J\mathbf{q} \cdot \nabla_x \theta = -\frac{1}{\theta} \mathbf{Q} \cdot \nabla_X \theta \geq 0. \quad (2.54)$$

Incorporation of the spatial energy balance equation (2.41) in the first version of the Clausius-Planck inequality (2.52) leads to the equation formulated in terms of the internal energy density

$$\mathcal{D}_{loc} := \rho \dot{\eta} \theta - \rho \dot{e} + \boldsymbol{\sigma} : (\mathbf{g}\mathbf{l}) \geq 0. \quad (2.55)$$

This form can be rewritten per unit reference volume by multiplying (2.55) with the Jacobian J . For the sake of brevity, we re-define the quantities $\eta \leftarrow J\rho\eta = \rho_0\eta$, $e \leftarrow J\rho e = \rho_0e$ and obtain

$$J\mathcal{D}_{loc} := \dot{\eta}\theta - \dot{e} + \mathbf{g}\mathbf{P} : \dot{\mathbf{F}} \geq 0. \quad (2.56)$$

There are four basic thermomechanical potentials widely encountered in the thermomechanics literature. The choice of an appropriate potential is generally made according to circumstances of experiments or properties of the material at hand. In the context of continuum thermomechanics, these potentials generally depend on a set of variables which is formed through a mutual combination between the sets $\{\mathbf{g}\mathbf{P}, \mathbf{F}\}$ and $\{\eta, \theta\}$. The first set can, of course, be replaced with any of the work conjugate pairs given in (2.47). For inelastic materials, these sets are supplemented by additional *internal variables*, say $\{\mathcal{I}\}$, employed for the description of inelastic dissipative processes. The concept of internal variables has widely been used in the constitutive formulation of dissipative materials through the initial value problems governing their temporal evolution. The set $\{\mathcal{I}\}$ may have scalar, tensorial or n -vector character. The internal variables may be observable but generally cannot be externally controlled, see MAUGIN [133] for an excellent review. The *thermodynamical forces*, say $\{\mathcal{F}\}$, conjugate to the set $\{\mathcal{I}\}$ on the bases of dissipation, generally are not externally defined. Thus, it should also be noted that the internal variables do not explicitly appear up to the energy balance equation (2.41).

By looking at the time derivatives of the fields in the Clausius-Planck inequality (2.56) one can readily conclude that the internal energy e can be considered as a thermodynamical potential depending primarily upon the deformation \mathbf{F} and the entropy η , i.e. $e = \hat{e}(\mathbf{F}, \eta, \dots)$. We then define the *Helmholtz free energy* through the partial Legendre transformation $\Psi := e - \theta\eta$ implying the functional dependency $\Psi = \hat{\Psi}(\mathbf{F}, \theta, \dots)$. Similarly, we can also introduce the *Gibbs free energy* $g = \hat{g}(\mathbf{g}\mathbf{P}, \theta, \dots) := \Psi - \mathbf{g}\mathbf{P} : \mathbf{F}$ and the *enthalpy* $h = \hat{h}(\mathbf{g}\mathbf{P}, \eta, \dots) := e - \mathbf{g}\mathbf{P} : \mathbf{F}$. Use of the Gibbs free energy can be preferred to the others, for example, in modeling of gaseous materials on which some experiments under constant pressure or temperature conditions are carried out. Throughout this thesis, however, we will be concerned with the modeling solid polymers where we mostly utilize the Helmholtz free energy. Hence, the version of the Clausius-Planck inequality in terms of the Helmholtz free energy, or simply free energy, is of interest. Inserting its definition $\Psi = e - \theta\eta$ into (2.56), we end up with

$$J\mathcal{D}_{loc} := \mathbf{g}\mathbf{P} : \dot{\mathbf{F}} - \dot{\Psi} - \eta\dot{\theta} \geq 0. \quad (2.57)$$

To fix the ideas, let us focus on a problem of thermoelasticity for a homogeneous material where the free energy does not depend on the internal variables. Being consistent with the *principle of equipresence*, we assume that the constitutive equations, the free energy Ψ and the heat flux vector \mathbf{Q} , depend upon the same set of field variables

$$\Psi = \hat{\Psi}(\mathbf{g}; \mathbf{F}, \theta, \mathcal{G}) \quad \text{and} \quad \mathbf{Q} = \hat{\mathbf{Q}}(\mathbf{g}; \mathbf{F}, \theta, \mathcal{G}) \quad (2.58)$$

where $\mathcal{G} := \nabla_x \theta$ denotes the material gradient of the temperature field and the spatial metric \mathbf{g} is needed to compute the deformation measures in the reference configuration. Based on this assumption, we can include the time derivative of the free energy $\dot{\Psi} = \partial_{\mathbf{F}} \Psi : \dot{\mathbf{F}} + \partial_{\theta} \Psi : \dot{\theta} + \partial_{\mathcal{G}} \Psi : \dot{\mathcal{G}}$ in the Clausius-Planck inequality given in (2.57). Gathering the coefficients of the time rates of the common terms, we obtain

$$J\mathcal{D}_{loc} := (\mathbf{g}\mathbf{P} - \partial_{\mathbf{F}} \Psi) : \dot{\mathbf{F}} - (\eta + \partial_{\theta} \Psi) \dot{\theta} - \partial_{\mathcal{G}} \Psi \cdot \dot{\mathcal{G}} \geq 0. \quad (2.59)$$

Following the celebrated reasoning of COLEMAN & NOLL [37] and COLEMAN & GURTIN [35] within the framework of thermodynamics with internal variables, we contend that the thermodynamic restriction should be fulfilled for an arbitrary rate of the deformation gradient, temperature and temperature gradient. Therefore, (2.59) implies a particular form of constitutive equations such that

$$\mathbf{g}\mathbf{P} := \partial_{\mathbf{F}} \Psi \quad , \quad \eta := -\partial_{\theta} \Psi \quad \text{and} \quad \partial_{\mathcal{G}} \Psi = \mathbf{0}. \quad (2.60)$$

The first two equations of (2.60) state that the free energy acts as a potential for the stresses and the entropy while (2.60)₃ implies that the free energy does not depend on the temperature gradient \mathcal{G} , i.e. $\Psi = \hat{\Psi}(\mathbf{g}; \mathbf{F}, \theta)$. From the results (2.60), it is also clear that the local dissipation \mathcal{D}_{loc} vanishes identically for thermoelastic problems. In a general problem of thermoinelasticity, however, the free energy is also a function of the internal variables $\{\mathcal{I}\}$. With the results obtained in (2.60), the Clausius-Planck inequality can be recast into its *reduced* form

$$J\mathcal{D}_{loc} := \mathcal{F} : \dot{\mathcal{I}} \geq 0 \quad \text{with} \quad \mathcal{F} := -\partial_{\mathcal{I}} \Psi. \quad (2.61)$$

The *principle of material frame invariance* requires the invariance of the energy stored under rigid body rotations superimposed on the current spatial configuration. Therefore, we locally demand $\Psi(\mathbf{g}; \mathbf{F}, \theta) = \Psi(\tilde{\mathbf{g}}; \tilde{\mathbf{F}}, \theta)$ where $\tilde{\mathbf{F}} := \mathbf{Q}_*(\mathbf{F}) := \mathbf{Q}\mathbf{F}$ and $\tilde{\mathbf{g}} := \mathbf{Q}_*(\mathbf{g}) := \mathbf{Q}^{-T} \mathbf{g} \mathbf{Q}^{-1}$ for all $\mathbf{Q} \in \mathcal{SO}(\beta)$. Observe that the right Cauchy-Green tensor $\mathbf{C} := \mathbf{F}^T \mathbf{g} \mathbf{F} = \tilde{\mathbf{F}}^T \tilde{\mathbf{g}} \tilde{\mathbf{F}}$ automatically satisfies this condition. Therefore, the storage function $\hat{\Psi}$ in terms of $\mathbf{C} = \mathbf{F}^T \mathbf{g} \mathbf{F}$ is a priori objective and the form $\hat{\Psi}(\mathbf{C}, \theta) = \Psi(\mathbf{F}^T \mathbf{g} \mathbf{F}, \theta)$ represents its reduced form. Based on this restriction, we can rewrite the term $(\mathbf{g}\mathbf{P} - \partial_{\mathbf{F}} \Psi) : \dot{\mathbf{F}}$ in (2.59) as $(\mathbf{S} - 2\partial_{\mathbf{C}} \hat{\Psi}) : \frac{1}{2} \dot{\mathbf{C}}$ due to the stress power equalities (2.45), (2.46). This yields the functional definition of the second Piola-Kirchhoff stress tensor

$$\mathbf{S} = 2\partial_{\mathbf{C}} \hat{\Psi}(\mathbf{C}, \theta). \quad (2.62)$$

Starting from this equality, we can further continue to obtain

$$\left(\mathbf{S} - 2\partial_{\mathbf{C}} \hat{\Psi} \right) : \frac{1}{2} \dot{\mathbf{C}} = \boldsymbol{\tau} : \frac{1}{2} \mathcal{L}_v \mathbf{g} - 2\partial_{\mathbf{C}} \Psi : \frac{1}{2} \mathbf{F}^T \mathcal{L}_v \mathbf{g} \mathbf{F} = (\boldsymbol{\tau} - 2\mathbf{F} \partial_{\mathbf{C}} \Psi \mathbf{F}^T) : \frac{1}{2} \mathcal{L}_v \mathbf{g}$$

where it can be shown through the chain rule that $2\mathbf{F} \partial_{\mathbf{C}} \hat{\Psi} \mathbf{F}^T = 2\partial_{\mathbf{g}} \Psi$, see MARS DEN & HUGHES [131], p.197. This equality leads us to the *Doyle-Ericksen* formula

$$\boldsymbol{\tau} = 2\partial_{\mathbf{g}} \Psi(\mathbf{g}; \mathbf{F}, \theta) \quad (2.63)$$

originally derived by DOYLE & ERICKSEN [48].

3. The Non-Affine Micro-Sphere Model of Rubber Elasticity

This chapter presents the recently developed *non-affine network model* of finite rubber elasticity. The exposition set out in the current chapter follows the notions of the recent work by MIEHE, GÖKTEPE & LULEI [149]. This approach, henceforth denoted as the *non-affine micro-sphere model*, advances characteristics of the full network model and the eight-chain model through a substantial improvement of their modeling capabilities. This chapter lays the basis for the subsequent developments in this thesis concerning the inelasticity of rubbery and glassy polymers. Key underlying concept is the construction of a micro-macro approach to elasticity governed by the following two features. Core of the model is a two-dimensional constitutive setting of the micromechanical response of a *single polymer chain in a constrained environment* defined by two micro-kinematic variables: the stretch λ of the chain and the contraction ν of the cross section of a micro-tube that surrounds the chain under consideration. The second feature of the model is a new *non-affine micro-macro transition* that defines the three-dimensional overall response of the polymer network based on a characteristic homogenization procedure of micro-state variables defined on the micro-sphere of space orientations. This micro-macro transition links the two micro-kinematic variables λ and ν in a non-affine format to the line-stretch $\bar{\lambda}$ and the area-stretch $\bar{\nu}$ of the macro-continuum. The successive build up of the constitutive model may be subdivided into three steps. The first two steps are concerned with the partial modeling of the above mentioned two kinematic mechanisms, i.e. the *non-affine stretch part* and the *non-affine tube part*. We describe these two parts by kinematically decoupled free energies, yielding superimposed contributions to the overall stress response. The third step deals with an effective numerical evaluation of the micro-macro transition by a *discretization of state variables on the micro-sphere*.

i) Non-Affine Stretch Part. The response of an unconstrained prototype chain of the network is assumed to be governed by the classical non-Gaussian statistics in terms of the micro-stretch λ . The basic idea of the proposed non-affine stretch part for an idealized network, free of conformation constraints, is the introduction of a field of *stretch fluctuations* f defined on the micro-sphere \mathcal{S} of space orientations. This fluctuation field links the micro-stretch λ of the single chain to the line-stretch $\bar{\lambda}$ of the continuum in the multiplicative format $\lambda = \bar{\lambda}f$. The fluctuation field f is determined by a variational *principle of minimum averaged free energy* conceptually in line with homogenization concepts for composites as outlined for example in PONTE CASTAÑEDA & SUQUET [166], MIEHE, SCHOTTE & LAMBRECHT [152] or MIEHE [144]. The minimization principle is assumed to be constrained through a p -root averaging condition, yielding the closed-form result of a non-affine *constant micro-stretch* $\lambda = (\int_{\mathcal{S}} \bar{\lambda}^p dA / |\mathcal{S}|)^{1/p}$. Here, $p > 0$ is considered as a material parameter that describes the non-affine stretch characteristics. For $p = 2$, the proposed model recovers the eight-chain model as a special case. As shown in the numerical examples, the new non-affine stretch model substantially enhances the performance of the eight-chain model when the *non-affine stretch parameter* p is used in addition to the two effective parameters μ and N of the non-Gaussian free energy of the single chain. It provides considerable flexibility with respect to independent modeling of locking characteristics for different deformation modes such as simple tension and equi-biaxial deformations.

ii) Non-Affine Tube Part. The basic idea of the proposed non-affine tube part for topological constraints of the network is the introduction of a fictitious *straight micro-tube* that

contains the single chain and constrains its free movement. For this elementary scenario, a constrained free energy contribution is available in DOI & EDWARDS [45] from elementary statistical mechanics, governed by the cross-section of the straight tube. Based on this observation, we introduce the tube-area-contraction ν as a second micro-kinematic variable of the single chain. In order to link this micro-kinematic variable to the macroscopic deformation as a micro-mechanical mechanism, we assume the existence of *forest chains* located transversally to the prototype chain under consideration. An increase of stretch of these forest chains is then considered to increase the conformation constraint on the prototype chain by reducing the cross section of the fictitious tube. In an affine setting, the stretch of the forest chains is governed by the macroscopic area-stretch $\bar{\nu}$ of an area element with a normal aligned to the orientation of the prototype chain. We generalize this affine assumption to the non-affine relationship $\nu = \bar{\nu}^q$ between the tube contraction ν and the area-stretch $\bar{\nu}$ of the continuum where $q > 0$ is an additional *non-affine tube parameter* besides the effective stiffness parameter U of the tube statistics. The macroscopic contribution to the free energy is obtained by a homogenization of the associated state variables on the sphere of space orientations. The proposed new geometric approach to a tube contribution yields the desired increase of stiffness at moderate stretches.

iii) Field discretizations on the Micro-Sphere. The third key contribution is the computational exploitation of averaging operations on the micro-sphere. In contrast to the eight-chain model, the above outlined generalized non-affine stretch and tube contributions do not have closed-form macroscopic representations in terms of conventional macroscopic strain measures. As a consequence, the homogenization procedure is performed via a direct numerical evaluation of the averaging integrals $\int_{\mathcal{S}} \nu dA/|\mathcal{S}| \approx \sum_{i=1}^m \nu^i w^i$ by replacing the continuous orientation manifold on the micro-sphere by a *discrete set of m orientations*. A comparative study of numerical examples shows that an $m = 21$ -point integration as outlined in BAŽANT & OH [10] yields sufficient accuracy. The numerical integration of state variables on the micro-sphere results in simple algebraic expressions and is computationally very efficient. The computational effort is absolutely competitive with purely macroscopic models of rubber elasticity formulated in terms of spectral decompositions of macroscopic strain measures. Furthermore, the approach inherently provides the visualization of local micro-states via stereographic pole figure plots at typical Gauss points of finite element meshes. We develop separate algorithms for the decoupled contributions due to the non-affine stretch and tube parts, which are finally superimposed to obtain the overall response of the model. This framework is very attractive with regard to an extension to inelasticity in order to incorporate visco-elastic overstress phenomena and the Mullins effect of strain-softening.

The current chapter is organized as follows. In Section 3.1, we briefly outline a spatial geometric setting of decoupled volumetric-isochoric finite elasticity. Section 3.2 is devoted to discussion on the micro-mechanics of a single chain constrained in a straight tube-like environment. Here, we introduce two micro-kinematic variables for the chain stretch and the tube area contraction, point out the associated mechanism of statistical mechanics and summarize their decoupled contributions to the free energy of the single chain. Having this statistically-based constitutive modeling at hand, in Section 3.3 we further proceed with the construction of the non-affine network contributions associated with the two micro-mechanical mechanisms. To this end, we first introduce the micro-macro transition as a homogenization of state variables on the micro-sphere of space orientations. Then, the two non-affine network models associated with the free motion part and the constrained

tube part of the chains are established. We derive explicit representations of the free and constraint network contributions to the macroscopic free energy, and the Eulerian stresses and tangent moduli. Section 3.4 is concerned with the algorithmic aspects of the constitutive model. The performance of the proposed micro-sphere model is assessed in Section 3.5. The evaluation of the model is carried out with respect to several aspects of the formulation. These involve the accuracy of the algorithmic formulation, comparison with some other network models, parameter sensitivity analysis and simulation of benchmark data obtained from homogeneous and inhomogeneous experiments.

3.1. Macroscopic Spatial Elasticity of a Polymer Network

Let $\varphi : \mathbf{X} \mapsto \mathbf{x}$ be the nonlinear deformation map at time $t \in \mathbb{R}_+$ of an elastic body undergoing finite deformation, see Figure 2.1. The boundary-value problem of macroscopic finite elasticity is governed by the principle of minimum potential energy

$$I = \inf_{\varphi \in \mathcal{W}} \left[\int_{\mathcal{B}} \Psi \, dV - \Pi_{load} \right] \quad (3.1)$$

that is subjected to $\varphi \in \mathcal{W} := \{\varphi \in \mathcal{W}^{1,p}(\mathcal{B}) \mid \varphi = \bar{\varphi}(\mathbf{X}) \text{ on } \partial\mathcal{B}_\varphi\}$ associated with prescribed deformations $\bar{\varphi}$ at $\mathbf{X} \in \partial\mathcal{B}_\varphi$ on the boundary. The term $\Pi_{load}(\varphi) = \int_{\mathcal{B}} \varphi \cdot \boldsymbol{\gamma} \, dV + \int_{\partial\mathcal{B}_t} \varphi \cdot \mathbf{T} \, dA$ is an assumed global load potential of dead body forces $\boldsymbol{\gamma}(\mathbf{X}, t)$ in \mathcal{B} and surface tractions $\mathbf{T}(\mathbf{X}, t)$ on $\partial\mathcal{B}_t$. The minimum principle (3.1) contains the macroscopic free energy Ψ stored in a unit reference volume. It is a function of the spatial metric \mathbf{g} and the deformation gradient \mathbf{F}

$$\Psi = \Psi(\mathbf{g}; \mathbf{F}) . \quad (3.2)$$

The free energy function is assumed to be normalized to a zero energy level and a stress-free state at the reference configuration, i.e. $\Psi(\mathbf{g}; \mathbf{1}) = 0$ and $\partial_{\mathbf{F}} \Psi(\mathbf{g}; \mathbf{1}) = \mathbf{0}$. The function must satisfy the principle of material frame invariance $\Psi(\mathbf{g}; \mathbf{Q}\mathbf{F}) = \Psi(\mathbf{g}; \mathbf{F})$ for all rotations $\mathbf{Q} \in SO(3)$. Following the standard argument of zero dissipation in an elastic solid, the free energy function determines the Eulerian Kirchhoff stresses and the associated spatial elasticity moduli by the Doyle-Ericksen formulae (2.63)

$$\boldsymbol{\tau} = 2\partial_{\mathbf{g}} \Psi(\mathbf{g}; \mathbf{F}) \quad \text{and} \quad \mathbb{C} = 4\partial_{\mathbf{g}\mathbf{g}}^2 \Psi(\mathbf{g}; \mathbf{F}) . \quad (3.3)$$

The spatial elasticity moduli link the Lie derivative or Oldroyd rate $\boldsymbol{\mathcal{L}}_{\mathbf{v}} \boldsymbol{\tau} := \dot{\boldsymbol{\tau}} - \mathbf{l}\boldsymbol{\tau} - \boldsymbol{\tau}\mathbf{l}^T$ of the Kirchhoff stresses via $\boldsymbol{\mathcal{L}}_{\mathbf{v}} \boldsymbol{\tau} = \mathbb{C} : \boldsymbol{\mathcal{L}}_{\mathbf{v}} \mathbf{g}/2$ to the Lie derivative of the spatial metric $\boldsymbol{\mathcal{L}}_{\mathbf{v}} \mathbf{g}/2 := (\mathbf{g}\mathbf{l} + \mathbf{l}^T \mathbf{g})/2$, often denoted as the Eulerian rate of deformation tensor as defined in (2.44). The evaluation of the tensors defined in (3.3) is required in typical finite element implementations of finite elasticity. In particular, the moduli $(3.3)_2$ play a central role in Newton-type methods applied to an iterative solution of the nonlinear variational problem (3.1), see for example SIMÓ & TAYLOR [185] or MIEHE [137, 140].

As discussed in Chapter 1, rubber-like materials undergo nearly incompressible deformations. To this end, we consider a decoupled volumetric-isochoric formulation of elasticity based on the introduction of the unimodular part

$$\bar{\mathbf{F}} := J^{-1/3} \mathbf{F} \quad (3.4)$$

of the deformation gradient. This tensor is assumed to govern the deviatoric stresses. The decoupled volumetric-isochoric framework of finite elasticity is obtained by considering the

specific form

$$\Psi = U(J) + \bar{\Psi}(\mathbf{g}; \bar{\mathbf{F}}) \quad (3.5)$$

of the stored energy. This additive split of the free energy leads to analogous form for the stresses (3.3)₁ that additively decompose into spherical and deviatoric contributions

$$\boldsymbol{\tau} = p\mathbf{g}^{-1} + \bar{\boldsymbol{\tau}} : \mathbb{P}. \quad (3.6)$$

The elasticity moduli (3.3)₂ also assume the decoupled representation

$$\mathbb{C} = (p + \kappa)\mathbf{g}^{-1} \otimes \mathbf{g}^{-1} - 2p\mathbb{I} + \mathbb{P}^T : [\bar{\mathbb{C}} + \frac{2}{3}(\bar{\boldsymbol{\tau}} : \mathbf{g})\mathbb{I}] : \mathbb{P} - \frac{2}{3}(\mathbb{P}^T : \bar{\boldsymbol{\tau}} \otimes \mathbf{g}^{-1} + \mathbf{g}^{-1} \otimes \bar{\boldsymbol{\tau}} : \mathbb{P}) \quad (3.7)$$

where $\mathbb{I}^{abcd} := [\delta^{ac}\delta^{bd} + \delta^{ad}\delta^{bc}]/2$ and $\mathbb{P}^{abcd} := [\delta^a_c\delta^b_d + \delta^a_d\delta^b_c]/2 - \frac{1}{3}\delta^{ab}\delta_{cd}$ are the fourth-order identity tensor and deviatoric projection operator, respectively. The volumetric stresses and moduli in (3.6) and (3.7) are defined by

$$p := JU'(J) \quad \text{and} \quad \kappa := J^2U''(J) \quad (3.8)$$

as derivatives of the volumetric part U of the free energy function (3.5). For an almost incompressible response of the polymer network, the volumetric free energy U can be considered as a penalty function which approximatively enforces the incompressibility constraint. The stresses and moduli in (3.6) and (3.7) associated with the isochoric deformation space are defined as

$$\bar{\boldsymbol{\tau}} := 2\partial_{\mathbf{g}}\bar{\Psi}(\mathbf{g}; \bar{\mathbf{F}}) \quad \text{and} \quad \bar{\mathbb{C}} := 4\partial_{\mathbf{g}\mathbf{g}}^2\bar{\Psi}(\mathbf{g}; \bar{\mathbf{F}}) \quad (3.9)$$

the derivatives of the isochoric part $\bar{\Psi}$ of the free energy function (3.5). The derivation of the expressions for the Kirchhoff stresses (3.6) and the associated moduli (3.7) in the context of the decoupled volumetric-isochoric formulation of elasticity are set out in Appendix B. In the forthcoming part of this chapter *we construct macroscopic free energy functions $\bar{\Psi}$ for exactly incompressible polymer networks* and derive explicit formulae for the above defined spatial stresses $\bar{\boldsymbol{\tau}}$ and moduli $\bar{\mathbb{C}}$.

3.2. Micromechanics of a Single Polymer Chain in a Tube

The elementary entropic molecular theory of polymer networks rests on the postulation that the entropic elastic free energy of a network is equal to the sum of the elastic free energies of the individual chains. Hence, the setting up of a micromechanically-based theory for polymer networks in a first step requires a precise description of the mechanical response of an individual polymer chain. To this end, in this section we summarize classical results of the Gaussian and non-Gaussian statistical mechanics of unconstrained single polymer chains. In order to model interactions of chains in a real network, we consider the single chain to be constrained by a straight tube. The key aspect of the subsequent development is to assume the free energy of the single chain in a cross-linked network to be governed by *two micro-kinematic variables: the stretch and the tube contraction*.

3.2.1. Definition of Micro-Kinematic Variables of the Chain. In the statistical treatment of a single polymer chain, its geometrical structure is idealized to be composed of N segments of equal length l , the so-called Kuhn segment length. The contour length L of the chain is $L := Nl$. In the classical statistical treatments of a single polymer chain as outlined in KUHN [112, 113], KUHN & GRÜN [114] and JAMES & GUTH [101], the

single chain is unconstrained and has an entirely random orientation in space as visualized in Figure 3.1, which a priori ignores a dependency on the motion of neighboring chains. The key phenomenological kinematic variable of the single chain is the current *end-to-end distance* r depicted in Figure 3.1a. For an unstrained free chain this distance assumes the random walk-type root-mean-square value $r_0 := \sqrt{Nl}$ as also discussed in Appendix C. Alternative dimensionless kinematic variables to measure the deformation of the chain are the *stretch* λ or the *relative stretch* λ_r defined as

$$\lambda := \frac{r}{r_0} \quad \text{and} \quad \lambda_r := \frac{r}{L} = \frac{\lambda}{\sqrt{N}}, \quad (3.10)$$

with $\lambda \in [0, \sqrt{N})$ and $\lambda_r \in [0, 1)$, respectively. The maximum values of these measures are obtained for the situation where the end-to-end distance r approaches the contour length L .

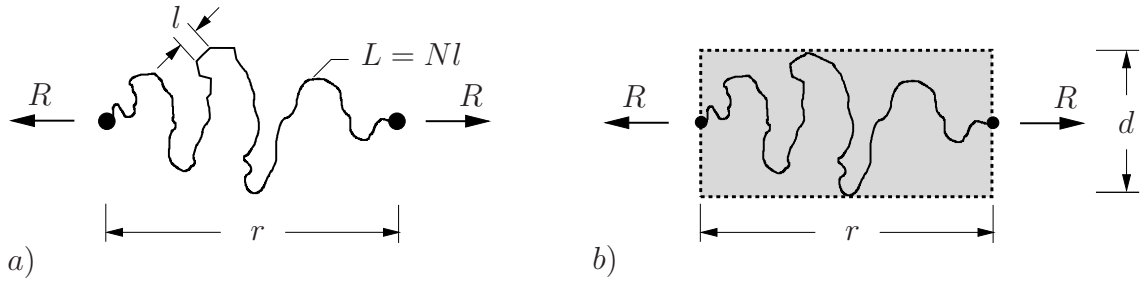


Figure 3.1: Geometry of a single polymer chain. a) Free single chain consisting of N segments with length l , end-to-end distance r and contour length $L = Nl$. b) Chain topology constrained by a straight tube of diameter d .

Classical treatments of polymers consider a free motion of the single chain in the cross-linked network. These theories do not account for the interaction between different molecules which form the network. Concepts from molecular statistics that incorporate these effects are the so-called *constrained junction* and *constrained segment theories*. A recent development associated with the latter group is the so-called *tube model* of rubber elasticity, see DEAM & EDWARDS [40], EDWARDS & VILGIS [53] and HEINRICH, STRAUBE & HELMIS [95] for an overview. The tube model characterizes the cross-links and entanglement topology of a polymer network by a set of worm-like network-chain paths. The basic physical argument for the tube approach is the large degree of coil interpenetrations of network chains. These can be viewed as obstacles that constrain the free motion of the chain of interest. An important aspect of this paper is to define a tube-like constraint to a single chain in a new elementary simple format. To this end, we assume the polymer chain to be confined by a *tube of constant diameter* d as visualized in Figure 3.1b, with both ends fixed at the center of the end cross sections. This simplified geometry restricts the number of accessible conformations of the chain to the free space inside of the tube. We then assume that the network constraint to the single chain under consideration can be described by the dimensionless kinematic variable *tube area contraction*

$$\nu := \left(\frac{d_0}{d}\right)^2 \quad (3.11)$$

with $\nu \in (0, \infty)$. Here, d_0 is the initial diameter of the tube, which can be considered as a material parameter of the undeformed network. Estimates of d_0 in terms of the Kuhn

segment length l and the number of segments per unit volume are given in HEINRICH & STRAUBE [93, 94], HEINRICH, STRAUBE & HELMIS [95] and HEINRICH & KALISKE [92]. In our model of a single chain in a straight tube, Figure 3.1, the allowed conformations of the single chain are assumed to be determined by the *two micro-kinematic variables* λ and ν defined (3.10) and (3.11), respectively.

3.2.2. Free Energy of a Single Chain. The key problem in the statistical mechanics of a polymer chain is the determination of its *entropy*. The entropy essentially describes the number of allowed conformations available to the chain. Now consider the above outlined model of a single chain in a straight micro-tube governed by the micro-kinematic variables λ and ν . The infinitesimal probability dP that the conformation of the chain falls between the micro-tube geometries (λ, ν) and $(\lambda + d\lambda, \nu + d\nu)$ is

$$dP(\lambda, \nu) = p(\lambda, \nu) d\lambda d\nu \quad (3.12)$$

with the joint probability density

$$p(\lambda, \nu) = p_f(\lambda) p_c(\nu). \quad (3.13)$$

Here, p_f and p_c are probability densities which independently describe the free chain response (index f) and the tube constraint (index c). Then the entropy η of the single chain is governed by Boltzmann's equation $\eta = k \ln p$ in terms of the Boltzmann constant k . For purely entropic response we then obtain the *free energy* ψ of the chain

$$\psi = -\theta \eta, \quad (3.14)$$

where $\theta > 0$ denotes the absolute temperature. The assumed joint probabilities immediately leads to the *additive split*

$$\boxed{\psi(\lambda, \nu) = \psi_f(\lambda) + \psi_c(\nu)} \quad (3.15)$$

of the free energy of the chain into a contribution ψ_f associated with the free motion of the chain and a contribution ψ_c due to the tube-like network constraint, respectively. In (3.15), for the sake of brevity, the explicit dependence of the free energy on the temperature θ is suppressed. The part ψ_f is the classical contribution to the free energy for the unconstrained motion of the chain between the cross-link positions shown in Figure 3.1a. The additional part ψ_c characterizes the constraint action of the tube depicted in Figure 3.1b. In the decoupled representation (3.15), the forces dual to the kinematic variables stretch λ and tube-contraction ν are given per definition by

$$F_f := \frac{\partial \psi_f(\lambda)}{\partial \lambda} \quad \text{and} \quad F_c := \frac{\partial \psi_c(\nu)}{\partial \nu}, \quad (3.16)$$

where F_f may be considered as an axial force and F_c as a radial force acting on the single chain.

3.2.3. The Free Energy of an Unconstrained Single Chain. The free energy of a chain for an unconstrained motion between two fixed cross-link positions has been outlined in the classical works by KUHN [112, 113] and KUHN & GRÜN [114]. The simplest statistical treatment yields a Gaussian distribution of the end-to-end distance of the chain. The more advanced non-Gaussian model accounts for the finite extensibility of the chain. The more detailed discussion of these theories is outlined in Appendix C along with some basics of statistical mechanics.

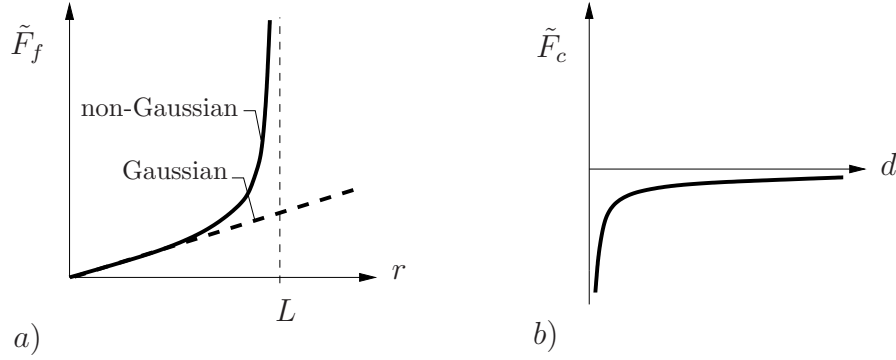


Figure 3.2: a) Axial force $\tilde{F}_f(r) := \partial\psi_f(r)/\partial r$ in terms of end-to-end distance r acting on a free chain for Gaussian and non-Gaussian statistics. b) Additional radial force $\tilde{F}_c(d) := \partial\psi_c(d)/\partial d$ in terms of the tube diameter d acting on a constrained chain.

The Gaussian Statistics. The classical Gaussian statistics of a single polymer chain was derived by KUHN [112, 113]. It considers an unconstrained freely jointed chain with end-to-end distance $r \ll L$ much smaller than the contour length L , i.e. for moderate deformations of the chain. The free energy of a free Gaussian chain has the following quadratic form

$$\psi_f(\lambda) = \frac{3}{2}k\theta\lambda^2 + \psi_0 \quad (3.17)$$

in terms of the stretch λ defined in (3.10) with constant ψ_0 , see TRELOAR [196] p.47 and (C.11) in Appendix C. Thus the force (3.16)₁ acting on a chain with assumed Gaussian statistics is a linear function of the stretch

$$F_f = 3k\theta\lambda \quad (3.18)$$

as depicted in Figure 3.2a. Therefore, application of the model is restricted to moderate deformations of the chain with $\lambda \ll \sqrt{N}$.

The Non-Gaussian Statistics. Owing to its quadratic form, the Gaussian model does not account for the finite extensibility of the chain. A theory that is valid for large stretches up to the limiting end-to-end distance governed by the contour length L is provided by the non-Gaussian model introduced by KUHN & GRÜN [114] and JAMES & GUTH [101]. The non-Gaussian free energy whose canonical derivation is also discussed in Appendix C (C.30) has the form

$$\psi_f(\lambda) = Nk\theta \left(\lambda_r \mathcal{L}^{-1}(\lambda_r) + \ln \frac{\mathcal{L}^{-1}(\lambda_r)}{\sinh \mathcal{L}^{-1}(\lambda_r)} \right) + \psi_0 \quad (3.19)$$

in terms of the relative stretch λ_r defined in (3.10)₂, see also TRELOAR [196] p.104. Here, $\mathcal{L}(\beta) = \coth \beta - 1/\beta$ is the well-known Langevin function and ψ_0 a constant. The associated force (3.16)₁ acting on a chain with assumed non-Gaussian statistics

$$F_f = k\theta\sqrt{N}\mathcal{L}^{-1}(\lambda_r) \quad (3.20)$$

has the nonlinear asymptotic property for the limiting end-to-end distance as depicted in Figure 3.2a. The force acting is directly proportional to the inverse Langevin function

$\mathcal{L}^{-1}(\lambda_r)$ and has the realistic singular behavior as relative stretch λ_r approaches the limiting value one. The inverse Langevin function can be evaluated by a Padé approximation

$$\mathcal{L}^{-1}(\lambda_r) \approx \lambda_r(3 - \lambda_r^2)/(1 - \lambda_r^2) \quad (3.21)$$

as outlined in COHEN [34]. It should also be observed that the first term of the Taylor series expansion of the non-Gaussian model reproduces the Gaussian model for small deformations.

3.2.4. Free Energy Due to the Tube-Like Constraint of the Chain. The contribution to the free energy due to the tube constraint can be based on the hypothesis that the polymer takes a random walk confined by the tube. The probability of the straight tube constraint has the simple form

$$p_c(\nu) = p_0 \exp[-\alpha(\frac{r_0}{d_0})^2\nu] , \quad (3.22)$$

where p_0 denotes a normalization constant, see DOI & EDWARDS [45], p.205. The variable ν is the tube-contraction defined in (3.11). The kinematic variable $r_0 := \sqrt{N}l$ denotes the end-to-end distance of an unconstrained chain and d_0 is a given tube diameter in the undeformed configuration. The factor α depends on the shape of the cross section of the tube. Incorporation of (3.11) and (3.22) in Boltzmann's equation leads us to the free energy due to the tube constraint

$$\psi_c(\nu) = \alpha k\theta N(\frac{l}{d_0})^2\nu + \psi_0 \quad (3.23)$$

with constant ψ_0 . The associated additional force (3.16)₂ acting on a chain

$$F_c = \alpha k\theta N(\frac{l}{d_0})^2 \quad (3.24)$$

is independent of the tube contraction measure. Variation of its version conjugate to the tube diameter d is depicted in Figure 3.2b.

3.3. Network Models for Affine and Non-Affine Stretches

Having the free energy functions of the single chain at hand, we now develop new network models for an aggregate of cross-linked polymer chains. To this end, we link the above introduced kinematic *micro-variables* λ and ν through *characteristic affine and non-affine approaches* to suitably defined kinematic *macro-variables* $\bar{\lambda}$ and $\bar{\nu}$. The resulting new network models are isotropically defined by equally-distributed orientations of the chains in space. The associated micro-macro transition is interpreted as a *homogenization of state variables on a micro-sphere* with unit radius.

3.3.1. Split of the Macroscopic Free Energy of the Network. Goal of this section is to construct full network models which define the macroscopic free energy $\bar{\Psi}$, stresses $\bar{\boldsymbol{\tau}}$ and elasticity moduli $\bar{\mathbb{C}}$ of the polymer network. The macroscopic free energy $\bar{\Psi}$ of a network is related to the sum of the elastic free energies of the individual chains

in a unit volume. Then the split (3.15) of the free energy of a single chain induces the additive split of the macroscopic free energy

$$\boxed{\bar{\Psi} = \bar{\Psi}_f(\mathbf{g}; \bar{\mathbf{F}}) + \bar{\Psi}_c(\mathbf{g}; \bar{\mathbf{F}})} . \quad (3.25)$$

The first part describes the contribution to the free energy for an idealized network with *free fluctuations* of the chains between junctions of the cross-linked network. The second part represents the additional free energy due to the *interactions among the chains*. Then the overall stresses and moduli (3.9) split into two contributions

$$\bar{\boldsymbol{\tau}} = \bar{\boldsymbol{\tau}}_f + \bar{\boldsymbol{\tau}}_c \quad \text{and} \quad \bar{\mathbb{C}} = \bar{\mathbb{C}}_f + \bar{\mathbb{C}}_c . \quad (3.26)$$

These contributions are obtained by inserting the split (3.25) into (3.9), yielding

$$\bar{\boldsymbol{\tau}}_f := 2\partial_{\mathbf{g}}\bar{\Psi}_f(\mathbf{g}; \bar{\mathbf{F}}) \quad \text{and} \quad \bar{\mathbb{C}}_f := 4\partial_{\mathbf{g}\mathbf{g}}^2\bar{\Psi}_f(\mathbf{g}; \bar{\mathbf{F}}) \quad (3.27)$$

for the unconstrained contributions to the stresses and moduli, and

$$\bar{\boldsymbol{\tau}}_c := 2\partial_{\mathbf{g}}\bar{\Psi}_c(\mathbf{g}; \bar{\mathbf{F}}) \quad \text{and} \quad \bar{\mathbb{C}}_c := 4\partial_{\mathbf{g}\mathbf{g}}^2\bar{\Psi}_c(\mathbf{g}; \bar{\mathbf{F}}) \quad (3.28)$$

for the additional contributions due to the constrained motion of the single chains. In the subsequent part of this section, we successively develop details of full network theories which define these two contributions to the free energy, the stresses and the elasticity moduli. Firstly, we focus on approaches to the unconstrained contributions and in the last subsection treat the additional constrained parts.

3.3.2. The Affine Full Network Model for Unconstrained Chains.

The Affine Stretch Assumption. The key aspect of network theories is to link the deformation of a single chain to the macroscopic isochoric deformation $\bar{\mathbf{F}}$ of the continuum defined in (3.4) that represents the network aggregate. Let \mathbf{r} be a Lagrangian orientation unit vector with $|\mathbf{r}|_{\mathbf{G}} := \sqrt{\mathbf{r}_b \cdot \mathbf{r}} = 1$, where $\mathbf{r}_b := \mathbf{G}\mathbf{r}$ is the co-vector of \mathbf{r} obtained by a mapping with the standard metric $\mathbf{G} = \delta_{AB}$ (Kronecker symbol) of the reference configuration. A mapping of the orientation vector \mathbf{r} by the isochoric deformation of the continuum gives the isochoric stretch vector

$$\mathbf{t} = \bar{\mathbf{F}}\mathbf{r} . \quad (3.29)$$

Then the *macro-stretch* of a material line element with orientation \mathbf{r} in the reference configuration is

$$\bar{\lambda} = |\mathbf{t}|_{\mathbf{g}} := \sqrt{\mathbf{t}_b \cdot \mathbf{t}} \quad \text{with} \quad \mathbf{t}_b := \mathbf{g}\mathbf{t} , \quad (3.30)$$

evaluated with the metric $\mathbf{g} = \delta_{ab}$ (Kronecker symbol) of the current configuration. For an *affine stretch model*, we assume the relationships

$$\lambda = \bar{\lambda} \quad (3.31)$$

between the micro-stretch λ of a single chain defined in (3.10) and the above defined macro-stretch $\bar{\lambda}$. This assumption is in line with classical affine network models which consider a single polymer chain between junctions of the cross-linked network. These models postulate the junctions to be embedded in the network structure without showing fluctuations over the time. As a consequence, the micro-stretch of an individual chain introduced in (3.10) is assumed to be identical to the isochoric stretch of the continuum defined in (3.30). This standard assumption reflects the classical approach to polymer networks as outlined in TRELOAR & RIDING [197]. A descriptive explanation of this assumption is illustrated in Figure 3.3b.

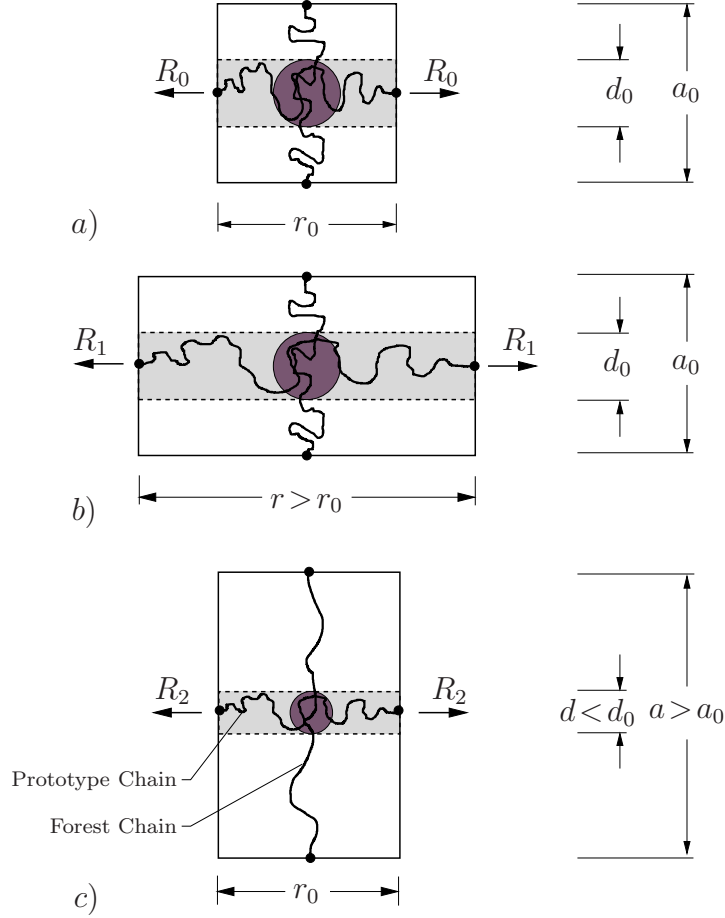


Figure 3.3: Conceptual link of kinematic micro-variables λ and ν to isochoric macro-variables $\bar{\lambda}$ and $\bar{\nu}$ of the continuum. *a)* Undeformed macroscopic volume element. *b)* The *chain-stretch* $\lambda := r/r_0$ in the affine deformation assumption is identical with the *macro-line-stretch* $\bar{\lambda} := |\bar{\mathbf{F}}\mathbf{r}| = r/r_0$ of a continuum line element with direction \mathbf{r} . *c)* We assume the *tube-area-contraction* $\nu := (d_0/d)^2$ related to the *macro-area-stretch* $\bar{\nu} := |\bar{\mathbf{F}}^{-T}\mathbf{n}| = a/a_0$ of a continuum area element with normal \mathbf{n} , because an increase of $\bar{\nu}$ extends *forest chains* which determine the tube diameter as obstacles.

Contribution to the Macroscopic Free Energy. With the above definitions at hand, we are now in a position to define the macroscopic energy of the network. It is assumed that the undeformed network is *homogeneous* and *isotropic* from the macroscopic viewpoint, consisting of n chains per unit volume. Then the macroscopic free energy is the sum of the n chain energies ψ_f^i which are present in a unit volume, i.e. $\bar{\Psi}_f = \sum_{i=1}^n \psi_f^i(\bar{\lambda}^i)$. The micro-energies are evaluated in terms of the isochoric macro-deformation $\bar{\mathbf{F}}$ through (3.30) based on the affinity assumptions (3.31). An isotropic overall response of the network is associated with an equal space distribution of the chains in the three-dimensional space. This equal space orientation is obtained by replacing the above discrete sum by the continuous representation

$$\bar{\Psi}_f(\mathbf{g}; \bar{\mathbf{F}}) = \langle n\psi_f(\bar{\lambda}) \rangle \quad (3.32)$$

where $\langle v \rangle$ denotes the *continuous averaging* for an equal orientation distribution of the variable v in space. This equal orientation distribution can be based on the parametriza-

tion of the above introduced Lagrangian unit vectors \mathbf{r} in terms of spherical coordinates

$$\mathbf{r}(\varphi, \vartheta) = \cos \varphi \sin \vartheta \mathbf{e}_1 + \sin \varphi \sin \vartheta \mathbf{e}_2 + \cos \vartheta \mathbf{e}_3 \quad (3.33)$$

in a fixed standard Cartesian frame $\{\mathbf{e}_i\}_{i=1,2,3}$ with $\varphi \in \mathcal{D}_\varphi := [0, 2\pi]$ and $\vartheta \in \mathcal{D}_\vartheta := [0, \pi]$, see Figure 3.4. Associated with an *equipartitioning of the orientation in space* are the probability densities $p(\varphi) = 1/2\pi$ and $p(\vartheta) = \sin \vartheta/2$ of the spherical angles φ and ϑ . While φ is equally distributed, ϑ is not due to its nonlinear relationship to the projection $l_3 := \cos \vartheta$ of the vector \mathbf{t} on the \mathbf{e}_3 -direction that is equally distributed. Then the infinitesimal probability that the orientation vector \mathbf{t} falls between the position (φ, ϑ) and $(\varphi + d\varphi, \vartheta + d\vartheta)$ is

$$dP(\varphi, \vartheta) = p(\varphi)p(\vartheta)d\varphi d\vartheta = \frac{1}{4\pi} \sin \vartheta d\varphi d\vartheta \quad (3.34)$$

In this equation $dA = \sin \vartheta d\varphi d\vartheta$ is the infinitesimal area element of the unit sphere \mathcal{S} with total area $|\mathcal{S}| = 4\pi$. Thus when introducing the area variable $A := \int_0^\vartheta \int_0^\varphi \sin \vartheta d\varphi d\vartheta$ with $A \in \mathcal{S}$, the probability density for the equal distribution of area on the unit sphere \mathcal{S} reads

$$p(A) = \frac{1}{|\mathcal{S}|} . \quad (3.35)$$

Then the infinitesimal probability that the orientation vector \mathbf{t} falls between the position A and $A + dA$ on the unit sphere is

$$dP(A) = p(A)dA = \frac{1}{|\mathcal{S}|} dA . \quad (3.36)$$

This expression being equivalent to the representations (3.34) is used in the subsequent development. With this formulation at hand, we define the average of the microscopic free energies for continuous space distribution via

$$\langle v \rangle = \int_{\mathcal{S}} v(A) dP(A) = \frac{1}{|\mathcal{S}|} \int_{\mathcal{S}} v(A) dA . \quad (3.37)$$

This average is interpreted as a *homogenization* of the state variable $v(A)$ on a micro-sphere with unit radius. The numerical evaluation of this mean value is based on the discretization of the continuous integral over the unit sphere, see Section 3.4.

Contribution to Macroscopic Stresses and Moduli. With the macro-energy at hand, we compute the Eulerian stresses and elasticity moduli based on a straightforward exploitation of formulae (3.27). To this end, we first compute the derivatives of the macro-stretch (3.30) by the Eulerian metric

$$2\partial_{\mathbf{g}} \bar{\lambda} = \bar{\lambda}^{-1} \mathbf{t} \otimes \mathbf{t} . \quad (3.38)$$

Its insertion into (3.27)₁ gives the representation of the macroscopic Kirchhoff stresses

$$\bar{\boldsymbol{\tau}}_f = \langle n\psi'_f \bar{\lambda}^{-1} \mathbf{t} \otimes \mathbf{t} \rangle . \quad (3.39)$$

Further derivation of the stresses with respect to the Eulerian metric yields the spatial elasticity moduli defined in (3.27)₂. Using the results (3.38) and $2\partial_{\mathbf{g}}(\mathbf{t} \otimes \mathbf{t}) = 0$, we obtain

$$\bar{\mathbf{C}}_f = \langle (n\psi''_f - n\psi'_f \bar{\lambda}^{-1}) \bar{\lambda}^{-2} \mathbf{t} \otimes \mathbf{t} \otimes \mathbf{t} \otimes \mathbf{t} \rangle . \quad (3.40)$$

The numerical implementation of the macro-stresses (3.39) and -moduli (3.40) is based on the discretization of the continuous integral (3.37) over the unit sphere. It is further set out in Section 3.4.

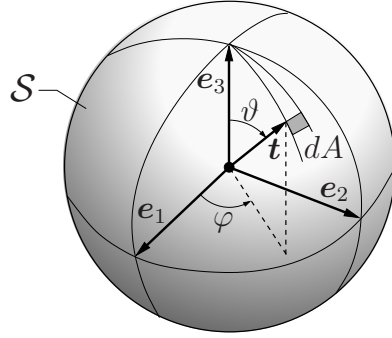


Figure 3.4: Unit sphere micro-structure. The orientation unit vector \mathbf{t} can be parametrized by the spherical angles (φ, ϑ) or the area variable $A := \int_0^\vartheta \int_0^\varphi \sin \vartheta d\varphi d\vartheta$. For equally distributed orientations in space, the infinitesimal probability that the vector \mathbf{t} falls in the infinitesimal surface area dA of the sphere \mathcal{S} is $dP = dA/|\mathcal{S}|$ with $|\mathcal{S}| = 4\pi$.

3.3.3. A Non-Affine Network Model for Unconstrained Chains.

A Non-Affine Stretch Assumption. As clearly pointed out by ARRUDA & BOYCE [8, 25] the assumption of the affine stretch of the polymer chains made in equation (3.31) is not appropriate in the non-Gaussian region at large strains. In real networks, chains which lie along the maximum principle stretch direction would begin to stretch less with continuing deformation once they begin to approach their maximum extensibility. At that moment, other chains in the network will stretch more than predicted by the affine deformation in order to accommodate the applied total stretches. Therefore, the affinity of chain deformation will be lost. The affine network model outlined above, therefore at large strains overestimates the stress-stretch behavior of chains along the principal directions. This observation motivated ARRUDA & BOYCE [8] to construct the eight-chain model.

In this section we develop a generalization of the eight-chain model that opens up the possibility to scale observations made in uniaxial and equi-biaxial tension experiments through the introduction of an additional material parameter. The key underlying concept is to allow the micro-stretches λ to fluctuate around the macro-stretches $\bar{\lambda}$ defined in (3.30). To this end, we relax equation (3.31) by writing

$$\lambda = \bar{\lambda} f. \quad (3.41)$$

The multiplier f is a stretch-fluctuation field on the unit sphere that in a multiplicative format acting on the affine stretch. The fluctuation field is assumed to be defined on the unit sphere of space orientations introduced above. The non-affine micro-stretch is assumed to be constrained by the condition

$$\langle \lambda \rangle_p = \langle \bar{\lambda} \rangle_p \quad (3.42)$$

in terms of the p -root averaging operator

$$\langle v \rangle_p := \sqrt[p]{\langle v^p \rangle} = \left(\frac{1}{|\mathcal{S}|} \int_{\mathcal{S}} v^p dA \right)^{1/p} \quad (3.43)$$

of a scalar micro-variable $v > 0$ defined on the unit sphere. The constraint (3.42) states that the p -root average of the non-affine stretch λ of the single polymer chain is identical to the p -root average of the macroscopic stretch $\bar{\lambda}$. In the forthcoming treatment we consider the parameter p in (3.42) as an additional material parameter of the network.

Contribution to Macroscopic Free Energy. The fluctuation field f on the unit sphere of spatial orientations is determined by a *principle of minimum averaged free energy* conceptually in line with homogenization principles for composites. This minimization principle determines the macroscopic free energy by the expression

$$\bar{\Psi}_f(\mathbf{g}; \bar{\mathbf{F}}) = \sup_{\kappa} \inf_f \{ \langle n\psi_f(\bar{\lambda}f) \rangle - \kappa(\langle \bar{\lambda}f \rangle_p - \langle \bar{\lambda} \rangle_p) \} \quad (3.44)$$

where the Lagrange multiplier κ enforces the constraint (3.42). The minimization problem defines the overall macroscopic free energy of the non-affine stretch model. The necessary conditions of the minimization problem (3.44) are met by

$$n\psi'_f(\bar{\lambda}f) - \kappa(\langle \bar{\lambda}f \rangle_p)^{(1-p)}(\bar{\lambda}f)^{(p-1)} = 0 \quad (3.45)$$

defined locally at $A \in \mathcal{S}$, and the global constraint (3.42). The above local condition can be recast into the instructive form

$$n\psi'_f(\bar{\lambda}f)(\langle \bar{\lambda}f \rangle_p)^{(p-1)}(\bar{\lambda}f)^{(1-p)} = \kappa, \quad (3.46)$$

where $\kappa = \text{constant}$ on the sphere. For particular free energy functions with derivatives of the form $\psi'_f(\bar{\lambda}f) = c(\bar{\lambda}f)^{(p-1)}$, a *trivial solution* is obtained for zero fluctuations on the sphere $f = 1$ at $A \in \mathcal{S}$, which recovers the affine network model (3.32) with $\lambda = \bar{\lambda}$. A *non-trivial solution* of (3.46) with non-zero fluctuations $f \neq 0$ on the sphere for arbitrary nonlinear energy functions ψ_f can be derived only if the argument $\lambda = \bar{\lambda}f$ is constant. Then from (3.42) we conclude the simple closed-form result of the minimization problem (3.44) that defines the non-affine micro-stretch

$$\lambda = \langle \bar{\lambda} \rangle_p. \quad (3.47)$$

This condition identifies the micro-stretch on the sphere with the constant p -root average of the macro-stretches. This non-affine relation relaxes the conditions (3.31) of the affine model. The associated micro-stretch fluctuation field is then defined by (3.41). The insertion of the non-trivial solution (3.47) into (3.44) gives the simple representation

$$\boxed{\bar{\Psi}_f(\mathbf{g}; \bar{\mathbf{F}}) = n\psi_f(\langle \bar{\lambda} \rangle_p)} \quad (3.48)$$

as the contribution to the macroscopic free energy of the non-affine network model for unconstrained chains. It is important to note that the eight-chain model of ARRUDA & BOYCE [8] can be obtained from the above outlined formulation as a *special case* for $p = 2$ where the micro-stretch (3.47) assumes the explicit form

$$\lambda = \langle \bar{\lambda} \rangle_2 = \sqrt{I_1/3} \quad \text{with} \quad I_1 := \text{tr}[\bar{\mathbf{F}}^T \mathbf{g} \bar{\mathbf{F}}] \quad (3.49)$$

in terms of the isochoric macroscopic deformation $\bar{\mathbf{F}}$.

Contribution to Macroscopic Stresses and Moduli. Having the macro-energy of the non-affine network model determined, we can proceed with computation of the Eulerian stresses and elasticity moduli based on a straightforward exploitation of formulae (3.27). To this end, we first compute the derivatives of the non-affine stretch (3.47) with respect to the current metric. Using the result (3.38), we obtain

$$2\partial_{\mathbf{g}}\lambda = \lambda^{1-p}\mathbf{h} \quad \text{with} \quad \mathbf{h} := \langle \bar{\lambda}^{p-2}\mathbf{t} \otimes \mathbf{t} \rangle. \quad (3.50)$$

Insertion of (3.48) into (3.27)₁ yields the representation of the macroscopic Kirchhoff stresses

$$\bar{\boldsymbol{\tau}}_f = n\psi'_f \lambda^{1-p} \mathbf{h} . \quad (3.51)$$

A further derivative of the stresses by the Eulerian metric yields the spatial elasticity moduli defined in (3.27)₂. In a first step, starting from (3.38), we compute the derivatives of the tensor \mathbf{h} introduced in (3.50)

$$\mathbb{H} := 2\partial_{\mathbf{g}} \mathbf{h} = \langle (p-2)\bar{\lambda}^{p-4} \mathbf{t} \otimes \mathbf{t} \otimes \mathbf{t} \otimes \mathbf{t} \rangle . \quad (3.52)$$

Then the contribution to the Eulerian tangent moduli appears in the form

$$\bar{\mathbb{C}}_f = (n\psi''_f \lambda^{2(1-p)} - (p-1)n\psi'_f \lambda^{(1-2p)}) \mathbf{h} \otimes \mathbf{h} + n\psi'_f \lambda^{1-p} \mathbb{H} . \quad (3.53)$$

The numerical evaluation of the tensors \mathbf{h} and \mathbb{H} defined in (3.50), (3.52) is based on the discretization of the continuous integral over the unit sphere, see Section 3.4.

3.3.4. A Non-Affine Network Model for the Tube Constraint.

Deformation Assumption for Tube Contraction. Consider the isochoric deformation of an area element with normal \mathbf{r}_b in the reference configuration, yielding the area vector

$$\mathbf{n}_b = \bar{\mathbf{F}}^{-T} \mathbf{r}_b . \quad (3.54)$$

Then the *macro-area-stretch* of a material area element with normal \mathbf{r}_b in the reference configuration is

$$\bar{\nu} = |\mathbf{n}|_{\mathbf{g}} := \sqrt{\mathbf{n}_b \cdot \mathbf{n}} \quad \text{with} \quad \mathbf{n} := \mathbf{g}^{-1} \mathbf{n}_b , \quad (3.55)$$

where \mathbf{n} is the vector associated with the co-vector \mathbf{n}_b . We propose the relationship

$$\nu = (\bar{\nu})^q \quad (3.56)$$

between the micro-tube contraction ν defined in (3.11) and the macro-area-stretch defined in (3.55). This equation relates the tube contraction to the area change of a cross section with normal \mathbf{r}_b in the reference configuration. The additional material parameter q governs a nonlinearity between the microscopic tube contraction and the macroscopic area change. A descriptive interpretation of the above assumption is given in Figure 3.3c. In the case of a macroscopic area extension of the cross section, chains in a direction perpendicular to the prototype chain under consideration are stretched. The perpendicular chains, which we referred to as *forest chains*, are assumed to be obstacles for the extension of the *prototype chain*. Up on their stretch they assume a straighter topology that decreases the diameter of the fluctuation of the cross section projection as indicated by the shaded circle in Figure 3.3c. This diameter of the fluctuations of the perpendicular obstacle chain is interpreted as the diameter of the tube that constrains the prototype chain. Hence, our proposed model constitutes an inverse relationship between the microscopic tube diameter and the macroscopic area change: *the diameter of the tube decreases with increasing area stretch.*

Contribution to Macroscopic Free Energy. With the above link of the tube contraction to the macro deformation at hand, we are able to define the macroscopic energy associated with the tube constraint. In analogy to (3.32) we write

$$\bar{\Psi}_c(\mathbf{g}; \bar{\mathbf{F}}) = \langle n\psi_c(\bar{\nu}^q) \rangle \quad (3.57)$$

where $\langle v \rangle$ denotes the continuous averaging for an equal orientation distribution of the variable v in the space as defined in (3.37).

Contribution to Macroscopic Stresses and Moduli. We first compute the derivatives of the macroscopic area stretch $\bar{\nu}$ defined in (3.55) by the Eulerian metric, yielding

$$2\partial_{\mathbf{g}}\bar{\nu} = -\bar{\nu}^{-1}\mathbf{n} \otimes \mathbf{n}. \quad (3.58)$$

The insertion of this result into (3.28)₁ gives the contribution to the macroscopic Kirchhoff stresses

$$\bar{\boldsymbol{\tau}}_c = -\langle n\psi'_c q \bar{\nu}^{(q-2)} \mathbf{n} \otimes \mathbf{n} \rangle. \quad (3.59)$$

Further derivation of the stresses with respect to the Eulerian metric yields the contribution to the spatial elasticity moduli defined in (3.28)₂. They are computed from (3.59) by using the result (3.58) and

$$2\partial_{\mathbf{g}}(\mathbf{n} \otimes \mathbf{n}) = -2\text{sym}[\mathbf{g}^{-1} \odot (\mathbf{n} \otimes \mathbf{n}) + (\mathbf{n} \otimes \mathbf{n}) \odot \mathbf{g}^{-1}]. \quad (3.60)$$

Here, the introduced direct notation is associated with the index representation $\text{sym}[\mathbf{g}^{-1} \odot (\mathbf{n} \otimes \mathbf{n})]^{abcd} := (\delta^{ac}n^bn^d + \delta^{bc}n^an^d)/2$. With these definitions at hand, the contribution to the Eulerian tangent moduli appear in the form

$$\begin{aligned} \bar{\mathbb{C}}_c = & \langle (n\psi''_c q^2 \bar{\nu}^q + n\psi'_c q(q-2))\bar{\nu}^{(q-4)} \mathbf{n} \otimes \mathbf{n} \otimes \mathbf{n} \otimes \mathbf{n} \\ & + 2n\psi'_c q \bar{\nu}^{(q-2)} \text{sym}[\mathbf{g}^{-1} \odot (\mathbf{n} \otimes \mathbf{n}) + (\mathbf{n} \otimes \mathbf{n}) \odot \mathbf{g}^{-1}] \rangle. \end{aligned} \quad (3.61)$$

The numerical implementation of the macro-stresses (3.59) and macro-moduli (3.61) based on the discretization of the continuous integral is commented on below.

3.4. Algorithmic Setting of the Constitutive Model

This section summarizes the key constitutive equations of the proposed non-affine network model and introduces effective material parameters. Furthermore, we comment on details of the numerical implementation by a suitable discretization of the orientation space associated with the micro-sphere.

3.4.1. Summary of the Effective Material Parameters. The proposed model is governed by the local constitutive equations for a prototype single chain in a tube and the non-affine network assumptions outlined in Sections 3.2 and 3.3, respectively. For the *non-Gaussian stretch model* of the unconstrained chain, from (3.19) and by using the Padé approximation (3.21) we obtain the approximative expressions

$$n\psi'_f(\lambda) = \mu \frac{3N - \lambda^2}{N - \lambda^2} \lambda \quad \text{and} \quad n\psi''_f(\lambda) = \mu \frac{\lambda^4 + 3N^2}{(N - \lambda^2)^2} \quad (3.62)$$

for the derivatives of the micro-energy required in expressions (3.39) and (3.40) of the stresses and tangent moduli. Here, we made use of the classical definition of the *effective shear modulus*

$$\mu := nk\theta \quad (3.63)$$

in terms of the n chains per volume, Boltzmann's constant k and the absolute temperature θ . For the proposed *tube model* that describes the interactions of the chains, we obtain the derivatives

$$n\psi'_c(\nu) = \mu NU \quad \text{and} \quad n\psi''_c(\nu) = 0 \quad (3.64)$$

of the micro-energy (3.23) required in the expressions (3.59) and (3.61) for the stresses and tangent moduli. Here, we introduced the *effective tube geometry parameter*

$$U := \alpha\left(\frac{l}{d_0}\right)^2 \quad (3.65)$$

as a function of Kuhn's segment length l and the initial tube diameter d_0 . The two equations (3.62) and (3.64) govern, with the three effective material parameters μ , N and U , the micromechanical response of a prototype chain in a tube. The characteristics of the non-affine network model for the stretch and tube-contraction are determined by further two material parameters p and q introduced in (3.47) and (3.56), respectively. Thus the model in total contains *five material parameters*, which we again summarize in Table 3.1. As shown in the numerical studies of Section 3.5, all these parameters may directly be associated with particular phenomenological effects and characteristics visuable in stress-stretch experiments of rubbery polymer aggregates. A rough statement concerning these qualitative influences is given in Table 3.1.

Table 3.1: Material Parameters of the Non-Affine Micro-Sphere Model

No.	Parameter	Name	Eq.	Effect
1	$\mu := nk\theta$	shear modulus	(3.19)	ground state stiffness
2	N	number of chain segments	(3.19)	chain locking response
3	p	non-affine stretch parameter	(3.47)	3D locking characteristics
4	$U := \alpha(l/d_0)^2$	tube geometry parameter	(3.23)	additional constraint stiffness
5	q	non-affine tube parameter	(3.56)	shape of constraint stress

3.4.2. Discretization of Fields on the Micro-Sphere. The implementation of the affine and non-affine network models outlined in the preceding two sections into computer codes requires a numerical evaluation of the integral over the continuous space orientations. This is carried out by discretizing the continuous orientation distribution of the unit sphere \mathcal{S} by m *discrete Lagrangian orientation vectors* $\{\mathbf{r}^i\}_{i=1\dots m}$ and *weight factors* $\{w^i\}_{i=1\dots m}$. Then the continuous averaging (3.37) of a micro-variable v defined on the sphere is transformed into the discrete sum

$$\langle v \rangle := \frac{1}{|\mathcal{S}|} \int_{\mathcal{S}} v(A) dA \approx \sum_{i=1}^m v^i w^i \quad (3.66)$$

Here, $\{v^i\}_{i=1\dots m}$ are the micro-variables on the sphere evaluated at the discrete points A^i with orientation vector \mathbf{r}^i . In order to preserve properties of isotropy and a stress-free state of the reference configuration in the discrete setting, the numerical integration

scheme is required to fulfill some constraints. Consider the continuous averaging of the orientation vector and its dyadic product

$$\langle \mathbf{r} \rangle = \mathbf{0} \quad \text{and} \quad \langle \mathbf{r} \otimes \mathbf{r} \rangle = \frac{1}{3} \mathbf{1}, \quad (3.67)$$

which can easily be proven through the Gauss theorem. The latter constraint is necessary in order to ensure a stress-free state of the macro-continuum in the reference configuration. Preservation of the above properties in the discrete setting yields the constraints

$$\sum_{i=1}^m \mathbf{r}^i w^i = \mathbf{0} \quad \text{and} \quad \sum_{i=1}^m \mathbf{r}^i \otimes \mathbf{r}^i w^i = \frac{1}{3} \mathbf{1} \quad (3.68)$$

on the integration scheme. Sets of orientation vectors $\{\mathbf{r}^i\}_{i=1\dots m}$ and associated weight factors $\{w^i\}_{i=1\dots m}$ which satisfy these constraints are given in BAŽANT & OH [10].

Table 3.2: Integration Points and Weights on Unit Sphere

No.	r_1^i	r_2^i	r_3^i	$w^i/2$
1	0.0	0.0	1.0	0.0265214244093
2	0.0	1.0	0.0	0.0265214244093
3	1.0	0.0	0.0	0.0265214244093
4	0.0	0.707106781187	0.707106781187	0.0199301476312
5	0.0	-0.707106781187	0.707106781187	0.0199301476312
6	0.707106781187	0.0	0.707106781187	0.0199301476312
7	-0.707106781187	0.0	0.707106781187	0.0199301476312
8	0.707106781187	0.707106781187	0.0	0.0199301476312
9	-0.707106781187	0.707106781187	0.0	0.0199301476312
10	0.836095596749	0.387907304067	0.387907304067	0.0250712367487
11	-0.836095596749	0.387907304067	0.387907304067	0.0250712367487
12	0.836095596749	-0.387907304067	0.387907304067	0.0250712367487
13	-0.836095596749	-0.387907304067	0.387907304067	0.0250712367487
14	0.387907304067	0.836095596749	0.387907304067	0.0250712367487
15	-0.387907304067	0.836095596749	0.387907304067	0.0250712367487
16	0.387907304067	-0.836095596749	0.387907304067	0.0250712367487
17	-0.387907304067	-0.836095596749	0.387907304067	0.0250712367487
18	0.387907304067	0.387907304067	0.836095596749	0.0250712367487
19	-0.387907304067	0.387907304067	0.836095596749	0.0250712367487
20	0.387907304067	-0.387907304067	0.836095596749	0.0250712367487
21	-0.387907304067	-0.387907304067	0.836095596749	0.0250712367487

The integration schemes exploit the symmetry of the unit sphere by defining discrete points only for the half-sphere. A set of $m = 21$ integration points for the half sphere

$$\mathbf{r}^i = r_1^i \mathbf{e}_1 + r_2^i \mathbf{e}_2 + r_3^i \mathbf{e}_3 \quad (3.69)$$

and associated weights w^i are summarized in Table 3.2 for a cartesian standard base. In Section 3.5 we show that the selected 21-point integration scheme provides sufficient accuracy for all numerical investigations considered. Thus all the above outlined continuous average operations in the discrete setting appear as a *simple algebraic sum over 21 discrete space orientations*. The numerical implementation of the affine and non-affine micro-sphere models are summarized in Tables 3.3 and 3.4, respectively.

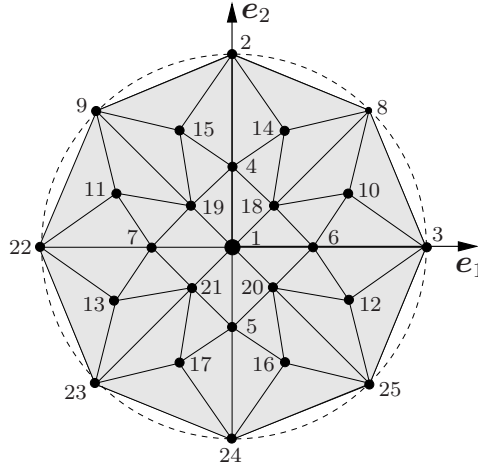


Figure 3.5: Stereographic pole projection of the unit sphere describing the microstructure of the network model. The proposed numerical setting uses $m = 21$ integration points with cartesian coordinates defined in Table 3.3 for the discrete micro-state evaluation on the sphere. The points 22-25 are introduced by symmetry conditions for plotting purposes.

The discrete space orientations of the half space are visualized in Figure 3.5 by the labeled points of a stereographic pole projection. The pole plots allow a visualization of the discretized micromechanical fields on the micro-sphere. This descriptive representations of the micromechanical state is considered to be an important advantage of the proposed network model. As an example, Figure 3.6 visualizes the affine micro-stretches $\bar{\lambda}$ and the affine area-stretch $\bar{\nu}$ for typical homogeneous deformation modes. The figure also indicates the quality of the plot interpolation for the $m = 21$ -point discretization scheme.

Table 3.3: Implementation of the Affine-Stretch Micro-Sphere Model.

1. *Initialization.* Get unimodular part $\bar{\mathbf{F}} \in SL(3)$ of deformation gradient from equation (3.4). Set discrete orientation vectors \mathbf{r}^i and weights w^i for the $m = 21$ -point integration scheme summarized in Table 3.2.
2. *Affine Stretch Model.* Compute deformed tangents $\mathbf{t}^i = \bar{\mathbf{F}}\mathbf{r}^i$ and affine micro-stretches $\bar{\lambda}^i = |\mathbf{t}^i|$ for $i = 1 \dots m$. Calculate the macro-stresses

$$\bar{\boldsymbol{\tau}}_f = \mu \sum_{i=1}^m \frac{3N - \bar{\lambda}^{i2}}{N - \bar{\lambda}^{i2}} \mathbf{t}^i \otimes \mathbf{t}^i w^i ,$$

the macro-moduli

$$\bar{\mathbb{C}}_f = \mu \sum_{i=1}^m \left[\frac{\bar{\lambda}^{i4} + 3N^2}{(N - \bar{\lambda}^{i2})^2} \bar{\lambda}^{i-2} - \frac{3N - \bar{\lambda}^{i2}}{N - \bar{\lambda}^{i2}} \bar{\lambda}^{i-2} \right] \mathbf{t}^i \otimes \mathbf{t}^i \otimes \mathbf{t}^i \otimes \mathbf{t}^i w^i$$

and proceed with deviatoric projections defined in equations (3.6) and (3.7).

Table 3.4: Implementation of the Non-Affine Micro-Sphere Model.

1. *Initialization.* Get unimodular part $\bar{\mathbf{F}} \in SL(3)$ of deformation gradient from equation (3.4). Set discrete orientation vectors \mathbf{r}^i and weights w^i for the $m = 21$ -point integration scheme summarized in Table 3.2.

2. *Non-Affine Stretch Part.* Compute deformed tangents $\mathbf{t}^i = \bar{\mathbf{F}}\mathbf{r}^i$ and affine micro-stretches $\bar{\lambda}^i = |\mathbf{t}^i|$ for $i = 1 \dots m$. Compute non-affine stretches and their derivatives

$$\begin{aligned}\lambda &= [\sum_{i=1}^m (\bar{\lambda}^i)^p w^i]^{1/p}, \\ \mathbf{h} &= \sum_{i=1}^m (\bar{\lambda}^i)^{p-2} \mathbf{t}^i \otimes \mathbf{t}^i w^i, \\ \mathbb{H} &= (p-2) \sum_{i=1}^m (\bar{\lambda}^i)^{p-4} \mathbf{t}^i \otimes \mathbf{t}^i \otimes \mathbf{t}^i \otimes \mathbf{t}^i w^i.\end{aligned}$$

Calculate micro-stresses and micro-moduli

$$\tau_f = \mu(3N - \lambda^2)/(N - \lambda^2)\lambda \quad \text{and} \quad c_f = \mu(\lambda^4 + 3N^2)/(N - \lambda^2)^2$$

and compute the macro-stresses and macro-moduli

$$\bar{\boldsymbol{\tau}}_f = \tau_f \lambda^{1-p} \mathbf{h} \quad \text{and} \quad \bar{\mathbb{C}}_f = (c_f \lambda^{2-2p} - (p-1)\tau_f \lambda^{1-2p}) \mathbf{h} \otimes \mathbf{h} + \tau_f \lambda^{1-p} \mathbb{H}$$

3. *Non-Affine Tube Part.* Compute deformed normals $\mathbf{n}^i = \bar{\mathbf{F}}^{-T}\mathbf{r}^i$ and affine area-stretches $\bar{\nu}^i = |\mathbf{n}^i|$ for $i = 1 \dots m$. Compute derivatives

$$\begin{aligned}\mathbf{k} &= q \sum_{i=1}^m (\bar{\nu}^i)^{q-2} \mathbf{n}^i \otimes \mathbf{n}^i w^i, \\ \mathbb{K} &= q(q-2) \sum_{i=1}^m (\bar{\nu}^i)^{q-4} \mathbf{n}^i \otimes \mathbf{n}^i \otimes \mathbf{n}^i \otimes \mathbf{n}^i w^i, \\ \mathbb{G} &= 2q \sum_{i=1}^m (\bar{\nu}^i)^{q-2} \text{sym}[\mathbf{g}^{-1} \odot (\mathbf{n}^i \otimes \mathbf{n}^i) + (\mathbf{n}^i \otimes \mathbf{n}^i) \odot \mathbf{g}^{-1}] w^i\end{aligned}$$

and compute the macro-stresses and macro-moduli

$$\bar{\boldsymbol{\tau}}_c = -\mu N U \mathbf{k} \quad \text{and} \quad \bar{\mathbb{C}}_c = \mu N U (\mathbb{K} + \mathbb{G})$$

4. *Superimposed Stress Response.* Add macroscopic contributions of stretch and tube deformation part

$$\bar{\boldsymbol{\tau}} = \bar{\boldsymbol{\tau}}_f + \bar{\boldsymbol{\tau}}_c \quad \text{and} \quad \bar{\mathbb{C}} = \bar{\mathbb{C}}_f + \bar{\mathbb{C}}_c$$

and proceed with deviatoric projections defined in equations (3.6) and (3.7).

3.5. Assessment of the Modeling Capacity of the Model

In the foregoing sections, the network models for rubber elasticity incorporating constraint effects for both affine and non-affine kinematic measures have been introduced. This covers explicit constitutive expressions for the Eulerian Kirchhoff stresses and moduli outlined in Section 3.3 and their algorithmic counterparts developed in Section 3.4 based on the discretization of mean value operations on the micro-sphere. The algorithms for

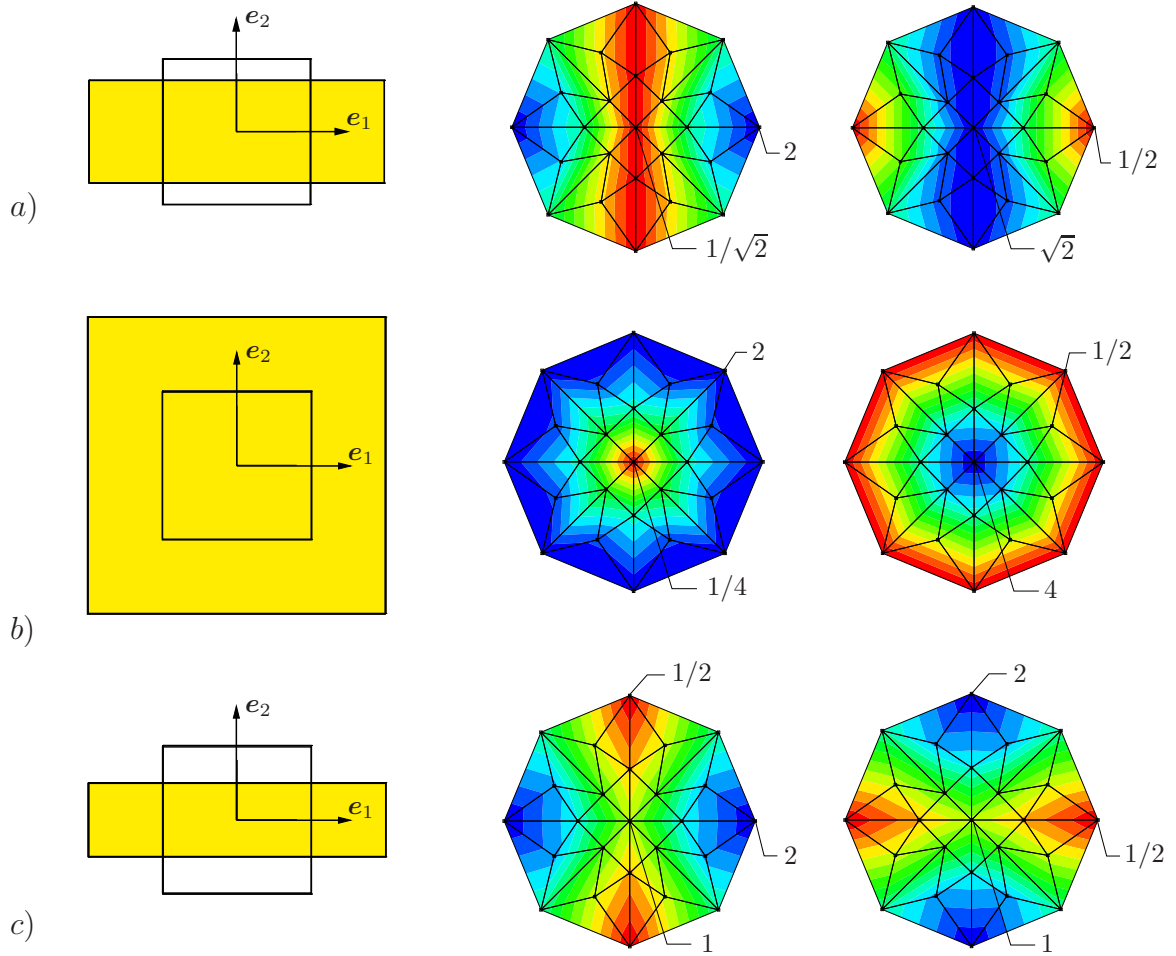


Figure 3.6: Stereographic projection plots of *affine micro-stretches* $\lambda = \bar{\lambda} := |\bar{\mathbf{F}}\mathbf{r}|$ and *affine tube-contractions* $\nu = \bar{\nu} := |\bar{\mathbf{F}}^{-T}\mathbf{r}|$ for homogeneous macro-deformation modes a) simple uniaxial tension, b) equibiaxial tension and c) pure shear. The figure demonstrates the plot interpolation quality of the $m = 21$ -point integration on the micro-sphere.

the *affine and non-affine micro-sphere models* summarized in Tables 3.3 and 3.4 represent constitutive network processors suitable for the implementation into finite element codes. Objective of this section is to assess the modeling capacity of the new non-affine network model summarized in Table 3.4. The subsequent five subsections are intended to discuss the following aspects of the proposed formulation:

1. Investigation of the *accuracy* of the numerical approximations due to (i) Padè's approximation (3.21) of the inverse Langevin function and (ii) the discrete integration (3.66) over the micro-sphere where we compare the present formulation with the previously developed full network models of TRELOAR [195] and TRELOAR & RIDING [197].
2. Comparison of affine network models with the eight-chain model of ARRUDA & BOYCE [8] with regard to *locking stretch* values in uniaxial and equi-biaxial tension.
3. Investigation of the *stress sensitivity* of the proposed non-affine micro-sphere model with respect to the five material parameters summarized in Table 3.1.
4. Demonstration of the excellent *performance* of the proposed non-affine micro-sphere model against representative benchmark experimental data.

5. Application of the new non-affine micro-sphere model to a typical finite element simulation of a three-dimensional *inhomogeneous shear test*.

In the subsequent investigations, the identification of the material parameters based on experimental data is carried out through SQP gradient-type solution methods of least-square-type optimization problems as outlined in MIEHE & KECK [150], SCHEDAY [179].

3.5.1. Performance of the Proposed Algorithmic Implementation. The numerical formulations of the micro-sphere models summarized in Tables 3.3 and 3.4 are based on two approximations. First, we use the computationally efficient discrete integration scheme (3.66) for the averaging of state functions defined on the sphere. We then apply Padé’s approximation (3.21) for the computation of the inverse Langevin function. In what follows we compare these proposed formulations with previously developed full network models, the so-called “uniaxial full network model” and the “biaxial full network model” introduced by TRELOAR [195] and TRELOAR & RIDING [197], respectively. They used discontinuous power series approximation for the computation of the inverse Langevin function for different ranges of its argument and employed an adaptive grid integration for micro-macro transition. In the latter paper the normalized Cauchy stress values σ_{11}/μ for uniaxial and biaxial deformation processes are reported for different values of the material parameter N , see Tables A4, A2 and A3 in [197].

The numerical performance of the affine micro-sphere model, summarized in Table 3.3, for a $m = 37$ -point integration is compared in Figures 3.7a-d to the results of TRELOAR & RIDING [197] for tensile uniaxial and biaxial deformations. With these high-resolution integrations, both affine network models are in good agreement for all types of deformations and for all values of N . The numerical accuracy of the $m = 21$ -point integration scheme for uniaxial and biaxial deformations are illustrated in Figures 3.8a-d. This comparison shows that the $m = 21$ -point integration used in the proposed models of Tables 3.3 and 3.4 is precise enough. The observed minor accuracy error due to the numerical approximation in the neighborhood of limiting stretch value is assumed to be circumvented by the appropriate use of material parameters. In other words, we consider the discrete $m = 21$ -point computation of state variables on the sphere as a part of the constitutive model. All subsequent computations use the $m = 21$ -point integration scheme and their corresponding weighting factors provided in Table 3.2.

3.5.2. Comparison of Affine Network Models with the Eight-Chain Model. It has already been pointed out in several contributions that the affine network models yield results that are not in agreement with experimental data, in particular for the simultaneous simulation of equi-biaxial and uniaxial test data. In the excellent review paper BOYCE & ARRUDA [25], it was argued that at the instant when the limited extension is reached among chains a *redistribution* takes place and other chains in the network experience more extension than the one predicted by the affine kinematics.

In the light of this discussion, we compare the response of three affine network models (the three-chain model of JAMES & GUTH [101], the three dimensional full network model of WU & VAN DER GIESSEN [206] and the proposed affine micro-sphere model summarized in Table 3.3) with the eight-chain model of ARRUDA & BOYCE [8] in Figures 3.9a and 3.9b for simple tension and equi-biaxial deformations, respectively. In this investigation, the two material parameters are chosen to be $\mu = 0.25$ MPa, $N = 64$. In Figure 3.9, it can easily be observed that the affine network models show *asymptotic behavior at*

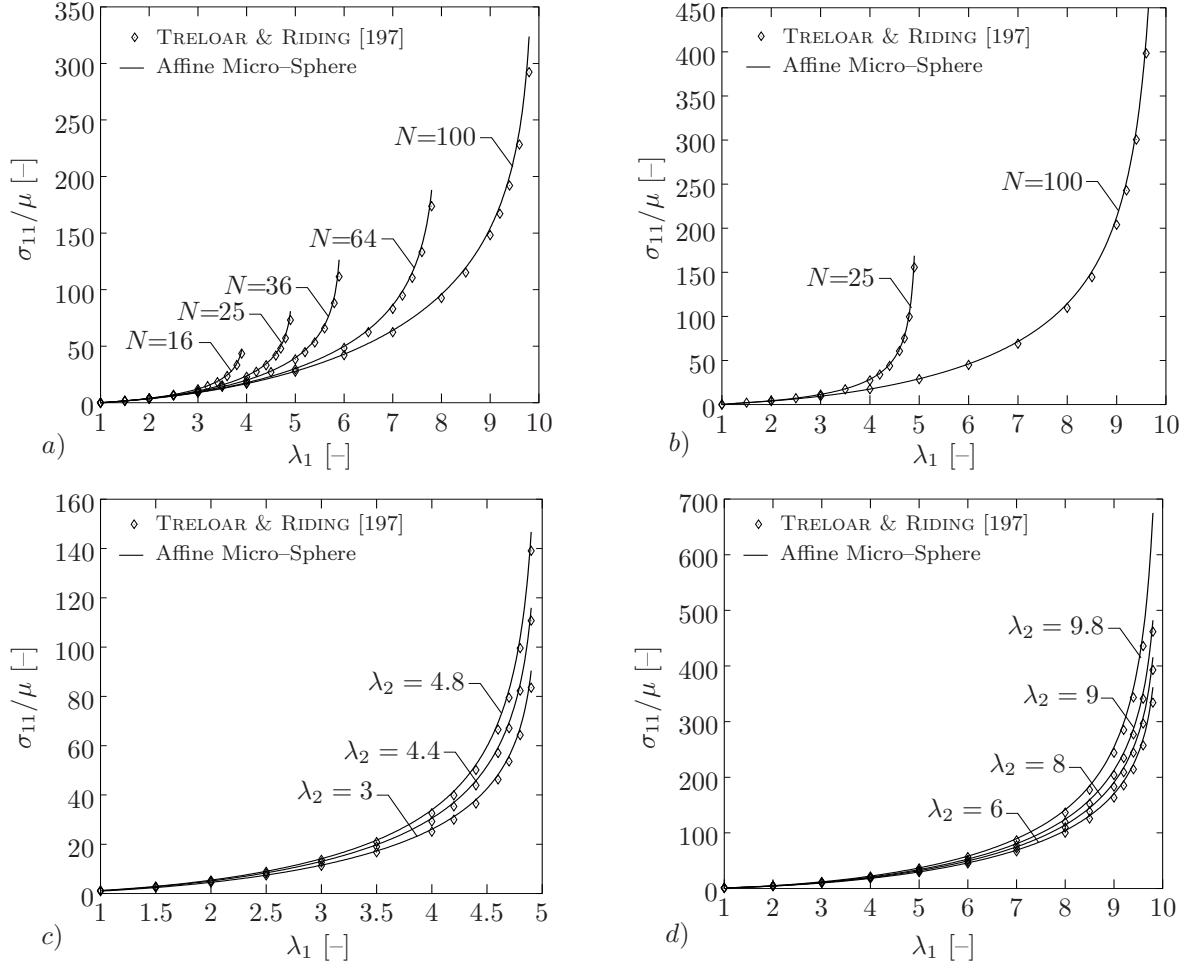


Figure 3.7: Comparison of the Affine Micro-Sphere model with the affine biaxial full network model of TRELOAR & RIDING [197] for $m = 37$ -point integration scheme on micro-sphere. a) Simple tension and b) equi-biaxial tension for different values of the material parameter N . Plots c) and d) compare the models in case of biaxial tension at different values of the macro-stretch λ_2 for $N = 25$ and $N = 100$, respectively.

the same values of stretch, corresponding to the value of \sqrt{N} , for both uniaxial and equi-biaxial deformations. This behavior can also be observed in Figures 3.7a,b or in Figures 3.8a,b by the affine full network model of TRELOAR & RIDING [197]. As expected, the response exhibited by proposed affine micro-sphere model in Table 3.3 closely resembles that of the three-dimensional full network model of WU & VAN DER GIESSEN [206]. In contrast to the affine network models, the eight chain model shows *singular behavior at different values of stretch* for uniaxial and equi-biaxial deformations.

Recalling the formulation of the eight chain model, we make the following phenomenological observation. As pointed out in equation (3.49), the free energy of the eight-chain model is a function of the non-affine network stretch $\lambda = \sqrt{I_1/3}$, where I_1 is the first principal invariant of the isochoric right Cauchy-Green tensor. The derivative of this free energy with respect to an appropriate deformation measure yields the function for the stresses which comes out to be proportional to the inverse Langevin function $\mathcal{L}^{-1}(\lambda)$, see also equation (3.20). The replacement of the inverse Langevin function by Padé's approximation (3.21) yields $\mathcal{L}^{-1}(\lambda) \approx \lambda(3N - \lambda^2)/\sqrt{N}(N - \lambda^2)$. Apparently, the source of the finite extensibility is the value of λ making the denominator of this expression vanishing.

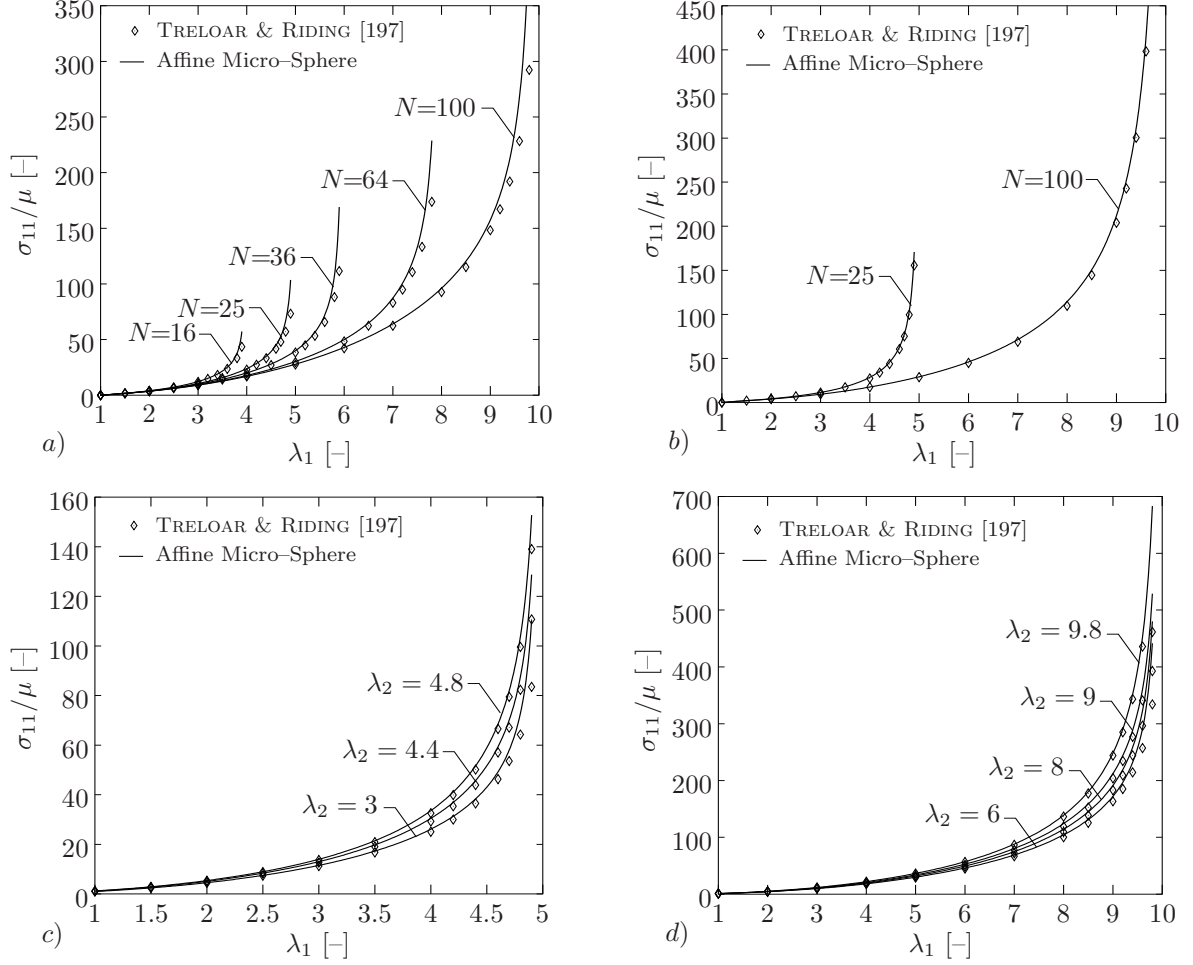


Figure 3.8: Comparison of the affine micro-sphere model with the affine biaxial full network model of TRELOAR & RIDING [197] for $m = 21$ -point integration scheme on micro-sphere. a) Simple tension and b) equi-biaxial tension for different values of the material parameter N . Plots c) and d) compare the models in case of biaxial tension at different values of the macro-stretch λ_2 for $N = 25$ and $N = 100$, respectively.

This is achieved by $\lambda = \sqrt{N}$. Hence, we obtain the *locking criterion*

$$\lambda_{lock,8-chain} \approx \arg\{I_1(\lambda) = 3N\} \quad (3.70)$$

of the eight-chain model. For a constant value of N , we can compute the value of what we call the *locking stretch* for different kinds of isochoric deformations. For uniaxial deformation with $I_1 = \lambda^2 + 2\lambda^{-1}$ and $N = 64$, we get $\lambda_{lock}^{uni} = 13.86$. Likewise, for equi-biaxial deformation with $I_1 = 2\lambda^2 + \lambda^{-4}$ and $N = 64$, we obtain $\lambda_{lock}^{eqb} = 9.8$. These estimated values are none other than the asymptotes observed in Figure 3.9.

The celebrated experimental benchmark data reported by TRELOAR [193] on rubber undergoing simple tension, tensile equi-biaxial and pure shear deformations, see Figure 3.10, have singular behavior similar to that exhibited by the eight-chain model. Using the value of $N = 26.5$ in the eight-chain model, we obtain the different locking stretches $\lambda_{lock}^{uni} = 8.9$ and $\lambda_{lock}^{eqb} = 6.31$, which reflect the trend of the experimental data depicted in Figure 3.10. Similar investigations on locking stretch values of successful models such as KALISKE & HEINRICH [104] yield similar results for representative values. As already shown in Figure 3.9, the affine network models cannot achieve this characteristic material

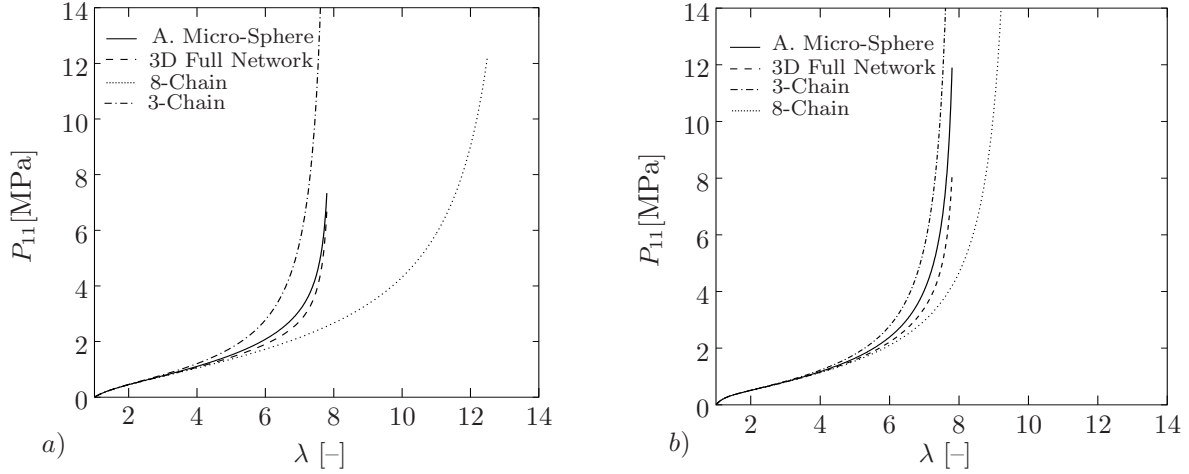


Figure 3.9: Comparison of the different affine network models with the eight-chain model for *a)* simple tension and *b)* equi-biaxial tension for the material parameters $\mu = 0.25\text{MPa}$, $N = 64$.

behavior of rubbers showing different locking stretches for different deformation modes. This handicap of the affine models is the key motivation for the introduction of non-affine network models.

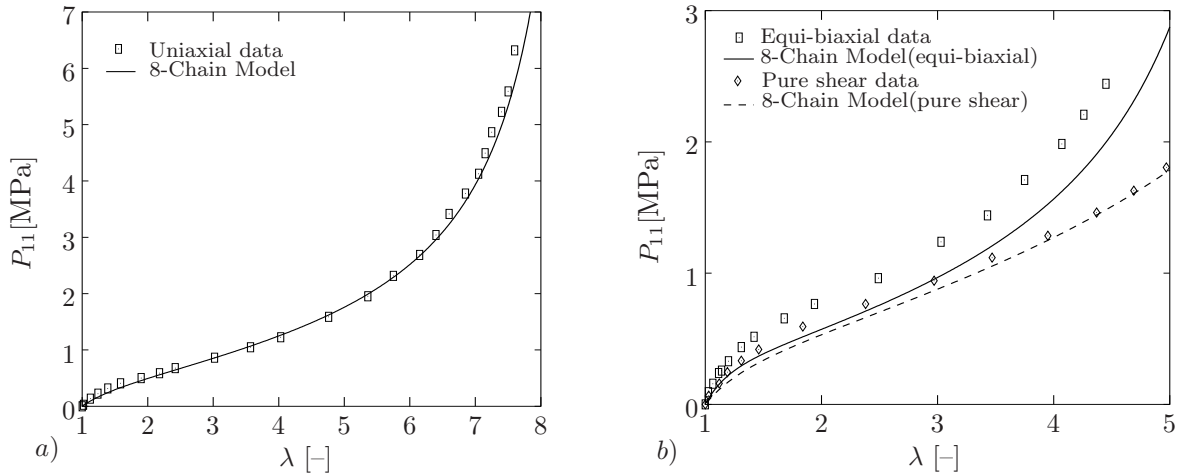


Figure 3.10: Performance of the eight-chain model with the material parameters $\mu = 0.27\text{MPa}$, $N = 26.5$ in comparison with the well known TRELOAR [193] data.

The first attempt in this direction was the development of the eight-chain model by ARRUDA & BOYCE [8]. Though the response of this model with respect to the number of just two material parameters is excellent, it still seems to have restrictions due to its inherent *fixed relationship between locking stretches* for different deformation modes characterized by the locking criterion (3.70). Furthermore, it *underestimates the data* of TRELOAR [193] for the equi-biaxial and the pure shear deformations especially *at moderate deformations*, see Figure 3.10. These two aspects motivated us to develop the non-affine micro-sphere model summarized in Table 3.4. The introduction of the *non-affinity parameter* p in the proposed non-affine micro-sphere model, which reproduces the eight-chain model for $p = 2$, significantly improves the flexibility of the locking stretch behavior in particular for equi-biaxial deformation, see Figure 3.11 and compare it with Figure 3.10. The necessary additional contribution to the stress at moderate deformations

is obtained by the tube contribution to the free energy governed by the *tube parameters* U and q , which model constraint effects on the conformation of a chain, see Figure 3.14.

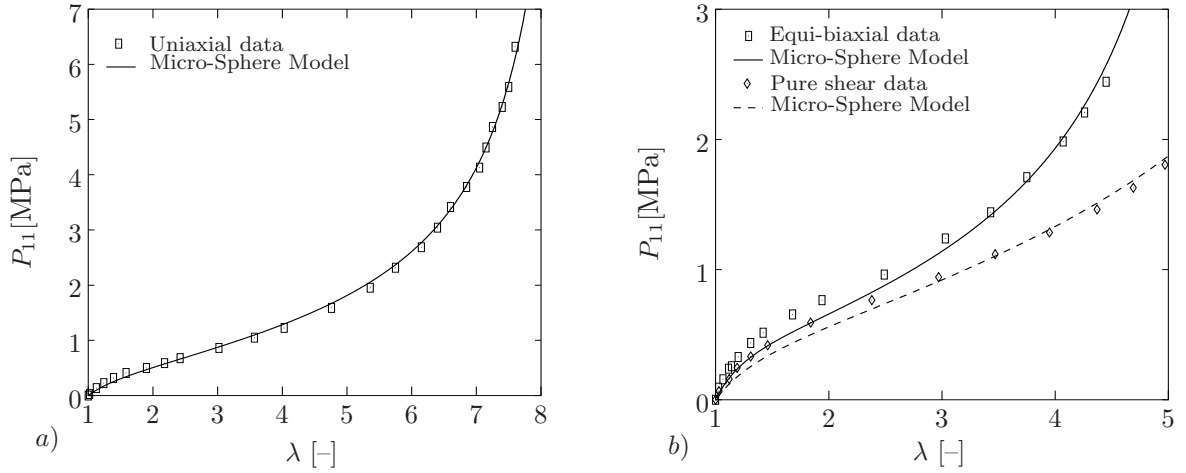


Figure 3.11: Performance of the non-affine micro-sphere model without tube-like constraint contribution with the material parameters $\mu = 0.325$ MPa, $N = 22.263$, $p = 1.39$ in comparison to the well-known TRELOAR [193] data.

3.5.3. Characteristics of the Proposed Non-Affine Micro-Sphere Model.

In this section, we investigate the stress sensitivity of the proposed non-affine micro-sphere model with respect to the five material parameters, summarized in Table 3.1, by performing uniaxial and equi-biaxial deformations tests. Firstly, the contribution to the free energy from the constraint effects on its conformation is ignored. That is, the sensitivity of the model to only the parameters μ , N , p is investigated in the left and the right columns of Figure 3.12 for uniaxial and equi-biaxial deformations, respectively. In Figures 3.12a,b the values of the parameters $N = 25$ and $p = 1.5$ are fixed and different values to the $\mu = 0.1, 1, 3, 5$ MPa are assigned. The stress response of the model for the different loading schemes are plotted for each value of μ . The increase in the parameter μ causes the stress ordinate of the curve to be scaled for both cases of deformation. The sensitivity of the stress-stretch curves to the parameter $N = 10, 20, 30, 50$ at fixed $\mu = 0.3$ MPa and $p = 1.5$ for uniaxial and equi-biaxial deformations are depicted in Figures 3.12c,d. As it can be seen, the larger the value of N , the greater the locking stretch value gets. In other words, a change of N shifts the value of λ_{lock} , leaving the compressive behavior almost untouched. Furthermore, the amount of λ_{lock} -shift in the uniaxial case is greater than the one in the equi-biaxial deformation for the same amount of increase in N . In Figure 3.12e,f the values of the parameters $\mu = 0.3$ MPa and $N = 25$ are kept constant and different values of $p = 1, 1.5, 2, 4$ are assigned. The qualitative effect of altering p is similar to that of the sensitivity of the model response to the parameter N . The smaller the value of p , the greater the locking stretch. Within the scale considered, compressive response again is almost unaltered. The amount of λ_{lock} -shift in equi-biaxial deformation is, however, much less than the shift in the uniaxial case. This property of the model provides the desired flexibility in the fitting of the experimental data, see e.g. Figure 3.11.

As already mentioned above, the non-affine formulation of a free chain network alone is not completely adequate especially in the simultaneous simulation of different deformation processes, see Figure 3.11. The effect of the additional contribution to the free energy due to the proposed tube-like constraint is investigated for uniaxial and equi-biaxial deforma-

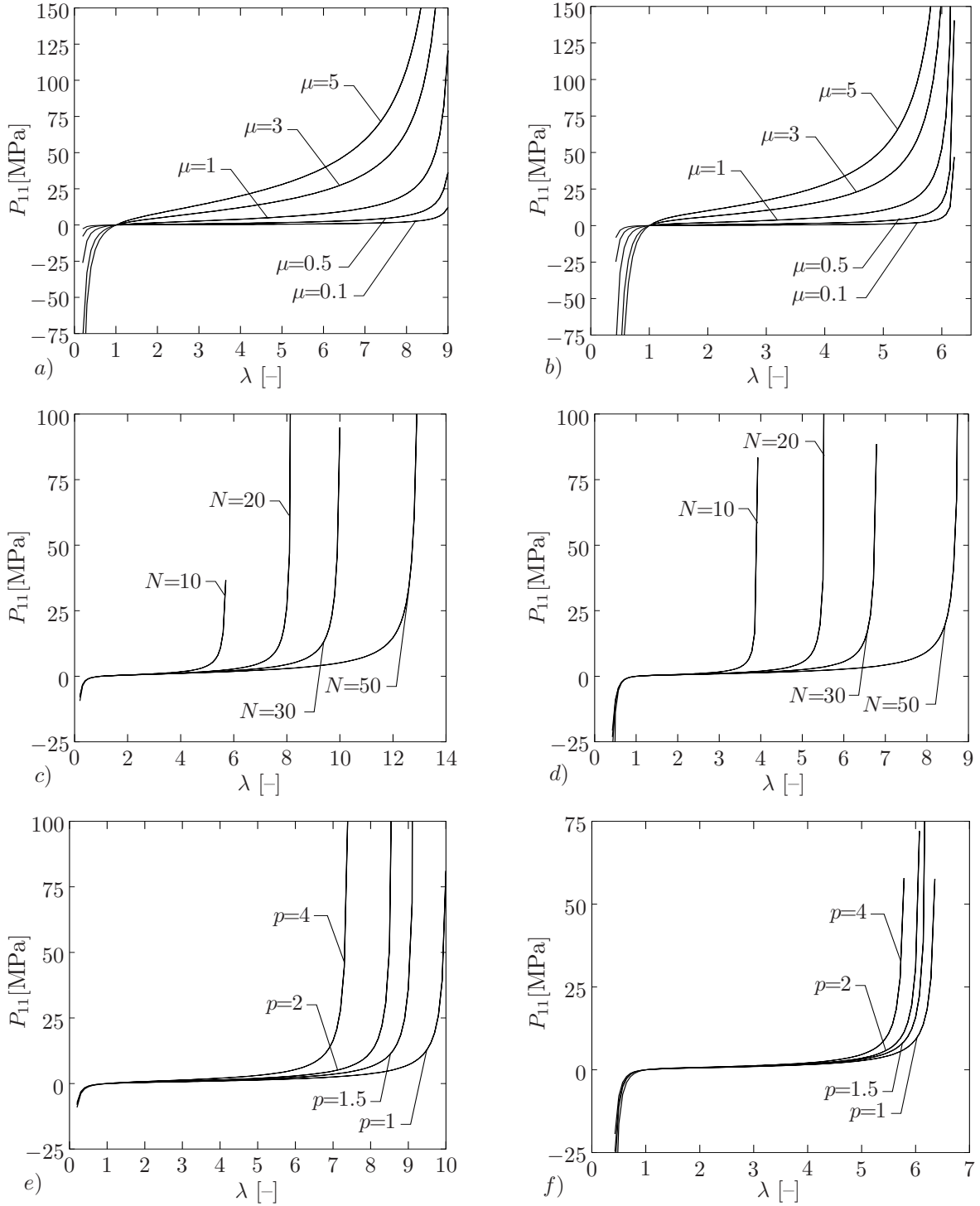


Figure 3.12: Sensitivity investigation of the model contribution to material parameters a) & b) $\mu = [0.1, 1, 3, 5]$ MPa, $N = 25$, $p = 1.5$, ($U = 0$, $q = 0$), c) & d) $\mu = 0.3$ MPa, $N = [10, 20, 30, 50]$, $p = 1.5$, ($U = 0$, $q = 0$) e) & f) $\mu = 0.3$ MPa, $N = 25$, $p = [1, 1.5, 2, 4]$, ($U = 0$, $q = 0$). The figures in the left column denote the uniaxial response of the material, and the ones in right column show equi-biaxial response.

tions in Figure 3.13. The contribution is governed by two additional material parameters U and q . In this study, the values of $\mu = 0.3$ MPa, $N = 25$, $p = 1.5$ are fixed and different values of U and q are prescribed. The stress-stretch curves in Figures 3.13a,b are obtained for the different values of $U = 0.5, 2, 5, 10$, whereas $q = 1$ is kept frozen. In both

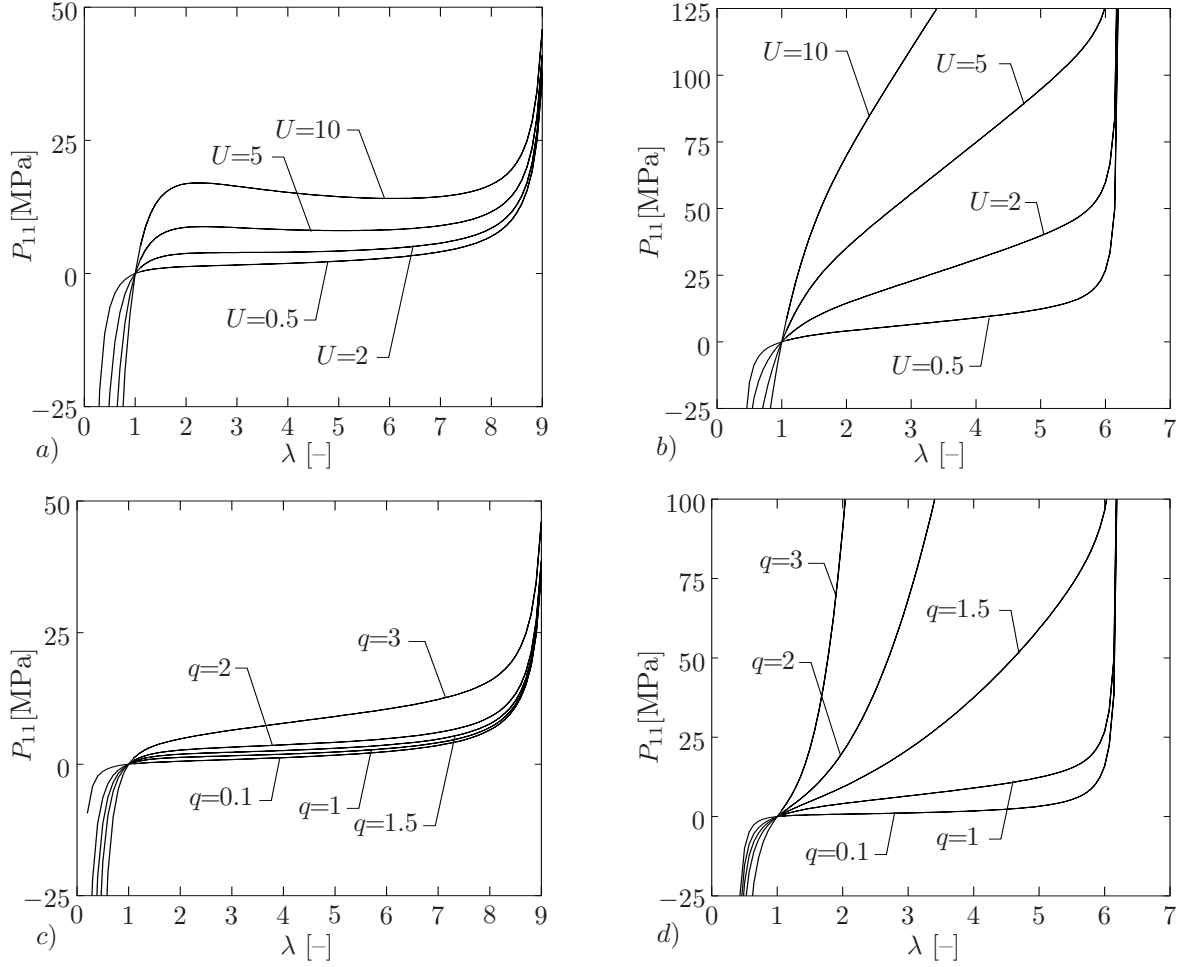


Figure 3.13: Sensitivity investigation of the model contribution to material parameters *a*) & *b*) $\mu = 0.3$ MPa, $N = 25$, $p = 1.5$, $U = [0.5, 2, 5, 10]$, $q = 1$, *c*) & *d*) $\mu = 0.3$ MPa, $N = 25$, $p = 1.5$, $U = 0.5$, $q = [0.1, 1, 1.5, 2, 3]$. The figures in the left column denote the uniaxial response of the material, and the ones in right column show equi-biaxial response.

deformation cases, the desired additional contribution to the stress response at small and moderate stretch values is obtained in the both compressive and tensile regions. Observe that the value of λ_{lock} remains unchanged. The diagrams shown in Figures 3.13c,d exhibit the effect of the change in $q = 0.1, 1, 1.5, 2, 3$ for a constant $U = 0.5$. The increase in the parameter q results in a scaling of the stress ordinate similar to a change of μ . Moreover, it can be seen that the equi-biaxial response of the model is much more sensitive to the parameters U and q than the uni-axial curves.

3.5.4. Modeling Capacity of the Non-Affine Micro-Sphere Model. In this section, the modeling capacity of the proposed non-affine micro-sphere model is investigated regarding the fitting of some well-known experimental data of finite rubber elasticity. These data have already been extensively used for testing of previously proposed network models, see e.g. ARRUDA & BOYCE [8, 25], WU & VAN DER GIESSEN [206], KALISKE & HEINRICH [104], LULEI & MIEHE [125], MARCKMANN & VERRON [127].

The first set of experimental data considered was reported by TRELOAR [193] for the cases of tensile uniaxial, pure shear and equi-biaxial deformation on 8% sulphur-vulcanized unfilled natural rubber. These celebrated data are well accepted in the literature as repre-

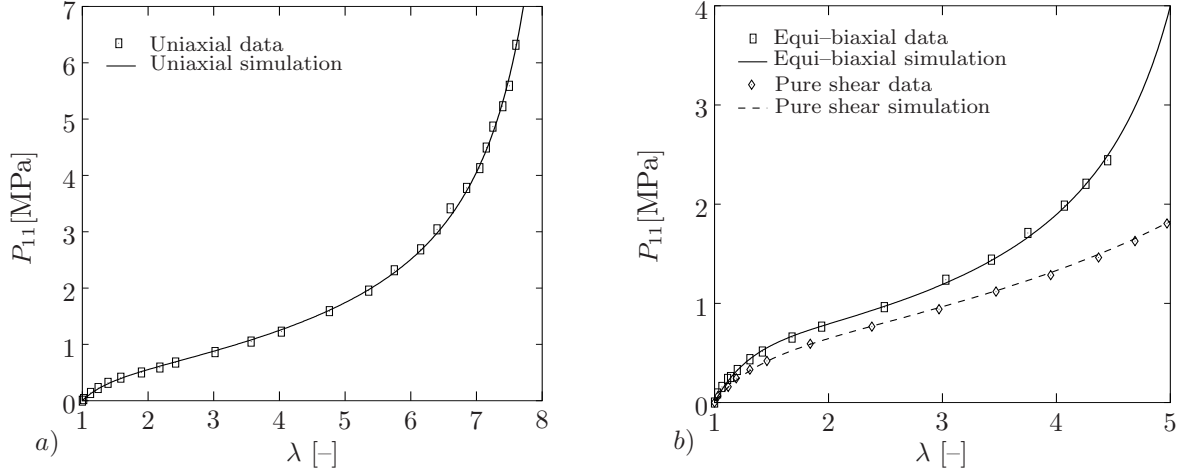


Figure 3.14: Performance of the proposed model with the set of material parameters $\mu = 0.292$ MPa, $N = 22.01$, $p = 1.472$, $U = 0.744$, $q = 0.1086$ in comparison with the well known data from TRELOAR [193].

sentative benchmarks of rubber-like material behavior. The data have already been used in Section 3.5.2 to motivate the development of the non-affine network model incorporating constraint effects. In Figure 3.14 the performance of the model against the data is illustrated. The material parameters are obtained by a parameter identification tool simultaneously employed for all available data. The comparison of the simulation given in Figure 3.14 with Figures 3.11 and 3.10 clearly indicates that the incorporation of both the tube-like constraint and the non-affinity makes the model response excellent. The material response is very well traced by the proposed five-parameter model.

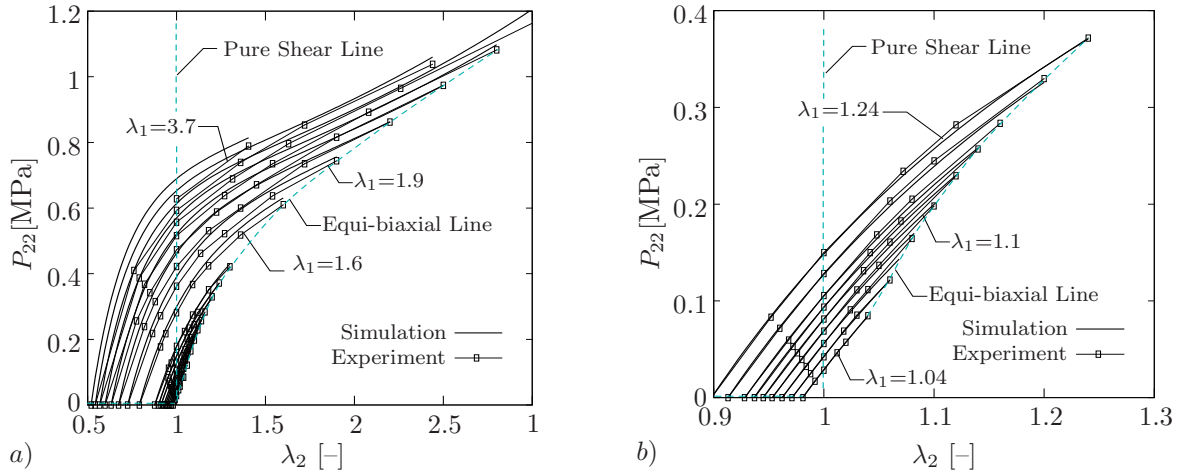


Figure 3.15: Simulation of the biaxial data reported by KAWABATA ET AL. [107] with the model parameters identified based on the data of TRELOAR [193] illustrated in Figure 3.14.

Secondly, we consider the set of data reported by KAWABATA ET AL. [107] for series of tensile biaxial deformations on vulcanized unfilled polyisoprene sheets. This material exhibits similar behavior to the vulcanized natural rubber considered in Figure 3.14. For specified constant values of $\lambda_1 \in [1.04, 3.7]$, the stretch in the perpendicular direction λ_2 is increased from the value corresponding to a stress-free (uniaxial) state in that direction to the state corresponding to the equi-biaxial ($\lambda_1 = \lambda_2$) deformation. During each biaxial experiment, the nominal stresses P_{11} and P_{22} in the both directions were

recorded. A partial set of these data (only P_{22} vs. λ_2) combined with Treloar's data have recently been utilized by MARCKMANN & VERRON [127] to assess the modeling performance of twenty hyperelasticity models. They have also considered the non-affine micro-sphere model and tested its performance against these data with the material parameters identified for Treloar's data, see Figure 3.14. We also illustrate the outstanding performance of our model in Figure 3.15 for complete range of deformations. The close-up in Figure 3.15b provides a detailed representation of nominal stress-stretch diagram at moderate stages of deformation. Apart from the comparison based on the direct nominal stress measurements in the deformation direction, the nominal stresses P_{11} corresponding to the perpendicular direction are also compared to the measured data in Figure 3.16 which is again supplemented by the detailed diagram corresponding to relatively small deformation stages. It has been shown by MARCKMANN & VERRON [127] that there are few constitutive models able to simultaneously simulate the both multi-dimensional data with a unique set of material parameters. The celebrated models such as the eight-chain model, the Ogden model fail to simulate these data with a unique set of model parameters, the reader is referred to [127] for further details.

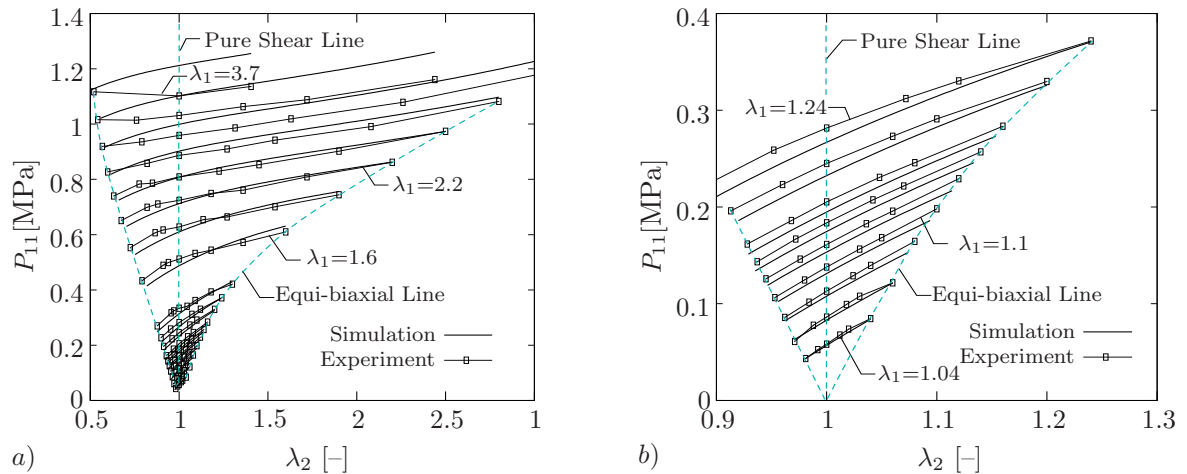


Figure 3.16: Simulation of the biaxial data reported by KAWABATA ET AL. [107] with the model parameters identified based on the data of TRELOAR [193] illustrated in Figure 3.14.

The third set of experimental data is taken from Table 2 of JAMES, GREEN & SIMPSON. [100]. The λ_1 and P_{11} values corresponding to $\lambda_2=1$ were employed as pure shear data and those corresponding to $\lambda_1=\lambda_2$ are used as equi-biaxial data. Following an identification procedure similar to the one above, the proposed model successfully captures the material response over all stages of deformation as depicted in Figure 3.17a. The performance of the three-chain model, the eight-chain model and the so-called “full-network model” of WU & VAN DER GIESSEN [206] in fitting the data are presented in Figure 8 of the latter paper. In addition, the proposed model is compared with experimental data of ARRUDA & BOYCE [8] in Figure 3.17b. Silicone rubber specimens were subjected to the compressive monotonic uniaxial and plane strain loading at a deformation rate -1 mm/s. Actually this set of data does not exhibit the characteristics of non-affine and constraint effects. As illustrated in Figure 9 of WU & VAN DER GIESSEN [206] or in LULEI [124], even affine models are able to describe these data with sufficient accuracy. However, for the sake of completeness we also include these data.

The last homogeneous experimental data of interest have been reported by LULEI &

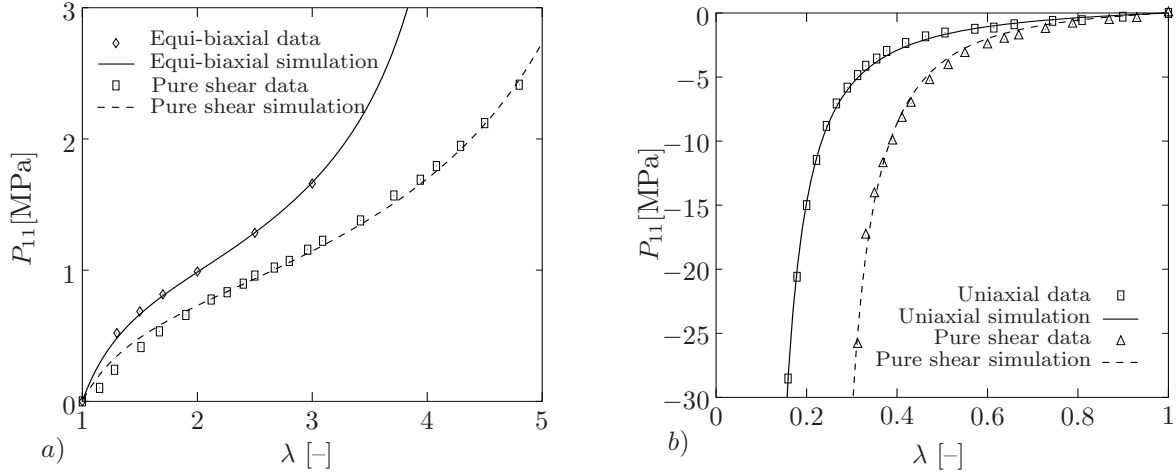


Figure 3.17: Simulation of the data from a) JAMES ET AL. [100] with the model parameters $\mu = 0.289$ MPa, $N = 14.44$, $p = 1.742$, $U = 0.176$, $q = 0.692$ and from b) ARRUDA & BOYCE [8] with the parameter values $\mu = 0.314$ MPa, $N = 7.214$, $p = 3.04$, $U = 9.383$, $q = 0.017$.

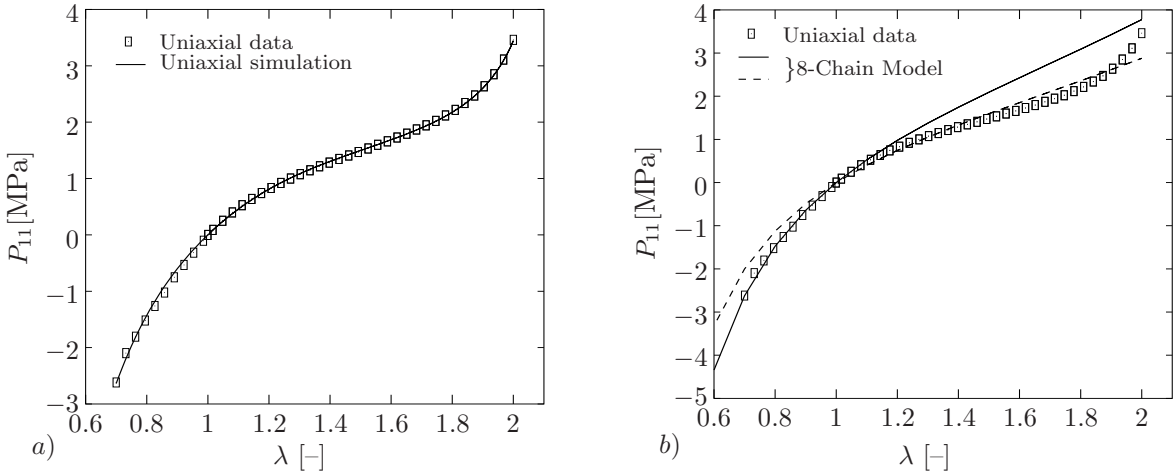


Figure 3.18: Simulation of data from LULEI & MIEHE [125] a) by the proposed model with parameters $\mu = 0.153$ MPa, $N = 2.903$, $p = 8.56$, $U = 13.227$, $q = 0.838$, and b) by the eight-chain model with $\mu = 1.278$ MPa, $N = 5.536$ (solid line) and with $\mu = 1.674$ MPa, $N = 5.52$ (dashed line).

MIEHE [125], see Figure 3.18. The uniaxial data are important in the sense that they include both tensile and compressive response. In Figure 3.18a, the excellent fitting of the current model is reported. In order to compare the flexibility of the proposed non-affine micro-sphere model, the eight-chain model is also tested against these data by identifying its parameters at tensile and compressive regions, see Figure 3.18b.

3.5.5. Three-Dimensional Analysis of a Non-Homogeneous Shear Test. The last numerical example is concerned with the simulation of a three dimensional inhomogeneous shear experiment on vulcanized rubber. The experimental data are reported in VAN DEN BOGERT & DE BORST [199]. In their experiment four prismatic rubber specimens with dimensions $20 \text{ mm} \times 10 \text{ mm} \times 20 \text{ mm}$ are rigidly connected to the steel frame members at their upper and lower faces during the cross-linking process, as shown in Figure 3.19. Internal steel members were displaced in the x - and the opposite directions by 15 mm, respectively. During shearing, no vertical restraint was imposed, i.e. the lower specimens

were allowed to translate in the vertical direction freely. The experiment was conducted cyclicly in order to eliminate the Mullins effect and to obtain a reproducible response. For the same material, a homogeneous simple tension test was also carried out.

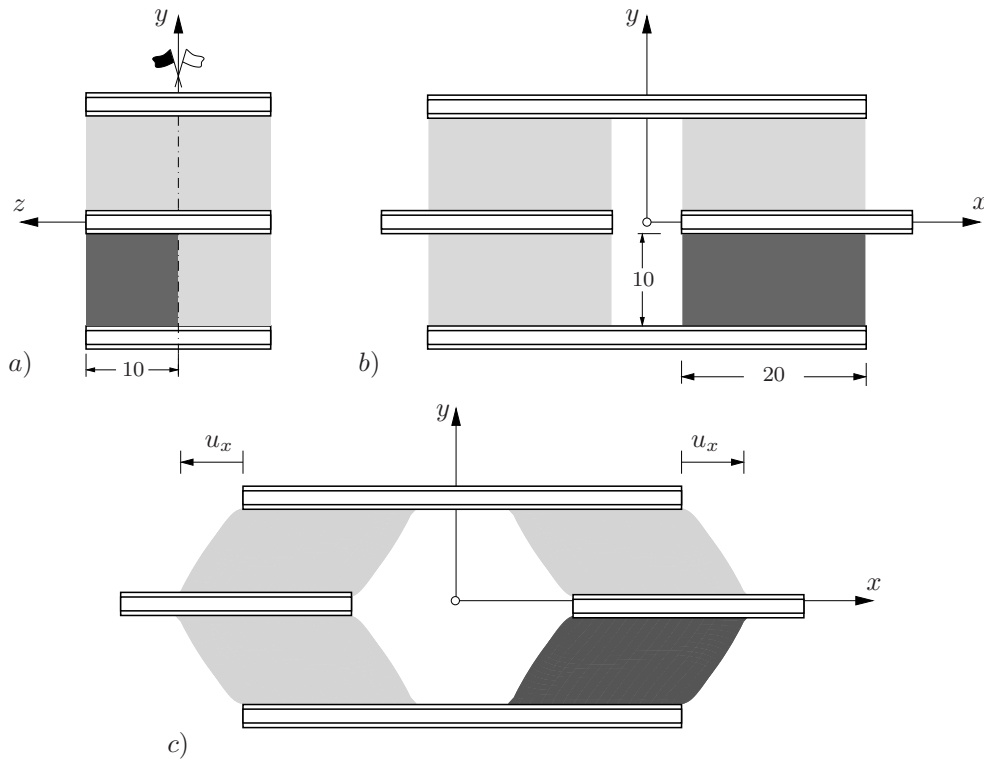


Figure 3.19: Schematic description of the boundary-value problem. The darker shaded specimens are discretized with $16 \times 20 \times 8$ eight-node Q1P0 elements in x , y and z directions, respectively. *a)* Side view of the experimental set-up denotes the symmetry boundary conditions on the xy -plane. *b)-c)* Front view of the test set-up at undeformed and deformed states, respectively. It illustrates the top and bottom plane boundary conditions.

In the finite element model of the problem, only one half of the specimen that is depicted by the darker shaded parts in Figure 3.19 is discretized by exploiting the apparent symmetry conditions. The spatial discretization is carried out with $16 \times 20 \times 8$ mixed Q1P0 eight-node brick elements. While the bottom face of the specimen is clamped and fixed in all directions, its top surface is clamped in all directions and fixed in z -direction such that all nodes on this face deform equally in x - and y -directions. The symmetry face in xy -plane is restrained in z -direction, see Figure 3.19.

An ideal identification procedure of the material parameters should be based on homogeneous test results such as uniaxial tension and equi-biaxial tests. However, as mentioned before, the parameter optimization process may yield several minimizing sets of parameters with an adequate quality of fitting for all. For example, for the simulation of the inhomogeneous shear test, KALISKE & HEINRICH [104] and VAN DEN BOGERT & DE BORST [199] obtained several sets of material parameters from the simple tension data. These parameters were then employed for the simulation of the inhomogeneous shear test. It was observed that some sets of material parameters, which perform quite well in uniaxial test, resulted in unexpected expansions of the specimen in transverse direction during shearing in lateral direction. These observations once more emphasize that a simple tension experiment does not provide sufficient information for an accurate simulation of a boundary value problem where the deformation field is not homogeneous any more.

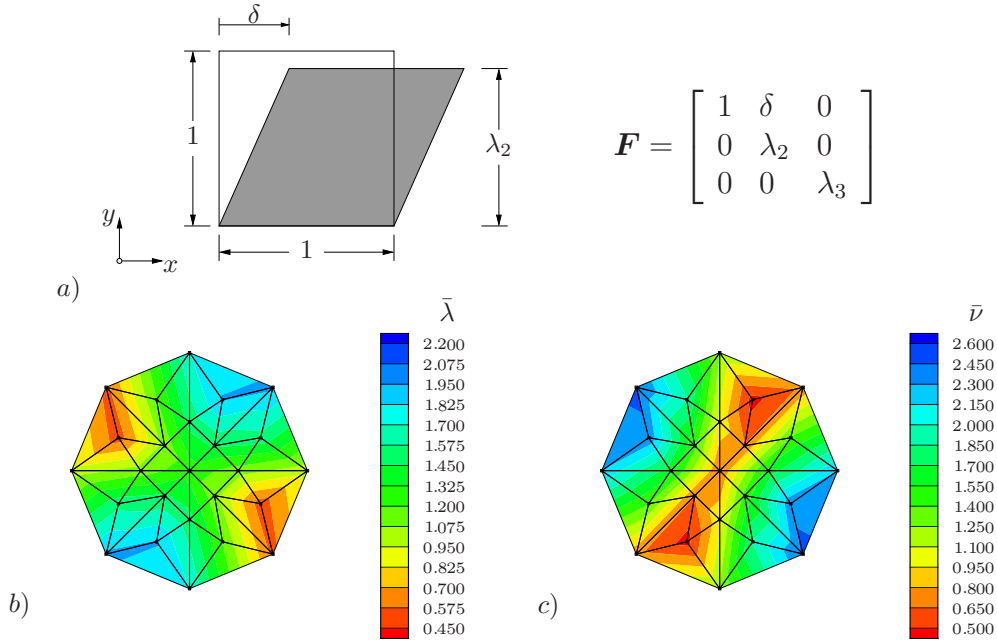


Figure 3.20: Homogeneous shear test with stress boundary conditions $P_{22} = 0$, $P_{33} = 0$ used for fitting of pseudo experimental data. *a)* Schematic form of the homogeneous shear test with corresponding deformation gradient. The stereographic projection plots of affine micro-kinematic variables *b)* stretch $\bar{\lambda} := |\bar{\mathbf{F}}\mathbf{r}|$ and *c)* tube contraction $\bar{\nu} := |\bar{\mathbf{F}}^{-T}\mathbf{r}^b|$ are plotted for the homogeneous shear test at deformation level $\delta = 1.50$, $\lambda_2 = 0.79$, $\lambda_3 = 1.27$.

In the light of this experience, we utilize the results obtained from the non-homogeneous shear test as *pseudo data for a fictitious homogeneous shear test* depicted in Figure 3.20 besides the simple tension data available. For exploitation of the pseudo homogeneous shear data, we use the non-homogeneous data reported in VAN DEN BOGERT & DE BORST [199], given also in Figure 3.22. Here, the total lateral force F_x is divided by the undeformed area of the top surface of the specimen ($A_0 = 200 \text{ mm}^2$). The value obtained is then utilized as a component of the first Piola-Kirchhoff stress P_{21} in the fictitious homogeneous shear test visualized in Figure 3.20. The displacement u_x/h with $h = 10 \text{ mm}$ is assigned to the driving coordinate of the deformation gradient $\mathbf{F}_{12} = \delta$. The values of λ_2 and λ_3 are computed in an iterative manner from the assumed stress boundary conditions of the problem, i.e. $P_{22} = 0$ and $P_{33} = 0$. With these pseudo shear data at hand, a second set of material parameters is obtained by solving the parameter optimization problem simultaneously with the uniaxial tension data. The performance of the two sets of material parameters is illustrated in Figure 3.21. As expected, both material sets obtained from fitting of only the simple tension data and the simultaneous identification of simple tension and pseudo shear data are able to simulate the uniaxial data of nearly the same quality, see Figure 3.21a. However, the curves in Figure 3.21b show that the model with the parameters obtained from simple tension overestimates the pseudo shear data. In contrast, the performance of the parameters obtained from both experimental data is also in good agreement with the pseudo shear data.

With this pre-study at hand, for the both sets of material parameters we carry out the finite element simulation of the boundary value problem. The resultant diagrams of F_x vs. u_x and F_x vs. u_y are shown in Figures 3.22a,b in comparison with the experimental results. Comparison of the response pattern in Figure 3.22a with Figure 3.21b justifies the procedure of using pseudo shear data in parameter identification. The model response

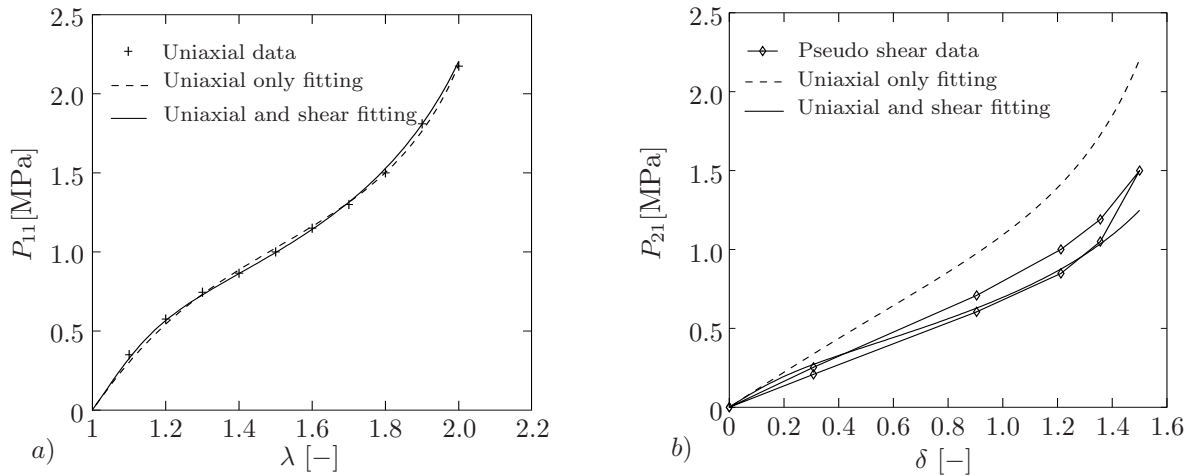


Figure 3.21: Performance of the two sets of material parameters in a) simple tension test and b) homogeneous shear test. The parameters of the model obtained from identification of a uniaxial test only are $\mu = 0.1475$ MPa, $N = 3.273$, $p = 9.31$, $U = 9.94$, $q = 0.567$ and the ones determined by simultaneous identification of uniaxial and pseudo shear data are $\mu = 0.207$ MPa, $N = 4.31$, $p = 16.76$, $U = 6.22$, $q = 0.1$.

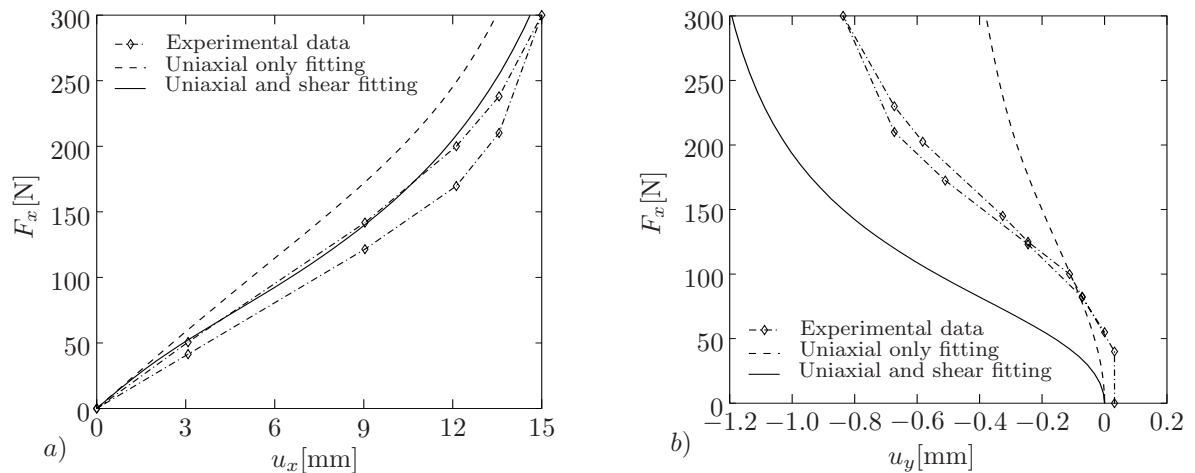


Figure 3.22: Performance of the two sets of material parameters in finite element simulations of a three-dimensional non-homogeneous shear test.

with the parameters identified from only uniaxial data behaves stiffer in non-homogeneous test, whereas the inclusion of analogous pseudo shear data in the identification process apparently improves the estimation capability of the model particularly in the simulation of the direct interest F_x vs. u_x diagram. Likewise, the model with the uniaxial data fitted-parameters behaves stiffer also in the lateral direction, see Figure 3.22b. On the other hand, the behavior of the model with the “successful” set of parameters comes out to be softer in the transversal deformation case. The shape of the experimental curve is, however, captured adequately. In the experimental data plotted in Figure 3.22b, it should be observed that the second data point corresponds to a state where the vertical deformation is almost zero $u_y \approx 0$ while the value of force (F_x) has a finite value, which equals nearly one sixth of the total force attained. This is somewhat questionable.

The deformed shape of the inhomogeneously sheared specimen is depicted in Figure 3.23. The deformation in the elements at the upper left and the lower right corners is highly inhomogeneous. The zone on the outer face of the specimen, particularly around

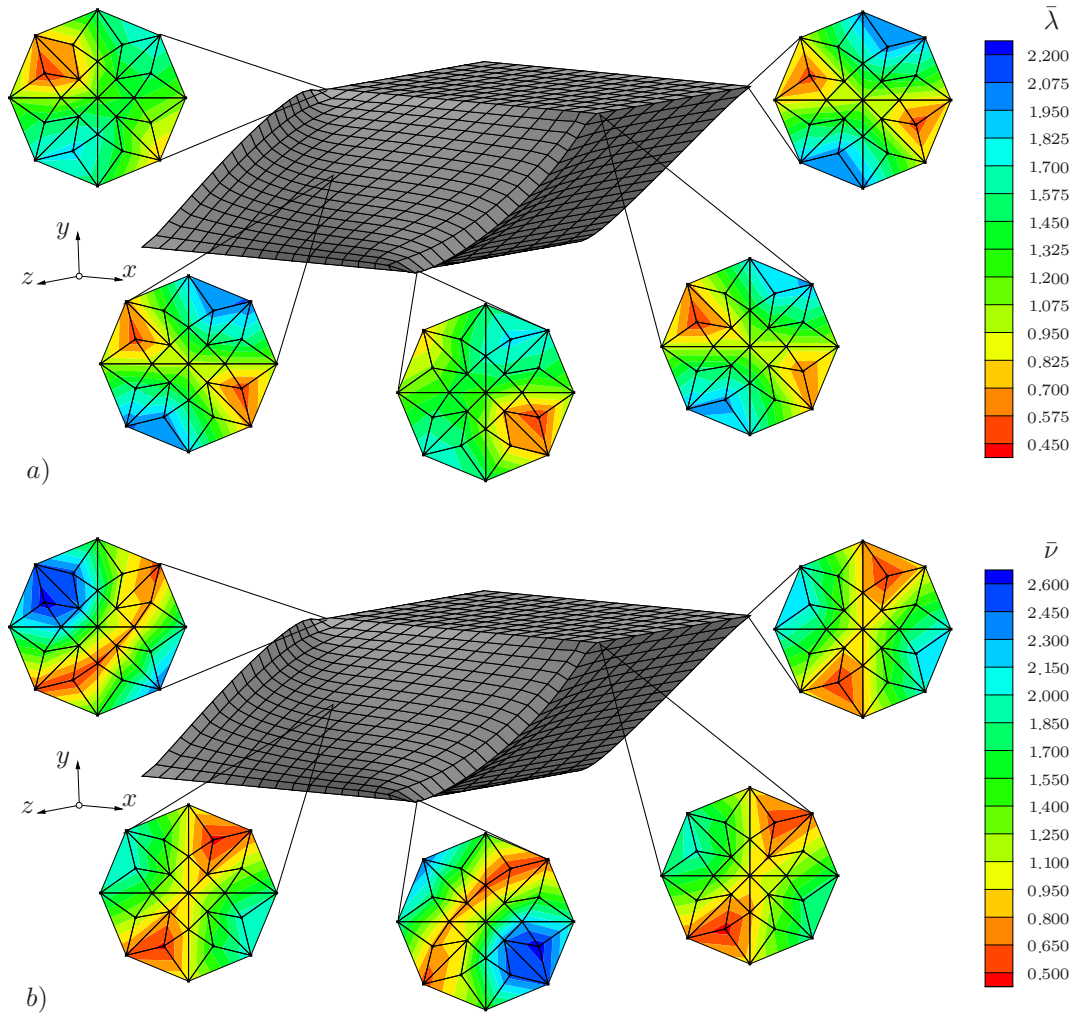


Figure 3.23: Stereographic projection plots of affine micro-kinematic variables *a*) stretch $\lambda = \bar{\lambda}$ and *b*) tube contraction $\nu = \bar{\nu}$ are plotted at different points of the fully deformed ($u_x = 15\text{mm}$) specimen. Comparison of these plots with those in Figure 3.20 indicates that the middle part of the front surface deforms almost homogeneously. Highly non-homogeneous deformations are observed at the upper left and lower right corners.

the diagonal direction opposite to the shearing direction, expands in lateral direction. A contraction in lateral direction is observed on the both off-sides of this diagonal. The overall deformation pattern mimics the incompressible material behavior. To visualize the type of micro-macro transitions inherent in the proposed non-affine micro-sphere model, we magnify some micro-states of the inhomogeneous problem by the stereographic plots introduced in Figure 3.5. Stereographic affine stretch contours on the xy -plane are depicted in Figure 3.23a at the selected material points. These plots also indicate the highly inhomogeneous deformation at the upper left and lower right corners, whereas the deformation at the middle points and the other corners remains almost homogeneous. Similar conclusions may be drawn from Figure 3.23b that shows pole plots of affine area-stretches. The inhomogeneous deformation characteristics become more transparent when we compare the plots presented here with those of the fictitious shear test depicted in Figure 3.20.

4. The Micro-Sphere Model of Finite Rubber Viscoelasticity

The micromechanically-based non-affine model of elasticity incorporating topological constraints was discussed in Chapter 3. The present chapter extends the *micro-sphere model* of finite rubber elasticity towards the description of finite rubber viscoelasticity. The material presented in this chapter is based on the ideas outlined in the recent work by MIEHE & GÖKTEPE [148]. In the preceding chapter on rubber elasticity, we introduced two basic micro-kinematic variables related to the deformation of a single chain: the end-to-end distance r and the tube diameter d as visualized in Figure 3.1. The tube diameter reflects the severity of constraints due to neighboring entangled chains: the smaller d , the more appreciable the constraints are. In our elasticity formulation we primarily focused on an idealized cross-linked ground-state network without any detanglement mechanisms. Following conceptually the work of BERGSTRÖM & BOYCE [14], we now consider a hierarchy of superimposed chains as schematically indicated in Figure 4.1. These superimposed chains are related to the ground-state network by entanglement mechanisms. We associate the ground-state network with the macroscopically observed equilibrium curve and the superimposed chains with the viscous overstress response of Figure 1.1. The latter effect is micromechanically motivated by a motion of the superimposed chains relative to the ground-state network. In this work, we are inspired from the ideas of the reptation model of DE GENNES [41], DOI & EDWARDS [45], and from the notions of constraint release effects, MARUCCI [130], see also PETERS [165] for a recent excellent review.

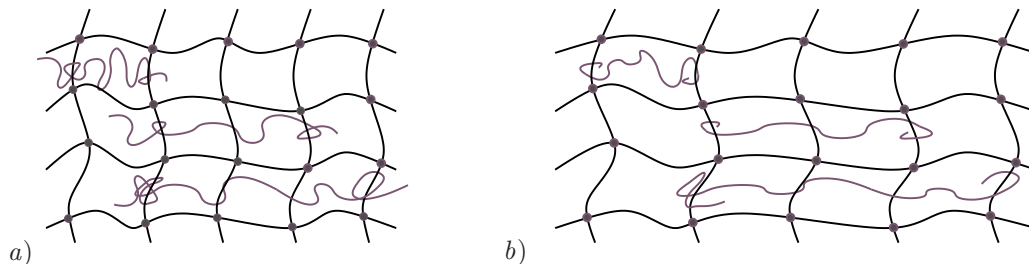


Figure 4.1: Micromechanical mechanism of viscoelasticity. A spectrum of superimposed non-equilibrium networks is indicated by the grey chains extending between two entanglements with the equilibrium network. At a deformation *a)* to *b)*, the dangling ends of the chains retract by Brownian motion yielding the relaxation of the non-equilibrium stresses. Different lengths of the grey chains motivate the utilization of the relaxation spectrum.

Our assumed micromechanical mechanism of viscoelasticity visualized in Figures 4.1 and 4.2 extends the two-variable mechanism of elasticity suggested in [149] to the time-dependent motion of the superimposed entangled chains. Consider a prototype chain, in Figure 4.2a, superimposed onto the ground-state network. This prototype chain and the one perpendicular to it are assumed to be extending between physical entanglements. During the deformation, both the chain of interest and surrounding chains accompany the ground-state equilibrium network but also experience *contour length fluctuations*. The overall relaxation process is a combination of both processes. Upon an instantaneous increase of end-to-end distance as shown in Figure 4.2b, the prototype chain retracts towards the interior of the tube by Brownian motion. Consequently, the force applied at the ends of the chain relaxes. In addition, a sudden stretch of a transversally located entangling chain at frozen end-to-end distance of the prototype chain is depicted in Figure 4.2c. This sudden extension of the forest chain is assumed to decrease the tube diameter. Similar to the previous picture, for a constant deformation, surrounding chains retract

and the degree of constraints gradually decreases. This relaxation mechanism results in an increase of tube diameter. The assumed two molecular scenarios depicted in Figures 4.2b and 4.2c provide the underlying key micromechanical motivation of our formulation. According to molecular dynamics theory of reptation outlined in DOI & EDWARDS [45], the rate of the relaxation process differ with the elapsed time in the relaxation process. This result of molecular dynamics theory is phenomenologically taken into account through a *discrete spectrum of relaxation times* in the both mechanisms: *chain retraction* and *constraint release*.

In contrast to the purely macroscopic approaches to finite viscoelasticity cited in Chapter 1, we avoid in our model a kinematical assumption concerning the definition of tensorial internal variables for a viscous strain or overstress. Macroscopic free energy and dissipation of the network are defined by a *homogenization of scalar internal variable fields* on the micro-sphere of space orientations. The effective constitutive modeling is essentially one-dimensional and related to a *prototype space orientation* of a chain associated with a local point on the micro-sphere. We outline a distinct physical model for the viscous overstress in terms of the above outlined two micro-kinematic variables and consider its numerical implementation in terms of a micro-stress update algorithm. Next, we propose an affine network model for the definition of the macroscopic overstress. The homogenization procedure is performed via a direct *numerical evaluation of averaging integrals* by replacing the continuous orientation space on the micro-sphere by a discrete set of directors. As already shown in Chapter 3, the model provides an outstanding fitting of the elastic equilibrium response in multi-dimensional applications. In this chapter, we further show that its viscoelastic extension also leads to predictive results in modeling of rate effects and hysteresis phenomena of rubbery polymers. After pointing out in Section 4.1 the macroscopic structure of the model, we focus on the micromechanical constitutive formulation with respect to a single chain orientation in Section 4.2. Then Section 4.3 introduces the viscoelastic network model that defines the homogenized overall response. The performance of the viscoelastic micro-sphere model is analyzed in Section 4.4, where we carry out several experimentally-based simulations of monotonous, cyclic and relaxation tests associated with both homogeneous and inhomogeneous deformations.

4.1. Macroscopic Spatial Viscoelasticity of a Polymer Network

This section summarizes the constitutive equations of macroscopic finite viscoelasticity for decoupled volumetric-isochoric and equilibrium-overstress response in a compact spatial setting, see e.g. MIEHE [141] for a comprehensive treatment of geometric settings of finite inelasticity. Let $\varphi : \mathbf{X} \mapsto \mathbf{x}$ be the nonlinear deformation map (2.2) at time $t \in \mathbb{R}_+$ of a viscoelastic body undergoing finite strains. A boundary value problem of macroscopic finite viscoelasticity is governed by the balance of linear momentum

$$\rho_0 \ddot{\varphi} = \text{Div}[\boldsymbol{\tau} \mathbf{F}^{-T}] + \bar{\gamma} \quad \text{in } \mathcal{B} \quad (4.1)$$

along with prescribed displacement boundary conditions $\varphi = \bar{\varphi}(\mathbf{X}; t)$ on $\partial\mathcal{B}_\varphi$ and the traction boundary conditions $[\boldsymbol{\tau} \mathbf{F}^{-T}] \mathbf{N} = \bar{\mathbf{T}}(\mathbf{X}; t)$ on $\partial\mathcal{B}_t$ with outward normal \mathbf{N} , see Figure 2.4. In (4.1), ρ_0 denotes the reference density and $\bar{\gamma}$ stands for a prescribed body force field with respect to unit volume of the reference configuration. The Kirchhoff stress tensor $\boldsymbol{\tau}$ is a function of the local deformation \mathbf{F} and some internal variables \mathcal{I} which describe viscous structural changes. We assume the constitutive structure

$$\boldsymbol{\tau} = 2\partial_{\mathbf{g}}\Psi(\mathbf{g}, \mathcal{I}; \mathbf{F}) \quad (4.2)$$

that generalizes the so-called Doyle-Ericksen formula (2.63), see also MIEHE [141] for its applications in finite inelasticity. In (4.2), Ψ denotes the macroscopic free energy per unit reference volume that is locally stored in a deformed polymer network. This stress potential must satisfy the principle of material frame invariance $\Psi(\mathbf{g}, \mathcal{I}; \mathbf{Q}\mathbf{F}) = \Psi(\mathbf{g}, \mathcal{I}; \mathbf{F})$ for all rotations $\mathbf{Q} \in SO(3)$. Analogous to the purely elastic response, we consider a class of weakly compressible polymers where the bulk response is assumed to be elastic and viscosity effects are exclusively restricted to the isochoric part of the deformation. A decoupling of the stress response into volumetric and isochoric contributions is based on the unimodular part $\bar{\mathbf{F}} := J^{-1/3}\mathbf{F}$ of the deformation gradient that is assumed to govern the deviatoric stresses. A decoupled volumetric-isochoric structure of finite viscoelasticity is obtained by considering the specific form

$$\Psi = U(J) + \bar{\Psi}(\mathbf{g}, \mathcal{I}; \bar{\mathbf{F}}) \quad (4.3)$$

of the stored energy. Consequently the stresses (4.2) additively decompose into spherical and deviatoric contributions

$$\boldsymbol{\tau} = p\mathbf{g}^{-1} + \bar{\boldsymbol{\tau}} : \mathbb{P} \quad \text{with} \quad p := JU'(J) \quad \text{and} \quad \bar{\boldsymbol{\tau}} := 2\partial_{\mathbf{g}}\bar{\Psi}(\mathbf{g}, \mathcal{I}; \bar{\mathbf{F}}), \quad (4.4)$$

where \mathbb{P} is the deviatoric projection tensor. For an almost incompressible response of the polymer network, the potential U can be considered as a penalty function which approximatively enforces the incompressibility constraint.

Based on the experimental arguments in rubber viscoelasticity outlined in Chapter 1, we further decompose the isochoric free energy into *elastic equilibrium* and *viscoelastic overstress response* through the additive split of the isochoric stress potential

$$\bar{\Psi} = \bar{\Psi}^e(\mathbf{g}; \bar{\mathbf{F}}) + \bar{\Psi}^v(\mathbf{g}, \mathcal{I}; \bar{\mathbf{F}}). \quad (4.5)$$

This induces a further split of the stresses $\bar{\boldsymbol{\tau}}$ defined in (4.4)₃ according to

$$\bar{\boldsymbol{\tau}} = \bar{\boldsymbol{\tau}}^e + \bar{\boldsymbol{\tau}}^v \quad \text{with} \quad \bar{\boldsymbol{\tau}}^e := 2\partial_{\mathbf{g}}\bar{\Psi}^e(\mathbf{g}; \bar{\mathbf{F}}) \quad \text{and} \quad \bar{\boldsymbol{\tau}}^v := 2\partial_{\mathbf{g}}\bar{\Psi}^v(\mathbf{g}, \mathcal{I}; \bar{\mathbf{F}}) \quad (4.6)$$

related to the two experimental curves in Figure 1.1. The dissipative viscoelastic overstresses $\bar{\boldsymbol{\tau}}^v$ of the network provide a *deformation-induced anisotropy* in the non-equilibrium state that is described by the evolution of the internal variables \mathcal{I} in time. This evolution must be consistent with the second axiom of thermodynamics that demands a positive macroscopic dissipation

$$\mathcal{D}_{mac} := \mathcal{F} \cdot \dot{\mathcal{I}} \geq 0 \quad \text{with} \quad \mathcal{F} := -\partial_{\mathcal{I}}\bar{\Psi}^v(\mathbf{g}, \mathcal{I}; \bar{\mathbf{F}}) \quad (4.7)$$

with respect to unit volume of the reference configuration. Typical form of this evolution system is provided by the constitutive initial value problem

$$\partial_{\mathcal{I}}\bar{\Psi}^v(\mathbf{g}, \mathcal{I}; \bar{\mathbf{F}}) + \partial_{\dot{\mathcal{I}}}\bar{\Phi}^v(\dot{\mathcal{I}}) = \mathbf{0} \quad \text{with} \quad \mathcal{I}(0) = \mathcal{I}_0 \quad (4.8)$$

in terms of a macroscopic dissipation function $\bar{\Phi}^v$ that depends smoothly on the evolution $\dot{\mathcal{I}}$ of the internal variables with normalization condition $\bar{\Phi}^v(\mathbf{0}) = 0$. Assuming $\bar{\Phi}^v$ to be convex and positive, we observe that (4.7) is automatically satisfied. The above equation is a generalization of the so-called Biot equation, see BIOT [18] and the recent treatment MIEHE, SCHOTTE & LAMBRECHT [152] on standard dissipative materials. Observe that the macroscopic constitutive model of isochoric viscoelasticity is governed by the three constitutive functions $\bar{\Psi}^e$, $\bar{\Psi}^v$ and $\bar{\Phi}^v$ for the equilibrium energy, the non-equilibrium free energy and the viscous dissipation potential, respectively. In the forthcoming part of this chapter we construct these functions for an exactly incompressible polymer network based on the distinct micro-macro transition.

4.2. Micromechanics of Chains in a Constrained Environment

In this section we briefly reiterate the micromechanical elasticity formulation for single polymer chains outlined in Section 3.2 and extend it to viscous overstress contributions.

4.2.1. Definition of Micro-Kinematic Variables of the Chain. The key aspect of the micro-sphere model of elasticity outlined in the preceding chapter was the introduction of *two micro-kinematic variables* associated with a single polymer chain. The first micro-kinematic variable measures the *length stretch* λ_f or the relative length stretch λ_{fr} of a single chain defined as

$$\lambda_f := \frac{r}{r_0} \quad \text{and} \quad \lambda_{fr} := \frac{r}{L} = \frac{\lambda_f}{\sqrt{N}}, \quad (4.9)$$

respectively, with $\lambda_f \in [0, \sqrt{N})$ and $\lambda_{fr} \in [0, 1)$, defined in terms of the current end-to-end distance r , the unperturbed distance $r_0 := l\sqrt{N}$ and the number N of chain segments as visualized in Figure 3.1a. The second micro-kinematic variable measures a *tube stretch* in form of the area contraction

$$\lambda_c := \left(\frac{d_0}{d} \right)^2, \quad (4.10)$$

with $\lambda_c \in (0, \infty)$, defined in terms of a tube diameter d that is assumed to be constant along the tube as depicted in Figure 3.1b.

4.2.2. Free Energy of the Elastic Ground State Response. The free energy of the elastic equilibrium response is assumed to be split up into a part due to the free chain motion and a contribution due to the tube constraint

$$\psi^e = \psi_f^e(\lambda_f) + \psi_c^e(\lambda_c). \quad (4.11)$$

As we set out in Section 3.2, the first unconstrained elastic part is governed by the non-Gaussian model introduced by KUHN & GRÜN [114] with

$$\psi_f^e(\lambda_f) = Nk\theta \left(\lambda_{fr} \mathcal{L}^{-1}(\lambda_{fr}) + \ln \frac{\mathcal{L}^{-1}(\lambda_{fr})}{\sinh \mathcal{L}^{-1}(\lambda_{fr})} \right) \quad (4.12)$$

in terms of the length stretch λ_f defined in (4.9). The second contribution is based on a probability of a straight tube constraint outlined in DOI & EDWARDS [45], yielding the expression

$$\psi_c^e(\lambda_c) = \alpha k\theta N \left(\frac{l}{d_0} \right)^2 \lambda_c \quad (4.13)$$

in terms of the tube stretch λ_c defined in (4.10).

4.2.3. Free Energy and Dissipation of Viscoelastic Overstress Response. The micromechanical mechanism of viscoelasticity is considered as a hierarchical length-spectrum of chains entangled with the ground state network, see Figure 4.1 for a schematic visualization. The phenomenological modeling is assumed to be governed by a *spectrum of* $a = 1 \dots s$ *of prototype chains* superimposed onto the ground state that produces discrete length stretches and tube stretches in a typical space direction. We denote this discrete spectrum as a *hierarchy of non-equilibrium stretches*. It is described by the two sets of internal strain-like variables $\{\varepsilon_f^a\}_{a=1 \dots s}$ and $\{\varepsilon_c^a\}_{a=1 \dots s}$, respectively. These micro-variables

are assumed to prevail the viscoelastic overstress in a typical space orientation. Owing to these time-dependent fluctuations of the superimposed hierarchical mechanism, we assume an additional micro-contribution to the free energy of the form

$$\psi^v = \psi_f^v(\lambda_f, \varepsilon_f^1 \dots \varepsilon_f^s) + \psi_c^v(\lambda_c, \varepsilon_c^1 \dots \varepsilon_c^s) \quad (4.14)$$

in analogy to (4.11). This additional free energy describes dynamic mechanisms of entangled chains relative to the ground state network as schematically indicated in Figure 4.1. The two contributions are assumed to be of the simple phenomenological form

$$\psi_y^v = \frac{1}{2} \sum_{a=1}^s \mu_y^a (\ln \lambda_y - \varepsilon_y^a)^2 \quad \text{for } y = f, c \quad (4.15)$$

in terms of $2s$ phenomenological parameters $\{\mu_y^a\}_{y=f,c}^{a=1\dots s}$. Observe that the equilibrium state is recovered for the case when the fluctuations of the superimposed entangled chains relative to the ground state network vanish, i.e. for

$$\varepsilon_y^a = \ln \lambda_y \quad \text{for } a = 1 \dots s \quad \text{and } y = f, c \quad (4.16)$$

the additional energy storage vanishes.

The hierarchy of $2s$ fluctuations $\{\varepsilon_y^a\}_{y=f,c}^{a=1\dots s}$ plays the role of kinematic internal variables of the micromechanical overstress model that describes viscous effects due to frictional-type entanglement mechanisms between the superimposed network and the ground-state network. The micro-dissipation due to the internal variables is

$$\mathcal{D}_{mic} := \sum_{a=1}^s [\beta_f^a \dot{\varepsilon}_f^a + \beta_c^a \dot{\varepsilon}_c^a] \geq 0, \quad (4.17)$$

where we introduced per definition the $2s$ micro-forces

$$\beta_y^a := -\partial_{\varepsilon_y^a} \psi_y^v = \mu_y^a (\ln \lambda_y - \varepsilon_y^a) \quad (4.18)$$

which drive the fluctuations $\{\varepsilon_y^a\}_{y=f,c}^{a=1\dots s}$. Note that these micro-forces become zero for the equilibrium state (4.16). In analogy to (4.14) we assume a decoupled structure of the micro-dissipation function

$$\phi^v = \phi_f^v(\dot{\varepsilon}_f^1 \dots \dot{\varepsilon}_f^s) + \phi_c^v(\dot{\varepsilon}_c^1 \dots \dot{\varepsilon}_c^s) \quad (4.19)$$

that governs the evolution of the internal variables in terms of the $2s$ decoupled evolution equations

$$\partial_{\varepsilon_y^a} \psi_y^v + \partial_{\dot{\varepsilon}_y^a} \phi_y^v = 0 \quad \text{with } \varepsilon_y^a(0) = 0. \quad (4.20)$$

We observe that equations (4.20) provide the counterpart of macroscopic equation (4.8) on the microscale of chain orientations. We assume dissipation functions of the form

$$\phi_y^v = \sum_{a=1}^s \frac{\delta_y^a}{\eta_y^a (1 + \delta_y^a)} (\eta_y^a |\dot{\varepsilon}_y^a|)^{(1+\delta_y^a)/\delta_y^a} \quad (4.21)$$

governed by $4s$ material parameters $\{\eta_y^a\}_{y=f,c}^{a=1\dots s}$ and $\{\delta_y^a\}_{y=f,c}^{a=1\dots s}$. The insertion of these constitutive functions into (4.20) gives $2s$ evolution equations for the strain fluctuations driven by the stress fluctuations (4.18), i.e.

$$\dot{\varepsilon}_y^a = \frac{1}{\eta_y^a} |\beta_y^a|^{\delta_y^a - 1} \beta_y^a \quad \text{with } \varepsilon_y^a(0) = 0. \quad (4.22)$$

Here, $|\cdot| := \{[(\cdot)/\text{unit}(\cdot)]^2\}^{1/2}$ is the norm operator coupled with a neutralization of the units. Insertion of (4.22) into (4.17) shows the thermodynamic consistency of the evolution equations for $\eta_y^a > 0$ and $\delta_y^a > 0$ when the dissipation functions (4.21) become convex. Taking the time derivatives of (4.18), we obtain through (4.22) the $2s$ nonlinear differential equations

$$\dot{\beta}_y^a + \frac{1}{\tau_y^a} |\beta_y^a|^{\delta_y^a - 1} \beta_y^a = \mu_y^a \frac{d}{dt} (\ln \lambda_y) \quad \text{with} \quad \beta_y^a(0) = 0 \quad (4.23)$$

for the spectrum of micro-forces $\{\beta_y^a\}_{y=f,c}^{a=1,\dots,s}$ in terms of the spectrum $\tau_y^a := \eta_y^a / \mu_y^a$ of relaxation times. Here, the micro-strains ε_y^a have been eliminated based on equation (4.22). Thus we may use the micro-forces β_y^a as internal variables instead of ε_y^a . Clearly, both are related by equation (4.18). The above system (4.23) exclusively governs the evolution of the over-stresses on the microlevel for a typical space orientation of superimposed prototype chains in terms of $2 \times 3 s = 6 s$ material parameters summarized in Table 4.1 additional to the elastic equilibrium response.

Table 4.1: Parameters of the Micro-Sphere Model of Rubber Viscoelasticity

Set	Parameter	Name	Eq.	Effect
e	$\mu := nk\theta$	shear modulus	(3.19)	ground state stiffness
	N	number of chain segments	(3.19)	chain locking response
	p	non-affine stretch parameter	(3.46)	3D locking characteristics
	$U := \alpha(l/d_0)^2$	tube geometry parameter	(3.23)	additional constraint stiffness
	q	non-affine tube parameter	(3.56)	shape of constraint stress
v	$\{\mu_y^a\}_{y=f,c}^{a=1,\dots,s}$	overstress moduli	(4.23)	overstress stiffness
	$\{\tau_y^a\}_{y=f,c}^{a=1,\dots,s}$	relaxation times	(4.23)	relaxation spectrum
	$\{\delta_y^a\}_{y=f,c}^{a=1,\dots,s}$	relaxation exponents	(4.23)	rate sensitivity

4.2.4. Algorithmic Representation of the Overstress Response. In the algorithmic setting one considers a time-incremental formulation at discrete time steps $\Delta t := t_{n+1} - t_n$ within a typical time interval $[t_n, t_{n+1}]$. All state variables at time t_n are given and henceforth indicated by the subscript n . The update of the micro-forces is then obtained from an algorithm that integrates the evolution equations (4.23) in the time interval. The simplest possibility is the explicit Euler-forward update

$$\beta_y^a = \mu_y^a \ln \frac{\lambda_y}{\lambda_{yn}} + \left(1 - \frac{\Delta t}{\tau_y^a} |\beta_{yn}^a|^{\delta_y^a - 1}\right) \beta_{yn}^a. \quad (4.24)$$

These algorithms provide closed-form expressions for the current micro-forces in terms of the current stretches and the micro-forces at time t_n which form the history database of the model. All variables without subscript are associated with the current time t_{n+1} . With the micro-force spectra at hand, one computes the current *effective overstress* by function evaluation of the free energy function (4.15)

$$\beta_y := \frac{d}{d\lambda_y} \psi_y^v = \frac{1}{\lambda_y} \sum_{a=1}^s \beta_y^a \quad \text{for} \quad y = f, c. \quad (4.25)$$

A further derivation with respect to the micro-stretches gives the *algorithmic tangent moduli* consistent with the algorithm (4.24)

$$c_y := \frac{d}{d\lambda_y} \beta_y = \frac{1}{\lambda_y^2} \sum_{a=1}^s \mu_y^a - \frac{1}{\lambda_y} \beta_y \quad \text{for} \quad y = f, c. \quad (4.26)$$

In a typical time step the equations (4.24), (4.25) and (4.26) provide a closed-form update of the viscous overstress above an equilibrium state.

In contrast to the explicit updates (4.24) of the micro-forces, an implicit integration of the evolution system (4.23) yields non-linear equations. For example, utilization of the backward Euler scheme leads us to the non-linear residual expression of β_y^a

$$r_y^a(\beta_y^a) := \left(1 + \frac{\Delta t}{\tau_y^a} |\beta_y^a|^{\delta_y^a - 1}\right) \beta_y^a - \beta_{yn}^a - \mu_y^a \ln \frac{\lambda_y}{\lambda_{yn}} = 0. \quad (4.27)$$

Starting with $\beta_y^a = \beta_{yn}^a$, these equations can be solved iteratively by Newton iterations with updates

$$\beta_y^a \Leftarrow \beta_y^a - r_y^a(\beta_y^a) / r_y^{a'}(\beta_y^a) \quad (4.28)$$

until convergence is obtained in the sense $|r_y^a| \leq \text{tol}$. The effective over-stress is then computed via (4.25). The algorithmic tangent moduli (4.26) are replaced by the expressions

$$c_y = \frac{1}{\lambda_y^2} \sum_{a=1}^s \mu_y^a / r_y^{a'}(\beta_y^a) - \frac{1}{\lambda_y} \beta_y, \quad (4.29)$$

which is obtained from (4.27) by using the implicit function theorem. All of the simulations in Section 4.4 were run with this unconditionally stable scheme, which replaces the formulations outlined in Step 3 of Table 4.2.

4.3. Network Model for Finite Rubber Viscoelasticity

In this section, we develop a homogenization procedure that averages the micro-stresses with respect to the space orientations. To this end, we link the above introduced micro-kinematic variables $\{\lambda_y\}_{y=f,c}$ through characteristic network assumptions to suitably defined macro-kinematic variables $\{\bar{\lambda}_y\}_{y=f,c}$. Following the treatment outlined in Chapter 3, the associated micro-macro transition is interpreted as a *homogenization of state variables on a micro-sphere* with unit radius.

4.3.1. Definition of Macroscopic Stretch and Area Deformation. The key aspect of network theories is to link the deformation of a single chain to the macroscopic isochoric deformation $\bar{\mathbf{F}}$ (3.4) of the continuum that represents the homogenized network aggregate. Let \mathbf{r} be a Lagrangian orientation unit vector with $|\mathbf{r}|_{\mathbf{G}} := \sqrt{\mathbf{r}_b \cdot \mathbf{r}} = 1$, where $\mathbf{r}_b := \mathbf{G}\mathbf{r}$. Mappings of \mathbf{r} and \mathbf{r}_b by the isochoric deformation results in the isochoric stretch vector and area co-vector

$$\mathbf{t} = \bar{\mathbf{F}}\mathbf{r} \quad \text{and} \quad \mathbf{n}_b = \bar{\mathbf{F}}^{-T}\mathbf{r}_b, \quad (4.30)$$

respectively. Then the macro-length-stretch $\bar{\lambda}_f$ of a material line element with orientation \mathbf{r} in the reference configuration and the macro-area-stretch $\bar{\lambda}_c$ of a material area element with normal \mathbf{r}_b in the reference configuration are

$$\bar{\lambda}_f = |\mathbf{t}|_{\mathbf{g}} := \sqrt{\mathbf{t}_b \cdot \mathbf{t}} \quad \text{and} \quad \bar{\lambda}_c = |\mathbf{n}_b|_{\mathbf{g}^{-1}} := \sqrt{\mathbf{n}_b \cdot \mathbf{n}}, \quad (4.31)$$

with $\mathbf{t}_b := \mathbf{g}\mathbf{t}$ and $\mathbf{n} := \mathbf{g}^{-1}\mathbf{n}_b$ evaluated with the current metric \mathbf{g} . The affine relationship of the micro-length-stretch λ_f to the macro-length-stretch $\bar{\lambda}_f$ is in line with the affine network model of TRELOAR & RIDING [197]. The conceptual link of the micro-tube-stretch

λ_c to the macro-area-stretch $\bar{\lambda}_c$ has been suggested in (3.56). A descriptive interpretation of this assumption for superimposed prototype chains entangled with the ground state network is visualized in Figure 4.2c. In the case of a instantaneous macroscopic area extension of the cross section, chains in a direction perpendicular to the prototype chain under consideration are stretched. The perpendicular chains, denoted in the preceding part as the forest chains, are assumed to be obstacles to the extension of the prototype chain. As a consequence of their sudden stretch they assume a straighter topology that decreases the diameter of the fluctuation of the cross section projection as indicated by the shaded circle in Figure 4.2c. The diameter of the fluctuations of the perpendicular obstacle chain is interpreted as the diameter of the tube that constrains the prototype chain, which decreases with increasing macro-area-stretch.

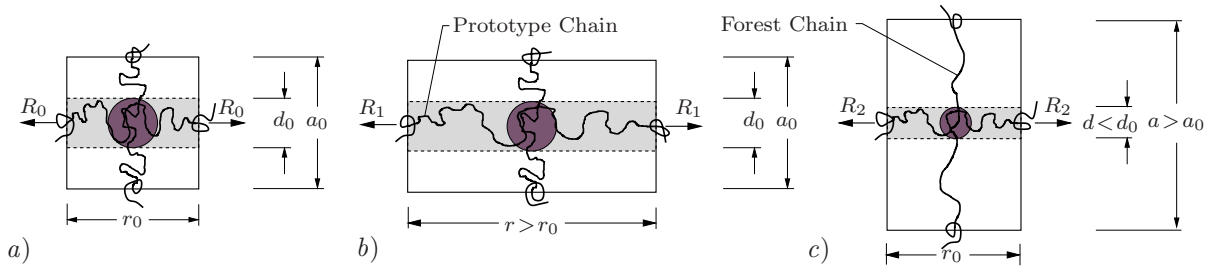


Figure 4.2: Link of micro- to macro-kinematic variables of an overstress producing chain entangled with the ground-state network. *a)* Undeformed macroscopic volume element. *b)* Instantaneous chain-stretch $\lambda_f := r/r_0$ in the affine deformation assumption is identical with the macro-line-stretch $\bar{\lambda}_f := |\mathbf{F}\mathbf{r}| = r/r_0$ of a continuum line element with direction \mathbf{r} . *c)* Sudden tube-stretch $\lambda_c := (d_0/d)^2$ is related to the macro-area-stretch $\bar{\lambda}_c := |\mathbf{F}^{-T}\mathbf{r}_b| = a/a_0$ of a continuum area element with normal \mathbf{r}_b . *Contour length fluctuations* due to detanglements relax both processes by *chain retraction mechanisms*.

4.3.2. Non-Affine Network Model for Elastic Equilibrium Response. The non-affine equilibrium network model set out in Chapter 3 defines the equilibrium part $\bar{\Psi}^e$ of the macroscopic free energy in (4.5) for the polymer aggregate. Clearly, these overall properties must be related to their micromechanical counterparts ψ^e in (4.11). The additive split of this micro-contribution also induces an additive split of the associated macro-contributions

$$\bar{\Psi}^e = \bar{\Psi}_f^e(\mathbf{g}; \bar{\mathbf{F}}) + \bar{\Psi}_c^e(\mathbf{g}; \bar{\mathbf{F}}). \quad (4.32)$$

A key result was the derivation of non-affine relationships between the micro- and macro-kinematic variables

$$\lambda = \langle \bar{\lambda}_f \rangle_p \quad \text{and} \quad \nu = (\bar{\lambda}_c)^q \quad (4.33)$$

in terms of two material parameters p and q of the ground state network. Here, $\langle v \rangle_p := \sqrt[p]{\langle v^p \rangle}$ is the p -root averaging operator of a scalar micro-variable $v > 0$. The notation $\langle v \rangle$ denotes the *continuous averaging* for an uniform orientation distribution of the variable v in space. We defined the average of the microscopic free energies for continuous space distribution via

$$\langle v \rangle := \frac{1}{|\mathcal{S}|} \int_{\mathcal{S}} v(\mathbf{r}; t) dA. \quad (4.34)$$

This averaging is interpreted as a *homogenization* of the state variable $v(\mathbf{r}; t)$ at position \mathbf{r} and time t on a *micro-sphere* \mathcal{S} with unit radius as depicted in Figure 3.4. The macroscopic

free energy of the equilibrium state is obtained by summarizing the micro-energies (4.12) and (4.13) of the unconstrained and constrained chain motion parts for n chains, yielding

$$\bar{\Psi}^e(\mathbf{g}; \bar{\mathbf{F}}) = n\psi_f(\langle \bar{\lambda}_f \rangle_p) + \langle n\psi_c(\langle \bar{\lambda}_c \rangle^q) \rangle. \quad (4.35)$$

Note that the dependence on \mathbf{g} and $\bar{\mathbf{F}}$ is due to the definitions (4.31). Further details of the non-affine model of rubber elasticity and its numerical implementation are outlined in Chapter 3.

4.3.3. Affine Network Model for Viscoelastic Overstress Response. We now develop a network model which defines the non-equilibrium part $\bar{\Psi}^v$ of the macroscopic free energy in (4.5) and the macroscopic dissipation function $\bar{\Phi}^v$ in (4.8) for the polymer aggregate. Clearly, these overall properties must be related to their micromechanical counterparts ψ^v and ϕ^v in (4.14) and (4.19), respectively. Then the additive split of these micro-contributions also induces an additive split of the associated macro-contributions

$$\bar{\Psi}^v = \bar{\Psi}_f^v(\mathbf{g}, \mathcal{I}_f; \bar{\mathbf{F}}) + \bar{\Psi}_c^v(\mathbf{g}, \mathcal{I}_c; \bar{\mathbf{F}}) \quad \text{and} \quad \bar{\Phi}^v = \bar{\Phi}_f^v(\dot{\mathcal{I}}_f) + \bar{\Phi}_c^v(\dot{\mathcal{I}}_c). \quad (4.36)$$

The first parts describe the overstress contributions to the free energy and the dissipation function for an idealized network with *free fluctuations* of superimposed chains entangled with the ground state network. The second parts represent the additional contributions due to the *interactions of the chains*. In the above expressions, the macroscopic internal state may alternatively be described by

$$\mathcal{I} := \{\varepsilon_y^1(\mathbf{r}; t) \dots \varepsilon_y^s(\mathbf{r}; t)\}_{y=f,c} \quad \text{or} \quad \mathcal{F} := \{\beta_y^1(\mathbf{r}; t) \dots \beta_y^s(\mathbf{r}; t)\}_{y=f,c} \quad (4.37)$$

in terms of *2s fields on the micro-sphere*, representing viscous micro-strains and micro-forces, respectively. Here, \mathbf{r} is the spatial variable that parametrizes the fields on the micro-sphere as depicted in Figure 3.4.

In contrast to the basic network assumption (4.33) for the equilibrium response, we assume for the viscous overstresses the *affine relationships*

$$\lambda_f = \bar{\lambda}_f \quad \text{and} \quad \lambda_c = \bar{\lambda}_c \quad (4.38)$$

between the micro-kinematic variables and their continuum counterparts. With these relationships at hand, we define the non-equilibrium part of the macroscopic energy by homogenizing the orientation contributions over the micro-sphere

$$\bar{\Psi}^v(\mathbf{g}, \mathcal{I}; \bar{\mathbf{F}}) = \langle \psi_f^v(\bar{\lambda}_f, \varepsilon_f^1 \dots \varepsilon_f^s) \rangle + \langle \psi_c^v(\bar{\lambda}_c, \varepsilon_c^1 \dots \varepsilon_c^s) \rangle. \quad (4.39)$$

Similarly, the macroscopic dissipation function is obtained by the homogenization procedure

$$\bar{\Phi}^v(\dot{\mathcal{I}}) = \langle \phi_f^v(\dot{\varepsilon}_f^1 \dots \dot{\varepsilon}_f^s) \rangle + \langle \phi_c^v(\dot{\varepsilon}_c^1 \dots \dot{\varepsilon}_c^s) \rangle. \quad (4.40)$$

Insertion of the two above functions $\bar{\Psi}^v$ and $\bar{\Phi}^v$ into the macroscopic evolution system (4.8) identifies the microscopic evolution system (4.20) pointwise at $\mathbf{r} \in \mathcal{S}$ on the micro-sphere \mathcal{S} . Owing to the convexity of the micro-dissipation functions ϕ_y^v in (4.21), the macro-dissipation function $\bar{\Phi}^v$ is also convex. Thus the overall macroscopic model of viscoelasticity satisfies the thermodynamic consistency condition (4.7) through the relationship

$$\mathcal{D}_{mac} = \langle \mathcal{D}_{mic} \rangle \geq 0 \quad (4.41)$$

to the positive micro-dissipation (6.24).

Having the macro-energy defined, we compute the Eulerian stresses based on a straightforward exploitation of (4.6)₃. To this end, at first we compute the derivatives of the macro-length-stretch and the macro-area-stretch in (4.31) with respect to the Eulerian metric, yielding $2\partial\mathbf{g}\bar{\lambda}_f = \bar{\lambda}_f^{-1}\mathbf{t} \otimes \mathbf{t}$ and $2\partial\mathbf{g}\bar{\lambda}_c = -\bar{\lambda}_c^{-1}\mathbf{n} \otimes \mathbf{n}$, respectively. Then we obtain from (4.39) the representation of the macroscopic Kirchhoff stresses

$$\bar{\boldsymbol{\tau}}_{algo}^v = \langle \beta_f \bar{\lambda}_f^{-1} \mathbf{t} \otimes \mathbf{t} - \beta_c \bar{\lambda}_c^{-1} \mathbf{n} \otimes \mathbf{n} \rangle \quad (4.42)$$

in terms of the algorithmic over stresses on the micro-sphere defined in (4.25). Note that this representation includes the update algorithms (4.24) and (4.27) of the micro-forces. Then a further derivation of the above stress expression with respect to the Eulerian metric yields the spatial algorithmic tangent moduli consistent with the update algorithms

$$\bar{\mathbb{C}}_{algo}^v := 2\partial\mathbf{g}\bar{\boldsymbol{\tau}}_{algo}^v(\mathbf{g}, \mathcal{F}, \bar{\mathbf{F}}; \bar{\mathbf{F}}_n, \mathcal{F}_n) . \quad (4.43)$$

Using the results $2\partial\mathbf{g}(\mathbf{t} \otimes \mathbf{t}) = \mathbb{0}$ and $2\partial\mathbf{g}(\mathbf{n} \otimes \mathbf{n}) = -2\text{sym}[\mathbf{g}^{-1} \odot (\mathbf{n} \otimes \mathbf{n}) + (\mathbf{n} \otimes \mathbf{n}) \odot \mathbf{g}^{-1}]$ with the definition $\text{sym}[\mathbf{g}^{-1} \odot (\mathbf{n} \otimes \mathbf{n})]^{abcd} := (\delta^{ac}n^b n^d + \delta^{bc}n^a n^d)/2$, we obtain

$$\begin{aligned} \bar{\mathbb{C}}_{algo}^v = \langle & (c_f - \beta_f \bar{\lambda}_f^{-1}) \bar{\lambda}_f^{-2} \mathbf{t} \otimes \mathbf{t} \otimes \mathbf{t} \otimes \mathbf{t} \\ & + (c_c - \beta_c \bar{\lambda}_c^{-1}) \bar{\lambda}_c^{-2} \mathbf{n} \otimes \mathbf{n} \otimes \mathbf{n} \otimes \mathbf{n} \\ & + 2\beta_c \bar{\lambda}_c^{-1} \text{sym}[\mathbf{g}^{-1} \odot (\mathbf{n} \otimes \mathbf{n}) + (\mathbf{n} \otimes \mathbf{n}) \odot \mathbf{g}^{-1}] \rangle \end{aligned} \quad (4.44)$$

with the algorithmic contributions outlined in (4.25)-(4.29).

4.3.4. Discretization of Fields on the Micro-Sphere. The implementation of the viscoelastic network model outlined above in computer codes needs a numerical evaluation of the integral over the continuous space orientations. As outlined in Section 3.4.2, this is achieved by discretizing the continuous orientation distribution of the unit sphere \mathcal{S} by m discrete Lagrangian orientation vectors $\{\mathbf{r}^i\}_{i=1\dots m}$ and weight factors $\{w^i\}_{i=1\dots m}$. Then the continuous averaging (4.34) of a micro-variable v defined on the sphere is transformed into the discrete sum

$$\langle v \rangle \approx \sum_{i=1}^m v^i w^i , \quad (4.45)$$

where $\{v^i\}_{i=1\dots m}$ are the micro-variables on the sphere evaluated at the discrete points \mathbf{r}^i . Suitable sets of orientation vectors $\{\mathbf{r}^i\}_{i=1\dots m}$ and associated weight factors $\{w^i\}_{i=1\dots m}$ are discussed in BAŽANT & OH [10]. The integration schemes exploit the symmetry of the unit sphere by defining discrete points only for the half-sphere. It has been shown in the foregoing chapter that a 21-point integration scheme provides sufficient accuracy for numerical investigations of rubber elasticity. Hence, we use for all subsequent numerical examples the 21-point integration scheme for the half-sphere, see Table 3.2 for further details. Then the discretization of the internal variable fields (4.37) on the micro-sphere yields the effective history storage of $2s \times m = 42s$ scalar variables

$$\mathcal{F}_n = \{\beta_y^1(\mathbf{r}^i; t_n) \dots \beta_y^s(\mathbf{r}^i; t_n)\}_{y=f,c}^{i=1\dots m=21} \quad (4.46)$$

for the discrete spectrum of micro-forces at time t_n . All the above outlined continuous average operations in the discrete setting appear as a simple algebraic sum over 21 discrete space orientations. Table 4.2 summarizes the numerical implementations of the affine overstress model.

Table 4.2: Stress Update of Viscoelastic Overstresses on Micro–Sphere.

1. *Data Base.* Given are history data $\{\bar{\lambda}_{yn}, \beta_{yn}^1 \dots \beta_{yn}^s\}_{y=f,c}^{i=1\dots m}$ of stretches and over-stress spectrum at time t_n at $m = 21$ discrete points on the micro–sphere. Get discrete orientation vectors \mathbf{r}^i and weights w^i from Table 3.2.

2. *Current Micro-Stretches.* Given is the unimodular deformation map $\bar{\mathbf{F}}$ at time t_{n+1} . Get the $i = 1\dots m$ deformed tangents $\mathbf{t}^i = \bar{\mathbf{F}}\mathbf{r}^i$ and normals $\mathbf{n}^i = \bar{\mathbf{F}}^{-T}\mathbf{r}^i$ and compute the affine micro-stretches and micro-area-stretches

$$\bar{\lambda}_f^i = |\mathbf{t}^i| \quad \text{and} \quad \bar{\lambda}_c^i = |\mathbf{n}^i|$$

3. *Current Micro-Stresses and Micro-Moduli.* Update over-stress fluctuations for the spectrum $a = 1\dots s$ at $i = 1\dots m$ discrete points of the micro–sphere

$$\beta_y^{ai} = \mu_y^a \ln \frac{\bar{\lambda}_y^i}{\lambda_{yn}^i} + \left(1 - \frac{\Delta t}{\tau_y^a} |\beta_{yn}^{ai}|^{\delta_y^a - 1}\right) \beta_{yn}^{ai} \quad \text{for } y = f, c$$

compute the algorithmic over-stresses $\beta_y^i = (\sum_{a=1}^s \beta_y^{ai}) / \bar{\lambda}_y^i$ and moduli $c_y^i = (\sum_{a=1}^s \mu_y^a) / \bar{\lambda}_y^{i2} - \beta_y^i / \bar{\lambda}_y^i$ for $y = f, c$.

4. *Current Macro–Stresses and Macro–Moduli.* Get homogenized over-stresses

$$\bar{\boldsymbol{\tau}}_{algo}^v = \sum_{i=1}^m [\beta_f^i \bar{\lambda}_f^{i-1} \mathbf{t}^i \otimes \mathbf{t}^i - \beta_c^i \bar{\lambda}_c^{i-1} \mathbf{n}^i \otimes \mathbf{n}^i] w^i$$

and algorithmic tangent moduli

$$\begin{aligned} \bar{\mathbb{C}}_{algo}^v = \sum_{i=1}^m [& (c_f^i - \beta_f^i \bar{\lambda}_f^{i-1}) \bar{\lambda}_f^{i-2} \mathbf{t}^i \otimes \mathbf{t}^i \otimes \mathbf{t}^i \otimes \mathbf{t}^i \\ & + (c_c^i - \beta_c^i \bar{\lambda}_c^{i-1}) \bar{\lambda}_c^{i-2} \mathbf{n}^i \otimes \mathbf{n}^i \otimes \mathbf{n}^i \otimes \mathbf{n}^i \\ & + 2\beta_c^i \bar{\lambda}_c^{i-1} \text{sym}[\mathbf{g}^{-1} \odot (\mathbf{n}^i \otimes \mathbf{n}^i) + (\mathbf{n}^i \otimes \mathbf{n}^i) \odot \mathbf{g}^{-1}]] w^i \end{aligned}$$

and proceed with deviatoric projections as outlined in (4.4) and (3.7).

4.4. Numerical Examples

We now assess the modeling capacity of the proposed model by comparing its simulations against new and already published experimental data. The experimental data considered here were obtained through different types of loading programs, which include both monotonous and cyclic processes at different loading rates involving relaxation tests. Apart from homogeneous experiments, finite element analyses of three-dimensional inhomogeneous experiments under different loading conditions are conducted.

4.4.1. Simulation of Homogeneous Experiments. The stress-stretch response of a pre-conditioned cylindrical highly saturated nitrile rubber HNBR50 specimen under cyclic uniaxial loading with a relaxation period has already been presented in Figure 1.1. Results of our experimental investigations justify the absence of an equilibrium hysteresis

due to convergence of the relaxation curves to the same stress ordinate at the end of very long relaxation periods on both loading and unloading paths. Having concluded that the elastic equilibrium response can be extracted from the experiments on a pre-damaged material, uniaxial and equi-biaxial tensile tests with several relaxation periods were carried out. An arithmetic average of the stress values attained at the end of the two hours relaxation periods at the same deformations on loading and unloading paths are assigned as an elastic response of the material. Results of uniaxial and equi-biaxial experiments are depicted in Figure 4.3. The five parameters μ , N , p , U , q in Table 4.1 of the non-affine micro-sphere model of elasticity were identified with respect to these data of HNBR50 material. As can be seen in Figure 4.3, the elastic response of the material in both uniaxial and equi-biaxial tests is traced very well. For the sensitivity of the elastic stress-stretch response of the model with regard to the individual material parameters in both uniaxial and equi-biaxial deformations we refer to Figures 3.12 and 3.13.

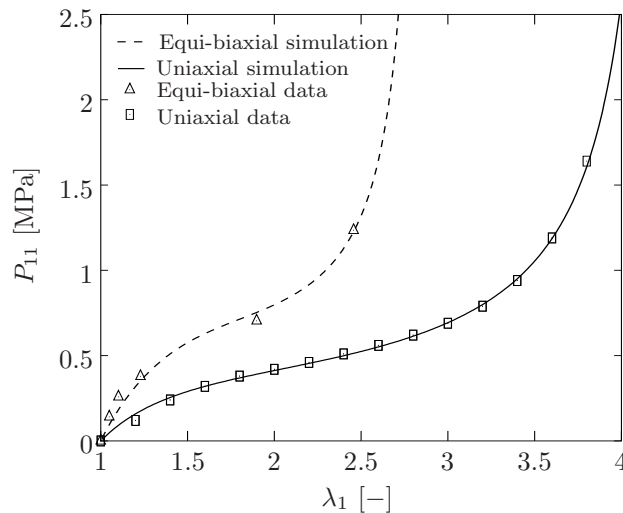


Figure 4.3: Uniaxial and equi-biaxial experiments of a cylindrical HNBR50 rubber specimen at room temperature. The data points are obtained by relaxation periods during the cyclic loading in both the loading and unloading paths. The parameters of the non-affine elasticity model are identified as $\mu = 0.139$ MPa, $N = 5.18$, $p = 1.166$, $U = 11.2$, $q = 0.126$.

In order to investigate the dependence of the stress response on the loading rate, pre-conditioned cylindrical specimens of the same material are subjected to cyclic uniaxial loading between the stretch values $\lambda_1 = 2$ and $\lambda_1 = 0.75$ at three different absolute loading rates $d|\lambda_1|/dt = 5 \cdot 10^{-2}$ 1/min, $5 \cdot 10^{-1}$ 1/min, 5 1/min. The uniaxial nominal stress-stretch response of the three specimens to the first two loading cycles is illustrated in Figure 4.4a, see also MÉNDEZ [135]. As can be clearly noticed, when the loading rate is increased the material response becomes stiffer; that is, at the same value of stretch one attains larger value of the absolute stress in faster experiments. This is expected rate-dependent response of any viscoelastic material. Furthermore, the area in the hysteresis, which is proportional to the integrated dissipation, becomes larger as the loading rate increases. An additional conclusion which might be drawn from the cyclic experiments is that the difference between the first and the second stress-stretch curves becomes more pronounced when the loading rate is increased. In order to determine the material parameters of the viscous overstress part of the network model, tension-compression cyclic uniaxial tests performed at the loading rates $d|\lambda_1|/dt = 5 \cdot 10^{-2}$ 1/min, 5 1/min are utilized. We model the observed response with a *spectrum* of $s = 3$ overstress on the micro-

sphere. During the identification process, the 6 relaxation times of the unconstrained and tube parts are *a priori assigned* to the values $\{\tau_y^a\}_{y=f,c}^{a=1,2,3} = \{0.1, 10, 1000\}_{y=f,c}$ and kept frozen during the identification process. Identified values of the remaining 12 material parameters are given in the caption of Figure 4.4. Simulation of all three experiments are depicted in Figures 4.4b-d in comparison with the experiments. They clearly show a capability of the proposed approach in capturing the real material response. The experimental observations regarding viscous stiffening, hysteresis thickness changes and the apparent difference between the first two cycles at relatively faster experiments are incorporated very well.

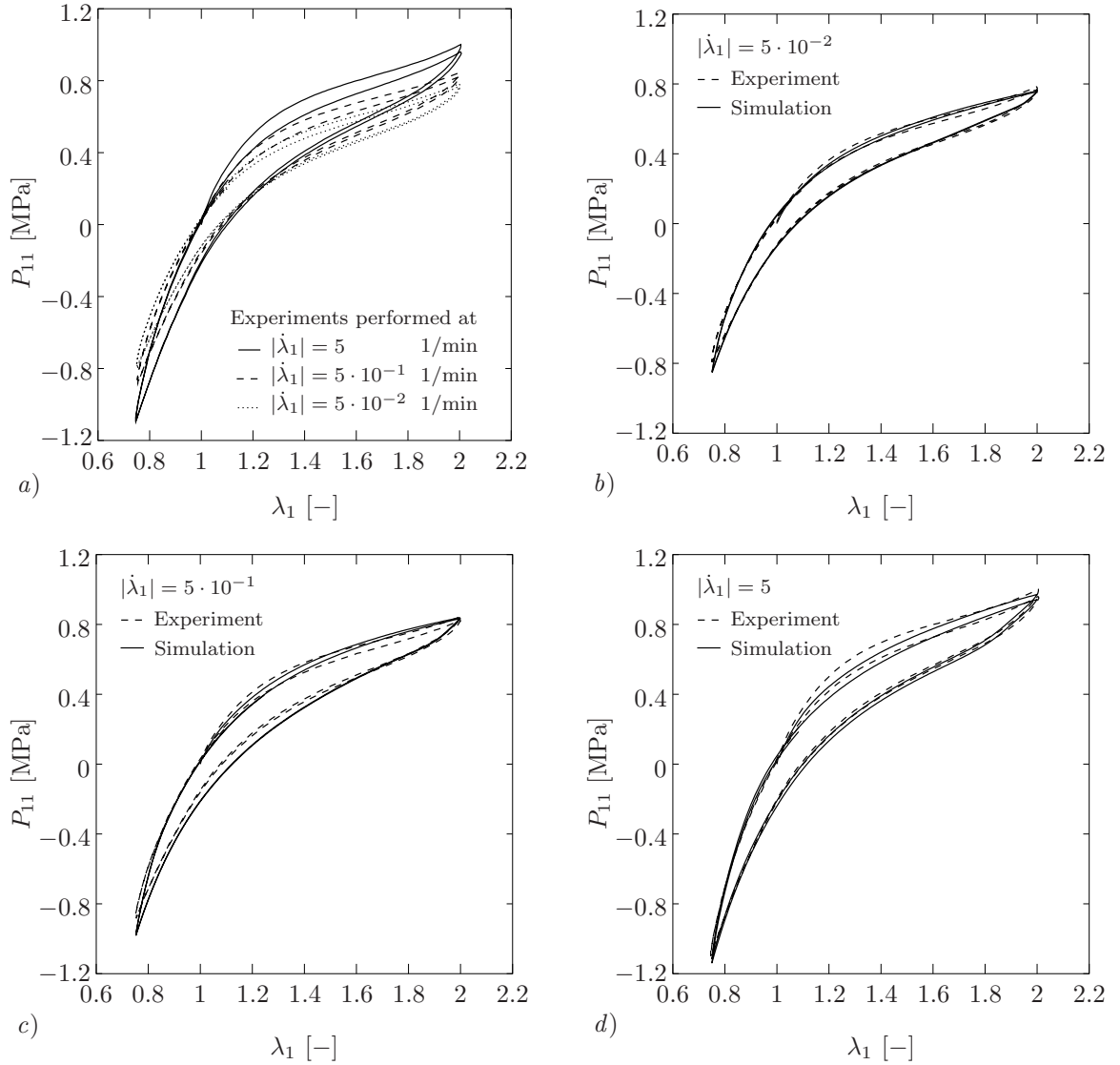


Figure 4.4: Cyclic experiments and their simulations. *a)* Cyclic experiments performed at different loading rates $\dot{\lambda}_1 = 5 \cdot 10^{-2}$, $5 \cdot 10^{-1}$, 5 1/min. The larger the loading rate, the stiffer the material response and the larger the hysteresis. Simulations of the experiments are depicted in *b)*, *c)* and *d)* for the loading rates $\dot{\lambda}_1 = 5 \cdot 10^{-2}$, $5 \cdot 10^{-1}$ and 5 , respectively. The viscous material parameters identified for the experiments plotted in *b)* and *d)* are $\mu_f = \{6.16, 1.35, 1.76\}$ MPa, $\mu_c = \{7.19, 1.13, 1.63\}$ MPa, $\delta_f = \{2.97, 2.46, 24.46\}$, $\delta_c = \{1.02, 2.05, 16.47\}$, $\tau_{f,c} = \{0.1, 10, 1000\}$.

Further investigation on the validity of the identified material parameters and the modeling capabilities of the proposed constitutive approach is conducted against purely

compressive uniaxial cyclic experiments depicted in Figure 4.5a. These experiments were conducted between the stretch values $\lambda_1 = 1$ and $\lambda_1 = 0.75$ at three different absolute loading rates $d|\lambda_1|/dt = 5 \cdot 10^{-2}$ 1/min, $5 \cdot 10^{-1}$ 1/min, 5 1/min on pre-conditioned specimens with the same geometry as those used in the cyclic tests, see MÉNDEZ [135]. The above mentioned observations for the tension-compression cyclic experiments related to rate-dependent stiffening, hysteresis enlargement and difference between the first and the second cycles are also valid for the compressive cyclic uniaxial tests. These data are simulated by using the same material parameters previously identified with the two sets of tension-compression cyclic uniaxial data. Comparison of the simulations with the experiments is presented in Figures 4.5b-d for different loading rates. The simulation captures the experiments adequately, in particular the ones with slower loading rates, in an excellent manner. For the fastest experiment, the quality of the simulation can be considered as sufficiently adequate. The overall compressive time dependent viscoelastic material behavior in cyclic tests can be said to be captured very well.

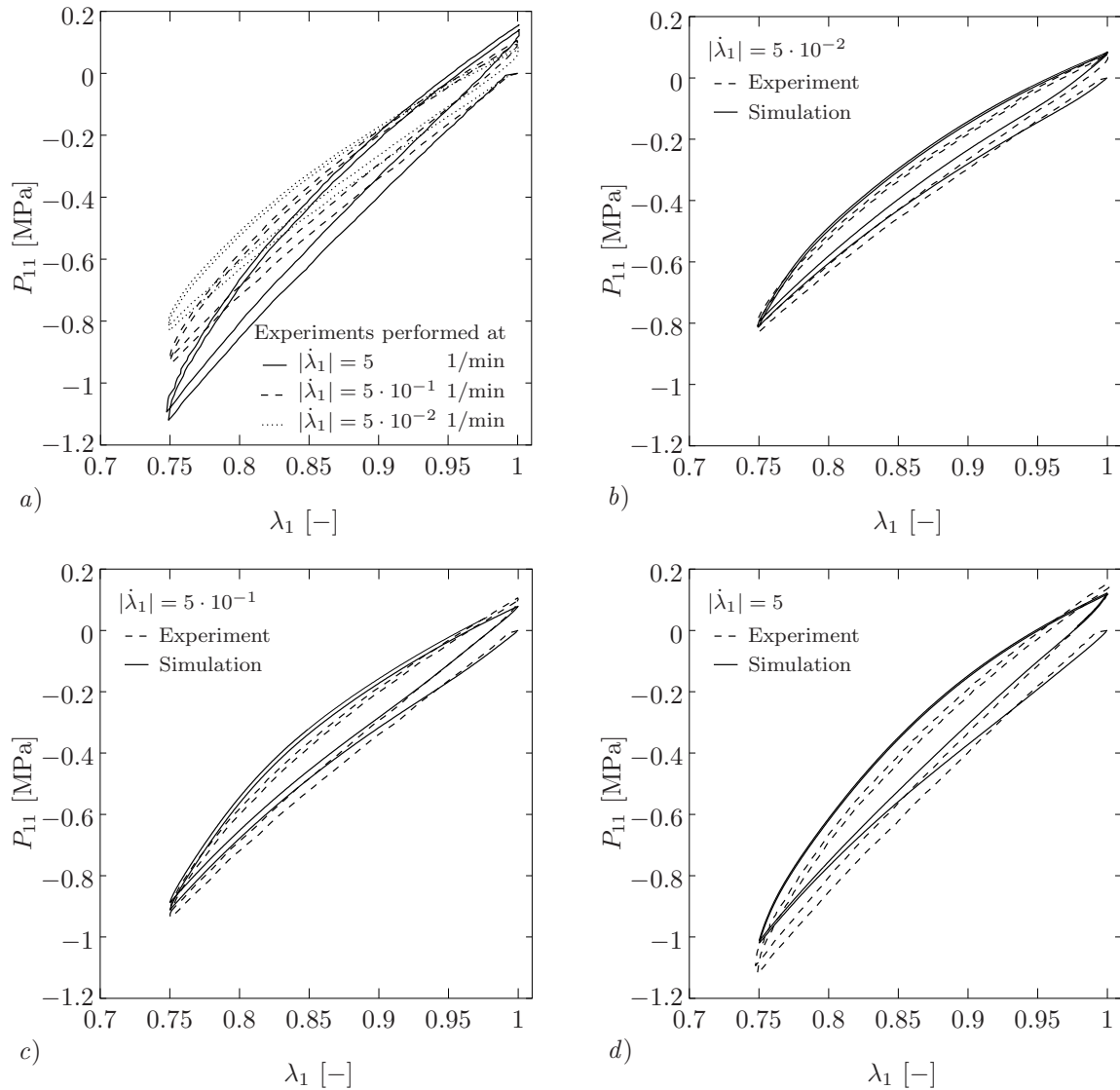


Figure 4.5: Compressive cyclic experiments and simulations. *a)* Cyclic experiments carried out at different loading rates $\dot{\lambda}_1 = 5 \cdot 10^{-2}$, $5 \cdot 10^{-1}$, 5 1/min. Respective simulations of the experiments at the three different rates are depicted in *b)*, *c)* and *d)*. For the simulation the same parameters as those in Figure 4.4 were used.

The last homogeneous experiment on HNBR50 investigates the relaxation behavior in tension-compression cyclic tests in both loading and unloading paths of both tensile and compressive stretch intervals. A total twelve relaxation tests, one hour each, were conducted at the stretch values $\lambda_1 = 0.75, 0.875, 1, 1.25, 1.50, 1.75, 2$. Figure 4.6 depicts the material response to the discontinuous cyclic loading between the stretch values $\lambda_1 = 0.75$ and $\lambda_1 = 2$ at an absolute loading rate $d|\lambda_1|/dt = 3 \text{ 1/min}$. Simulation of this relaxation experiment is performed again by using the previously identified material parameters given in Figure 4.4. A plot of the simulation against the experiment in Figure 4.6 shows that the proposed constitutive model captures the relaxation behavior very well, too. Especially the thickness of the hysteresis agrees excellently. The assumed separation of the material response into equilibrium and viscous non-equilibrium parts is justified by the overall quantitative agreement between experiments and simulations for the loading cases illustrated in Figures 4.3-4.6.

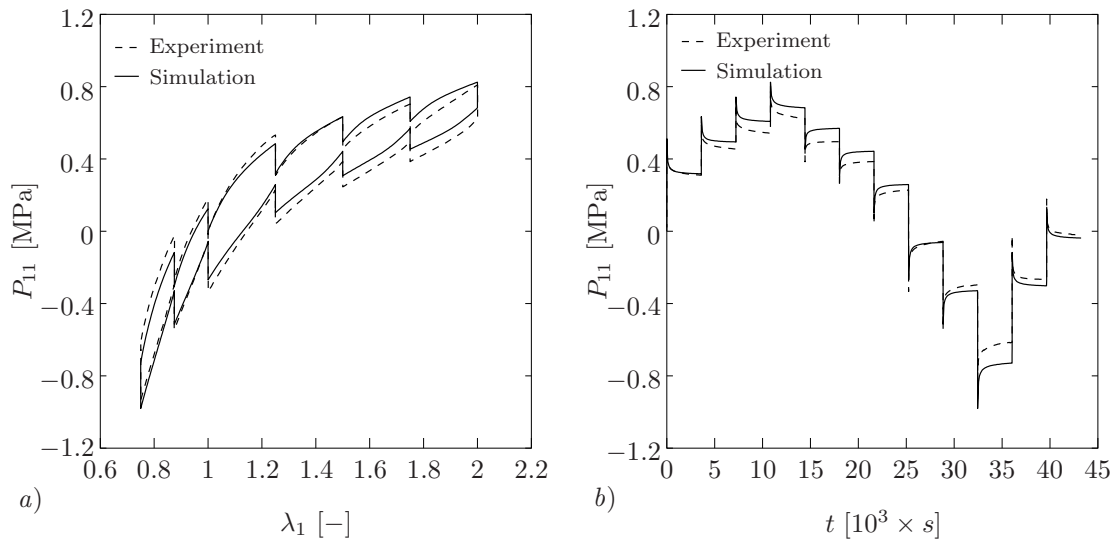


Figure 4.6: a) Stress vs. stretch and b) stress vs. time plots in a cyclic tension-compression uniaxial experiment performed at an absolute loading rate $|\dot{\lambda}_1| = 3 \text{ 1/min}$ with relaxation breaks. The cyclic experiment was performed between the stretch values $\lambda_1 = 0.75$ and $\lambda_1 = 2$. During the experiment twelve one hour relaxation breaks were performed. For the simulation the same material parameters as those of Figure 4.4 were employed.

As a last numerical example of homogeneous experiments, besides the preceding study on the HNBR50 rubber, we now consider the data acquired from another rubbery polymer B186 produced by the Continental AG. This study aims to show that the predictive capabilities of the proposed model are not restricted to a single type of rubber. The experimental data on B186 originally reported by MIEHE & KECK [150] involve monotonous tensile and compressive tests performed at three loading rates $d|\lambda_1|/dt = 5.4 \cdot 10^{-4} \text{ 1/s}$, $5.4 \cdot 10^{-3} \text{ 1/s}$, $5.4 \cdot 10^{-1} \text{ 1/s}$, presented in Figures 4.7a and 4.7b. For the simulations of both elastic and viscous effects, the parameters were simultaneously identified by monotonous tensile and compressive uniaxial experiments, see Figures 4.7a and 4.7b together with the corresponding simulations. The identified model parameters are given in Figure 4.7. With these material parameters at hand, relaxation tests are simulated both for the tensile and the compressive loadings. Comparison of the simulations and the experiments are depicted in Figures 4.7c and 4.7d, respectively. Clearly, the simulations capture the material behavior quite well.

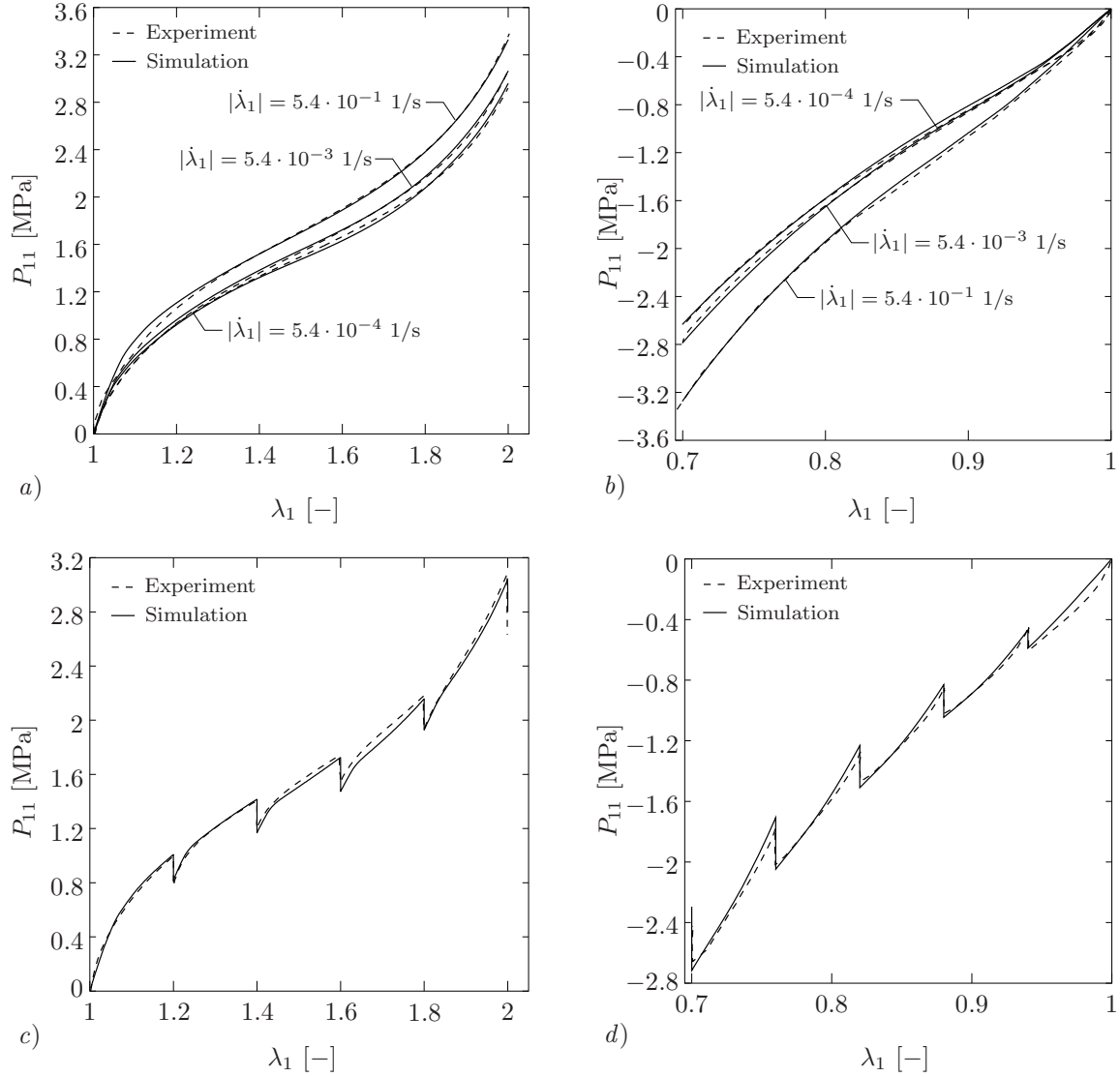


Figure 4.7: Monotonous tensile and compressive uniaxial experiments, reported by MIEHE & KECK [150], and their simulations with the proposed model. *a, b)* Monotonous uniaxial experiments performed at loading rates $|\dot{\lambda}_1| = 5.4 \cdot 10^{-4}$, $5.4 \cdot 10^{-3}$, $5.4 \cdot 10^{-1}$ 1/s. and corresponding fittings. The material parameters identified using the data in a,b) are $\mu = 0.34$ MPa, $N = 1.96$, $p = 1.56$, $U = 11.62$, $q = 0.22$, $\mu_f = \{25.58, 2.44, 0.47\}$ MPa, $\mu_c = \{10.84, 4.02, 2.93\}$ MPa, $\delta_f = \{14.93, 8.57, 24.46\}$, $\delta_c = \{0.79, 7.29, 16.38\}$, $\tau_{f,c} = \{0.1, 10, 1000\}$. These parameters are employed for simulating tensile and compressive relaxation experiments shown in *c)* and *d)* performed at the loading rate $|\dot{\lambda}_1| = 5.4 \cdot 10^{-2}$ 1/s with five equally spaced one hour relaxation periods.

The simulations of the experiments carried out hitherto show that the proposed model captures the material behavior for the both materials exhibiting rubber-like response successfully. Therefore, our approach to model finite viscoelasticity can be concluded to be very suitable for rate-dependent rubber-like materials.

4.4.2. 3-D Analyses of a Non-Homogeneous Shear Test. In addition to the evaluation of the proposed approach based on the homogeneous experiments presented in the preceding subsection, we further present the capabilities of the proposed model in simulating the non-homogeneous three-dimensional experiment. The specimen is made up of highly saturated nitrile rubber HNBR50 and was produced by the Robert Bosch

GmbH. The three-dimensional geometry of the specimen, having a varying hyperbolic transversal and a circular planar cross-section together with its dimensions, is depicted in Figure 4.8. The specimen is discretized into 1152 eight-node Q1P0 mixed brick finite elements. The bottom face of the specimen is fixed in all three directions. The degrees of freedom on its top surface in y - and z - directions are restrained and the deformation in x - direction is prescribed, see Figure 4.8.

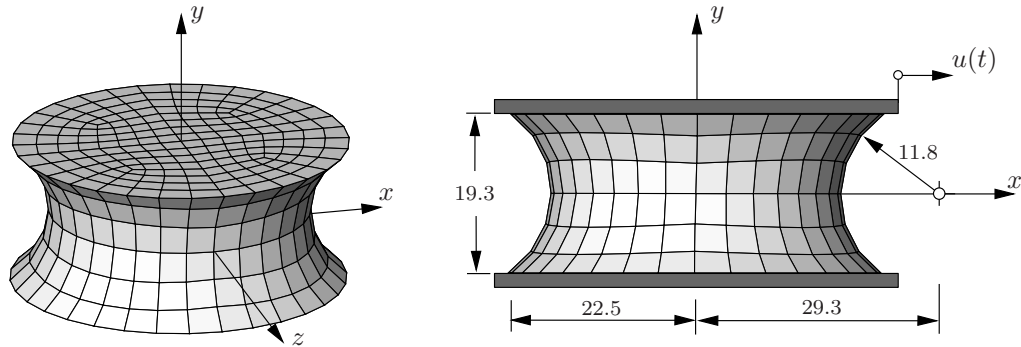


Figure 4.8: Three dimensional view and dimensions of the specimen. Spatial finite element discretization and boundary conditions of the problem are illustrated. All dimensions are in millimeters.

The finite element analyses of the boundary value problem were carried out for three different loading functions $u_i(t)$ for $i=1, 2, 3$ depicted in Figure 4.9a. The first two loading processes $u_1(t)$ and $u_2(t)$ correspond to cyclic deformations applied between -10 and 10 mm at loading rates $|\dot{u}_1(t)| = 40$ mm/min and $|\dot{u}_2(t)| = 4$ mm/min, respectively. The third loading $u_3(t)$ is designed for a relaxation process, in which the top surface of the specimen is deformed up to $u_3 = 20$ mm at the loading rate $\dot{u}(t) = 40$ mm/min and thereafter the deformation is kept constant until $t = 90$ s.

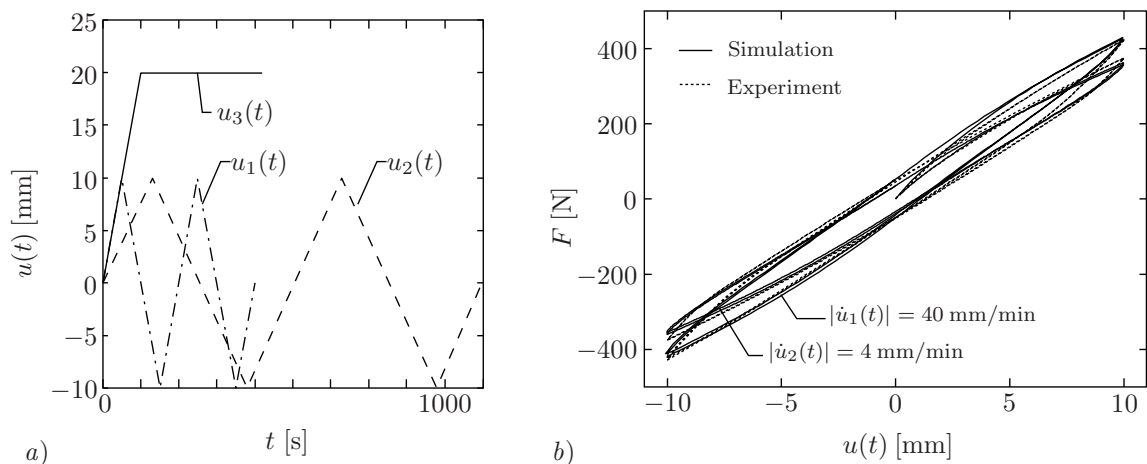


Figure 4.9: Loading processes and the load–deflection diagrams. *a*) Three different loading functions $u_i(t)$ for $i = 1, 2, 3$ used in the finite element analyses of the boundary value problem. The first two loading processes $u_1(t)$ and $u_2(t)$ are also used in the three–dimensional experiments. *b*) Comparison of the load–deflection diagrams with the experimental ones for the loading processes $u_1(t)$ and $u_2(t)$.

For the loading processes $u_1(t)$ and $u_2(t)$, non-homogeneous three-dimensional experiments were carried out on the pre-conditioned specimens, see also MÉNDEZ [135].

Load-deflection diagrams of the specimens are compared with the FE simulations in Figure 4.9b. In the FE analyses the material parameters identified from the homogenous experiments on HNBR50 are used, see Figure 4.4. The predictive capabilities of the put forward approach is once more illustrated in Figure 4.9b. They concern not only capturing the maximal load value attained but also the shape and thickness of the hysteresis of the load-deflection curves. If the followed systematic procedure is considered, the results obtained in the simulation of the three-dimensional inhomogeneous experiment is promising in the context of quantitative simulations of the three-dimensional non-homogeneous experiments which are of great interest in practical engineering applications.

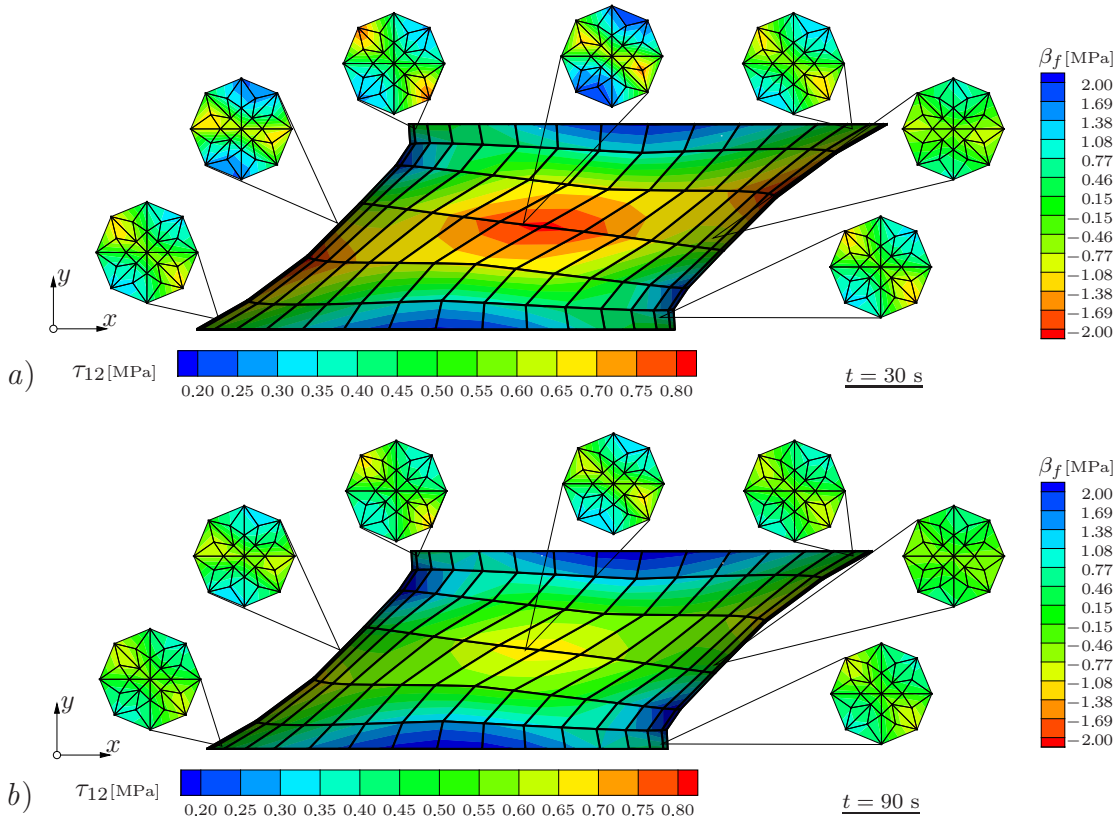


Figure 4.10: Total macroscopic shear stress and unconstrained viscous micro-stress $\beta_f := \sum_{a=1}^{s=3} \beta_f^a$ contours zoomed out at selected Gauss points are depicted in *a*) at the beginning ($t = 30 \text{ s}$) and in *b*) at the end ($t = 90 \text{ s}$) of the relaxation loading $u_3(t)$.

The results depicted in Figures 4.10a and 4.10b present the total shear stress contours τ_{12} at the beginning and at the end of the relaxation period of the loading $u_3(t)$, see Figure 4.9a. Besides the macroscopic shear stress distributions, pole figure contours of the effective unconstrained viscous overstress β_f defined in (4.25) are magnified at the selected material points. Comparison of the macroscopic shear stress contours in Figures 4.10a and 4.10b clearly indicates a difference between fully evolved and relaxed non-equilibrium stresses and their distribution over the specimen. Owing to the fixed boundary conditions at the upper and the lower faces of the specimen, shear stresses concentrate in the middle region of the mesh. Also the pole contours of summed unconstrained viscous chain stresses plotted at representative points support this conclusion. The micro-stress contours in Figure 4.10b indicate that the viscous non-equilibrium stresses in the unconstrained network are almost totally relaxed out.

5. The Micro-Sphere Model of Anisotropic Mullins-Type Damage

In the preceding Chapters 3 and 4 we outlined the micro-sphere models for the finite elasticity and viscoelasticity of rubber-like materials, respectively. In this chapter we further advance the *micro-sphere model* of finite rubber elasticity towards the incorporation of the deformation-induced softening commonly referred to as the Mullins effect. The description of the Mullins effect and the main approaches put forward in the literature have been outlined in Section 1.1. The formulation and results presented in this chapter are based on the ideas outlined in the recent work by GÖKTEPE & MIEHE [69]. We construct a continuum formulation through a superimposed modeling of a crosslink-to-crosslink (CC) and a particle-to-particle (PP) network, see Figure 5.1. The former is described by the non-affine elastic network model outlined in Chapter 3. The Mullins-type damage phenomenon is incorporated in the PP network and micromechanically motivated by a breakdown of bonds between chains and filler particles. In contrast to the previous works on the Mullins effect, our formulation inherently describes a *deformation-induced anisotropy* of the damage as observed in experiments. We show that the experimentally observed *permanent set* in stress-strain diagrams is achieved by this model automatically as an anisotropy effect. The performance of the model is demonstrated by means of several numerical examples that include fitting of homogeneous experimental benchmarks.

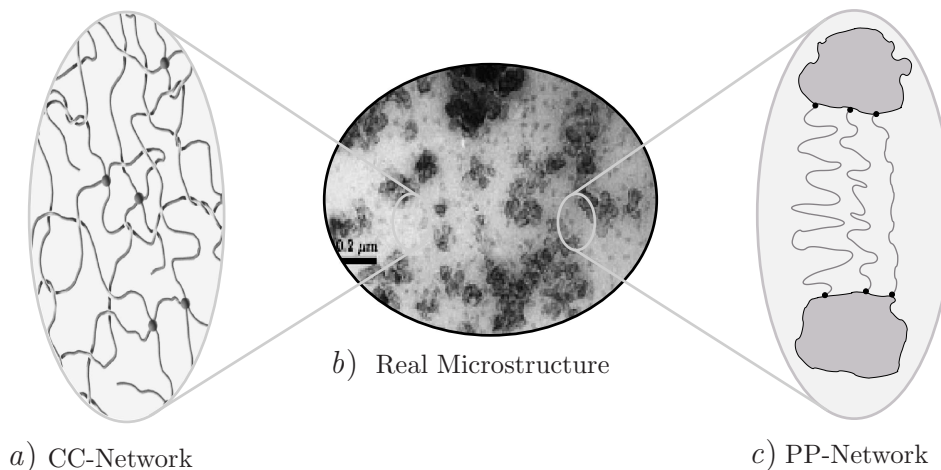


Figure 5.1: A TEM micrograph of real carbon-black filled (9%) natural rubber microstructure taken from Figure 1b of BERGSTRÖM & BOYCE [16]. The overall network behaviour is considered to be a superimposed response of a crosslink-to-crosslink (CC) network and a particle-to-particle (PP) network. Schematic pictures of representative CC- and PP-networks are depicted on the left and the right sides of the microstructure, respectively.

Although all of the continuum formulations cited in Chapter 1 model the damage in rubbers isotropically, MULLINS [155] (p.289) gave experimental evidence on deformation-induced anisotropic properties in stretching and swelling experiments. Similar observations were also reported by JAMES & GREEN [99] on the investigations on the tear strength. In this work we propose an *anisotropic constitutive model* for the description of the Mullins effect that extends the non-affine formulation of rubber elasticity in Chapter 3. The overall network model is constructed by additively dividing the total network structure into the crosslink-to-crosslink (CC) and the particle-to-particle (PP) parts as motivated in Figure 5.1 schematically. The response of the CC network is described by the non-affine elastic network model proposed in Chapter 3. The anisotropic damage phenomenon is embedded into the PP network. Here, we conceptually follow formulations of

BUECHE [31] and GOVINDJEE & SIMÓ [74] to a typical space orientation of a prototype chain mechanism. The key steps of our formulation are *i*) the set up micromechanically-based constitutive models for a *single chain orientation* and *ii*) the definition of the macroscopic stress response of the polymer network by a *directly evaluated micro-macro transition* based on homogenization of the orientation contributions. Owing to the intrinsic orientation distribution of the micro-variables, the model avoids the introduction of a tensorial damage variable and allows us to formulate an anisotropic damage evolution in terms of a one-dimensional inelastic model associated with a prototype chain orientation. Hence, the formulation inherently includes a deformation-induced anisotropy since different loading histories are experienced by different chain orientations. We show that the permanent set is achieved by our model in a natural way as an outcome of the anisotropic damage distribution. After pointing out in Section 5.1 the macroscopic structure of the model, we focus in Section 5.2 on the micromechanical constitutive formulation with respect to a single chain orientation. Then Section 5.3 treats the modeling of the CC and PP networks which define the homogenized overall response. The performance of the micro-sphere model of anisotropic Mullins-type damage is analyzed in Section 5.4, where we investigate several representative numerical examples.

5.1. Macroscopic Finite Elasticity with Damage

The fundamental formulae governing the momentum balance and the constitutive relations of macroscopic spatial finite inelasticity for decoupled volumetric-isochoric have been given in equations (4.1)-(4.4) of Section 4.1. Here, these equations describe a class of weakly compressible polymers where the bulk response is assumed to be elastic and damage effects are exclusively restricted to the isochoric part of the deformation. Following conceptually the works GOVINDJEE & SIMÓ [72, 74], we further decompose the isochoric free energy into a *crosslink-to-crosslink* and a *particle-to-particle response*

$$\bar{\Psi} = \bar{\Psi}^{cc}(\mathbf{g}; \bar{\mathbf{F}}) + \bar{\Psi}^{pp}(\mathbf{g}, \mathcal{I}; \bar{\mathbf{F}}) \quad (5.1)$$

associated with the CC and PP networks schematically depicted in Figure 5.1. The Mullins-type damage phenomenon is exclusively embedded into the particle-to-particle contribution. It includes the softening phenomena due to the breakdown of bonds between particles, which is phenomenologically described by a set \mathcal{I} of internal variables specified below. The above decomposition induces a split of the stresses $\bar{\boldsymbol{\tau}}$ defined in (4.4)₃

$$\bar{\boldsymbol{\tau}} = \bar{\boldsymbol{\tau}}^{cc} + \bar{\boldsymbol{\tau}}^{pp} \quad \text{with} \quad \bar{\boldsymbol{\tau}}^{cc} := 2\partial_{\mathbf{g}}\bar{\Psi}^{cc}(\mathbf{g}; \bar{\mathbf{F}}) \quad \text{and} \quad \bar{\boldsymbol{\tau}}^{pp} := 2\partial_{\mathbf{g}}\bar{\Psi}^{pp}(\mathbf{g}, \mathcal{I}; \bar{\mathbf{F}}) \quad (5.2)$$

into crosslink-to-crosslink and particle-to-particle response contributions. The PP network part $\bar{\boldsymbol{\tau}}^{pp}$ provides a *deformation-induced anisotropy* that is described by the evolution of the damage variables \mathcal{I} in time. This evolution must be consistent with the second axiom of thermodynamics that demands a positive macroscopic dissipation

$$\mathcal{D}_{mac} := \mathcal{F} \cdot \dot{\mathcal{I}} \geq 0 \quad \text{with} \quad \mathcal{F} := -\partial_{\mathcal{I}}\bar{\Psi}^{pp}(\mathbf{g}, \mathcal{I}; \bar{\mathbf{F}}) \quad (5.3)$$

with respect to unit volume of the reference configuration. A typical constitutive evolution system is provided by the initial-value problem

$$\mathbf{0} \in \partial_{\mathcal{I}}\bar{\Psi}^{pp}(\mathbf{g}, \mathcal{I}; \bar{\mathbf{F}}) + \partial_{\mathcal{I}}\bar{\Phi}^{pp}(\dot{\mathcal{I}}, \mathcal{I}) \quad \text{with} \quad \mathcal{I}(0) = \mathcal{I}_0 \quad (5.4)$$

in terms of a macroscopic dissipation function $\bar{\Phi}^{pp}$ that depends on the internal state \mathcal{I} and its evolution $\dot{\mathcal{I}}$. Assuming $\bar{\Phi}^{pp}$ to be convex with $\bar{\Phi}^{pp}(\mathbf{0}, \mathcal{I}) = 0$, we observe that (5.3) is automatically satisfied. The Mullins-type damage phenomenon in filled polymers is idealized to be a *rate-independent dissipative effect*. As a consequence, the macroscopic dissipation function is positively homogeneous of degree one $\bar{\Phi}^{pp}(\alpha\dot{\mathcal{I}}, \mathcal{I}) = \alpha\bar{\Phi}^{pp}(\dot{\mathcal{I}}, \mathcal{I})$ for $\alpha > 0$, enforcing $\bar{\Phi}^{pp}$ to be non-smooth at $\dot{\mathcal{I}} = \mathbf{0}$. Then the derivative $\partial_{\dot{\mathcal{I}}}\bar{\Phi}^{pp}$ in (5.4) is understood to be a set-like sub-gradient of $\bar{\Phi}^{pp}$. Equation (5.4) generalizes Biot's equation of smooth dissipative systems in BIOT [18] to non-smooth applications. For further details we refer to the recent work MIEHE, SCHOTTE & LAMBRECHT [152] on standard dissipative materials. Observe that the macroscopic constitutive model of isochoric elasticity with damage is governed by the three constitutive functions $\bar{\Psi}^{cc}$, $\bar{\Psi}^{pp}$ and $\bar{\Phi}^{pp}$ for the crosslink-to-crosslink free energy, the particle-to-particle free energy and the damage dissipation potential, respectively. In the subsequent part of this paper we construct these functions based on a distinct micro-macro transition.

5.2. Micromechanics of Chains in a Constrained Environment

In this section we briefly reiterate the micromechanical elasticity formulation for single polymer chains outlined in Section 3.2 and extend it towards damage effects. The key aspect of the micro-sphere model of elasticity outlined in Chapter 3 was the introduction of *two micro-kinematic variables* associated with a single polymer chain. The first micro-kinematic variable measures the *stretch* λ of a single chain $\lambda := r/r_0$ with $\lambda \in [0, \sqrt{N}]$, defined in terms of the current end-to-end distance r of the chain. The second micro-kinematic variable measures a *tube contraction* in form of the area deformation $\nu := (d_0/d)^2$ with $\nu \in (0, \infty)$, defined in terms of a tube diameter d that is assumed to be constant along the tube that contains the chain.

5.2.1. Free Energy of the Crosslink-to-Crosslink Response. The free energy of the CC network is assumed to be split into a part due to the free chain motion and a part due to the tube constraint

$$\psi^{cc} = \psi_f^{cc}(\lambda) + \psi_c^{cc}(\nu). \quad (5.5)$$

Here, the first unconstrained part is governed by the classical non-Gaussian model introduced by KUHN & GRÜN [114]

$$\psi_f^{cc}(\lambda) = N^{cc}k\theta\chi(\lambda) \quad \text{with} \quad \chi(\lambda) = \lambda_r^{cc}\mathcal{L}^{-1}(\lambda_r^{cc}) + \ln \frac{\mathcal{L}^{-1}(\lambda_r^{cc})}{\sinh \mathcal{L}^{-1}(\lambda_r^{cc})} \quad (5.6)$$

in terms of the relative stretch $\lambda_r^{cc} := \lambda/\sqrt{N^{cc}}$, where N^{cc} is the number of chain segments of the prototype chain in the CC network. In (5.6), $\mathcal{L}^{-1}(\lambda_r^{cc})$ denotes the inverse Langevin function defined by $\mathcal{L}(\lambda_r^{cc}) := \coth(\lambda_r^{cc}) - 1/\lambda_r^{cc}$. Henceforth, we call χ a *normalized free energy function*. The second contribution is based on a probability of a straight tube constraint outlined in DOI & EDWARDS [45], yielding the expression

$$\psi_c^{cc}(\nu) = \alpha k\theta N^{cc} \left(\frac{l}{d_0}\right)^2 \nu \quad (5.7)$$

in terms of the tube stretch ν defined in (3.11). Further details of the assumed CC network response are outlined in Section 3.2.

5.2.2. Free Energy and Dissipation of the Particle-to-Particle Response.

The micromechanical mechanism of the particle-to-particle response is considered to stem from the breakdown of bonds between particles and chains as outlined in BUECHE [31] and DANNENBERG [39]. This idea have been extensively exploited in GOVINDJEE & SIMÓ [72, 74] where they derived in their latter work the so-called *normalized stress function* for the description of the Mullins effect. As expressed in equation (5.20) below, this function represents the ratio of the stress in the damaged network to the stress in the undamaged network and serves as the key constitutive equation of the particle-to-particle response. We here conceptually apply notions of the macroscopic formulation of GOVINDJEE & SIMÓ [74] to the micromechanical response of a chain in a typical space orientation. In order to keep the formulation as compact as possible, we restrict the damage response to an unconstrained formulation of a chain in the PP network. The additional micro-contribution to the free energy is assumed to be of the form

$$\psi^{pp} = \psi^{pp}(\varphi(\lambda), \zeta) \quad \text{with} \quad \varphi(\lambda) = \lambda_r^{pp} \mathcal{L}^{-1}(\lambda_r^{pp}) + \ln \frac{\mathcal{L}^{-1}(\lambda_r^{pp})}{\sinh \mathcal{L}^{-1}(\lambda_r^{pp})} \quad (5.8)$$

dual to (5.6) in terms of a relative stretch $\lambda_r^{pp} := \lambda/\sqrt{N^{pp}}$, where N^{pp} is the number of chain segments of the prototype chain in the PP network. It is a function of the stretch λ defined in (3.10) and a scalar internal variable ζ that describes the state of damage. The dependence of the particle-to-particle free energy on λ is assumed to enter the function through the above defined normalized energy function φ . We assume the concrete phenomenological form

$$\psi^{pp}(\varphi(\lambda), \zeta) = k\theta N^{pp} \int_0^{\varphi(\lambda)} \xi(\tilde{\varphi}, \zeta) d\tilde{\varphi} + \psi_\zeta^{pp}(\zeta). \quad (5.9)$$

Here, $\psi_\zeta^{pp}(\zeta)$ is a non-specified function that depends exclusively on the damage variable ζ . The key constitutive function is the *normalized stress function* ξ , see also equation (5.20) below, that depends on the normalized energy φ and the internal damage variable ζ . At frozen damage variable ζ , this function essentially governs the unloading-reloading paths of the damaged material in a typical space orientation. We assume the quadratic dependence

$$\xi(\varphi, \zeta) = c_1(\zeta)[\varphi - c_2(\zeta)]^2 + c_3(\zeta) \quad (5.10)$$

on the normalized free energy φ . The change in the function with respect to accumulated damage is described by the three functions

$$c_a(\zeta) := k_a \exp[(-1)^a \vartheta_a \zeta] \quad \text{for} \quad a = 1, 2, 3 \quad (5.11)$$

in terms of the six material parameters $\{k_a, \vartheta_a\}$ for $a = 1, 2, 3$. These functions are similar to those proposed by GOVINDJEE & SIMÓ [74], see Figure 5.2 for visualization.

With the above explicit form of the particle-to-particle free energy at hand, we compute by standard arguments the micro-dissipation

$$\mathcal{D}_{mic} := f \dot{\zeta} \geq 0 \quad \text{with} \quad f(\varphi, \zeta) := -\partial_\zeta \psi^{pp}(\varphi(\lambda), \zeta). \quad (5.12)$$

Here, f is the internal force that drives the damage evolution. In order to specify the evolution $\dot{\zeta}$ of the damage, we assume a *micro-dissipation-function*

$$\phi^{pp} = \phi^{pp}(\dot{\zeta}, \zeta) \quad (5.13)$$

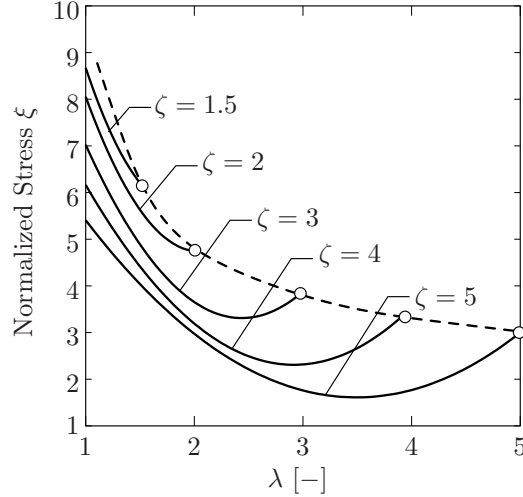


Figure 5.2: Schematic description of the normalized stress function $\xi(\lambda, \zeta) = c_1(\zeta)[\lambda - c_2(\zeta)]^2 + c_3(\zeta)$. For a continuously damaging material, the function ξ decreases monotonously with increasing λ value as depicted by the dashed line. In this case ζ is equal to λ . The solid iso-damage lines corresponding to different constant values of ζ have a parabolic form. The abscissa of minimum points of these iso-damage surfaces are gives by the values of $c_2(\zeta)$. Similarly, the ordinates of these minima are $c_3(\zeta)$ for a given value of ζ .

depending on the state ζ of damage and its rate $\dot{\zeta}$. We assume the concrete form

$$\phi^{pp}(\dot{\zeta}, \zeta) = \begin{cases} f(\zeta, \zeta)\dot{\zeta} & \text{for } \dot{\zeta} > 0, \\ \infty & \text{otherwise} \end{cases} \quad (5.14)$$

which is non-smooth and positively homogeneous of degree-one with respect to $\dot{\zeta}$. Having this function defined, the evolution of damage is assumed to be governed by the equation

$$0 \in \partial_{\zeta} \psi^{pp}(\varphi(\lambda), \zeta) + \partial_{\dot{\zeta}} \phi^{pp}(\dot{\zeta}, \zeta) \quad \text{with} \quad \zeta(0) = 0. \quad (5.15)$$

Observe that this equation provides the counterpart to the macroscopic equation (5.4) on the level of chain orientations. With the definition (5.11), note that (5.15) gives the set-like equation

$$f(\varphi, \zeta) \in \begin{cases} f(\zeta, \zeta) & \text{for } \dot{\zeta} > 0, \\ (-\infty, f(\zeta, \zeta)) & \text{otherwise} \end{cases} \quad (5.16)$$

for the internal forces. Thus the damage evolution $\dot{\zeta} > 0$ occurs only in the case when the micro-force reaches the current maximum value $f(\zeta, \zeta)$; that is, as the normalized free energy φ reaches the current damage state ζ . As a consequence, the evolution of the damage can be written in the simple form

$$\dot{\zeta} = \begin{cases} \dot{\varphi} & \text{for } \varphi = \varphi(\zeta) \text{ and } \dot{\varphi} > 0, \\ 0 & \text{otherwise.} \end{cases} \quad (5.17)$$

Hence, the internal damage state ζ represents the maximum normalized free energy of the PP network that was obtained in the history of deformation. Owing to $\dot{\zeta} \geq 0$ from the specific evolution system (5.17), the dissipation inequality (5.12) is satisfied for *positive internal forces*

$$f(\zeta, \zeta) = -\partial_{\zeta} \psi^{pp}(\varphi, \zeta)|_{\varphi=\zeta} \geq 0. \quad (5.18)$$

Then the dissipation function ϕ^{pp} defined in (5.14) is convex. It can easily be shown that this condition is satisfied for positive material parameters $k_a > 0$ and $\vartheta_a > 0$ of the normalized stress function ξ in (5.10) and a suitable choice of the function ψ_ζ^{pp} in (5.9). Hence, the constitutive model of damage evolution associated with a chain-orientation outlined above is thermodynamically admissible. The above system of constitutive equations governs the particle-to-particle response for a typical space orientation of a prototype chain in terms of the eight material parameters as summarized in Table 5.1.

Table 5.1: Parameters of the Micro-Sphere Damage Model for Filled Rubbers

Set	Parameter	Name	Eq.	Effect
CC	$\mu^{cc} := n^{cc}k\theta$	shear modulus	(3.19)	CC network stiffness
	N^{cc}	segments in CC chain	(3.19)	CC chain locking response
	p	non-affine parameter	(3.46)	3D locking characteristics
	$U := \alpha(l/d_0)^2$	tube geometry parameter	(3.23)	additional CC constraint stiffness
	q	non-affine tube parameter	(3.56)	shape of constraint stress
PP	$\mu^{pp} := n^{pp}k\theta$	shear modulus	(5.9)	PP network stiffness
	N^{pp}	segments in PP chain	(5.9)	PP chain locking response
	$\{k_a\}_{a=1,2,3}$	damage evolution	(5.10)	hysteresis response
	$\{\vartheta_a\}_{a=1,2,3}$	damage evolution	(5.10)	hysteresis response

5.2.3. Algorithmic Representation of the PP Micro-Stresses. In the algorithmic setting of the damage model one considers an incremental formulation at discrete steps $\Delta t := t_{n+1} - t_n$ within a typical time interval $[t_n, t_{n+1}]$. The damage variable ζ_n at time t_n is given and in what follows indicated by the subscript n . The update of the damage variable is then obtained from an algorithm that integrates the evolution equation (5.17) in the time interval. We use the update

$$\zeta = \text{Max}[\varphi(\lambda), \zeta_n] \quad (5.19)$$

which provides a simple closed-form expression in terms of the current stretch λ . All variables without subscript are associated with the current time t_{n+1} . With the updated damage variable at hand, we compute the micro-stress associated with the particle-to-particle mechanism by evaluation of the free energy function (5.9)

$$\beta^{pp} = \partial_\lambda \psi^{pp}(\varphi(\lambda), \zeta) = \xi(\varphi, \zeta) \beta_0^{pp} \quad \text{with} \quad \beta_0^{pp} := k\theta N^{pp} \varphi'(\lambda). \quad (5.20)$$

Here, φ' is proportional to the inverse Langevin function with the singular behavior as the stretch λ approaches the limiting value. In the above equations, the inverse Langevin function can be evaluated by a Padé approximation yielding the approximation $\sqrt{N^{pp}} \varphi'(\lambda) = \mathcal{L}^{-1}(\lambda_r^{pp}) \approx \lambda_r^{pp} (3 - \lambda_r^{pp2}) / (1 - \lambda_r^{pp2})$, see for example COHEN [34]. A further derivative of the micro-stress β^{pp} gives the *algorithmic tangent moduli* consistent with the algorithm (5.19)

$$c^{pp} := \frac{d}{d\lambda} \beta^{pp} = k\theta N^{pp} [\xi \varphi'' + (\xi_{,\varphi} + s_\zeta \xi_{,\zeta}) \varphi'^2], \quad (5.21)$$

where we have introduced per definition the damage-loading flag

$$s_\zeta := \begin{cases} 1 & \text{for } \zeta > \zeta_n, \\ 0 & \text{otherwise.} \end{cases} \quad (5.22)$$

In a typical time step, equations (5.19), (5.20) and (5.21) provide a closed-form update of the stress due to particle-to-particle interaction.

5.3. Anisotropic Network Model of Mullins-Type Damage

Now we develop a homogenization procedure that averages the micro-stresses with respect to the space orientations. To this end, we link the above introduced micro-kinematic variables λ and ν by characteristic network assumptions to suitably defined macro-kinematic variables $\bar{\lambda}$ and $\bar{\nu}$. Following our treatment in Chapter 3, the associated micro-macro transition is interpreted as a *homogenization of state variables on a micro-sphere* with unit radius.

5.3.1. Definition of Macro-Kinematic Variables of the Continuum. The key aspect of network theories is to link the deformation of a single chain to the macroscopic isochoric deformation $\bar{\mathbf{F}}$ defined in (3.4) of the continuum that represents the homogenized network aggregate. Let \mathbf{r} be a Lagrangian orientation unit vector with $|\mathbf{r}|_{\mathbf{G}} := \sqrt{\mathbf{r}_b \cdot \mathbf{r}} = 1$ where $\mathbf{r}_b := \mathbf{G}\mathbf{r}$ is the co-vector of \mathbf{r} . As introduced in (4.30) and (4.31), mappings of \mathbf{r} and \mathbf{r}_b by the isochoric deformation give the isochoric stretch vector and area co-vector

$$\mathbf{t} = \bar{\mathbf{F}}\mathbf{r} \quad \text{and} \quad \mathbf{n}_b = \bar{\mathbf{F}}^{-T}\mathbf{r}_b, \quad (5.23)$$

respectively. Then the macro-stretch of a material line element with orientation \mathbf{r} in the reference configuration and the macro-deformation of a material area element with normal \mathbf{r}_b in the reference configuration are defined as

$$\bar{\lambda} = |\mathbf{t}|_{\mathbf{g}} := \sqrt{\mathbf{t}_b \cdot \mathbf{t}} \quad \text{and} \quad \bar{\nu} = |\mathbf{n}_b|_{\mathbf{g}^{-1}} := \sqrt{\mathbf{n}_b \cdot \mathbf{n}}, \quad (5.24)$$

where $\mathbf{t}_b := \mathbf{g}\mathbf{t}$ and $\mathbf{n} := \mathbf{g}^{-1}\mathbf{n}_b$ evaluated with the current metric \mathbf{g} .

5.3.2. Non-Affine Network Model for Crosslink-to-Crosslink Response. The non-affine network model outlined in Chapter 3 defines the crosslink-to-crosslink part $\bar{\Psi}^{cc}$ of the macroscopic free energy in (5.1) for the polymer aggregate. Clearly, this overall quantity must be related to their micromechanical counterparts ψ^{cc} in (5.5). The additive split of this micro-contribution induces an additive split of the associated macro-contributions

$$\bar{\Psi}^{cc} = \bar{\Psi}_f^{cc}(\mathbf{g}; \bar{\mathbf{F}}) + \bar{\Psi}_c^{cc}(\mathbf{g}; \bar{\mathbf{F}}). \quad (5.25)$$

A key result of the work [149] was the derivation of non-affine relationships between the micro- and macro-kinematic variables

$$\lambda = \langle \bar{\lambda} \rangle_p \quad \text{and} \quad \nu = (\bar{\nu})^q \quad (5.26)$$

in terms of two material parameters p and q of the ground state network. Here, $\langle v \rangle_p := \sqrt[p]{\langle v^p \rangle}$ is the p -root averaging operator of a scalar micro-variable $v > 0$. $\langle v \rangle$ denotes the continuous averaging for an equal orientation distribution of the variable v in space. We define the average of the microscopic free energies for a continuous space distribution via

$$\langle v \rangle := \frac{1}{|\mathcal{S}|} \int_{\mathcal{S}} v(\mathbf{r}; t) dA. \quad (5.27)$$

This averaging is interpreted as a *homogenization* of the state variable $v(\mathbf{r}; t)$ at position \mathbf{r} and time t on a *micro-sphere* \mathcal{S} with unit radius as depicted in Figure 3.4. The macroscopic free energy is obtained by summarizing the micro-energies (5.6) and (5.7) of

the unconstrained and constrained chain motion parts for n^{cc} chains in a representative volume of the CC network, yielding

$$\bar{\Psi}^{cc}(\mathbf{g}; \bar{\mathbf{F}}) = n^{cc} \psi_f^{cc}(\langle \bar{\lambda} \rangle_p) + \langle n^{cc} \psi_c^{cc}((\bar{\nu})^q) \rangle. \quad (5.28)$$

The dependence on \mathbf{g} and $\bar{\mathbf{F}}$ is due to the definitions (5.24). Details of the non-affine model of rubber elasticity and its numerical implementation are outlined in Chapter 3.

5.3.3. Affine Network Model for Particle-to-Particle Response. We now develop a network model which defines the particle-to-particle contribution $\bar{\Psi}^{pp}$ to the macroscopic free energy in (5.1) and the macroscopic dissipation function $\bar{\Phi}^{pp}$ in (5.4) for the polymer aggregate. Clearly, these overall properties must be related to their micromechanical counterparts ψ^{pp} and ϕ^{pp} in (5.6) and (5.13), respectively. In these expressions, the anisotropic macroscopic internal state is described by

$$\mathcal{I} := \{\zeta(\mathbf{r}; t)\} \quad (5.29)$$

in terms of the *field* ζ of damage on the micro-sphere. Here, \mathbf{r} is the spatial variable that parametrizes the field on the micro-sphere as depicted in Figure 3.4. In contrast to the basic network assumption (5.26) for the crosslink-to-crosslink response, we assume for the particle-to-particle response the *affine relationship*

$$\lambda = \bar{\lambda} \quad (5.30)$$

between the micro-stretch and their continuum counterpart. With this relationship at hand, we define the particle-to-particle contribution to the macroscopic energy and dissipation functions by the sum of all orientation contributions

$$\bar{\Psi}^{pp}(\mathbf{g}, \mathcal{I}; \bar{\mathbf{F}}) = \langle n^{pp} \psi^{pp}(\varphi(\bar{\lambda}), \zeta) \rangle \quad \text{and} \quad \bar{\Phi}^{pp}(\dot{\mathcal{I}}, \mathcal{I}) = \langle n^{pp} \phi^{pp}(\dot{\zeta}, \zeta) \rangle, \quad (5.31)$$

where n^{pp} is the number of particle-to-particle chains in the representative volume under consideration. Insertion of the two above functions $\bar{\Psi}^{pp}$ and $\bar{\Phi}^{pp}$ into the macroscopic evolution system (5.4) identifies the microscopic evolution system (5.15) in a pointwise manner at $\mathbf{r} \in \mathcal{S}$ on the microsphere \mathcal{S} . Owing to the convexity of the micro-dissipation function ϕ^{pp} in (5.14), the macro-dissipation function $\bar{\Phi}^{pp}$ is also convex. Thus the overall macroscopic model of damage satisfies the thermodynamic consistency condition (5.3) through the relationship

$$\mathcal{D}_{mac} = \langle n^{pp} \mathcal{D}_{mic} \rangle \geq 0 \quad (5.32)$$

to the positive micro-dissipation (5.12).

With the macro-energy at hand, we compute the Eulerian stresses based on a straightforward exploitation of (5.2)₃. To this end, at first we compute the derivatives of the macro-stretch in (5.24) with respect to the Eulerian metric, yielding $2\partial_{\mathbf{g}} \bar{\lambda} = \bar{\lambda}^{-1} \mathbf{t} \otimes \mathbf{t}$. Then we obtain from (5.31) the representation of the macroscopic Kirchhoff stresses

$$\bar{\boldsymbol{\tau}}_{algo}^{pp} = \langle n^{pp} \beta^{pp} \bar{\lambda}^{-1} \mathbf{t} \otimes \mathbf{t} \rangle \quad (5.33)$$

in terms of the micro-stress β^{pp} defined in (5.20). Note that this representation includes the update algorithm (5.19) of the damage variable. A further derivation of the above

stress expression with respect to the Eulerian metric yields the spatial algorithmic tangent moduli consistent with the update algorithm

$$\bar{\mathbb{C}}_{algo}^{pp} := 2\partial_{\mathbf{g}}\bar{\boldsymbol{\tau}}_{algo}^{pp}(\mathbf{g}, \mathcal{I}, \bar{\mathbf{F}}; \mathcal{I}_n). \quad (5.34)$$

Using the result $2\partial_{\mathbf{g}}(\mathbf{t} \otimes \mathbf{t}) = 0$, we obtain the closed-form representation

$$\bar{\mathbb{C}}_{algo}^{pp} = \langle n^{pp}(c^{pp} - \beta^{pp}\bar{\lambda}^{-1})\bar{\lambda}^{-2}\mathbf{t} \otimes \mathbf{t} \otimes \mathbf{t} \otimes \mathbf{t} \rangle \quad (5.35)$$

with the algorithmic micro-contributions defined in (5.20) and (5.21).

5.3.4. Discretization of Fields on the Micro-Sphere. The implementation of the Mullins-type damage network model outlined above into computer codes requires a numerical evaluation of the integral over the continuous space orientations. As outlined in Chapter 3, this is achieved by discretizing the continuous orientation distribution of the unit sphere \mathcal{S} by m discrete Lagrangian orientation vectors $\{\mathbf{r}^i\}_{i=1\dots m}$ and weight factors $\{w^i\}_{i=1\dots m}$. Then the continuous averaging (5.27) of a micro-variable v defined on the sphere is transformed into the discrete sum

$$\langle v \rangle \approx \sum_{i=1}^m v^i w^i, \quad (5.36)$$

where $\{v^i\}_{i=1\dots m}$ are the micro-variables on the sphere evaluated at the discrete points \mathbf{r}^i . Suitable sets of orientation vectors $\{\mathbf{r}^i\}_{i=1\dots m}$ and associated weight factors $\{w^i\}_{i=1\dots m}$ are given in BAŽANT & OH [10]. The integration schemes exploit the symmetry of the unit sphere by defining discrete points only for the half-sphere. It has been shown in Chapter 3 that a 21-point integration scheme provides sufficient accuracy for numerical investigations of rubber elasticity. Hence, we use for all subsequent numerical examples the 21-point integration scheme for the half-sphere, see Table 3.2 for further details. Then the discretization of the internal variable fields (5.29) on the micro-sphere yields an effective history storage of 21 scalar variables

$$\mathcal{I}_n = \{\zeta(\mathbf{r}^i; t_n)\}_{i=1\dots m=21} \quad (5.37)$$

for the discrete damage variables at time t_n . All the above outlined continuous average operations in the discrete setting appear as a simple algebraic sum over 21 discrete space orientations. Table 5.2 summarizes the numerical implementation of the anisotropic damage model.

5.4. Representative Numerical Examples

This section is devoted to illustrations that assess the modeling capacity and exhibit the main features of the proposed model. To this end, we consider first simulations of homogeneous benchmark experiments from the literature. Next, additional examples essentially focus on the illustration of softening-induced anisotropy during homogenous uniaxial and simple shear deformations. In addition, we perform an inhomogeneous finite element analysis of a cube subjected to combined longitudinal and lateral deformations. The orientational distributions of the damage at selected Gauss points are shown.

Table 5.2: Stress Update of PP Overstress Response on Micro-Sphere.

1. *Data Base.* Given are history data $\{\zeta_n^i\}_{i=1\dots m}$ of internal damage variables at time t_n at $m = 21$ discrete points on the micro-sphere. Get discrete orientation vectors \mathbf{r}^i and weights w^i from Table 3.2.
2. *Current Micro-Stretches.* Given is the unimodular deformation map $\bar{\mathbf{F}}$ at time t_{n+1} . Compute the $i = 1\dots m$ deformed tangents $\mathbf{t}^i = \bar{\mathbf{F}}\mathbf{r}^i$ and the affine micro-stretches $\bar{\lambda}^i = |\mathbf{t}^i|$.
3. *Current Micro-Stresses and Micro-Moduli.* Update the damage variables $\zeta^i = \text{Max}[\varphi(\bar{\lambda}^i), \zeta_n^i]$. Evaluate the normalized stress function $\xi(\varphi(\bar{\lambda}^i), \zeta^i) = c_1(\zeta^i)[\varphi(\bar{\lambda}^i) - c_2(\zeta^i)]^2 + c_3(\zeta^i)$ with $c_a(\zeta^i) := k_a \exp[(-1)^a \vartheta_a \zeta^i]$. Compute the micro-stresses

$$\beta^{ppi} = \xi(\varphi(\bar{\lambda}^i), \zeta^i) \beta_0^{ppi} \quad \text{with} \quad \beta_0^{ppi} := \mu^{pp} N^{pp} \varphi'(\bar{\lambda}^i)$$

and the consistent micro-moduli with damage loading flag $s_\zeta \in \{0, 1\}$

$$c^{ppi} = \mu^{pp} N^{pp} [\xi(\varphi(\bar{\lambda}^i), \zeta^i) \varphi''(\bar{\lambda}^i) + (\xi_{,\varphi}(\varphi(\bar{\lambda}^i), \zeta^i) + s_\zeta \xi_{,\zeta}(\varphi(\bar{\lambda}^i), \zeta^i)) \varphi'^2(\bar{\lambda}^i)]$$

4. *Current Macro-Stresses and Macro-Moduli.* Get homogenized overstresses

$$\bar{\boldsymbol{\tau}}_{algo}^{pp} = \sum_{i=1}^m [\beta^{ppi} \bar{\lambda}^{i-1} \mathbf{t}^i \otimes \mathbf{t}^i] w^i ,$$

the macroscopic algorithmic tangent moduli

$$\bar{\mathbf{C}}_{algo}^{pp} = \sum_{i=1}^m [(c^{ppi} - \beta^{ppi} \bar{\lambda}^{i-1}) \bar{\lambda}^{i-2} \mathbf{t}^i \otimes \mathbf{t}^i \otimes \mathbf{t}^i \otimes \mathbf{t}^i] w^i$$

and proceed with deviatoric projections as outlined in (4.4) and (3.7).

5.4.1. Numerical Investigations on Homogeneous Tests. The first two examples are concerned with two-cycle uniaxial tensile tests. In these experiments the amplitude of the cycles is increased progressively. One of the earliest set of experimental data illustrating the Mullins-type softening on carbon-black filled rubber was recorded by MULLINS & TOBIN [157], see Figure 5.3a. Although these data were obtained by subtracting the appreciable permanent set from measurements, they were used by many researchers as an experimental benchmark. For this reason, the proposed model is also tested against these data. The quite good agreement between the experiment and the proposed model is depicted in Figure 5.3a. In contrast to the idealized data, it should be noted that the residual deformation, the so-called permanent set, is attained at the zero stress level as is observed by Mullins and Tobin. The amount of permanent set gradually increases with increasing deformation. This is in agreement with the experimental obser-

variations, see for example Figure 1.2a. Apart from the data considered above, we further test our model in a simulation of another set of data of HAF black filled SBR reported by BUECHE [32]. The comparative study in Figure 5.3b illustrates that the proposed model captures these data very well. Fittings of the both experiments in Figure 5.3 indicate that the proposed model is able to trace the experimental behavior satisfactorily. The residual deformation attained at the zero stress level is considered as a natural consequence of anisotropic evolution of the damage internal variables.

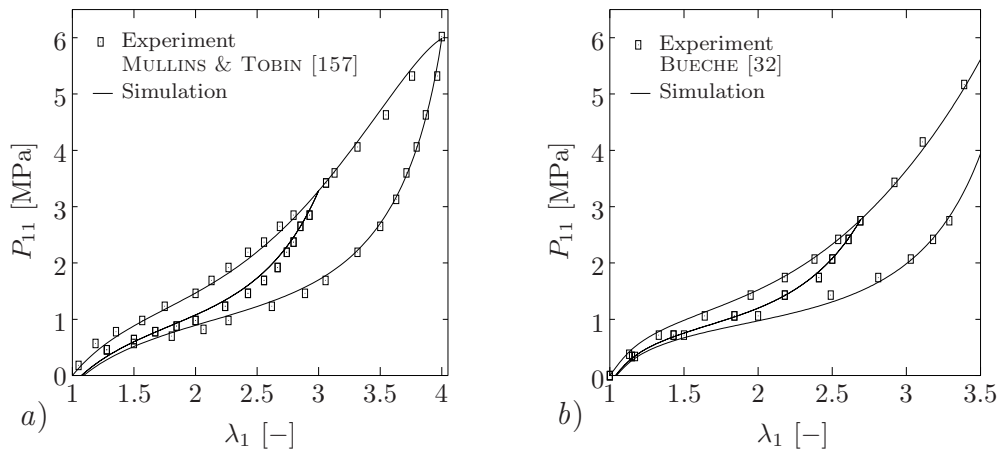


Figure 5.3: Simulations of experimental data. *a)* MULLINS & TOBIN [157] (Fig.4 p.559) data are simulated with the material parameters of the non-affine CC network $\mu^{cc} = 0.41$ MPa, $N^{cc} = 26.5$, $U = 0.53$, $q = 0.1$, $p = 1.7$ and the affine PP network $\mu^{pp} = 1.46$ MPa, $N^{pp} = 18$, $k_a = \{5.1, 0.15, 0.33\}$, $\vartheta_a = \{1.9, 0.8, 2.6\}$. *b)* Simulation of data reported by BUECHE [32] (Fig. 3 p.273) is carried out with the material parameters of the respective network parts $\mu^{cc} = 0.11$ MPa, $N^{cc} = 12.8$, $U = 2.03$, $q = 0.55$, $p = 1.95$, $\mu^{pp} = 1.21$ MPa, $N^{pp} = 14.5$. Owing to the similarities of the hystereses, for the sake of simplicity the same values of k_a 's and ϑ_a 's with the ones used in Figure 5.3a are employed.

The first experimental evidence on the anisotropic nature of the Mullins effect in stretching and swelling experiments was given by MULLINS [155], p.289. He reported the observations on the stress-stretch response of dumbbell-shaped specimens cut from a pre-stretched sheet. These were subjected to post-deformation in the same direction with the previous one and in the direction perpendicular to it. The stress-stretch behavior in the latter case came out to be stiffer than the one having the same direction with pre-extension. Moreover, swelling experiments conducted on these specimens indicated that the amount of swelling is greater in the direction of the pre-stretch. Similar observations were also reported by JAMES & GREEN [99] from their investigations on the tear strength. Reduction in the tear strength in the direction of pre-stretching and increased tear strength in the perpendicular direction were observed.

In order to qualitatively reproduce the experimental observations previously made by MULLINS [155], we carried out a numerical experiment. A virgin specimen is subjected to the two-cycle stretching in the \mathbf{e}_1 direction up to the stretch values $\lambda_1 = 3, 4$, respectively. After unloading to the undeformed state the same material is deformed in an analogous manner in the \mathbf{e}_2 direction up to the stretch values $\lambda_3 = 3, 4$, see the loading function in Figure 5.4a. Corresponding stress-stretch curves are plotted in Figure 5.4b. During the deformation in \mathbf{e}_1 direction the nominal stress response P_{11} softens as observed in the experiments. After changing the deformation direction from \mathbf{e}_1 to \mathbf{e}_2 , the stress response P_{22} of the material to the deformation in direction \mathbf{e}_2 becomes softer than the

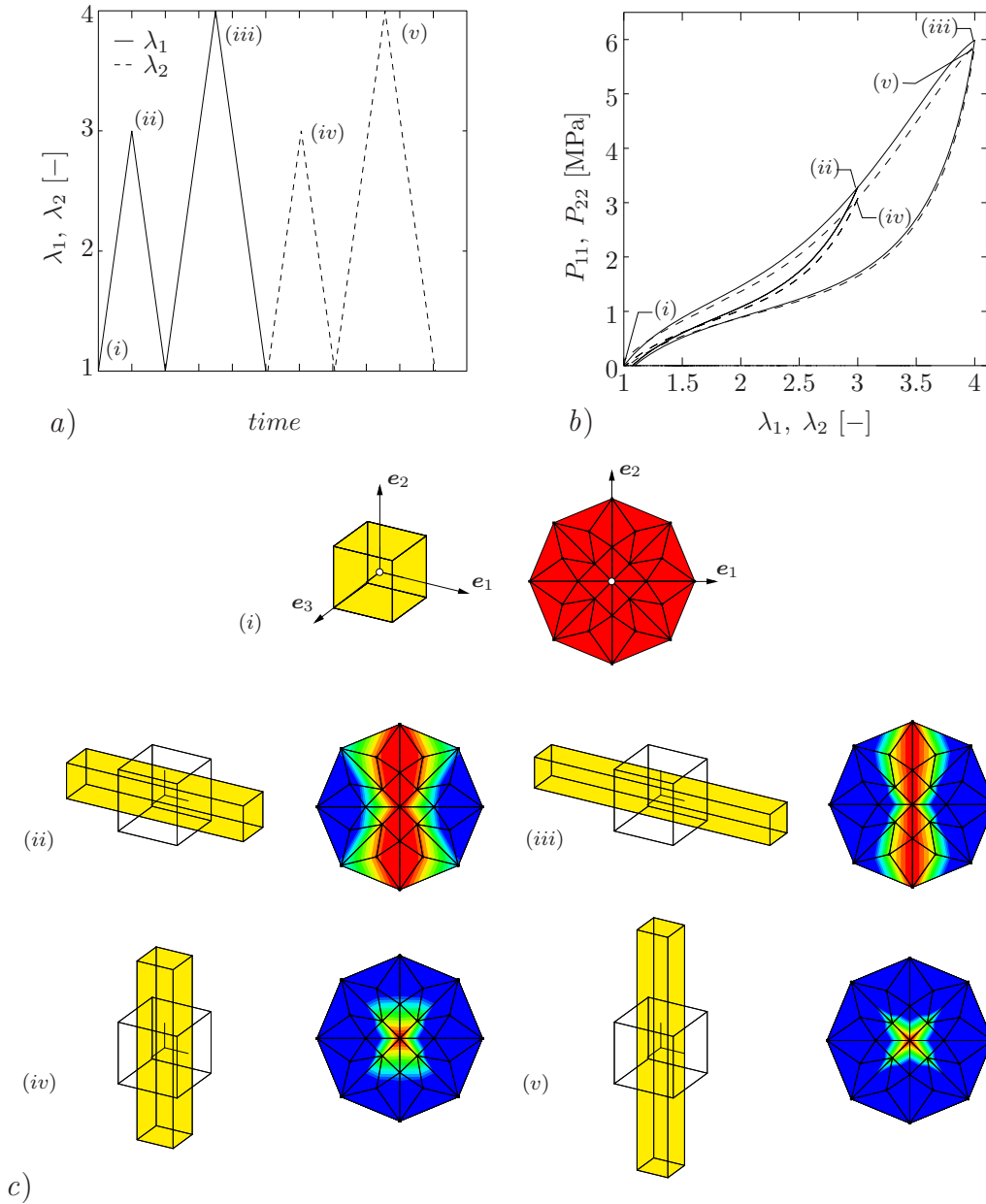


Figure 5.4: Anisotropic evolution of the damage field ζ in the cyclic simple tension test. *a)* The material is cyclicly subjected to stretches $\lambda_1 = 3$ and $\lambda_1 = 4$ and from the totally undeformed state it is further deformed in the same manner in \mathbf{e}_2 direction. *b)* Corresponding stress-stretch curves. *c)* Deformed shapes and the evolution of the damage field ζ corresponding to the loading stages enumerated from (i) to (v).

virgin material but stiffer than its response in \mathbf{e}_1 direction. Furthermore, as can be seen in Figure 5.4b, the amount of permanent set attained at the end of the deformation in the \mathbf{e}_1 direction decreases during stretching in the \mathbf{e}_2 direction. This indicates that deformation in other directions reduces the anisotropic distribution of softening.

In addition to the stress-stretch curves, the deformed shapes of the specimen and the stereographic projection of the damage distribution are depicted in Figure 5.4c for the five stages of deformation labeled as (i) – (v) in Figures 5.4a and 5.4b. The scale of the ζ contours in the stereographic pole projection plots is increasing from the red zone to the blue one. Evolution of the softening during the deformation process supports the

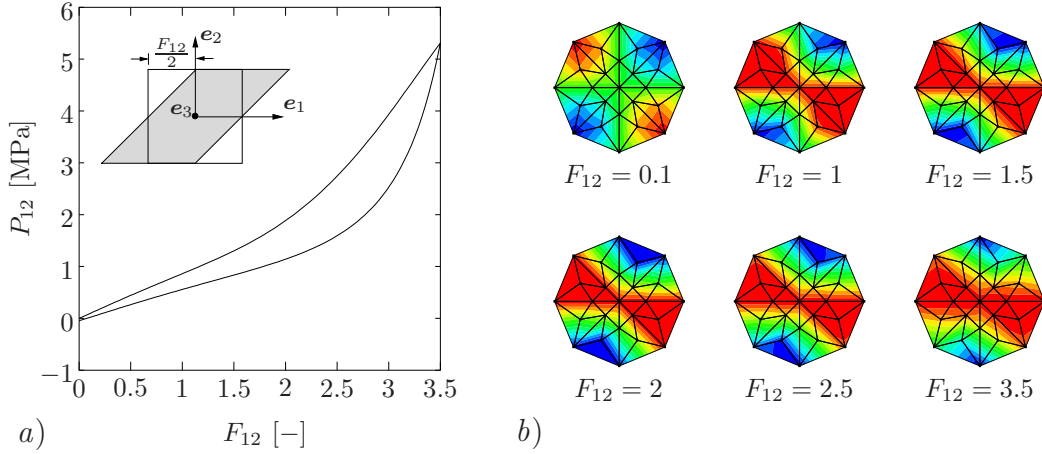


Figure 5.5: Evolution of the damage field ζ in the simple shear test. *a)* One-cycle simple shear deformation between the $F_{12} = [0, 3.5]$. Shear stress vs. shear deformation behavior is presented. *b)* ζ contours are illustrated at six stages of the loading path in the stereographic pole figures. At each level of the deformation, the amount of damage at blue and red zones corresponds to the maximum and the minimum values of the associated deformation level. In this illustration the material parameters given in Figure 5.3b are used.

above idea of reduction in the induced-anisotropy, and consequently in the permanent set, through the successive deformation in the perpendicular direction. In this study the material parameters are taken to be the same as the ones used in Figure 5.3a.

The last homogeneous deformation example illustrates the evolution of deformation-induced anisotropy in a simple shear test. Cyclic shear deformation is defined by assigning the values for the component of deformation gradient $F_{12} = [0, 3.5]$. A schematic picture of the deformation mode and the stress-deformation curve are shown in Figure 5.5a. The evolution of the softening at the different loading stages $F_{12} = 0.1, 1, 1.5, 2, 2.5, 3.5$ is plotted in the pole projections in Figure 5.5b. A rotation of the maximum damage direction in the counterclockwise direction during the deformation is observed.

5.4.2. A Cube Subjected to Combined Tension and Shear. Additional to the above homogeneous problems, in what follows we investigate an inhomogeneous boundary value problem of a cube subjected to combined tension and shear. The benchmark is taken from GOVINDJEE & SIMÓ [74]. A cube of 10 mm edge is simultaneously subjected to the combined deformation in longitudinal \mathbf{e}_1 and lateral direction \mathbf{e}_2 , see Figure 5.6a. The finite element model exploits symmetry properties of the structure. Therefore, only one half of it is discretized. The analysis domain is meshed into 10, 10 and 5 equal parts in the directions $\mathbf{e}_1, \mathbf{e}_2$ and \mathbf{e}_3 , respectively. Consequently, in the analysis 500 eight-node Q1P0 brick elements are employed. The bottom face of the specimen is fixed in all three directions. The degrees of freedom on its top surface in \mathbf{e}_1 and \mathbf{e}_2 directions are prescribed and the deformation in \mathbf{e}_3 direction is restrained, see Figure 5.6a. In both directions \mathbf{e}_1 and \mathbf{e}_2 maximum deformation values $u_1 = u_2 = 10$ mm are attained. The material parameters given in Figure 5.3b are used.

At two stages of deformation $u_1 = u_2 = 5$ mm and $u_1 = u_2 = 10$ mm, averaged damage contours $\langle \zeta \rangle := \sum_{i=1}^m \zeta_i w_i$ on the deformed shapes and the orientational distribution of damage ζ on pole figures at selected material points on a symmetry face are depicted in Figures 5.6b and 5.6c, respectively. The contour plots of the averaged softening and pole figures show that the softening concentrates on the diagonal yielding an asymmetric soft-

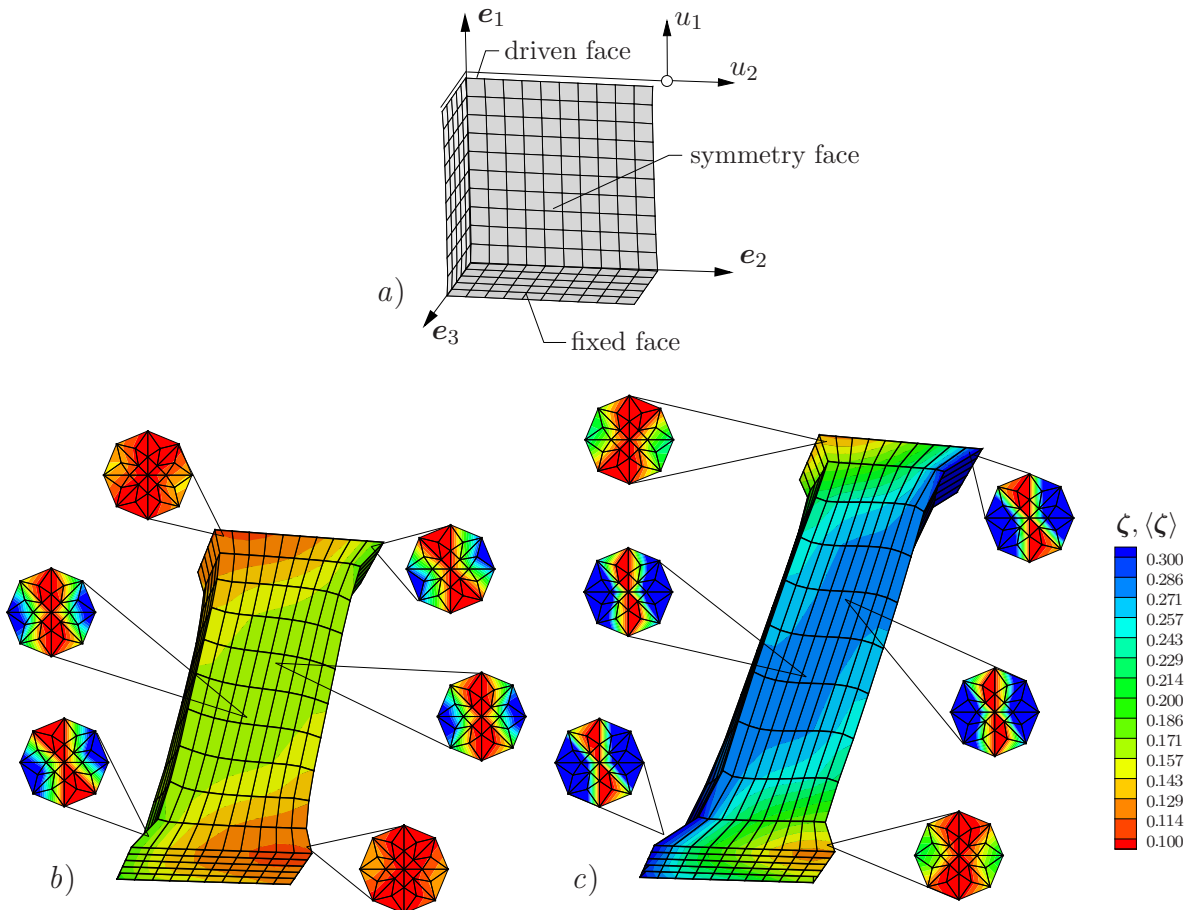


Figure 5.6: Finite element analysis of a cube subjected to combined longitudinal and lateral deformations. *a)* Geometry, boundary conditions and finite element discretization of the cube used in the FE analysis. Distribution of an equivalent damage $\langle \zeta \rangle$ over the body at the two levels of deformation, *b)* $u_1 = u_2 = 5$ mm and *c)* $u_1 = u_2 = 10$ mm, respectively. The pole figures illustrate the anisotropic distribution of damage at different Gauss points for both stages of deformation.²¹

ening distribution. Furthermore, the pole figures illustrate the orientation of anisotropic damage at several material points for different stages of deformation.

6. Finite Viscoplasticity of Amorphous Glassy Polymers

The primary focus of this chapter is laid on the modeling of rate-dependent finite elastoplastic behavior of ductile amorphous glassy polymers under isothermal conditions, at temperatures well below the glass transition temperature θ_g . The characteristics of the intrinsic material behavior and the fundamental micromechanical and macroscopic constitutive approaches suggested in the literature have been discussed in Section 1.1.2. In contrast to the kinematic approaches to the finite elastoplasticity of amorphous polymers put forward so far, we adopt the kinematical framework of finite elasto-plasticity recently proposed by MIEHE, APEL & LAMBRECHT [147]. This framework makes use of the ideas of the so-called *additive metric plasticity* akin to the geometrically linear theory of elastoplasticity. The constitutive framework is constructed in the *logarithmic strain space* where the elastic part $\boldsymbol{\varepsilon}^e$ of the Lagrangian Hencky strain $\boldsymbol{\varepsilon} := \ln[\mathbf{C}]/2$ is defined as $\boldsymbol{\varepsilon}^e := \boldsymbol{\varepsilon} - \ln[\mathbf{G}^p]/2 = \boldsymbol{\varepsilon} - \boldsymbol{\varepsilon}^p$ where \mathbf{C} denotes the right Cauchy-Green tensor defined in (2.21) and \mathbf{G}^p is the reference plastic metric. This additive form allows us to formulate finite plasticity in a framework analogous to the geometrically linear theory which in turn leads to a very attractive algorithmic setting. Within this framework the evolution of viscoplastic strains $\boldsymbol{\varepsilon}^p$ is adopted from the celebrated *double kink* model of ARGON [5]. As conventionally accepted in the literature, the kinematical hardening mechanism due to the plastic alignment of the chains may be modeled by network models of rubber elasticity, such as the *eight-chain model* of ARRUDA & BOYCE [8] and our *non-affine micro-sphere model* outlined in the foregoing chapters. The modeling capacity of the proposed approach is assessed by comparing the simulation results with experimental data. For this purpose, we consider macroscopically homogeneous uniaxial and plane strain compression experiments on PC specimens under isothermal conditions. These data are used to identify the limited material parameters. The performance of the model with the identified material parameters is tested in the three-dimensional finite element simulation of the cold drawing experiment described in Figures 1.3 and 1.4. The simulation is not limited only to the load-displacement diagram but also the three-dimensional strain fields are considered. Comparison of the simulations with the experimental results indicate the quantitative modeling capability of the proposed approach. This chapter is organized as follows. Section 6.1 briefly outlines the additive kinematic approach to finite inelasticity in the logarithmic strain space and points out the model-independent modular algorithmic structure. Section 6.2 is devoted to the elasto-viscoplastic constitutive model in the logarithmic strain space and the details of its algorithmic implementation. In Section 6.3, the representative numerical examples illustrating the modeling capabilities of the proposed approach in comparison with the experimental results obtained from the homogenous and non-homogeneous tests are presented.

6.1. Additive Finite Plasticity in the Logarithmic Strain Space

Despite the intensive work carried out over the last four decades, the development of a canonical kinematic framework for finite elastoplasticity is still a topic of active research. An exhaustive review of the existing literature on kinematics of finite plasticity is not aimed here but only a few key references will be addressed. For a comprehensive review, the reader is referred to the critical state-of-art manuscripts by NAGHDI [159] and XIAO, BRUHNS & MEYERS [209], among others. Apart from the rate formulations (hypoelasticity), the kinematical approaches to finite plasticity may roughly be classified

into two main categories: *i*) The formulations based on the multiplicative decomposition of the deformation gradient into the elastic and inelastic parts, i.e. $\mathbf{F} = \mathbf{F}^e \mathbf{F}^p$. *ii*) The framework constructed on the notion of an additional primitive Lagrangean plastic strain \mathbf{E}^p . The *former* has been motivated from the micromechanical plasticity theory of crystalline materials and applied also to the phenomenological framework of plasticity. The multiplicative split of the deformation gradient, commonly referred to as *Kröner-Lee decomposition*, can be traced back to the seminal works of KRÖNER [111], LEE [115] and MANDEL [126]. The *latter* is based on the introduction of the Lagrangean plastic deformation measure \mathbf{E}^p as a primitive variable proposed by GREEN & NAGHDI [75]. This framework, the so-called *Green-Naghdi theory*, has been further extended by MIEHE [141, 142] based on the notion of the *evolving reference plastic metric* \mathbf{G}^p . Motivating from the notion of Lagrangean plastic metric, an additive framework for the finite plasticity has been recently proposed within a framework of the logarithmic strain space by MIEHE, APEL & LAMBRECHT [147], PAPADOPOULOS & LU [163, 164], and MIEHE & APEL [146]. In [147], they have compared the results of the additive finite plasticity in the logarithmic strain space with the results obtained from classical multiplicative plasticity for both isotropic and anisotropic materials. This comparative study indicates the closeness of the results obtained by the distinct formulations for a broad range of boundary value problems. The similarity between the formulation of finite plasticity in the logarithmic strain space and the geometrically linear theory of plasticity makes this formulation highly attractive, especially with regard to the algorithmic implementation.

The kinematic setting of almost all of the proposed approaches to the finite viscoplasticity of glassy polymers make use of the Kröner-Lee multiplicative decomposition of the deformation gradient. The immediate outcome of this approach is a stress-free relaxed intermediate configuration which is physically well-justified in the case of crystal plasticity. In the case of non-crystalline materials, however, some additional assumptions for the properties of the elastic part of the deformation gradient [28] or for the plastic spin [4] are required. Being distinct from the former, we here extend the recently proposed alternative additive kinematical approach in the logarithmic strain space by MIEHE, APEL & LAMBRECHT [147] to the finite viscoplasticity of glassy polymers. This framework a priori avoids the difficulties and assumptions associated with the fictitious intermediate configuration and serves as a key advantageous kinematical setting leading to an efficient algorithmic formulation in the six-dimensional symmetric strain space.

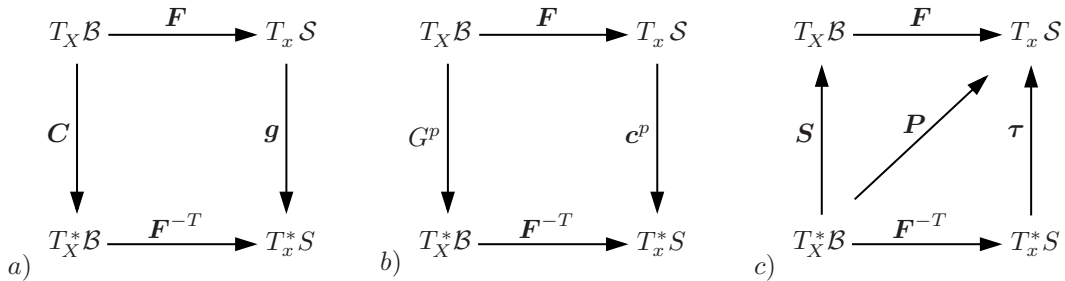


Figure 6.1: Definition of metric and stress tensors as mappings. *a*) *Current metric*: \mathbf{g} , in Lagrangean configuration $\mathbf{C} := \mathbf{F}^T \mathbf{g} \mathbf{F}$. *b*) *Plastic metric*: \mathbf{G}^p , in Eulerian configuration $\mathbf{c}^p := \mathbf{F}^{-T} \mathbf{G}^p \mathbf{F}^T$. *c*) *Nominal stress*: \mathbf{P} , Eulerian Kirchhoff stress $\boldsymbol{\tau} := \mathbf{P} \mathbf{F}^T$, Lagrangean second Piola-Kirchhoff stress $\mathbf{S} := \mathbf{F}^{-1} \mathbf{P}$.

6.1.1. Additive Kinematic Approach Based on Logarithmic Strains. Being consistent with the Kröner-Lee decomposition, a multiplicatively defined objective strain

variable of the form

$$\bar{\boldsymbol{\varepsilon}}_m^e := \mathbf{f}_m(\mathbf{F}^{p-T} \mathbf{C} \mathbf{F}^{p-1}) \quad (6.1)$$

enters an elastic energy storage function of the constitutive model. The convected current metric $\mathbf{C} := \mathbf{F}^T \mathbf{g} \mathbf{F}$ is a function of the deformation \mathbf{F} of the material, see Figure 6.1a. The plastic map \mathbf{F}^p is considered as an internal variable that describes the plastic flow through the crystal by multiple shearing on crystallographic slip planes in crystalline materials. For isotropic as well as anisotropic materials with preferred structural directors which deform with the material it can be shown that the plastic map enters stored energy functions through the metric $\mathbf{G}^p := \mathbf{F}^{pT} \tilde{\mathbf{G}} \mathbf{F}^p$, see Figure 6.1b. This justifies a framework of finite plasticity based on a plastic metric \mathbf{G}^p that is a priori considered as an internal variable. A particular additive dependence of the Lagrangean elastic strain variable on \mathbf{C} and \mathbf{G}^p is provided through

$$\boldsymbol{\varepsilon}_m^e := \mathbf{f}_m(\mathbf{C}) - \mathbf{f}_m(\mathbf{G}^p). \quad (6.2)$$

Here the tensor-valued isotropic tensor function \mathbf{f}_m characterizes the *Seth-Hill family of generalized strain measures* defined by

$$\mathbf{f}_m(\mathbf{A}) = \begin{cases} \frac{1}{m}(\mathbf{A}^{m/2} - \mathbf{1}) & \text{if } m \neq 0 \\ \frac{1}{2} \ln \mathbf{A} & \text{if } m = 0 \end{cases}, \quad (6.3)$$

where all $m \in \mathbb{R}$ and $\mathbf{A} \in \text{Sym}(3)_+$. The specific choices of $m = 0, 1, 2$ defines the Hencky strain, the Biot strain and the Green strain, respectively, in the Lagrangean geometric setting of finite elasticity. For the Green-Lagrangean strains with $m=2$ it is readily observed that the basic invariants of (6.1) coincide with those of (6.2) when the latter invariants are computed with respect to the plastic metric. This already makes clear for an isotropic integrity basis that the use of the Lagrangean elastic strain measure (6.2) is in general consistent with the approach (6.1) only if the energy storage function depends on $\boldsymbol{\varepsilon}_m^e$ and \mathbf{G}^p . However choosing $m = 0$ in (6.1) and (6.2), we observe $\bar{\boldsymbol{\varepsilon}}_0^e = \boldsymbol{\varepsilon}_0^e$ for the special case of co-axial total and plastic deformations where \mathbf{C} and \mathbf{G}^p commute and the plastic map is identified by $\mathbf{F}^p = \mathbf{G}^{p1/2}$. In this case, the logarithmic Lagrangean elastic strain measure defined by

$$\boldsymbol{\varepsilon}^e := \frac{1}{2} \ln \mathbf{C} - \boldsymbol{\varepsilon}^p \quad (6.4)$$

yields the additive split (6.2), which is at least *closer* to multiplicative form (6.1). The logarithmic plastic strain $\boldsymbol{\varepsilon}^p := \frac{1}{2} \ln \mathbf{G}^p$ defined in (6.4) with $\mathbf{G}^p(t_0) = \mathbf{G}$ may be considered as the internal variable that enters the constitutive formulation.

6.1.2. Modular Structure of the Constitutive Equations. The additive decomposition of the total strains into elastic and plastic parts is a typical feature of the geometrically linear theory of plasticity. Thus the form (6.4) provides a natural basis for a material-independent extension of constitutive structures from the geometrically linear theory to the non-linear theory at finite strains. The point of departure for this extension is an a priori six-dimensional approach to finite plasticity based on the notion of a plastic metric. Within this general framework, we consider three modules which define a class of finite plasticity models consistent with (6.4):

- **Geometric pre-processor** defines the total and plastic logarithmic strain measures, which are obtained from the current and plastic metric, respectively.
- **Constitutive model** describes the constitutive equations for elasto-visco-plasticity in the logarithmic strain space in a structure identical to geometrically linear theory.
- **Geometric post-processor** maps the objects obtained in the logarithmic strain space to their nominal, Lagrangean or Eulerian counterparts.

The attractive feature of the above outlined modular structure of finite plasticity is the possibility to adopt known constitutive models of the *infinitesimal theory* as a module in the logarithmic space. We apply this framework to a model of rate-dependent elastoplasticity for modeling of glassy polymers by taking into account the orientation hardening, which can be modeled by the network models of rubber elasticity. Now, we outline the fundamental steps of the Lagrangean geometric approach to finite plasticity with reference to a constitutive module in the logarithmic strain space framed by geometric the pre- and post-processing steps.

Geometric Pre-processing of the Logarithmic Strain Space. A key point in constructing a framework of finite plasticity is the definition of an elastic strain measure $\boldsymbol{\varepsilon}^e$. This measure enters as a variable the constitutive function that describes the macroscopic elastic energy storage. We assume this strain measure to be a function of the above introduced Lagrangean current and plastic metric tensors, i.e.

$$\boldsymbol{\varepsilon}^e = \boldsymbol{\varepsilon}^e(\mathbf{C}, \mathbf{G}^p). \quad (6.5)$$

The elastic strain can be conceptually defined based on the notion of additive form as

$$\boldsymbol{\varepsilon}^e := \boldsymbol{\varepsilon} - \boldsymbol{\varepsilon}^p \quad (6.6)$$

being consistent with (6.4) in terms of the logarithmic Lagrangean total and plastic strains

$$\boldsymbol{\varepsilon} := \frac{1}{2} \ln \mathbf{C} \quad \text{and} \quad \boldsymbol{\varepsilon}^p = \frac{1}{2} \ln \mathbf{G}^p, \quad (6.7)$$

respectively. The logarithmic tensor function \mathbf{f}_0 maps the multiplicative characteristics of large-strain elasto-plasticity to the additive structure of the geometrically linear theory. In particular, we note the relationship

$$J^p := \sqrt{\det[\mathbf{G}^p]} = \exp[\text{tr}[\boldsymbol{\varepsilon}^p]] \quad (6.8)$$

for the plastic Jacobian that governs the change of volume during plastic deformation. Recall that the plastic incompressibility condition demands

$$\det[\mathbf{G}^p] = 1 \quad \iff \quad \text{tr}[\boldsymbol{\varepsilon}^p] = 0. \quad (6.9)$$

Thus, the incompressibility constraint on the plastic metric \mathbf{G}^p in the context of an isochoric plastic flow is described by the additive constraint on the trace of the logarithmic plastic strain $\boldsymbol{\varepsilon}^p$. As already mentioned above, this is the key property that motivates the choice of the logarithmic strain measures (6.7). Owing to the one-to-one relationship between \mathbf{G}^p and $\boldsymbol{\varepsilon}^p$ in (6.7)₂, we may consider the logarithmic plastic strain measure $\boldsymbol{\varepsilon}^p$ as an internal variable alternative to \mathbf{G}^p . The evolution of $\boldsymbol{\varepsilon}^p$ is then exclusively defined in the constitutive box associated with the logarithmic strain space defined below.

Derivation of the transformation tensors of the logarithmic strain space is a purely geometrical operation that is based on the stress power (2.45)

$$\mathcal{P}(t) := \mathbf{g}\mathbf{P}(t) : \dot{\mathbf{F}}(t) \quad (6.10)$$

defined per unit reference volume of the material. The power expression in (6.10) is represented in terms of the non-symmetric nominal stress tensor \mathbf{P} depicted in Figure 6.1c. This tensor is said to be work-conjugate to the rate $\dot{\mathbf{F}}$ of deformation. The non-symmetric tensors $\mathbf{g}\mathbf{P}$ and \mathbf{F} are considered as the work pair of dual external variables of the local elastic-plastic material element. The logarithmic strain measure $\boldsymbol{\varepsilon}$ defined in (6.7)₁ is a function of the current metric \mathbf{C} , which in turn depends also on the deformation \mathbf{F} and the Eulerian standard metric \mathbf{g} due to the pull-back operation on \mathbf{g} illustrated in Figure 6.1a. The key intrinsic feature of the subsequent treatment is the computation of the sensitivity of this strain measure with respect to a change of the deformation. To this end, we introduce the relationships

$$\dot{\boldsymbol{\varepsilon}} = \mathbb{Q} : \dot{\mathbf{F}} \quad \text{and} \quad \dot{\mathbb{Q}} = \mathbb{L} : \dot{\mathbf{F}} \quad (6.11)$$

in terms of the fourth and sixth order nominal transformation tensors defined by

$$\mathbb{Q} := \partial_{\mathbf{F}}\boldsymbol{\varepsilon} \quad \text{and} \quad \mathbb{L} := \partial_{\mathbf{F}\mathbf{F}}^2\boldsymbol{\varepsilon}, \quad (6.12)$$

respectively. These transformation tensors play a central role in the forthcoming treatment. Insertion of the inverse form of (6.11)₁ into (6.10) leads us to an alternative description of the stress power

$$\mathcal{P}(t) := \boldsymbol{\sigma}(t) : \dot{\boldsymbol{\varepsilon}}(t) \quad (6.13)$$

where $\boldsymbol{\sigma} := \mathbf{g}\mathbf{P} : \mathbb{Q}^{-1}$ stands for the Lagrangean stress tensor work-conjugate to the logarithmic strain measure $\boldsymbol{\varepsilon}$. The symmetric Lagrangean tensors $\boldsymbol{\sigma}$ and $\boldsymbol{\varepsilon}$ provide a convenient pair of dual external variables of the local material element associated with the logarithmic strain space. It is worth remarking on that for an isotropic hyperelastic material, the stress tensor $\boldsymbol{\sigma} := \partial_{\boldsymbol{\varepsilon}}W(\boldsymbol{\varepsilon})$ coincides with the so-called *rotated stress tensor* obtained by the pull-back of the Kirchhoff stress tensor $\boldsymbol{\tau}$ with the rotational part \mathbf{R} of the deformation gradient \mathbf{F} , i.e. $\boldsymbol{\sigma} = \mathbf{R}^T\boldsymbol{\tau}\mathbf{R}$. For a different interpretation and a derivation of the rotated stress tensor $\boldsymbol{\sigma}$, the reader is referred to SIMÓ & MARSDEN [184].

Constitutive Model in the Logarithmic Strain Space. Now we consider a constitutive model of rate-dependent elastoplasticity that is exclusively restricted to the logarithmic strain space. This model is considered as a constitutive box, its input is being given by the logarithmic strain measure $\boldsymbol{\varepsilon}$ and a set $\mathcal{I} := \{\boldsymbol{\varepsilon}^p, \dots\}$ of internal variables consisting of the logarithmic plastic strain tensor $\boldsymbol{\varepsilon}^p$ and some additional internal variables. What comes out of the constitutive box is the current stress $\boldsymbol{\sigma}$ dual to the logarithmic strain $\boldsymbol{\varepsilon}$ and the associated algorithmic elastic-plastic tangent moduli \mathbb{E}_{algo}

$$\{\boldsymbol{\varepsilon}, \mathcal{I}\} \implies MODEL \implies \{\boldsymbol{\sigma}, \mathbb{E}_{algo}\}. \quad (6.14)$$

The attractive feature of the constitutive model is that it can preserve the structure of plasticity model of geometrically linear theory and thus the model can adopt standard constitutive structures of the small strain theory. The details of the specific constitutive model for viscoplasticity of glassy polymers are elucidated in Section 6.2.

Geometric Post-processing of Nominal Stresses and Moduli. Once the stresses and consistent tangent moduli in the logarithmic strain space have been obtained from the constitutive model in (6.14), we map them to the nominal stresses and nominal moduli based on the straight forward application of the transformation rules introduced in Section 6.1.2. Taking into account (6.13)₂ and (6.11), we obtain

$$\mathbf{gP} = \boldsymbol{\sigma} : \mathbb{Q} \quad \text{and} \quad \mathbb{A}_{algo} = \mathbb{Q}^T : \mathbb{E}_{algo} : \mathbb{Q} + \boldsymbol{\sigma} : \mathbb{L} \quad (6.15)$$

in terms of the transformation tensors introduced in (6.12) with respect to the rate of deformation. Clearly, the recovery of the plastic metric from the logarithmic strain space is obtained by the exponential map $\mathbf{G}^p = \exp[2\boldsymbol{\varepsilon}^p]$ as an inverse to the logarithmic map (6.7)₂. The equations (6.7), (6.14) and (6.15) represent the three key steps of the modular constitutive structure of finite plasticity in the continuous setting.

Geometric Post-processing of Lagrangean and Eulerian Objects. The symmetric Lagrangean stresses $\mathbf{S} := \mathbf{F}^{-1}\mathbf{P}$ considered in Figure 6.1c and their associated elasto-plastic tangent moduli \mathbb{C}_{algo}^L are obtained analogously to the above derivation of the nominal tensors. We get the representations

$$\mathbf{S} = \boldsymbol{\sigma} : \mathbb{Q}_L \quad \text{and} \quad \mathbb{C}_{algo}^L = \mathbb{Q}_L^{ep} : \mathbb{E}_{algo} : \mathbb{Q}_L + \boldsymbol{\sigma} : \mathbb{L}_L \quad (6.16)$$

in terms of the fourth and sixth order Lagrangean transformation tensors \mathbb{Q}_L and \mathbb{L}_L , respectively. They are defined as the derivatives of the logarithmic strain measure with respect to the convected current metric \mathbf{C} .

$$\mathbb{Q}_L := 2\partial_c \boldsymbol{\varepsilon} \quad \text{and} \quad \mathbb{L}_L := 4\partial_{cc}^2 \boldsymbol{\varepsilon}. \quad (6.17)$$

The Lagrangean consistent tangent moduli \mathbb{C}_{algo}^L govern the sensitivity of the symmetric Piola-Kirchhoff stress with respect to the Lagrangean rate $\dot{\mathbf{C}}$ of deformation by

$$\dot{\mathbf{S}} = \mathbb{C}_{algo}^L : \frac{1}{2}\dot{\mathbf{C}}. \quad (6.18)$$

For the sake of completeness, we also consider the Eulerian Kirchoff stresses $\boldsymbol{\tau} := \mathbf{P}\mathbf{F}^T$ and their associated tangent moduli \mathbb{c}_{algo} . Being analogous to (6.15) and (6.16), we get

$$\boldsymbol{\tau} = \boldsymbol{\sigma} : \mathbb{Q}_E \quad \text{and} \quad \mathbb{c}_{algo}^E = \mathbb{Q}_E^T : \mathbb{E}^{ep} : \mathbb{Q}_E + \boldsymbol{\sigma} : \mathbb{L}_E. \quad (6.19)$$

in terms of the Eulerian transformation tensors \mathbb{Q}_E and \mathbb{L}_E that are defined as derivatives of the logarithmic strain measure with respect to the Eulerian standard metric \mathbf{g} in the form

$$\mathbb{Q}_E := 2\partial_g \boldsymbol{\varepsilon} \quad \text{and} \quad \mathbb{L}_E := 4\partial_{gg}^2 \boldsymbol{\varepsilon}. \quad (6.20)$$

The Eulerian algorithmic tangent \mathbb{c}_{algo}^E governs the objective rate equation for the Lie derivative $\mathcal{L}_v \boldsymbol{\tau} = \mathbf{F}\dot{\mathbf{S}}\mathbf{F}^T$ of the Kirchoff stresses

$$\mathcal{L}_v \boldsymbol{\tau} = \mathbb{c}_{algo}^E : \frac{1}{2}\mathcal{L}_v \mathbf{g}. \quad (6.21)$$

For the explicit forms of the transformation tensors of the stresses and tangent in the logarithmic strain space to their nominal, Lagrangian or Eulerian counterparts we refer to MIEHE & LAMBRECHT [151].

6.2. Constitutive Model for Viscoplasticity of Glassy Polymers

In the preceding section, the modular overall kinematic framework of the proposed model was outlined in the logarithmic strain space. In this section, we first introduce the overall constitutive equations and then specify the constitutive functions in the logarithmic strain space analogous to the geometrically linear theory.

6.2.1. Overall Constitutive Structure. The state of the material a local material point is assumed to be described by the total Hencky strain $\boldsymbol{\varepsilon}$ and the plastic strain $\boldsymbol{\varepsilon}^p$ that have been introduced in (6.7). The selected thermomechanical potential, Helmholtz free energy, is then formulated in terms of the state variables

$$\psi = \hat{\psi}(\boldsymbol{\varepsilon}, \boldsymbol{\varepsilon}^p) = \psi^e(\boldsymbol{\varepsilon} - \boldsymbol{\varepsilon}^p) + \psi^p(\boldsymbol{\varepsilon}^p) \quad (6.22)$$

per unit reference volume. The free energy is additively split into an elastic part and a plastic part. The former represents the stored energy due to the elastic deformations, the latter, on the other hand, describes the transformational energy stored in the plastically deformed regions. This part acts as a potential for *back stresses* that drive essentially thermal recovery from the plastically deformed state to the undeformed state upon an increase in ambient temperature above the glass transition temperature θ_g . The total stresses $\boldsymbol{\sigma}$ and the back stresses $\boldsymbol{\beta}$ are then determined directly from the free energy by following the celebrated methodology in COLEMAN & GURTIN [35],

$$\boldsymbol{\sigma} := \partial_{\boldsymbol{\varepsilon}} \psi(\boldsymbol{\varepsilon} - \boldsymbol{\varepsilon}^p) \quad \text{and} \quad \boldsymbol{\beta} := \partial_{\boldsymbol{\varepsilon}^p} \psi^p(\boldsymbol{\varepsilon}^p) \quad (6.23)$$

respectively. With these definitions at hand, we can now express the local dissipation per unit reference volume in the form

$$\mathcal{D} := \boldsymbol{\sigma}^* : \dot{\boldsymbol{\varepsilon}}^p \geq 0 \quad (6.24)$$

where $\boldsymbol{\sigma}^* := -\partial_{\boldsymbol{\varepsilon}^p} \psi = \boldsymbol{\sigma} - \boldsymbol{\beta}$ denotes the thermodynamic driving stress tensor conjugate to the plastic strains $\boldsymbol{\varepsilon}^p$. In order to complete the overall constitutive framework what remains to be defined is the evolution rule for the plastic strains $\boldsymbol{\varepsilon}^p$. To this end, we consider the following viscoplastic flow rule

$$\dot{\boldsymbol{\varepsilon}}^p := \dot{\gamma}^p \frac{\text{dev}[\boldsymbol{\sigma}^*]}{\|\text{dev}[\boldsymbol{\sigma}^*]\|} \quad (6.25)$$

where $\dot{\gamma}^p \geq 0$ and $\text{dev}[\boldsymbol{\sigma}^*] := \boldsymbol{\sigma}^* - \frac{1}{3} \text{tr}[\boldsymbol{\sigma}^*] \mathbf{1}$ with $\text{tr}[\boldsymbol{\bullet}] := (\boldsymbol{\bullet}) : \mathbf{1}$. Notice that for the initial value of the plastic strain tensor $\boldsymbol{\varepsilon}^p(t_0) = \mathbf{0}$, the plastic deformation remains volume conserving, i.e. $\text{tr}[\boldsymbol{\varepsilon}^p(t)] = \mathbf{0}$. This is in accordance with the finite viscoplastic behavior of ductile glassy polymers that undergo plastic deformations chiefly through *shear yielding* without exhibiting dilative plastic flow, such as *crazing*. The only restriction dictated by the second law of thermodynamics (6.24) on the model is the positiveness of the amount of plastic strain rate $\dot{\gamma}^p$. That is, the model is said to be thermodynamically consistent if the viscoplastic evolution rule fulfills the condition $\dot{\gamma}^p \geq 0$. As will be shown in the subsequent part, this requirement is satisfied identically due to the exponential form of the Arrhenius-type flow rule.

6.2.2. Specific Forms of the Constitutive Equations. The above outlined model of viscoplasticity is basically governed by the three constitutive functions: The elastic $\hat{\psi}^e(\boldsymbol{\varepsilon} - \boldsymbol{\varepsilon}^p)$ and the plastic $\hat{\psi}^p(\boldsymbol{\varepsilon}^p)$ parts of the free energy, and the viscoplastic flow rule $\dot{\gamma}^p$. In this section, the specific forms of these constitutive functions shall be introduced.

The Elastic Free Energy. As discussed in Section 1.1.2, the experimental observations presented in Figures 1.3 and 6.4 as well as in the literature indicate that the deformation in the pre-yield branch is limited to small values compared to large plastic strains attained. In spite of the viscoelastic effects leading to a non-linearity prior to the macroscopic yield, we left them off the present formulation. For this reason, linear elasticity in the logarithmic strain space is considered to be sufficient for the current scope. To this end, we choose a quadratic form for the elastic free energy in terms of elastic strains $\boldsymbol{\varepsilon}^e := \boldsymbol{\varepsilon} - \boldsymbol{\varepsilon}^p$

$$\psi^e = \hat{\psi}^e(\boldsymbol{\varepsilon} - \boldsymbol{\varepsilon}^p) = \frac{\kappa}{2} \text{tr}^2[\boldsymbol{\varepsilon} - \boldsymbol{\varepsilon}^p] + \mu \text{dev}[\boldsymbol{\varepsilon} - \boldsymbol{\varepsilon}^p] : \text{dev}[\boldsymbol{\varepsilon} - \boldsymbol{\varepsilon}^p] \quad (6.26)$$

where κ and μ are the bulk modulus and the shear modulus, respectively. This particular form of $\hat{\psi}^e$ immediately yields the stress expression through (6.23)₁

$$\boldsymbol{\sigma} := -p\mathbf{1} + 2\mu \text{dev}[\boldsymbol{\varepsilon} - \boldsymbol{\varepsilon}^p] \quad \text{with} \quad p := -\kappa \text{tr}[\boldsymbol{\varepsilon} - \boldsymbol{\varepsilon}^p] . \quad (6.27)$$

It is worth noting that the ellipticity of the elastic free energy $\hat{\psi}^e$ given in (6.26) is restricted to a certain interval of elastic strains $\boldsymbol{\varepsilon}^e$, see e.g. MIEHE & LAMBRECHT [151], BRUHNS, XIAO & MEYERS [30]. For instance, it can readily be shown that the maximum value of the stretch λ in a uniaxial test is bounded by $\lambda = \exp[1]$ in the case of incompressible elasticity. For most of glassy polymers undergoing finite deformations well below the glass transition temperature, however, the range of elastic deformations is far below this limit. Therefore, the present formulation at hand does not run any practical risk of contradicting the ellipticity requirements.

The Plastic Free Energy Accounting for the Post-Yield Hardening. The second constitutive function to be specified is the plastic part of the free energy $\hat{\psi}^p$. It describes the viscoplastic kinematical hardening through the back stresses that have been introduced in (6.23)₂. As originally proposed by HAWARD & THACKRAY [91], the form of the plastic free energy has conventionally been adopted from the theory of entropic rubber elasticity based on finite extensibility of the polymer chains. This part essentially models the *intramolecular* resistance to the plastic flow due to the alignment of the chains in the principal deformation direction. The key physical motivation is due to the celebrated experiment which demonstrates that a plastically deformed glassy polymer test piece recovers its original undeformed shape upon heating above the glass transition temperature, see HAWARD & MANN [89], BOYCE & HAWARD [27]. The thermal energy input activates plastically stored energy in the material possessing an entangled network structure. For this reason, it is common practice to model the post-yield strain hardening via network models that provide a bridge between micro and macro deformations through particular kinematical assumptions. To this end, we consider two network models, the *eight-chain model* of ARRUDA & BOYCE [8] and the *non-affine micro-sphere model* of MIEHE, GÖKTEPE & LULEI [149], see also [148, 69] for its extensions to finite rubber inelasticity. In contrast to the affine network models, such as the *three-chain model* of JAMES & GUTH [101] and WANG & GUTH [203], and the *affine full network model* of TRELOAR & RIDING [195, 197], these non-affine network models define a single deformation measure for the whole polymer network. The advantage of the non-affine models compared to the models based on affine kinematics becomes more transparent as the plane strain and biaxial deformation states are considered besides the uniaxial stress state, see ARRUDA & BOYCE [7], WU & VAN DER GIESSEN [206], MIEHE, GÖKTEPE & LULEI [149], BOYCE & ARRUDA [25], MARCKMANN & VERRON [127] for a review.

The plastic network free energy modeling the post-yield hardening is specified in the non-Gaussian form in terms of the *network plastic stretch* $\lambda^p = \hat{\lambda}^p(\boldsymbol{\varepsilon}^p)$

$$\psi^p = \hat{\psi}^p(\lambda^p) = \mu_p N_p \left(\lambda_r^p \mathcal{L}^{-1}(\lambda_r^p) + \ln \frac{\mathcal{L}^{-1}(\lambda_r^p)}{\sinh \mathcal{L}^{-1}(\lambda_r^p)} \right) \quad (6.28)$$

where μ_p , N_p are the material parameters standing for the *plastic shear modulus* and the *number of segments* in a polymer chain, respectively. The function \mathcal{L}^{-1} denotes the inverse of the well-known Langevin function defined by $\mathcal{L}(\cdot) := \coth(\cdot) - 1/(\cdot)$. The parameter N_p controls the limited extensibility range of chains through the *relative plastic network stretch* defined by $\lambda_r^p := \lambda^p / \sqrt{N_p}$. For the particular form of $\hat{\psi}^p$ in (6.28), the back stresses can readily be computed through (6.23)₂

$$\boldsymbol{\beta} := \partial_{\boldsymbol{\varepsilon}^p} \psi^p(\lambda^p) = \psi^{p'} \partial_{\boldsymbol{\varepsilon}^p} \hat{\lambda}^p \quad (6.29)$$

where $\psi^{p'} := \partial_{\lambda^p} \psi^p = \mu^p \lambda^p (3N_p - \lambda^{p2}) / (N_p - \lambda^{p2})$. In the derivation of $\psi^{p'}$, we employed the Padè approximation of the inverse Langevin function $\mathcal{L}^{-1}(\lambda_r^p) \approx \lambda_r^p (3N_p - \lambda^{p2}) / (N_p - \lambda^{p2})$ as proposed by COHEN [34]. Before specifying the functional dependency of the plastic network stretch on the plastic strain tensor $\boldsymbol{\varepsilon}^p$ for the respective network models, we introduce the *reference plastic metric* in the inverse form of (6.7)₂

$$\mathbf{G}^p := \exp[2\boldsymbol{\varepsilon}^p] = \sum_{A=1}^3 (\lambda_A^p)^2 \mathbf{n}_A^p \otimes \mathbf{n}_A^p \quad (6.30)$$

being co-axial to the plastic strain tensor $\boldsymbol{\varepsilon}^p = \sum_{A=1}^3 \epsilon_A^p \mathbf{n}_A^p \otimes \mathbf{n}_A^p$ with $\epsilon_A^p := \ln \lambda_A^p$.

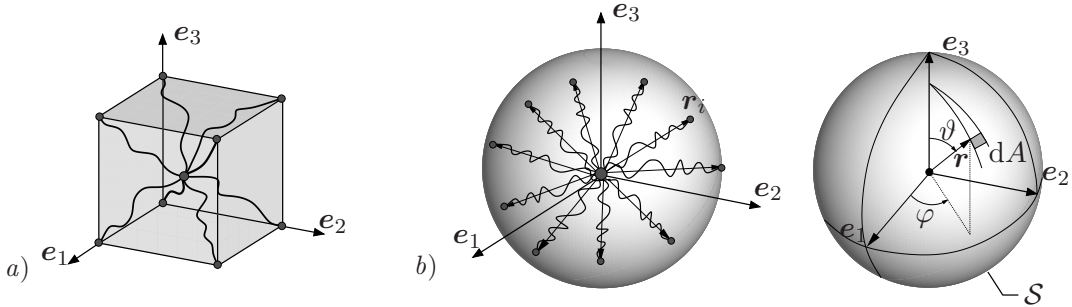


Figure 6.2: Polymer network models employed for modeling the post-yield kinematic hardening. a) The eight-chain model of ARRUDA & BOYCE [7] and b) the non-affine micro-sphere model of MIEHE, GÖKTEPE & LULEI [149].

In the *eight-chain model*, the plastic stretch of a chain extending from the center of a plastically deformed rectangular prism having the edges oriented in the principal plastic directions \mathbf{n}_A^p is assumed to be representative for the whole polymer network, see Figure 6.2a. Thus, the *plastic network stretch of the eight chain model* λ_{ec}^p is obtained in terms of the first invariant of the reference plastic metric \mathbf{G}^p

$$\lambda_{ec}^p := \sqrt{\frac{1}{3} \text{tr}[\mathbf{G}^p]} = \sqrt{\frac{1}{3} [(\lambda_1^p)^2 + (\lambda_2^p)^2 + (\lambda_3^p)^2]}. \quad (6.31)$$

One of the basic ideas proposed in the *non-affine micro-sphere model* was the introduction of a field of *stretch fluctuations* f defined on the micro-sphere \mathcal{S} of space orientations, see

Figure 6.2b. This fluctuation field multiplicatively links the micro-stretch λ of the single chain to the line-stretch $\bar{\lambda}$ of the continuum in the format $\lambda = \bar{\lambda}f$. The fluctuation field f was determined by a *principle of minimum averaged free energy* as discussed in Section 3.3.3. The minimization principle is assumed to be constrained by a m -root averaging condition, yielding a closed-form result for the non-affine *network stretch*

$$\lambda_{ms}^p := \left(\frac{1}{|\mathcal{S}|} \int_{\mathcal{S}} (\bar{\lambda}^p)^m dA \right)^{\frac{1}{m}} = \langle (\bar{\lambda}^p)^m \rangle^{\frac{1}{m}} \quad (6.32)$$

where $m > 0$ is considered as an additional material parameter that describes the non-affine stretch characteristics. The affine plastic stretches $\bar{\lambda}^p$ in the direction of the Lagrangean unit vectors \mathbf{r} are determined by

$$\bar{\lambda}^p := \sqrt{\mathbf{r} \cdot \mathbf{G}^p \mathbf{r}} \quad (6.33)$$

where the orientation of the Lagrangean unit vectors is governed by spherical coordinates $\mathbf{r}(\varphi, \vartheta) = \cos \varphi \sin \vartheta \mathbf{e}_1 + \sin \varphi \sin \vartheta \mathbf{e}_2 + \cos \vartheta \mathbf{e}_3$ in a fixed standard Cartesian frame $\{\mathbf{e}_i\}_{i=1,2,3}$ with $\varphi \in \mathcal{D}_\varphi := [0, 2\pi]$ and $\vartheta \in \mathcal{D}_\vartheta := [0, \pi]$, see Figure 6.2b. Notice that a special choice of $m = 2$, this model recovers the eight chain model as a special case due to the identity $\langle \mathbf{r} \otimes \mathbf{r} \rangle = \frac{1}{3} \mathbf{1}$.

Having the respective plastic network stretches defined in (6.31) and (6.32), we can proceed with the determination of the tensorial part of the back stresses $\partial_{\epsilon^p} \hat{\lambda}^p$ introduced in (6.29). For the eight chain model, we have $\lambda_{ec}^{p2} = \frac{1}{3} \text{tr}[\mathbf{G}^p] = \sum_{A=1}^3 \frac{1}{3} \exp[2\epsilon_A^p]$. Making use of the result $\partial_{\epsilon^p} \epsilon_A^p = \mathbf{n}_A^p \otimes \mathbf{n}_A^p$, we obtain

$$\partial_{\epsilon^p} \lambda_{ec}^p = \sum_{A=1}^3 \frac{\exp[2\epsilon_A^p]}{3\lambda_{ec}^p} \mathbf{n}_A^p \otimes \mathbf{n}_A^p = (3\lambda_{ec}^p)^{-1} \mathbf{G}^p \quad (6.34)$$

that yields the closed-form expression for the back stresses

$$\boxed{\boldsymbol{\beta}_{ec} = \hat{\mu}_{ec}^p(\lambda_{ec}^p) \mathbf{G}^p} \quad (6.35)$$

where $\hat{\mu}_{ec}^p(\lambda_{ec}^p) := \mu^p (3N_p - \lambda_{ec}^{p2}) / (3(N_p - \lambda_{ec}^{p2}))$. In order to compute the explicit form of the back stresses for the micro-sphere model, we determine $\partial_{\mathbf{G}^p} \bar{\lambda}^p = \mathbf{r} \otimes \mathbf{r} / (2\bar{\lambda}^p)$ and $\partial_{\mathbf{G}^p} \lambda_{ms}^p = \frac{(\lambda_{ms}^p)^{1-m}}{2} \langle (\bar{\lambda}^p)^{m-2} \mathbf{r} \otimes \mathbf{r} \rangle$. Incorporation of these results in (6.29) leads us to

$$\boxed{\boldsymbol{\beta}_{ms} = \hat{\mu}_{ms}^p(\lambda_{ms}^p) \langle (\bar{\lambda}^p)^{m-2} \mathbf{r} \otimes \mathbf{r} \rangle : \mathbb{P}^p} \quad (6.36)$$

where $\hat{\mu}_{ms}^p(\lambda_{ms}^p) := \mu^p \lambda_{ms}^{p(2-m)} (3N_p - \lambda_{ms}^{p2}) / (2(N_p - \lambda_{ms}^{p2}))$ and $\mathbb{P}^p := \partial_{\epsilon^p} \mathbf{G}^p$.

The flow rule based on the double-kink theory. As discussed in Section 1.1.2, the viscoplastic flow of amorphous glassy polymers is a thermally activated stochastic process the rate of which $\dot{\gamma}^p$ is conventionally described by the Arrhenius-type equation $\dot{\gamma}^p = \dot{\gamma}_o \exp(-\Delta G_f / k\theta)$ being proportional to the Boltzmann factor $\exp(-\Delta G_f / k\theta)$. In the present model, we conceptually follow the well-accepted *double-kink theory* of ARGON [5] based on the wedge disclinations, see Figure 6.3a. In this approach, the plastic flow is considered as a rotation of small polymer molecule segments from their initial randomly

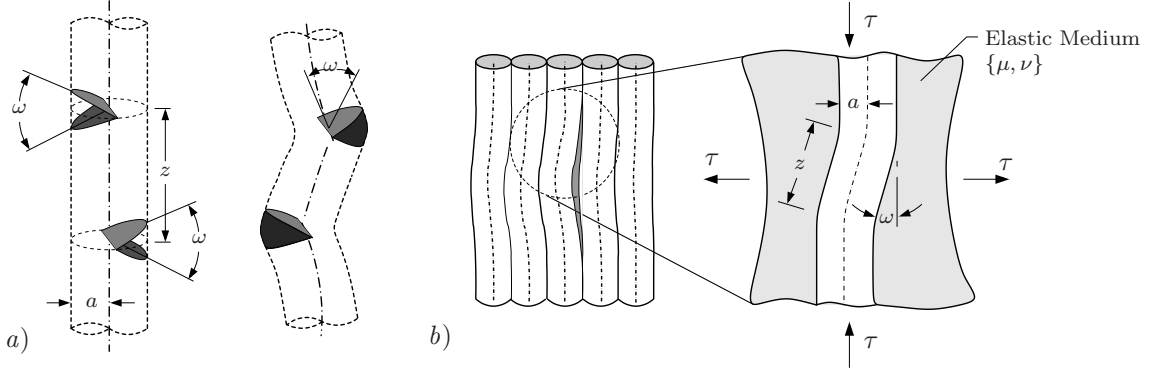


Figure 6.3: Double-kink theory of ARGON [5]. a) Formation of a molecular double-kink by a pair of wedge disclination loops. b) Reverse plastic flow mechanism by formation of a pair of kinks in a polymer molecule embedded in a surrounding elastic matrix, see also LI & GILMAN [117].

oriented, flexed state to the principal deformation direction. In order to compute the activation energy, the reverse process is modeled by the formation of a kink pair resisted both by intra- and intermolecular oppositions. At temperatures, well below the glass transition temperature, the intermolecular resistance due to the elastic interaction between a disclination loop and neighboring chains governs the major part of the overall activation energy necessary for the formation of a double kink.

The activation energy to be surmounted is determined by subtracting the amount of work ΔW done by externally applied effective shear stress τ from the the free energy ΔF stored during formation of a pair of disclination loops in the surrounding medium, see Figure 6.3b. The total micro-free energy ΔF was already computed in LI & GILMAN [117] where they employed the Volterra's method, LOVE [121], for the determination of the displacement field. The linear elasticity constitutive equations have then been used for determining the far stress field over the domain. The strain energy could be estimated by integrating the stress field σ_{zz} outside the disclination loop. This yields a free energy $\Delta F_{sing} = 3\pi a^3 \mu \omega^2 / (32(1 - \nu))$ for a single disclination loop. Apparently, there exists a negative interaction energy due to the integration of the stress field of one disclination loop over another. The interaction energy between two disclination loops having the same strength ω and cylinder radius a gets the form $\Delta F_{inte} = 9\pi \omega^2 a^8 / (8(1 - \nu) z^5)$. The overall free energy stored due to the two wedge disclinations surrounded by the elastic medium with the shear modulus μ and the Poisson's ratio ν is then $\Delta F = 2\Delta F_{sing} - \Delta F_{inte} = 3\pi a^3 \mu \omega^2 / (16(1 - \nu)) - 9\pi \omega^2 a^3 / (8(1 - \nu)(a/z)^5)$. When a pair of disclination loops is formed, the rotation ω yields a compressive strain field proportional to $z(1 - \cos \omega)$. The amount of work done by the externally applied constant shear stress is determined via incompressibility assumption $\Delta W = \pi a^3 \omega^2 \tau (z/a)$. The amount of the activation free enthalpy can then be expressed by combining these results

$$\Delta G_f = \Delta F - \Delta W = \frac{3\pi a^3 \mu \omega^2}{16(1 - \nu)} - \frac{9\pi \omega^2 a^3}{8(1 - \nu)} \left(\frac{a}{z}\right)^5 - \pi a^3 \mu \omega^2 \left(\frac{\tau}{\mu}\right) \left(\frac{z}{a}\right). \quad (6.37)$$

It can be immediately seen that ΔG_f does not contain any extremum in ω , but in the z coordinate due to the assumption that intermolecular interactions are dominating compared to the intramolecular ones. Setting the derivative of the activation free enthalpy with respect to the ratio z/a to zero yields $(z/a)^* = [45\mu / (8\tau(1 - \nu))]^{1/6}$, and its insertion

into (6.37) gives

$$\Delta G_f^* = \frac{3\mu\pi a^3 \omega^2}{16(1-\nu)} \left[1 - \left(\frac{\tau}{s_0} \right)^{\frac{5}{6}} \right] \quad (6.38)$$

where the athermal shear strength defined by $s_0 := 0.077\mu/(1-\nu)$. Use of this result in the Arrhenius equation $\dot{\gamma}^p = \dot{\gamma}_o \exp(-\Delta G_f^*/k\theta)$ leads us to the flow rule

$$\dot{\gamma}^p := \dot{\gamma}_o \exp \left[-\frac{As}{\theta} \left(1 - \left\{ \frac{\tau}{\tilde{s}} \right\}^{\frac{5}{6}} \right) \right] \quad (6.39)$$

where $\tau := \sqrt{J_2(\text{dev}[\boldsymbol{\sigma}^*])} = \sqrt{\text{dev}[\boldsymbol{\sigma}^*] : \text{dev}[\boldsymbol{\sigma}^*]/2}$ and $\dot{\gamma}_o$, $A = 39\pi\omega^2 a^3/16k$ are the material parameters. In (6.39), the athermal shear strength is taken to be different from s_0 in the original theory [5]. In order to account for the the pressure dependency of yielding as well as the succeeding true stress softening, we replace the original athermal shear strength s_0 with $\tilde{s} := s + \alpha p$ where α is a new material parameter controlling the pressure sensitivity of the yield stress. Its value ranges from 0.1 to 0.2 for most of glassy polymers, see e.g. RABINOWITZ, WARD & PARRY [167], BOWDEN & JUKES [22]. The stress softening is incorporated by employing the phenomenological evolution rule for s proposed by BOYCE, PARKS & ARGON [28]

$$\dot{s} = h(1 - s/s_{ss}) \dot{\gamma}^p \quad \text{with} \quad s(0) = s_0 \quad (6.40)$$

where h , s_0 and s_{ss} denote the additional material parameters describing the slope of the softening, initial and steady state values of the athermal shear strength s , respectively.

6.2.3. Algorithmic Setting of the Model. In the algorithmic treatment of the evolution equations, we consider an incremental formulation at discrete time steps $\Delta t := t_{n+1} - t_n$ within a typical time interval $[t_n, t_{n+1}]$. All state variables at time t_n are given and in what follows indicated by the subscript n .

Update of internal variables. The update of the plastic strain tensor $\boldsymbol{\varepsilon}^p$ and the athermal shear strength s is carried out by means of an algorithm that integrates the evolution equations (6.25) and (6.40) in the time interval. Here we employ a fully explicit numerical integration scheme for the update of s through (6.40) and a fully implicit update scheme for $\boldsymbol{\varepsilon}^p$ via (6.25). The update of the athermal shear strength then gets the form

$$s = s_n + \Delta t \dot{s}_n = s_n + \Delta t h(1 - s_n/s_{ss}) \dot{\gamma}_n^p \quad \text{and} \quad \tilde{s} = s + \alpha p_n . \quad (6.41)$$

Owing to the explicit update of the athermal shear strength \tilde{s} , hereafter it can be treated as a constant in the expressions containing \tilde{s} . Use of the backward Euler update for $\boldsymbol{\varepsilon}^p$ leads us to the form

$$\boldsymbol{\varepsilon}^p = \boldsymbol{\varepsilon}_n^p + \Delta t \dot{\gamma}^p \mathbf{N} \quad \text{with} \quad \mathbf{N} := \frac{\text{dev}[\boldsymbol{\sigma}^*]}{\|\text{dev}[\boldsymbol{\sigma}^*]\|} . \quad (6.42)$$

This update equation of the plastic strains is non-linear due to implicit dependencies of $\dot{\gamma}^p$ and \mathbf{N} on the current value of $\boldsymbol{\varepsilon}^p$. For this reason, a local Newton-type iterative update scheme has to be devised.

In order to start with the iterative scheme, we first introduce a non-linear residual function \mathbf{r} of the plastic strain tensor for a frozen deformation state $\boldsymbol{\varepsilon}$ at time t_{n+1}

$$\mathbf{r}(\boldsymbol{\varepsilon}^p) := \boldsymbol{\varepsilon}^p - \boldsymbol{\varepsilon}_n^p - \Delta t \dot{\gamma}^p \mathbf{N} = \mathbf{0} . \quad (6.43)$$

The linearization of the residuum \mathbf{r} is carried out at the k^{th} step of the Newton-Raphson iteration about $\boldsymbol{\varepsilon}_k^p$

$$\text{Lin } \mathbf{r}(\boldsymbol{\varepsilon}^p)|_{\boldsymbol{\varepsilon}_k^p} = \mathbf{r}(\boldsymbol{\varepsilon}_k^p) + \mathbf{a}_k : \Delta \boldsymbol{\varepsilon}^p = \mathbf{0} \quad (6.44)$$

where the local tangent of the Newton iteration is defined as

$$\mathbf{a}_k := \frac{\partial \mathbf{r}(\boldsymbol{\varepsilon}_k^p)}{\partial \boldsymbol{\varepsilon}^p} . \quad (6.45)$$

The update equation for $\boldsymbol{\varepsilon}^p$ at the k^{th} step is then obtained by solving (6.44) for $\boldsymbol{\varepsilon}^p$

$$\boldsymbol{\varepsilon}^p \leftarrow \boldsymbol{\varepsilon}_k^p - \mathbf{a}^{-1} : \mathbf{r}(\boldsymbol{\varepsilon}_k^p) . \quad (6.46)$$

The local tangent \mathbf{a} is computed by inserting the residual (6.43) into (6.45)

$$\mathbf{a} = \mathbb{I} - \Delta t \mathfrak{h} : \partial_{\boldsymbol{\varepsilon}^p} \text{dev}[\boldsymbol{\sigma}^*] \quad (6.47)$$

where we introduced the fourth-order tensor \mathfrak{h} defined by

$$\mathfrak{h} := \frac{\partial (\dot{\gamma}^p \mathbf{N})}{\partial \text{dev}[\boldsymbol{\sigma}^*]} = \alpha_1 \mathbb{I} + \alpha_2 \mathbf{N} \otimes \mathbf{N} \quad (6.48)$$

with the coefficients

$$\alpha_1 := \frac{\dot{\gamma}^p}{\|\text{dev}[\boldsymbol{\sigma}^*]\|} \quad \text{and} \quad \alpha_2 := \alpha_1 \left(\frac{5}{6} \frac{As}{\theta} \left\{ \frac{\tau}{\bar{s}} \right\}^{\frac{5}{6}} - 1 \right) .$$

For a frozen state of the total strain tensor $\boldsymbol{\varepsilon}$, we have

$$\partial_{\boldsymbol{\varepsilon}^p} \text{dev}[\boldsymbol{\sigma}^*] = \partial_{\boldsymbol{\varepsilon}^p} \text{dev}[\boldsymbol{\sigma}] - \partial_{\boldsymbol{\varepsilon}^p} \text{dev}[\boldsymbol{\beta}] = -(\mathfrak{c}^e + \mathfrak{c}^p) \quad (6.49)$$

where $\mathfrak{c}^e := \partial_{\boldsymbol{\varepsilon}} \text{dev}[\boldsymbol{\sigma}]|_{\boldsymbol{\varepsilon}^p} = -\partial_{\boldsymbol{\varepsilon}^p} \text{dev}[\boldsymbol{\sigma}]|_{\boldsymbol{\varepsilon}} = 2\mu \mathbb{P}$ and $\mathfrak{c}^p := \partial_{\boldsymbol{\varepsilon}^p} \text{dev}[\boldsymbol{\beta}]$. Insertion of these results into (6.47) yields

$$\mathbf{a} = \mathbb{I} + \Delta t \mathfrak{h} : (\mathfrak{c}^e + \mathfrak{c}^p) . \quad (6.50)$$

The explicit form of \mathfrak{c}^p directly depends on the network model employed for modeling the back stresses $\boldsymbol{\beta}$. For the sake of brevity, here we consider \mathfrak{c}^p corresponding only to the eight-chain model. To this end, we retrieve the definition of back stresses in (6.35) and recast it into the spectral form of a tensor-valued isotropic function of the plastic strains

$$\text{dev}[\boldsymbol{\beta}_{ec}] = \sum_{A=1}^3 \beta'_A \mathbf{n}_A^p \otimes \mathbf{n}_A^p \quad (6.51)$$

where $\beta'_A := \beta_A - \frac{1}{3} \sum_{B=1}^3 \beta_B$ denote the eigenvalues of the deviatoric back stress tensor with $\beta_A = \hat{\mu}_{ec}^p (\lambda_{ec}^p) \exp(2\epsilon_A^p)$ and \mathbf{n}_A^p stand for its eigenvectors. Having introduced the spectral form of $\text{dev}[\boldsymbol{\beta}_{ec}]$, its derivative with respect to $\boldsymbol{\varepsilon}^p$ can be obtained by

$$\mathfrak{c}^p := \partial_{\boldsymbol{\varepsilon}^p} \text{dev}[\boldsymbol{\beta}_{ec}] = \sum_{A=1}^3 \sum_{B=1}^3 c'_{AB} \mathbf{m}_A^p \otimes \mathbf{m}_B^p + \sum_{A=1}^3 \sum_{B \neq A}^3 \frac{1}{2} \frac{\beta'_A - \beta'_B}{\epsilon_A^p - \epsilon_B^p} (\mathfrak{g}_{AB} + \mathfrak{g}_{BA}) \quad (6.52)$$

where $\mathbf{m}_A^p := \mathbf{n}_A^p \otimes \mathbf{n}_A^p$, $\mathfrak{g}_{AB}^{ijkl} := m_A^{ik} m_B^{jl} + m_A^{il} m_B^{jk}$, see also Appendix A. In the spectral form of \mathfrak{c}^p , the coefficients c'_{AB} under the first summation are defined by $c'_{AB} := c_{AB} - \frac{1}{3} \sum_{K=1}^3 c_{KB}$ where c_{AB} stand for the derivatives of the principal backstresses β_A with respect to the plastic eigenstrains ϵ_B^p . Their explicit form is readily determined from the definition of the principal backstresses β_K

$$c_{KL} := \partial_{\epsilon_L^p} \beta_K = \frac{\hat{\mu}_{ec}^{pl}(\lambda_{ec}^p)}{3 \lambda_{ec}^p} \exp(2\epsilon_K^p) \exp(2\epsilon_L^p) + 2 \hat{\mu}_{ec}^p(\lambda_{ec}^p) \exp(2\epsilon_K^p) \delta_{KL} \quad (6.53)$$

where $\hat{\mu}_{ec}^{pl}(\lambda_{ec}^p) := \partial_{\lambda_{ec}^p} \hat{\mu}_{ec}^p = 4\mu_p(\lambda_{ec}^p - N_p)/(3(N_p - \lambda_{ec}^{p2})^2)$ and δ_{AB} denotes the Kronecker delta. Observe that the spectral form of \mathfrak{c}^p does not incorporate the cases where the equal eigenvalues lead to singularities in the second term of (6.52). For the treatment of these cases by limits and further details concerning representations in the eigen-space, the reader is referred to OGDEN [161], ŠILHAVÝ [182], MIEHE & LAMBRECHT [151] among others.

Algorithmic Tangent Moduli. In a typical implicit finite element analysis of a non-linear boundary value problem, global Newton-type iterative schemes necessitate the computation of the tangent moduli \mathbb{E}_{algo} being consistent with the numerical scheme used for the update of the internal variables. Use of a stable implicit scheme for the update of internal variables allows one to use larger time steps. The consistent tangent moduli are defined as the sensitivity of the stress tensor to the conjugate logarithmic strain tensor

$$\mathbb{E}_{algo} = \mathbf{d}_{\boldsymbol{\varepsilon}} \boldsymbol{\sigma} = \mathbb{E}^e - 2\mu \partial_{\boldsymbol{\varepsilon}} \boldsymbol{\varepsilon}^p \quad (6.54)$$

where $\mathbb{E}^e := \partial_{\boldsymbol{\varepsilon}} \boldsymbol{\sigma} = \kappa \mathbf{1} \otimes \mathbf{1} + 2\mu \mathbb{P}$, $\mathbb{P} := \mathbb{I} - \frac{1}{3} (\mathbf{1} \otimes \mathbf{1})$ and \mathbb{I} denotes the symmetric fourth-order identity tensor. Computation of the consistent tangent moduli, however, requires the sensitivity of strain-like internal variables to a total strain measure. For the present case, the sensitivity of $\boldsymbol{\varepsilon}^p$ to $\boldsymbol{\varepsilon}$ can be computed from the persistency condition implying the steady fulfillment of vanishing residuum defined in (6.43). Therefore, the total derivative of the residuum must also be zero at any instant of the deformation, i.e.

$$\mathbf{d}_{\boldsymbol{\varepsilon}} \mathbf{r} = \partial_{\boldsymbol{\varepsilon}} \mathbf{r}|_{\boldsymbol{\varepsilon}^p} + \partial_{\boldsymbol{\varepsilon}^p} \mathbf{r}|_{\boldsymbol{\varepsilon}} : \partial_{\boldsymbol{\varepsilon}} \boldsymbol{\varepsilon}^p = \mathbf{0} . \quad (6.55)$$

The left contractor of the second term is the local tangent $\partial_{\boldsymbol{\varepsilon}^p} \mathbf{r}|_{\boldsymbol{\varepsilon}} = \mathfrak{a}$ that has been already computed in the last local Newton iteration step in (6.50). The sought derivative can then be obtained from the condition (6.55) as

$$\partial_{\boldsymbol{\varepsilon}} \boldsymbol{\varepsilon}^p = -\mathfrak{a}^{-1} : \partial_{\boldsymbol{\varepsilon}} \mathbf{r}|_{\boldsymbol{\varepsilon}^p} . \quad (6.56)$$

Recalling the definition of the residuum in (6.43), the derivative $\partial_{\boldsymbol{\varepsilon}} \mathbf{r}|_{\boldsymbol{\varepsilon}^p}$ can be expressed in the form analogous to (6.47)

$$\partial_{\boldsymbol{\varepsilon}} \mathbf{r}|_{\boldsymbol{\varepsilon}^p} = -\Delta t \mathfrak{h} : \mathfrak{c}^e \quad (6.57)$$

where the tensor \mathfrak{h} has been defined in (6.48). Finally, the insertion of (6.57) into (6.56) leads us to the desired sensitivity

$$\partial_{\boldsymbol{\varepsilon}} \boldsymbol{\varepsilon}^p = \Delta t \mathfrak{a}^{-1} : \mathfrak{h} : \mathfrak{c}^e . \quad (6.58)$$

Incorporation of the result (6.58) in (6.54) yields

$$\mathbb{E}_{algo} = \mathbb{E}^e - 2\Delta t \mu \mathfrak{a}^{-1} : \mathfrak{h} : \mathfrak{c}^e . \quad (6.59)$$

Basic steps of the algorithmic treatment of the model are also summarized in Table 6.1.

Table 6.1: Algorithmic Update of the Plastic Strains

1. *Data Base.* The history data $\{\boldsymbol{\varepsilon}_n^p, s_n, \dot{\gamma}_n^p, p_n\}$ and the current total strain $\boldsymbol{\varepsilon}$ are given.

2. *Explicit Update of the Athermal Shear Strength.*

$$\tilde{s} = s_n + \Delta t h (1 - s_n/s_{ss}) \dot{\gamma}_n^p + \alpha p_n .$$

3. *Implicit Update of the Plastic Strains.*

i) Set $k = 0$ and initialize $\boldsymbol{\varepsilon}^p |_{k=0} \leftarrow \boldsymbol{\varepsilon}_n^p$

ii) Compute the dependent variables

$$\dot{\gamma}^p \text{ (6.39), } \boldsymbol{\sigma} \text{ (6.23)}_1, \boldsymbol{\beta} \text{ (6.23)}_2, \boldsymbol{\sigma}^* \text{ (6.24), } \tau \text{ (6.39)}_2 \text{ and } \mathbf{N} \text{ (6.42)}_2$$

iii) Compute the residual and its norm

$$\mathbf{r} := \boldsymbol{\varepsilon}^p - \boldsymbol{\varepsilon}_n^p - \Delta t \dot{\gamma}^p \mathbf{N}, \quad \|\mathbf{r}\| := \sqrt{\mathbf{r} : \mathbf{r}} \quad (6.43)$$

iv) Compute the local tangent $\mathbf{a} := \partial_{\boldsymbol{\varepsilon}^p} \mathbf{r} \quad (6.52)$

v) Update plastic strains $\boldsymbol{\varepsilon}^p \leftarrow \boldsymbol{\varepsilon}^p - \mathbf{a}^{-1} : \mathbf{r}$

vi) Convergence check:

If $\|\mathbf{r}\| \geq \text{tol}$, $k \leftarrow k + 1$ goto ii)
 else continue with 4.

4. *Store the history variables and proceed with the Consistent Moduli.*

6.3. Illustrative Numerical Examples

This section is devoted to the assessment of the modeling capacity of the proposed approach by comparing its results to homogeneous as well as inhomogeneous experimental data. The homogeneous test data involve the true stress-true strain curves obtained from the experiments conducted under different deformation rates and states on PMMA (Polymethylmethacrylate) and PC (Polycarbonate). While the tensile stress-strain diagrams of the former are taken from the literature, [98], the compressive uniaxial and plane strain experiments on PC have been newly carried out. The results of both are then used for the identification of the adjustable material parameters. In addition to the homogeneous experiments on PC, a three-dimensional cold drawing of a dumbbell-shaped test piece, already depicted Figure 1.3, was carried out. The data acquired from the inhomogeneous experiment contain not only the load-displacement diagram but also the three-dimensional surface strain fields. These results are compared with the finite element analysis of the cold drawing problem with the model parameters identified from the homogeneous experiments.

6.3.1. Investigations on Homogeneous Deformation States. As discussed in Section 1.1.2, the mechanical behavior of glassy polymers depends on many factors that involve loading rate, temperature, deformation state. In this section, we focus on the examples that particularly illustrate the rate and deformation state dependence of the stress-strain response of PMMA and PC, respectively. These are the two representative kinds of tough, high-density amorphous glassy polymers that are capable of undergoing large plastic deformations without exhibiting brittle failure at room temperature.

The first set of experimental data, presented in Figure 6.4a, was reported by HOPE, WARD & GIBSON [98]. The data exhibit the rate-dependent tensile true stress-strain behavior of polymethylmethacrylate (PMMA) under different loading rates at $\theta=90^\circ\text{C}$. In order to investigate the rate-dependent behavior of PMMA, they employed waisted specimens with 5 mm waist width. These test pieces were then subjected to extension at different constant cross-head speeds. During the deformation, the lateral contraction of each specimen was recorded so that they were able to compute the true stress-strain curves for each constant crosshead speed but with varying true strain rate. Employing the numerical differentiation and the interpolation techniques on these data, they could extract the true stress-strain diagrams for the different true strain rates. Although it is a well known fact that the deformation of PMMA at high strain rates, e.g. $\overline{\ln \lambda}=11/\text{s}$, leads to an appreciable heating resulting in around 20°C temperature increase, see ARRUDA, BOYCE & JAYACHANDRAN [9], these thermal changes and consequently softening in the post yield behavior of the material are not reflected in these data. Nevertheless, since the data clearly exhibit the rate dependence of the material response, they were already employed in the literature, e.g. [27, 28]. Here, we also tested the model response against these data. The simulations at three different rates of true strain are plotted together with the corresponding test results in Figure 6.4a. In the simulation of these data, the back-stress response is modeled by the eight-chain model. The values of the material parameters used in the simulations are given in the caption of Figure 6.4. The elastic material parameters κ, μ and the values of $A, \dot{\gamma}_0$ and α were taken be close to the values reported in the literature, [28, 9], and kept frozen during the identification. The parameters governing the yield stress and the stress softening behavior s_0, s_{ss}, h , and the post-yield hardening μ_p, N_p , however, were adjusted by fitting the experimental curves. The comparison shows the fairly good predictive capabilities of the proposed formulation in simulating the tensile stress-strain response of PMMA at different strain rates.

The uniaxial and plane strain compression experiments on polycarbonate (PC) samples depicted in Figure 6.4b aim at presenting the deformation state dependence of the material response. The ductile PC is produced by Bayer AG in Leverkusen under a commercial name *Makrolon 2607*. Both experiments were conducted at a constant true strain rate $\overline{\ln \lambda} = -1 \cdot 10^{-4} \text{ 1/s}$ on a MTS servohydraulic uniaxial testing machine at room temperature. The rate of deformation was purposely selected to be slow enough to suppress the temperature increase due to dissipative heating. For the compressive uniaxial experiments, cylindrical PC specimens having a 8 mm diameter and a 8 mm height were employed. In the case of plane strain compression tests, however, cubic test pieces with an edge length of 8 mm were used. In both experiments particular attention has been paid to the appropriate lubrication between the contact surfaces of the specimen and the steel platens of the test machine in order to avoid the severe barreling appearing due to the friction developing under compression, MÉNDEZ, GÖKTEPE & MIEHE [136]. For this purpose, a combination of Teflon film (solid lubricant) and commercial oil-based lubricant, WD-40, was employed as recently suggested in DUPAIX & BOYCE [52].

Experimental results presented in Figure 6.4b illustrate the typical yielding, stress softening and post-yield strain hardening behavior of glassy polymers. As is commonly applied, the value of true stress was determined based on the incompressibility assumption. The deformation state dependence of the material response especially with regard to the yield stress and the post-yield strain hardening is in agreement with the obser-

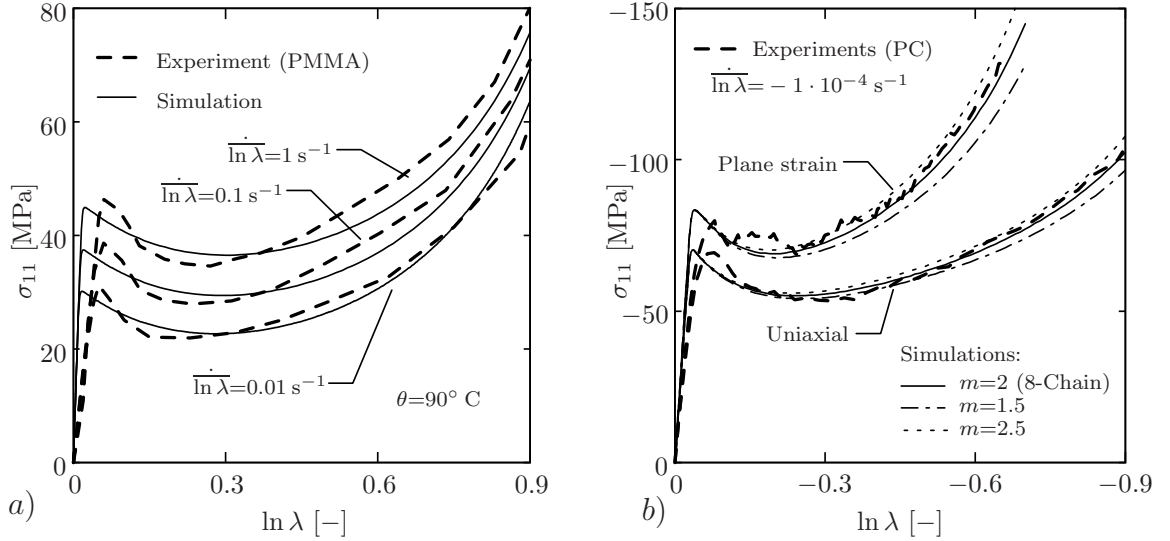


Figure 6.4: Rate and deformation state dependencies in mechanical response of PMMA and PC. *a)* True stress–true strain diagrams corresponding to the uniaxial tensile tests conducted at three different rates at $\theta=90^\circ\text{C}$. The set of material parameters used in the simulations are $\kappa=2633$ MPa, $\mu=1003$ MPa, $\mu_p=4.7$ MPa, $N_p=3.5$, $\dot{\gamma}_0=1.13 \cdot 10^{11}$ 1/s, $A=167$ K/MPa, $h=250$ MPa, $s_0=90$ MPa, $s_{ss}=76$ MPa, $\alpha=0.2$. *b)* True stress–true strain diagrams of the uniaxial and the plane strain compression experiments carried out at true strain rate $\dot{\ln \lambda} = -1 \cdot 10^{-4} \text{ s}^{-1}$ at room temperature. The set of material parameters used in the simulations are $\kappa=2000$ MPa, $\mu=900$ MPa, $\mu_p=11.5$ MPa, $N_p=2.35$, $\dot{\gamma}_0=6.24 \cdot 10^7$ 1/s, $A=140$ K/MPa, $h=500$ MPa, $s_0=102$ MPa, $s_{ss}=82$ MPa, $\alpha=0.11$.

vations reported in the literature, see for example ARRUDA & BOYCE [7]. The higher value of the yield stress encountered in the plane strain compression compared to the uniaxial compression is due to the excessive constraining boundary conditions in the plane strain deformation state and the pressure dependency of the yield stress, see SPITZIG & RICHMOND [187]. In the case of plane strain compression chain molecules have a freedom to plastically align in only one direction. In the uniaxial compression, however, they can freely orient themselves symmetrically in the plane perpendicular to a loading axis. If we consider those as nearly incompressible deformations, the chains aligning in a single direction in the plane strain compression state have to elongate more than the macromolecules stretch symmetrically in the uniaxial state. This leads to the apparent deformation state-dependent post-yield response and consequently evolution of different kinds of anisotropy.

Another aim of the homogeneous tests on PC samples was the determination of the material parameters to be used in finite elements analysis of the cold drawing example on the same material partially presented in Sections 1.1.2 and 6.3.2. During the identification of the model parameters, we followed a way analogous to the one employed for the parameters of the data in Figure 6.4a. The values of the model parameters given in the caption of Figure 6.4 were first determined for the model based on the eight chain model kinematics, i.e. $m=2$ for the micro-sphere model. The comparison of the simulations against the experimental results in Figure 6.4b clearly shows that the proposed approach in the logarithmic strain space is able to capture the deformation state dependence of the yield stress and the post-yield hardening very well. Apart from the fittings based on the eight chain model (solid line), the effect of the non-affinity parameter m of the micro-sphere model on the post-yield response is also investigated. The value of m is varied

from $m=2$ to $m=1.5, 2.5$. The larger the value of m , the stiffer the post-yield material behavior gets, see Figure 6.4b. This provides an additional degree of freedom that serves to improve the post-yield fittings. Observe that the quality of the post-yield hardening simulation in the both uniaxial and plane strain cases has been slightly improved for the values of the non-affinity parameter m greater than 2.

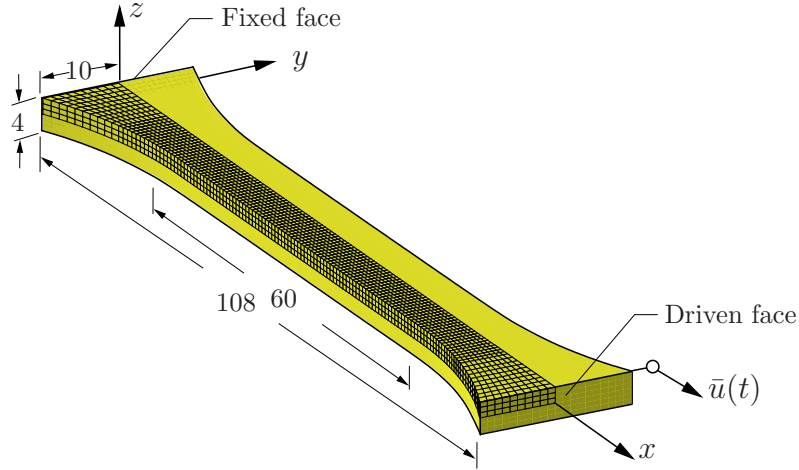


Figure 6.5: Geometry, boundary conditions and finite element discretization of the dumbbell-shaped polycarbonate test piece subjected to extension in the x -direction at the deformation rate $\dot{\bar{u}}=2$ mm/min. All dimensions are given in millimeters.

6.3.2. Cold Drawing of a Dumbbell-Shaped PC Specimen. In addition to the evaluation of the proposed approach with respect to the homogeneous experiments presented in the preceding section, we further test the capabilities of the proposed model with the parameters determined based on the homogeneous experiments against a three-dimensional cold drawing experiment. To this end, we consider a dumbbell-shaped PC test piece whose geometry is specified according to ISO 527 and also depicted in Figure 6.5. The compressive uniaxial and plane strain stress-strain response of the material of interest is presented in Figure 6.4b. The inhomogeneous tension experiment were carried out at a cross-head speed $\dot{\bar{u}}=2$ mm/min and analyzed with the optical measuring system called *Aramis*. The load-displacement diagram and the characteristics of the deformation process have been discussed in detail in Section 1.1.2. For the successful recognition of the three-dimensional surface of the specimen and its deformation via the grating method, the specimen must be coated in a specific manner depending on the kind of material to be tested. In the case of the transparent PC under the current investigation a suitable treatment for the surface is the dense-spraying of standard white glossy coating first, and next, while the former is still fresh, a more sparsely sprayed layer of matte graphite-based paint is superimposed. This provides the contrast over the surface that the grating method requires for determining the deformation and hereby calculating the inhomogeneous three-dimensional strain field on the material, MÉNDEZ, GÖKTEPE & MIEHE [136]. This is achieved by the use of a measuring arrangement with two CCD cameras. During the experiment the software acquires images with both cameras simultaneously allocating coordinates to every pixel on them. As a post-process the pixels of the recorded images are matched via mathematical transformations, see RITTER [174]. Once this has been done for the initial set of images, the process is repeated for the rest of the recorded stages of the deformation. From the difference of the coordinates of the pixels from the reference measurement to the others the displacement vectors are obtained. For further

details on the grating method and the system Aramis, the reader is referred to WINTER [205], BERGMANN & RITTER [13], GOM [1].

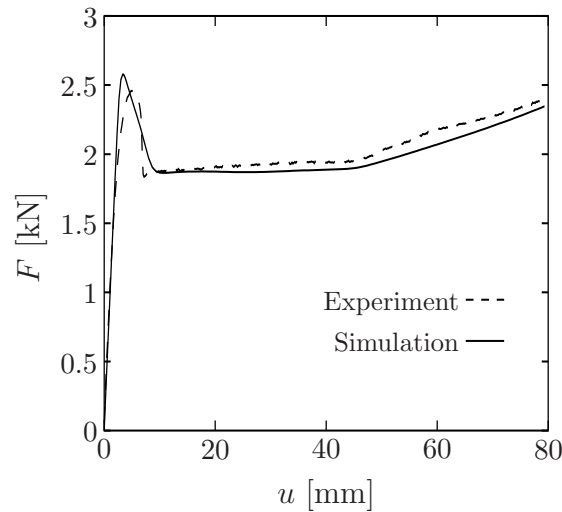


Figure 6.6: Simulation of the load-displacement curve of a dumbbell-shaped PC specimen subjected to extension at a cross-head speed $\dot{u}=2$ mm/min. The set of material parameters were determined based on the homogeneous uniaxial and plane strain compression experiments shown in Figure 6.4b.

Apart from the dimensions of the dumbbell-shaped specimen, the boundary conditions and the finite element (FE) discretization of its geometry are depicted in Figure 6.5. Owing to the apparent symmetries in its geometry, in the FE model of the specimen only its one quarter is discretized by 3750 eight-node Q1P0 mixed brick elements. While the end of the specimen at $x = 0$ mm is being fixed in all three directions, the degrees of freedom in y - and z -directions on its other end are restrained and the deformation in x -direction $\bar{u}(t)$ is prescribed, see Figure 6.5. Boundary conditions on the common facets with other quarters are governed by apparent geometrical symmetry conditions. The whole test piece is subjected to an extension at a cross-head speed $\dot{u} = 2$ mm/min at room temperature. In order to attain the neck initiating at the same place with the experiments, a slight geometrical imperfection at the end of the gauge section is imposed. The simulation of the global load-displacement response of the flat coupon extension is depicted in Figure 6.6 in comparison with the experimental curve. Characteristic features of the experimental load-displacement curve, which are discussed in detail in Section 1.1.2, are traced very well by the proposed model in the logarithmic strain space. Observe that the proposed model captures not only the load-level where the macro-yield occurs but also the amount of softening and the location of stress hardening where the neck reaches the end of the gauge section with the parameters determined from homogeneous compression experiments. This clearly justifies the procedure followed in identifying the model parameters and shows the multi-dimensional characteristics of the model.

In addition to the load-displacement diagram depicted in Figure 6.6, contour plots in Figure 6.7 compare the field of thickness change during the cold drawing. The results obtained from the FE analysis (first and second columns) are compared with the measurements conducted by the optical measurement facility (third column). The labels of the rows a)- f) in Figure 6.7 indicate the deformation stages corresponding to the levels labeled with the same letters as in Figures 1.3 and 1.4. The field of thickness change up to the macro-yield, stages a) and b), is homogeneous throughout the test piece. The

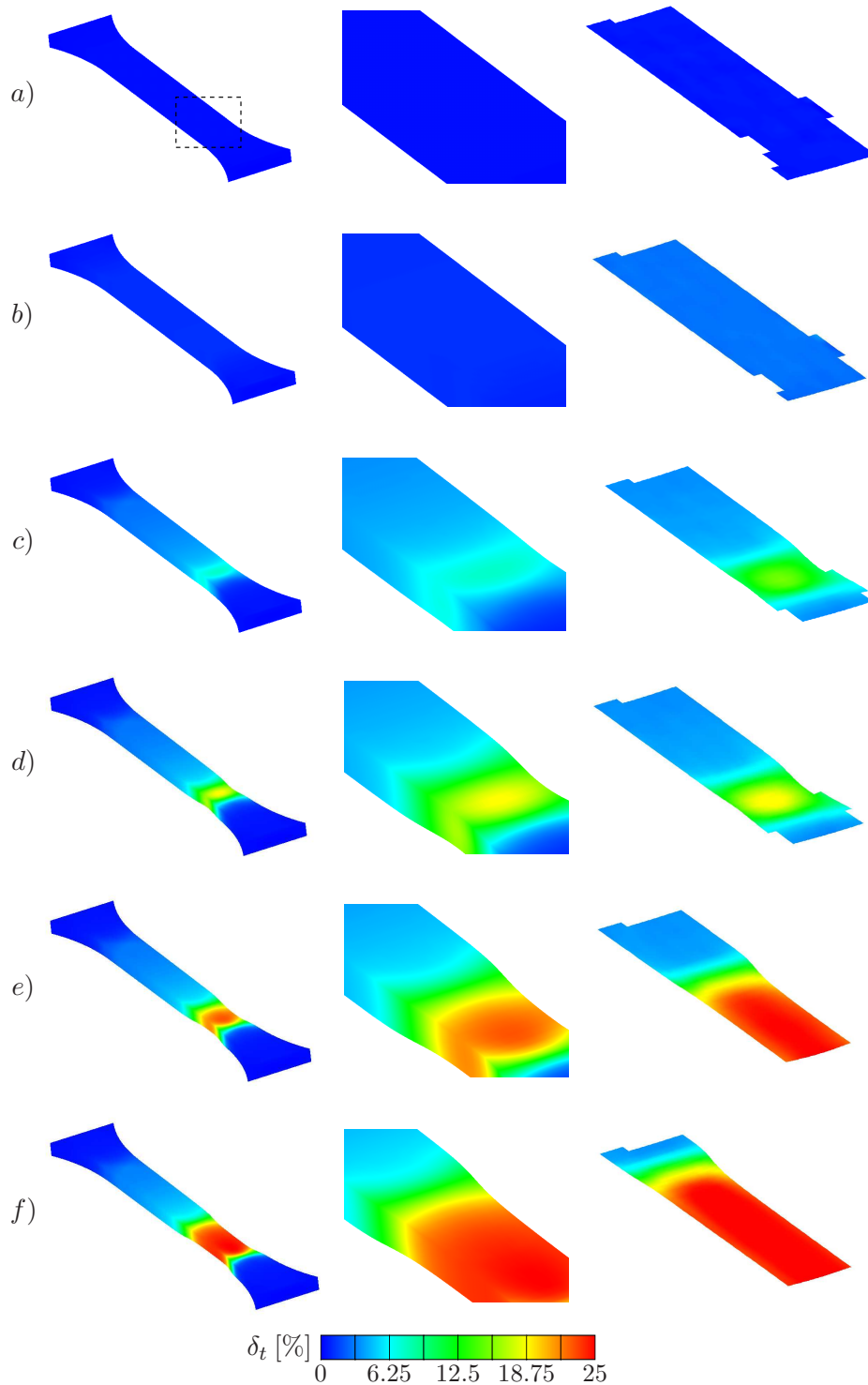


Figure 6.7: Thickness change computations obtained by the three-dimensional finite element analysis (first and second columns) are compared with their corresponding inhomogeneous experimental results (third column). The labels of the rows a)-f) indicate the deformation stages labeled with the same letters in Figures 1.3 and 1.4. In the FE analysis, the same material parameters as those given in Figure 1.3b have been used.

thickness change starts to localize in the softening branch between the load levels b) and d). It reaches the maximum value 25% at stage e) and is driven by the neck front along the gauge section. The computational results of the thickness change at almost all de-

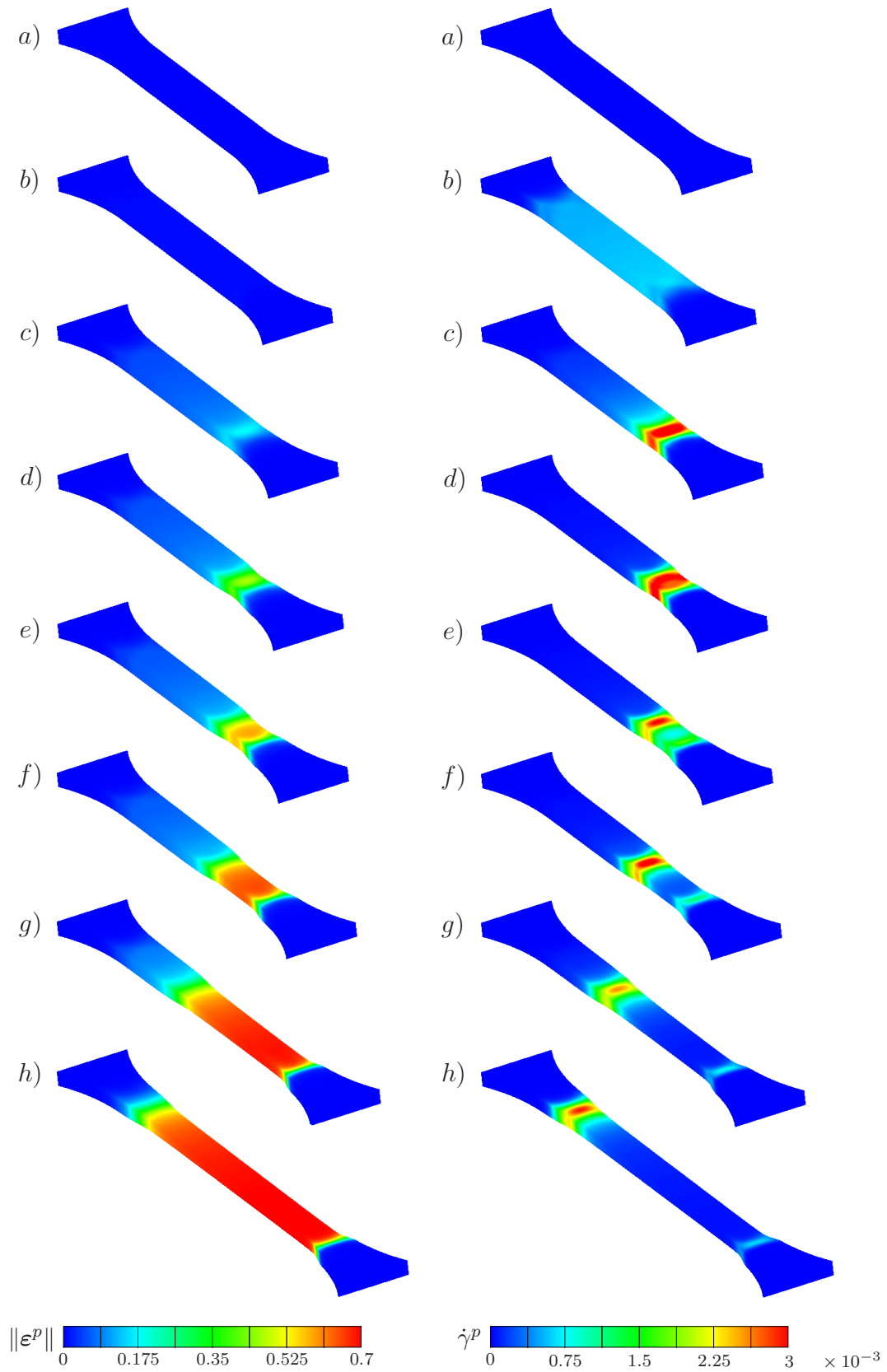


Figure 6.8: Contour plots of the equivalent plastic strain $\|\varepsilon^p\|$ [-] (left column) and the amount of plastic flow $\dot{\gamma}^p$ [1/s] (right column) at the stages a)-h) as denoted in Figure 1.3.

formation stages agree with the optical measurements quantitatively. These predictive results obtained from the simulation of the multi-axial inhomogeneous experiment once more indicate the validity of the proposed model.

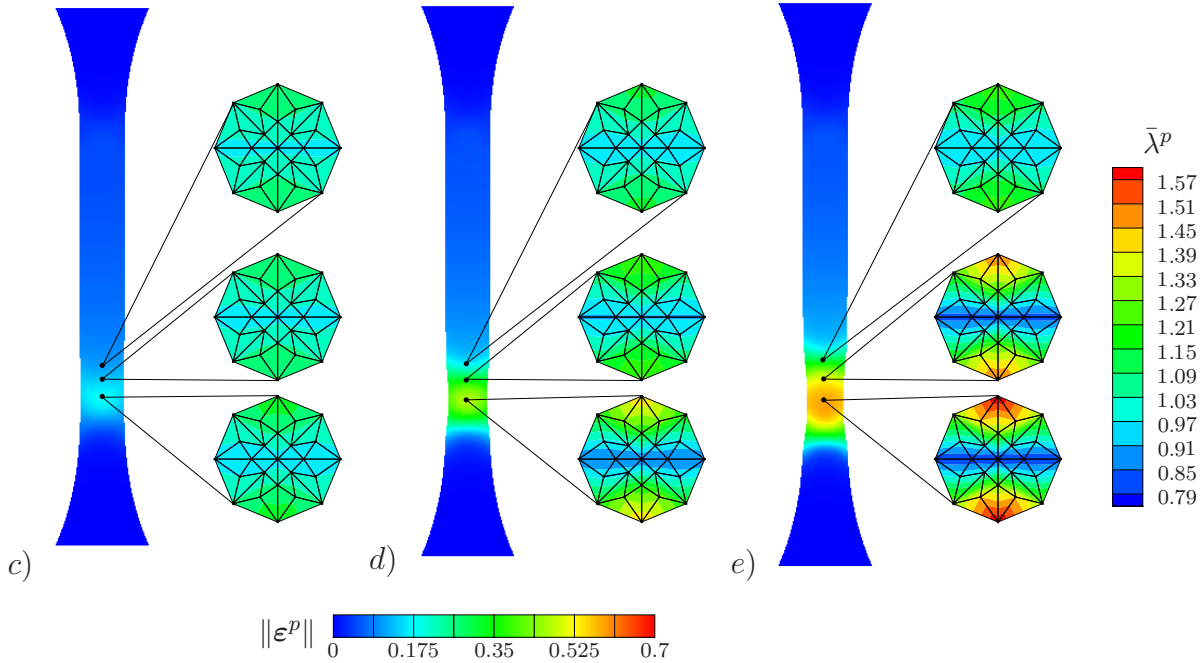


Figure 6.9: Stereographic projection plots of the plastic stretch $\bar{\lambda}^p$ (6.33) corresponding to the three stages *c)*, *d)* and *e)* of the deformation are plotted along with the macroscopic equivalent plastic strain contours at the depicted material points.

The contour plots in Figure 6.8 present the distributions of the equivalent plastic strain $\|\epsilon^p\|$ and the amount of plastic flow $\dot{\gamma}^p$ on the left and the right columns, respectively. The labels of the rows *a)*-*f)* indicate the deformation stages corresponding to the levels labeled with the same letters as in Figure 1.3. Although there is no geometrically apparent neck at the maximum load level *b)*, plastic flow starts to localize at the succeeding stage *c)* at the location where the slight initial geometrical imperfection has been assigned. The stage *d)* with the lowest post-yield load value corresponds to the stabilized state of the neck where the maximum plastic flow rate has been already achieved. At this stage the localized zone starts to separate at opposite directions drawing the shoulders of the neck towards grips. The states *e)*, *f)* and *g)* illustrate the different degrees of the neck propagation where the progressive drawing of the material has been clearly exhibited. Owing to the unsymmetric initiation of the neck along the specimen, its propagation towards right grip did not last as long as in the case of movement to the left end. When the neck shoulder reaches the end of the gauge section, load deflection curve gets stiffer, stage *h)*. The contour plots of the equivalent plastic strain field for the deformation stages *c)*-*e)* are repeated in Figure 6.9 together with the stereographic projection plots of the plastic stretch $\bar{\lambda}^p$ introduced in (6.33). The close-up pole figures of the plastic stretch corresponding to the indicated material points clearly depict the variation of its distribution and also the evolution of its intensity during the stages of neck stabilization and its propagation.

7. Concluding Remarks

This thesis is concerned with the development of new micromechanically motivated models for rubbery and glassy polymers. The particular types of material response considered cover the finite elasticity, viscoelasticity, Mullins effect in rubbery polymers, and the viscoplasticity of amorphous glassy polymers at large strains. The intrinsic micro-macro quality of the proposed approaches facilitates the incorporation of inherent microstructure-originated mechanisms. Despite the complicated phenomena embodied, the models equipped with associated algorithmic treatments are shown to be applicable to finite element analyses of three-dimensional boundary value problems.

An essential aspect of this work is the construction of a theoretical and algorithmic setting of a new network model for finite elasticity of rubber-like materials, which has been referred to as the *non-affine micro-sphere model*. This elasticity model acts as a cornerstone for all the subsequent development concerning the finite inelasticity of rubbery and glassy polymers. The motivating key phenomenological evidence for the necessity of non-affine network models is due to shortcomings of the affinity assumption with respect to locking stretch characteristics. Furthermore, the underestimation of experimental equi-biaxial elasticity data, especially within the moderate ranges of deformation, by network models of unconstrained chains has motivated the inclusion of topological constraint effects. Core of the proposed model is a new two-dimensional constitutive setting of the micro-mechanical response of a *single polymer chain in a constrained environment* that is defined by two micro-kinematic variables: the stretch of the chain and the contraction of the cross section of a micro-tube containing the chain. The second key feature is a new *non-affine micro-macro transition* that defines the three-dimensional overall response of the polymer network based on a characteristic homogenization procedure of micro-variables defined on the micro-sphere of space orientations. It determines a stretch fluctuation field on the micro-sphere by a principle of minimum averaged free energy and links the two micro-kinematic variables in a non-affine format to the line-stretch and the area-stretch of the macro-continuum. The elementary kinematic definition of topological constraints through a straight tube with a link to the macroscopic area deformation is based on the assumed mechanism of forest chains, which is a new aspect of rubber elasticity. The proposed model describes two superimposed contributions resulting from free chain motions and topological constraints in an attractive dual geometric structure on both the micro- and the macro-level. Averaging operations on the micro-sphere are carried out directly by an efficient numerical integration scheme. The computational effort is absolutely competitive with purely macroscopic models of rubber elasticity formulated in terms of spectral decompositions of macroscopic strain measures. The overall model contains five effective material parameters, which are obtained from the single chain statistics and properties of the network, with clearly identifiable relationships to characteristic phenomena observed in experimental stress-stretch curves. This allows a priori estimates of initial values for the parameter identification process by means of nonlinear programming tools. The approach advances features of the affine full network and the eight-chain models by a substantial improvement of their modeling capabilities. Interestingly, the eight chain model turns out to be a special case of the proposed model for a specific choice of material parameters. The truly predictive performance of the elasticity model was illustrated via comparative studies with previously developed network models and by fitting various available experimental data obtained from homogeneous and non-homogeneous tests.

The immediate extension of the non-affine micro-sphere model was made towards the finite viscoelastic constitutive framework of rubber-like materials. The formulation makes use of the intrinsic features of the original elasticity model. In contrast to purely phenomenological approaches to finite viscoelasticity formulated in terms tensorial internal variables, scalar fields of internal variables are introduced over a micro-sphere of space orientations. The macroscopic overstress response is defined by a distinct affine homogenization procedure of these internal variable fields. The proposed micromechanically-based model of viscous overstresses is formulated in terms of two key micro-kinematic mechanisms associated with the free chain retraction and the constraint release phenomena. The numerical implementation is achieved through a discretized averaging of the micro-fields on the unit-sphere of space orientations. The characteristics and modeling capabilities of the proposed micro-sphere model of finite viscoelasticity were reported for a broad spectrum of experimentally-based benchmark. They demonstrate the excellent performance of the model in simulations of rate and hysteresis effects of rubbery polymers. As outlined in the algorithmic boxes, the proposed overstress model is easy to implement into typical non-linear finite element codes. The framework of the micro-sphere model was further extended to the description of the Mullins-type stress softening effect due to the breakdown of chain-particle-bonds. The model is very attractive due to its constitutive formulation of damage mechanisms on an essentially one-dimensional micro-level of space orientations. The numerically evaluated homogenization with respect to the space orientations describes the experimentally observed deformation-induced anisotropy of the damage. The permanent set in stress-stretch diagrams is achieved by our model in a natural way as an anisotropy effect. The comparison of the proposed model with available experimental data indicate very good agreement. Owing to its simple algorithmic structure, the model is very suitable for the implementation into finite element codes.

In the final part of the thesis, a constitutive model for the finite viscoplastic deformation of ductile glassy polymers was developed. The kinematical setting of finite viscoplasticity was laid out in the logarithmic strain space framed by purely geometric, model-independent pre- and post-processing steps. This allowed us to construct the complete model within the framework akin to the geometrically linear theory. This framework leads us to an extremely attractive algorithmic structure for the implementation of finite viscoplasticity of amorphous glassy polymers. The micromechanically motivated Arrhenius-type flow rule for viscoplastic strains in the logarithmic strain space has been borrowed from the celebrated *double-kink* theory. The details of the implicit algorithm for the update of plastic strains were discussed. For the modeling of post-yield hardening both the eight chain and the non-affine micro-sphere models were employed and compared with respect to experimental data. The developed model has been tested against new experimental data based on homogeneous and inhomogeneous deformations. Besides the true stress-true strain curves obtained from the homogeneous experiments on polycarbonate specimens, the load-displacement diagram and the three-dimensional optical surface strain field measurements were also considered. The proposed model was shown to be able to successfully capture various phenomena exhibited by glassy polymers. The obtained results indicate the predictive performance of the proposed model and its high suitability for the FE analyses of boundary value problems.

A. Spectral Representation of the Right Cauchy-Green Tensor

We retrieve that the right Cauchy-Green tensor \mathbf{C} defined in (2.21) is a symmetric and positive definite (covariant) Lagrangean tensor of rank-two. The eigenvalue (principal value) problem of \mathbf{C} is defined as

$$\mathbf{C}\mathbf{N}^\alpha = \lambda_\alpha^2 \mathbf{N}_\alpha \quad , \quad C_{IJ}N^{\alpha J} = \lambda_\alpha^2 N_{\alpha I} \quad (\text{A.1})$$

where $\mathbf{N}^\alpha \in T_X\mathcal{B}$, $\mathbf{N}_\alpha \in T_X^*\mathcal{B}$ denote the unit eigenvector triads that belong to the tangent $T_X\mathcal{B}$ and co-tangent spaces $T_X^*\mathcal{B}$ of the reference configuration, respectively. As introduced in (2.17), the eigenvectors are related to each other through the reference metric $\mathbf{N}_\alpha = \mathbf{G}\mathbf{N}^\alpha$ for $\mathbf{G} : T_X\mathcal{B} \rightarrow T_X^*\mathcal{B}$, see also Figure 2.3. It can be shown that eigenvalues of a *symmetric* tensor are *real-valued* and so do its eigenvectors. The symmetry of a tensor also assures the mutual *orthogonality* of its eigenvectors, i.e. $\mathbf{N}^\alpha \cdot \mathbf{N}_\beta = \delta^\alpha_\beta$. Moreover, it can be further shown that the following identities hold

$$\mathbf{G} = \sum_{\alpha=1}^3 \mathbf{N}_\alpha \otimes \mathbf{N}_\alpha \quad , \quad \mathbf{G}^{-1} = \sum_{\alpha=1}^3 \mathbf{N}^\alpha \otimes \mathbf{N}^\alpha \quad \text{and} \quad \sum_{\alpha=1}^3 \mathbf{N}^\alpha \otimes \mathbf{N}_\alpha = \mathbf{1} . \quad (\text{A.2})$$

A sum of a dyadic product of the identity (A.1) with \mathbf{N}_α over α by incorporating the result (A.2)₃ yields the *spectral representation* of \mathbf{C}

$$\mathbf{C} = \sum_{\alpha=1}^3 \lambda_\alpha^2 \mathbf{N}_\alpha \otimes \mathbf{N}_\alpha . \quad (\text{A.3})$$

This representation requires knowledge of the eigenvalues and the eigenvectors of \mathbf{C} . The *eigenvalue problem* introduced in (A.1) indeed seeks for these three mutually perpendicular material principal directions \mathbf{N}^α that remain perpendicular but scaled by the eigenvalues λ_α^2 under the transformation by \mathbf{C} . The non-trivial solutions of the eigenvalue problem satisfy the equality $\det(\mathbf{C} - \lambda_\alpha^2 \mathbf{G}) = 0$ which can be expanded to the *characteristic equation*

$$\Lambda^3 - I_1(\mathbf{C})\Lambda^2 + I_2(\mathbf{C})\Lambda - I_3(\mathbf{C}) = 0 \quad (\text{A.4})$$

satisfied for each $\Lambda := \lambda_\alpha^2$ for $\alpha \in \{1, 2, 3\}$. The coefficients of the third order polynomial (A.4) of Λ are the *principal invariants* of \mathbf{C} defined as

$$I_1(\mathbf{C}) := \text{tr}(\mathbf{C}) \quad , \quad I_2(\mathbf{C}) := \frac{1}{2} (I_1^2(\mathbf{C}) - \text{tr}(\mathbf{C}^2)) \quad \text{and} \quad I_3(\mathbf{C}) := \det(\mathbf{C}) \quad (\text{A.5})$$

where the *trace* operator tr is defined as $\text{tr}(\mathbf{C}) := \mathbf{C}:\mathbf{G}^{-1}$. As their name imply, the principal invariants remain unchanged under the change of the coordinate system. Consequently, they can also be expressed as symmetric functions of the principal values λ_α^2

$$I_1(\mathbf{C}) := \lambda_1^2 + \lambda_2^2 + \lambda_3^2 \quad , \quad I_2(\mathbf{C}) := \lambda_1^2 \lambda_2^2 + \lambda_2^2 \lambda_3^2 + \lambda_3^2 \lambda_1^2 \quad \text{and} \quad I_3(\mathbf{C}) := \lambda_1^2 \lambda_2^2 \lambda_3^2 . \quad (\text{A.6})$$

It is worth noting that a repeated use of the definition (A.1) for any positive integer n leads to

$$\mathbf{C}^n \mathbf{N}^\alpha := (\mathbf{C}\mathbf{G}^{-1})^{n-1} \mathbf{C}\mathbf{N}^\alpha = (\lambda_\alpha^2)^n \mathbf{N}_\alpha . \quad (\text{A.7})$$

Insertion of this result into (A.4) for $\Lambda^n = (\lambda_\alpha^2)^n$ with $n = 1, 2, 3$ yields the well-known *Cayley-Hamilton theorem*

$$\mathbf{C}^3 - I_1 \mathbf{C}^2 + I_2 \mathbf{C} - I_3 \mathbf{G} = \mathbf{0}, \quad (\text{A.8})$$

which states that every tensor fulfills its own characteristic equation, OGDEN [161].

In the context of *isotropic* finite elasticity, the functional dependency of a stored energy is restricted to the rotation invariant eigenvalues or the principal invariants due to the material symmetry constraint on the free energy $\Psi(\mathbf{Q}\mathbf{C}\mathbf{Q}^T) = \Psi(\mathbf{C})$ with respect to the rotations $\mathbf{Q} \in \mathcal{SO}(\beta)$. That is, the free energy can either be formulated in terms of the principal values $\Psi = \hat{\Psi}(\lambda_1^2, \lambda_2^2, \lambda_3^2)$ or the invariants $\Psi = \hat{\Psi}(I_1, I_2, I_3)$. These representations cover almost all the phenomenological hyperelasticity models of rubber elasticity. Derivation of the stresses and fourth order elasticity tensors (moduli) from a free energy function constructed in terms of the principal stretches requires the explicit derivatives of eigenvalues and eigenvectors with respect to the tensor itself. Hence, in what follows, we address the determination of these results for the case restricted to the *distinct* principal stretches, i.e. $\lambda_1^2 \neq \lambda_2^2 \neq \lambda_3^2$.

Derivative of the eigenvalues. Recalling the definition in (2.13), the co-factor of \mathbf{C} can be determined by

$$\text{cof } \mathbf{C} := \partial_{\mathbf{C}} \det \mathbf{C} = I_3 \mathbf{C}^{-1}, \quad (\text{A.9})$$

or from the definition of I_3 in (A.6)₃ we obtain

$$\text{cof } \mathbf{C} := \partial_{\mathbf{C}} I_3 = \sum_{\alpha=1}^3 \partial_{\lambda_\alpha^2} I_3 \partial_{\mathbf{C}} \lambda_\alpha^2 = I_3 \sum_{\alpha=1}^3 \lambda_\alpha^{-2} \partial_{\mathbf{C}} \lambda_\alpha^2. \quad (\text{A.10})$$

Extending (A.3) for the inverse right Cauchy-Green tensor \mathbf{C}^{-1} through (A.7) for $n = -1$, we end up with the identity

$$\mathbf{C}^{-1} = \sum_{\alpha=1}^3 \lambda_\alpha^{-2} \mathbf{N}^\alpha \otimes \mathbf{N}^\alpha.$$

Incorporation this result in (A.9) and its comparison with (A.10) yield the sought derivative of eigenvalues

$$\partial_{\mathbf{C}} \lambda_\alpha^2 = \mathbf{N}^\alpha \otimes \mathbf{N}^\alpha, \quad \partial_{C_{IJ}} (\lambda_\alpha^2) = N^{\alpha I} N^{\alpha J}. \quad (\text{A.11})$$

A corollary of this key result can be shown by taking the derivative of (A.1) with respect to \mathbf{C} in indicial notation

$$\begin{aligned} \partial_{C_{KL}} (C_{IJ} N^{\alpha J}) &= \lambda_\alpha^2 N_{\alpha I}, \\ \mathbb{I}_{IJ}^{KL} N^{\alpha J} + C_{IJ} \partial_{C_{KL}} N^{\alpha J} &= \partial_{C_{KL}} (\lambda_\alpha^2) N_{\alpha I} + \lambda_\alpha^2 \partial_{C_{KL}} N_{\alpha I}, \end{aligned} \quad (\text{A.12})$$

and contracting this result by \mathbf{N}^α from the left

$$\left. \begin{aligned} N^{\alpha I} N^{\alpha J} \mathbb{I}_{IJ}^{KL} + N^{\alpha I} C_{IJ} \partial_{C_{KL}} N^{\alpha J} &= \partial_{C_{KL}} (\lambda_\alpha^2) N^{\alpha I} N_{\alpha I} + \lambda_\alpha^2 N^{\alpha I} \partial_{C_{KL}} N_{\alpha I}, \\ N^{\alpha K} N^{\alpha L} + \lambda_\alpha^2 N_{\alpha J} \partial_{C_{KL}} N^{\alpha J} &= \partial_{C_{KL}} (\lambda_\alpha^2) + \lambda_\alpha^2 N^{\alpha I} \partial_{C_{KL}} N_{\alpha I}, \\ \mathbf{N}^\alpha \otimes \mathbf{N}^\alpha + \lambda_\alpha^2 \mathbf{N}_\alpha \cdot \partial_{\mathbf{C}} \mathbf{N}^\alpha &= \partial_{\mathbf{C}} \lambda_\alpha^2 + \lambda_\alpha^2 \mathbf{N}^\alpha \cdot \partial_{\mathbf{C}} \mathbf{N}_\alpha, \\ \mathbf{N}_\alpha \cdot \partial_{\mathbf{C}} \mathbf{N}^\alpha &\stackrel{(\text{A.11})}{=} \mathbf{N}^\alpha \cdot \partial_{\mathbf{C}} \mathbf{N}_\alpha. \end{aligned} \right\} \quad (\text{A.13})$$

Furthermore, we have $\mathbf{N}_\alpha \cdot \mathbf{N}^\alpha = 1$ which implies $\mathbf{N}_\alpha \cdot \partial_{\mathbf{C}} \mathbf{N}^\alpha + \mathbf{N}^\alpha \cdot \partial_{\mathbf{C}} \mathbf{N}_\alpha = \mathbf{0}$ and further reduces the result (A.13)₄ to

$$\mathbf{N}_\alpha \cdot \partial_{\mathbf{C}} \mathbf{N}^\alpha = \mathbf{N}^\alpha \cdot \partial_{\mathbf{C}} \mathbf{N}_\alpha = \mathbf{0}.$$

Derivative of the tangential eigenvectors. Utilization of the result (A.11) together with (A.13) in (A.12)₂ results in

$$\left. \begin{aligned} \mathbb{I}_{IJ}^{KL} N^{\alpha J} + C_{IJ} \partial_{C_{KL}} N^{\alpha J} &= N^{\alpha K} N^{\alpha L} N_{\alpha I} + \lambda_\alpha^2 \partial_{C_{KL}} N_{\alpha I}, \\ C_{IJ} \partial_{C_{KL}} N^{\alpha J} - \lambda_\alpha^2 \partial_{C_{KL}} N_{\alpha I} &= N^{\alpha K} N^{\alpha L} N_{\alpha I} - \mathbb{I}_{IJ}^{KL} N^{\alpha J}, \\ \underline{(C_{IJ} - \lambda_\alpha^2 G_{IJ})} \partial_{C_{KL}} N^{\alpha J} &= N^{\alpha K} N^{\alpha L} N_{\alpha I} - \mathbb{I}_{IJ}^{KL} N^{\alpha J}. \end{aligned} \right\} \quad (\text{A.14})$$

Denoting the underlined term by $\mathbf{A} := \mathbf{C} - \lambda_\alpha^2 \mathbf{G} = \sum_{\beta \neq \alpha}^3 (\lambda_\beta^2 - \lambda_\alpha^2) \mathbf{N}_\beta \otimes \mathbf{N}_\beta$, we have

$$A_{IJ} \partial_{C_{KL}} N^{\alpha J} = N^{\alpha K} N^{\alpha L} N_{\alpha I} - \mathbb{I}_{IJ}^{KL} N^{\alpha J}. \quad (\text{A.15})$$

Multiplication of (A.15) from the left by $\mathbf{A}^{-1} = \sum_{\beta \neq \alpha}^3 (\lambda_\beta^2 - \lambda_\alpha^2)^{-1} \mathbf{N}^\beta \otimes \mathbf{N}^\beta$ leaves the sought derivative alone on the left-hand side

$$\left. \begin{aligned} A^{-1PI} A_{IJ} \partial_{C_{KL}} N^{\alpha J} &= A^{-1PI} (N^{\alpha K} N^{\alpha L} N_{\alpha I} - \mathbb{I}_{IJ}^{KL} N^{\alpha J}), \\ \partial_{C_{KL}} N^{\alpha P} &= -A^{-1PI} \mathbb{I}_{IJ}^{KL} N^{\alpha J}. \end{aligned} \right\} \quad (\text{A.16})$$

Owing to the orthogonality of eigenvectors, the first term in the parentheses in (A.16)₁ vanishes identically. Expanding \mathbf{A}^{-1} again in the spectral form in (A.16)₂, we obtain

$$\partial_{C_{KL}} N^{\alpha P} = \sum_{\beta \neq \alpha}^3 (\lambda_\alpha^2 - \lambda_\beta^2)^{-1} N^{\beta P} \underline{N^{\beta I} \mathbb{I}_{IJ}^{KL} N^{\alpha J}}. \quad (\text{A.17})$$

Employing the definition of fourth order identity tensor $\mathbb{I}_{IJ}^{KL} = (\delta_I^K \delta_J^L + \delta_I^L \delta_J^K)/2$, we can recast (A.17) into a tensorial expression

$$\boxed{\partial_{\mathbf{C}} \mathbf{N}^\alpha = \sum_{\beta \neq \alpha}^3 \frac{1}{2} \frac{1}{(\lambda_\alpha^2 - \lambda_\beta^2)} \mathbf{N}^\beta \otimes (\mathbf{N}^\alpha \otimes \mathbf{N}^\beta + \mathbf{N}^\beta \otimes \mathbf{N}^\alpha)}. \quad (\text{A.18})$$

Having the result (A.18) at hand, the derivative $\partial_{\mathbf{C}}(\mathbf{N}^\alpha \otimes \mathbf{N}^\alpha)$ can also be obtained as

$$\left. \begin{aligned} \partial_{C_{KL}} (N^{\alpha O} N^{\alpha P}) &= \partial_{C_{KL}} (N^{\alpha O}) N^{\alpha P} + N^{\alpha O} \partial_{C_{KL}} (N^{\alpha P}), \\ &\stackrel{(\text{A.18})}{=} \sum_{\beta \neq \alpha}^3 \frac{1}{2} \frac{1}{(\lambda_\alpha^2 - \lambda_\beta^2)} \left\{ N^{\beta O} N^{\alpha P} (N^{\beta K} N^{\alpha L} + N^{\beta L} N^{\alpha K}) \right. \\ &\quad \left. + N^{\alpha O} N^{\beta P} (N^{\beta K} N^{\alpha L} + N^{\beta L} N^{\alpha K}) \right\}. \end{aligned} \right\} \quad (\text{A.19})$$

Introducing the second order tensor \mathbf{M}^α and the fourth order tensor $\mathbb{G}^{\alpha\beta}$

$$\left. \begin{aligned} \mathbf{M}^\alpha &:= \mathbf{N}^\alpha \otimes \mathbf{N}^\alpha, \quad (M^\alpha)^{KL} := N^{\alpha K} N^{\alpha L}, \\ (\mathbb{G}^{\alpha\beta})^{OPKL} &:= (M^\alpha)^{OK} (M^\beta)^{PL} + (M^\alpha)^{OL} (M^\beta)^{PK}, \end{aligned} \right\} \quad (\text{A.20})$$

(A.19) can be recast into the following compact form

$$\partial_{\mathbf{C}} \mathbf{M}^\alpha = \sum_{\beta \neq \alpha}^3 \frac{1}{2} \frac{1}{(\lambda_\alpha^2 - \lambda_\beta^2)} (\mathbb{G}^{\alpha\beta} + \mathbb{G}^{\beta\alpha}). \quad (\text{A.21})$$

We immediately observe that computation of the results (A.11), (A.18) and (A.21) necessitates the knowledge of the tensor \mathbf{M}^α for $\alpha = 1, 2, 3$. Following MORMAN [154], SIMO & TAYLOR [185], MIEHE [138], the tensor \mathbf{M}^α can be obtained without explicitly computing the eigenvectors. For this purpose, we consider the following equalities for the distinct eigenvalues $\lambda_\alpha^2 \neq \lambda_\beta^2 \neq \lambda_\gamma^2$

$$\begin{aligned} \mathbf{C} - \lambda_\alpha^2 \mathbf{G} &= (\lambda_\beta^2 - \lambda_\alpha^2) \mathbf{M}_\beta + (\lambda_\gamma^2 - \lambda_\alpha^2) \mathbf{M}_\gamma, \\ \mathbf{C} - \lambda_\beta^2 \mathbf{G} &= (\lambda_\alpha^2 - \lambda_\beta^2) \mathbf{M}_\alpha + (\lambda_\gamma^2 - \lambda_\beta^2) \mathbf{M}_\gamma. \end{aligned}$$

Multiplication of these equations by exploiting the orthogonality of eigenvectors, we obtain

$$\mathbf{M}_\gamma = \frac{(\mathbf{C} - \lambda_\alpha^2 \mathbf{G}) \mathbf{G}^{-1} (\mathbf{C} - \lambda_\beta^2 \mathbf{G})}{(\lambda_\gamma^2 - \lambda_\alpha^2)(\lambda_\gamma^2 - \lambda_\beta^2)} = \prod_{\alpha \neq \gamma}^3 \frac{(\mathbf{C} - \lambda_\alpha^2 \mathbf{G})}{(\lambda_\gamma^2 - \lambda_\alpha^2)} \quad (\text{A.22})$$

and thus $\mathbf{M}^\gamma = \mathbf{G}^{-1} \mathbf{M}_\gamma \mathbf{G}^{-1}$. For the cases where the equal eigenvalues are to be accounted for, the reader is referred to SIMO & TAYLOR [185], MIEHE [140], MIEHE & LAMBRECHT [151] and the references therein.

B. Decoupled Volumetric-Isochoric Finite Elasticity

Many engineering materials exhibit distinct behavior under volumetric and isochoric deformations. Common examples include the nearly incompressible elasticity of rubber-like materials, shear-dominated ductile viscoplasticity of amorphous glassy polymers and volume conserving plasticity of metals. Although this appendix is specifically devoted to the spatial formulation of decoupled volumetric-isochoric hyperelasticity, its generalization to inelasticity may readily be carried out. Following the works of FLORY [61], SIMO, TAYLOR & PISTER [186], MIEHE [137], the deformation gradient \mathbf{F} is multiplicatively split into the volumetric (spherical) \mathbf{F}_{vol} and isochoric (unimodular) $\bar{\mathbf{F}}$ parts

$$\mathbf{F} = \bar{\mathbf{F}}\mathbf{F}_{vol} \quad \text{with} \quad \mathbf{F}_{vol} := J^{1/3}\mathbf{1} \quad \text{and} \quad \bar{\mathbf{F}} := J^{-1/3}\mathbf{F}. \quad (\text{B.1})$$

This immediately implies that the volume map introduced in (2.11) is solely described by the volumetric part \mathbf{F}_{vol} , i.e. $\det\mathbf{F}_{vol}=J$, and therefore, the deformation under the unimodular part $\bar{\mathbf{F}}$ with $\det\bar{\mathbf{F}}=1$ does not include any volume change but purely isochoric deformations. Having this multiplicative kinematic split at hand, as already introduced in (3.5), the free energy of a hyperelastic material can be additively decomposed into the volumetric $U(J)$ and isochoric $\bar{\Psi}$ parts

$$\Psi = U(J) + \bar{\Psi}(\mathbf{g}; \bar{\mathbf{F}}). \quad (\text{B.2})$$

Owing to the material frame objectivity requirement, the isochoric part of the free energy can also be considered as $\bar{\Psi} = \hat{\Psi}(\bar{\mathbf{F}}^T \mathbf{g} \bar{\mathbf{F}}) = \hat{\Psi}(\bar{\mathbf{C}})$. In isothermal hyperelasticity, the dissipation vanishes identically $J\mathcal{D} = J\mathcal{D}_{loc} = \mathcal{P} - \dot{\Psi} = 0$ and thus the equality $\mathcal{P} = \dot{\Psi}$ holds. The additive decomposition of the free energy (B.2) leads to analogous form for the stress power $\mathcal{P} = \mathcal{P}_{vol} + \bar{\mathcal{P}}$ that are defined as

$$\mathcal{P}_{vol} := \dot{U}(J) \quad \text{and} \quad \bar{\mathcal{P}} := \dot{\hat{\Psi}}(\bar{\mathbf{F}}^T \mathbf{g} \bar{\mathbf{F}}). \quad (\text{B.3})$$

This split automatically induces the stress expression where the total stresses are also expressed as a summation of the spherical and deviatoric kinds. We first consider the volumetric part (B.3)₁

$$\begin{aligned} \mathcal{P}_{vol} &= 2\partial_{\mathbf{C}}U(J) : \frac{1}{2}\dot{\mathbf{C}} &= 2\partial_{\mathbf{C}}U(J) : \mathbf{F}^T \frac{1}{2}\mathcal{L}_{\mathbf{v}}\mathbf{g}\mathbf{F} \\ &= \mathbf{F}2\partial_{\mathbf{C}}U(J)\mathbf{F}^T : \frac{1}{2}\mathcal{L}_{\mathbf{v}}\mathbf{g} &= 2\partial_{\mathbf{g}}U(J) : \frac{1}{2}\mathcal{L}_{\mathbf{v}}\mathbf{g} \\ &=: \underline{p} \mathbf{g}^{-1} : \frac{1}{2}\mathcal{L}_{\mathbf{v}}\mathbf{g} \end{aligned} \quad (\text{B.4})$$

where we used the definition $J := \det\mathbf{F} = \det(F^a_A)\sqrt{\det(g_{ab})/\det(G_{AB})}$ yielding

$$2\partial_{\mathbf{g}}J = J\mathbf{g}^{-1} \quad \text{and} \quad 2\partial_{\mathbf{g}}U(J) = p \mathbf{g}^{-1} \quad (\text{B.5})$$

with $p := JU'(J)$ as in (3.8)₁. Likewise the isochoric stress power in $\bar{\mathcal{P}}$ can be recast into the form of a product of the deviatoric Kirchhoff stresses and the Lie derivative of the current metric \mathbf{g} by taking (B.3)₂ as a departure point

$$\begin{aligned} \bar{\mathcal{P}} &= 2\partial_{\bar{\mathbf{C}}}\bar{\Psi} : \frac{1}{2}\dot{\bar{\mathbf{C}}} &= 2\partial_{\bar{\mathbf{C}}}\bar{\Psi} : \bar{\mathbf{F}}^T \frac{1}{2}\bar{\mathcal{L}}_{\mathbf{v}}\mathbf{g}\bar{\mathbf{F}} \\ &= \bar{\mathbf{F}}2\partial_{\bar{\mathbf{C}}}\bar{\Psi}\bar{\mathbf{F}}^T : \frac{1}{2}\bar{\mathcal{L}}_{\mathbf{v}}\mathbf{g} &= 2\partial_{\mathbf{g}}\bar{\Psi} : \frac{1}{2}\bar{\mathcal{L}}_{\mathbf{v}}\mathbf{g} \\ &=: \bar{\boldsymbol{\tau}} : \frac{1}{2}\bar{\mathcal{L}}_{\mathbf{v}}\mathbf{g} \end{aligned} \quad (\text{B.6})$$

where we introduced $\bar{\boldsymbol{\tau}} := 2\partial_{\mathbf{g}}\bar{\Psi}$ and the isochoric Lie derivative $\bar{\mathcal{L}}_{\mathbf{v}}\mathbf{g}$ of the current metric

$$\bar{\mathcal{L}}_{\mathbf{v}}\mathbf{g} := \bar{\mathbf{F}}^{-T} \frac{d}{dt} \left(\bar{\mathbf{F}}^T \mathbf{g} \bar{\mathbf{F}} \right) \bar{\mathbf{F}}^{-1} = \mathbf{g}\bar{\mathbf{l}} + \bar{\mathbf{l}}^T \mathbf{g} \quad (\text{B.7})$$

analogous to (2.43). The deviatoric spatial velocity gradient is defined as $\bar{\mathbf{l}} := \dot{\bar{\mathbf{F}}}\bar{\mathbf{F}}^{-1}$ and it can be shown that

$$\mathbf{g}\bar{\mathbf{l}} = \mathbf{g}\mathbf{l} - \frac{1}{3} \text{tr}(\mathbf{l})\mathbf{g} = \mathbf{g}\mathbf{l} - \frac{1}{3} \left(\frac{1}{2} \mathcal{L}_{\mathbf{v}}\mathbf{g} : \mathbf{g}^{-1} \right) \mathbf{g}. \quad (\text{B.8})$$

Incorporation of this result in (B.7) yields

$$\bar{\mathcal{L}}_{\mathbf{v}}\mathbf{g} = \mathcal{L}_{\mathbf{v}}\mathbf{g} - \frac{1}{3} \mathcal{L}_{\mathbf{v}}\mathbf{g} : \mathbf{g}^{-1} \mathbf{g} = \mathcal{L}_{\mathbf{v}}\mathbf{g} : \mathbb{P}^T \quad (\text{B.9})$$

where the major transpose \mathbb{P}^T of the deviatoric projection tensor $\mathbb{P} := \mathbb{I} - \frac{1}{3} \mathbf{g} \otimes \mathbf{g}^{-1}$ has been used. Having the identity (B.9) at hand, we can rewrite (B.6) as

$$\bar{\mathcal{P}} = \bar{\boldsymbol{\tau}} : \frac{1}{2} \bar{\mathcal{L}}_{\mathbf{v}}\mathbf{g} = \bar{\boldsymbol{\tau}} : \left(\frac{1}{2} \mathcal{L}_{\mathbf{v}}\mathbf{g} : \mathbb{P}^T \right) = \underline{(\bar{\boldsymbol{\tau}} : \mathbb{P})} : \frac{1}{2} \mathcal{L}_{\mathbf{v}}\mathbf{g} \quad (\text{B.10})$$

Insertion of the results (B.4) and (B.10) into $\mathcal{P} = \boldsymbol{\tau} : \frac{1}{2} \mathcal{L}_{\mathbf{v}}\mathbf{g} = \mathcal{P}_{\text{vol}} + \bar{\mathcal{P}}$ yields the overall Kirchhoff stress tensor

$$\boxed{\boldsymbol{\tau} = p\mathbf{g}^{-1} + \bar{\boldsymbol{\tau}} : \mathbb{P}} \quad (\text{B.11})$$

in additively decomposed form of spherical and deviatoric contributions as in (3.6).

The objective rate sensitivities of the Kirchhoff stresses $\boldsymbol{\tau}$ and $\bar{\boldsymbol{\tau}}$ to the associated Lie derivatives of the spatial metric \mathbf{g}

$$\mathcal{L}_{\mathbf{v}}\boldsymbol{\tau} = \mathbb{C} : \frac{1}{2} \mathcal{L}_{\mathbf{v}}\mathbf{g} \quad \text{and} \quad \bar{\mathcal{L}}_{\mathbf{v}}\bar{\boldsymbol{\tau}} = \bar{\mathbb{C}} : \frac{1}{2} \bar{\mathcal{L}}_{\mathbf{v}}\mathbf{g}, \quad (\text{B.12})$$

are related through the the spatial elasticity moduli \mathbb{C} and $\bar{\mathbb{C}}$ defined as

$$\mathbb{C} = 4\partial_{\mathbf{g}\mathbf{g}}^2 \Psi(\mathbf{g}; \mathbf{F}) \quad \text{and} \quad \bar{\mathbb{C}} := 4\partial_{\mathbf{g}\mathbf{g}}^2 \bar{\Psi}(\mathbf{g}; \bar{\mathbf{F}}), \quad (\text{B.13})$$

respectively. The objective Lie derivatives of the contravariant stress tensors $\mathcal{L}_{\mathbf{v}}\boldsymbol{\tau}$ and $\bar{\mathcal{L}}_{\mathbf{v}}\bar{\boldsymbol{\tau}}$ can be obtained through the definition (2.43)

$$\mathcal{L}_{\mathbf{v}}\boldsymbol{\tau} = \dot{\boldsymbol{\tau}} - \mathbf{l}\boldsymbol{\tau} - \boldsymbol{\tau}\mathbf{l}^T \quad \text{and} \quad \bar{\mathcal{L}}_{\mathbf{v}}\bar{\boldsymbol{\tau}} = \dot{\bar{\boldsymbol{\tau}}} - \bar{\mathbf{l}}\bar{\boldsymbol{\tau}} - \bar{\boldsymbol{\tau}}\bar{\mathbf{l}}^T. \quad (\text{B.14})$$

We first treat the volumetric part

$$\begin{aligned} \mathcal{L}_{\mathbf{v}}(p\mathbf{g}^{-1}) &= \dot{p}\mathbf{g}^{-1} - p(\mathbf{l}\mathbf{g}^{-1} + \mathbf{g}^{-1}\mathbf{l}^T) \\ &= (p + \kappa) \mathbf{g}^{-1} \otimes \mathbf{g}^{-1} : \frac{1}{2} \mathcal{L}_{\mathbf{v}}\mathbf{g} - p\mathbf{g}^{-1} \mathcal{L}_{\mathbf{v}}\mathbf{g}\mathbf{g}^{-1} \\ &= \underline{\underline{((p + \kappa) \mathbf{g}^{-1} \otimes \mathbf{g}^{-1} - 2p\mathbb{I}_{\mathbf{g}^{-1}})}} : \frac{1}{2} \mathcal{L}_{\mathbf{v}}\mathbf{g} \end{aligned} \quad (\text{B.15})$$

where $\kappa := J^2 U''(J)$ as in (3.8)₂ and we employed the following results

$$\begin{aligned} \dot{J} &= J\mathbf{g}^{-1} : \frac{1}{2} \mathcal{L}_{\mathbf{v}}\mathbf{g}, \\ \mathbf{g}^{-1} \mathcal{L}_{\mathbf{v}}\mathbf{g}\mathbf{g}^{-1} &\equiv \mathbb{I}_{\mathbf{g}^{-1}} : \mathcal{L}_{\mathbf{v}}\mathbf{g} \quad \text{with} \quad (\mathbb{I}_{\mathbf{g}^{-1}})^{abcd} = \frac{1}{2} (g^{ac}g^{bd} + g^{ad}g^{bc}). \end{aligned} \quad (\text{B.16})$$

For the determination of the isochoric part of the moduli we start with

$$\mathcal{L}_v(\bar{\tau} : \mathbb{P}) = \mathcal{L}_v(\bar{\tau}) : \mathbb{P} + \bar{\tau} : \mathcal{L}_v(\mathbb{P}). \quad (\text{B.17})$$

By using the results (B.8), (B.9) and the definitions (B.14)₂, (B.12)₂, the Lie derivative of $\bar{\tau}$ appearing in the first term on the right-hand side of (B.17) can be recast into the form

$$\begin{aligned} \mathcal{L}_v(\bar{\tau}) &= \dot{\bar{\tau}} - l\bar{\tau} - \bar{\tau}l^T \\ &= \bar{\mathcal{L}}_v\bar{\tau} - \frac{2}{3}(\bar{\tau} \otimes \mathbf{g}^{-1}) : \frac{1}{2}\mathcal{L}_v\mathbf{g} \\ &= \bar{\mathbb{C}} : \frac{1}{2}\bar{\mathcal{L}}_v\mathbf{g} - \frac{2}{3}(\bar{\tau} \otimes \mathbf{g}^{-1}) : \frac{1}{2}\mathcal{L}_v\mathbf{g} \\ &= \underline{(\bar{\mathbb{C}} : \mathbb{P} - \frac{2}{3}(\bar{\tau} \otimes \mathbf{g}^{-1}))} : \frac{1}{2}\mathcal{L}_v\mathbf{g}. \end{aligned} \quad (\text{B.18})$$

Contraction of this result with the deviatoric projection tensor yields the first term of (B.17)

$$\begin{aligned} \mathcal{L}_v(\bar{\tau}) : \mathbb{P} &= (\bar{\mathbb{C}} : \mathbb{P} - \frac{2}{3}(\bar{\tau} \otimes \mathbf{g}^{-1})) : \frac{1}{2}\mathcal{L}_v\mathbf{g} : \mathbb{P} \\ &= \mathbb{P}^T : (\bar{\mathbb{C}} : \mathbb{P} - \frac{2}{3}(\bar{\tau} \otimes \mathbf{g}^{-1})) : \frac{1}{2}\mathcal{L}_v\mathbf{g} \\ &= \underline{(\mathbb{P}^T : \bar{\mathbb{C}} : \mathbb{P} - \frac{2}{3}(\mathbb{P}^T : \bar{\tau} \otimes \mathbf{g}^{-1}))} : \frac{1}{2}\mathcal{L}_v\mathbf{g}. \end{aligned} \quad (\text{B.19})$$

Computation of the second term on the right-hand side of (B.17) necessitates the Lie derivative of \mathbb{P}

$$\begin{aligned} \mathcal{L}_v(\mathbb{P}) &= -\frac{1}{3}(\mathcal{L}_v\mathbf{g} \otimes \mathbf{g}^{-1} + \mathbf{g} \otimes \mathcal{L}_v\mathbf{g}^{-1}) \\ &= -\frac{1}{3}(\mathcal{L}_v\mathbf{g} \otimes \mathbf{g}^{-1} - \mathbf{g} \otimes [\mathbf{g}^{-1}\mathcal{L}_v\mathbf{g}\mathbf{g}^{-1}]) \\ &\stackrel{(\text{B.16})_2}{=} -\frac{1}{3}(\mathcal{L}_v\mathbf{g} \otimes \mathbf{g}^{-1} - \mathbf{g} \otimes [\mathbb{I}_{\mathbf{g}^{-1}} : \mathcal{L}_v\mathbf{g}]). \end{aligned} \quad (\text{B.20})$$

With this result at hand, we can rewrite the term $\bar{\tau} : \mathcal{L}_v(\mathbb{P})$ in (B.17) as

$$\begin{aligned} \bar{\tau} : \mathcal{L}_v(\mathbb{P}) &= -\frac{2}{3}(\mathbf{g}^{-1} \otimes \bar{\tau} - (\bar{\tau} : \mathbf{g}) \mathbb{I}_{\mathbf{g}^{-1}}) : \frac{1}{2}\mathcal{L}_v\mathbf{g} \\ &= -\frac{2}{3}(\mathbf{g}^{-1} \otimes \bar{\tau} : \mathbb{P} - (\bar{\tau} : \mathbf{g})(\mathbb{I}_{\mathbf{g}^{-1}} - \frac{1}{3}\mathbf{g}^{-1} \otimes \mathbf{g}^{-1})) : \frac{1}{2}\mathcal{L}_v\mathbf{g} \\ &= \underline{-\frac{2}{3}(\mathbf{g}^{-1} \otimes \bar{\tau} : \mathbb{P} - (\bar{\tau} : \mathbf{g}) \mathbb{P}_{\mathbf{g}^{-1}})} : \frac{1}{2}\mathcal{L}_v\mathbf{g} \end{aligned} \quad (\text{B.21})$$

where $\mathbb{P}_{\mathbf{g}^{-1}} := \mathbb{I}_{\mathbf{g}^{-1}} - \frac{1}{3}\mathbf{g}^{-1} \otimes \mathbf{g}^{-1} = \mathbb{P}^T : \mathbb{I}_{\mathbf{g}^{-1}} : \mathbb{P}$. Merging the results (B.19), (B.21) and inserting it into (B.17), we obtain

$$\mathcal{L}_v(\bar{\tau} : \mathbb{P}) = \underline{[\mathbb{P}^T : (\bar{\mathbb{C}} + \frac{2}{3}(\bar{\tau} : \mathbf{g})\mathbb{I}_{\mathbf{g}^{-1}}) : \mathbb{P} - \frac{2}{3}(\mathbb{P}^T : \bar{\tau} \otimes \mathbf{g}^{-1} + \mathbf{g}^{-1} \otimes \bar{\tau} : \mathbb{P})]} : \frac{1}{2}\mathcal{L}_v\mathbf{g}. \quad (\text{B.22})$$

Combination of the underlined results obtained in (B.15) and (B.22) leads us to the sought expression for the total spatial moduli \mathbb{C}

$$\begin{aligned} \mathbb{C} &= (p + \kappa)\mathbf{g}^{-1} \otimes \mathbf{g}^{-1} - 2p\mathbb{I}_{\mathbf{g}^{-1}} \\ &\quad + \mathbb{P}^T : [\bar{\mathbb{C}} + \frac{2}{3}(\bar{\tau} : \mathbf{g})\mathbb{I}_{\mathbf{g}^{-1}}] : \mathbb{P} - \frac{2}{3}(\mathbb{P}^T : \bar{\tau} \otimes \mathbf{g}^{-1} + \mathbf{g}^{-1} \otimes \bar{\tau} : \mathbb{P}). \end{aligned} \quad (\text{B.23})$$

This is none other than the overall moduli expression we used in (3.7). The main results given in (B.11) and (B.23) complete the derivation. Clearly, these formulae can also be obtained by starting from the purely Lagrangean setting and performing corresponding push-forward operations on the Lagrangean stress and moduli expressions.

C. Statistics of the Freely Jointed Chain

Almost all of the network models of rubber elasticity proposed in the literature are based on the results of the statistical theory of an idealized chain of freely rotating links, commonly referred to as the *freely jointed chain*. It may be considered as the most simplified representation of a real polymer molecule that can randomly fluctuate under sufficiently high thermal energy in the absence of kinematic constraints. The freely jointed chain is composed of N bonds each of a fixed equal length l , see Figure 3.1. Its *end-to-end* distance denoted by r is the primary kinematic variable. The angle between any two adjacent bonds, the *bond angle*, is free to assume an arbitrary value, each of equal probability, so do the rotations about each bond. That is, no mutual correlation exists between adjacent bonds. This uncorrelated state immediately implies that at the unperturbed load-free state, the mean-square value of the distance r is identical to $r_0^2 = Nl^2$. This is one of the celebrated characteristics of freely jointed chains of finite length N . It has often erroneously been attributed to the special case, a Gaussian chain, of freely jointed chains, as noted by FLORY [64], p.11. In fact, bond angles of real chains such as polymethylene are limited to a pre-defined interval. The high deformability of a flexible real polymer chain is chiefly achieved through the rotations about the bonds, i.e. *torsion angle* variations. According to the isomeric state theory, see for example VOLKENSTEIN [202], MARK & ERMAN [129], ERMAN [55], a molecule with fixed end points experiences many isomeric configurations at which torsional angles assume average values, which are characterized by the energy minima called *trans*, *gauge*⁺ and *gauge*⁻ for an elementary case. This is, however, beyond the scope of the current appendix. For comprehensive treatment of the subject and more general polymer chains, the reader is referred to the classical texts by FLORY [60, 64], VOLKENSTEIN [202], TRELOAR [196].

The micro-free energy of the *unconstrained* part of the micro-sphere model outlined in Chapter 3 hinges also on the the freely jointed chain. For this reason, this appendix is devoted to the statistical elasticity of the idealized molecule. Despite the idealization of real chains through the freely jointed chain assumption, calculation of a computationally feasible, exact closed-form expression for an idealized chain of any length N is still a challenging task. To this end, in the subsequent part we construct two approximate free energy functions $\psi(\lambda)$ for the idealized chain. One of them, the *Gaussian theory*, assumes that a chain is composed of infinitely many modules and extensions are much less than the contour length $L := Nl$, i.e. $r \ll L$. This results in non-physical non-vanishing probability as the chain is fully stretched, i.e. $r \approx L$. The latter, the *non-Gaussian* treatment overcomes this deficiency of non-vanishing probability at fully extended state through some approximations and incorporates the finite chain extensibility.

The Gaussian Chain. Let us consider a freely jointed chain with one end fixed at the origin and its other end P freely occupies a position in the three-dimensional space, see Figure C.1. Provided that the number of chain segments N large enough, the distribution of the end-to-end distance $p(r)$ approaches to the celebrated *Gaussian* from

$$p(r) = \frac{1}{\sigma\sqrt{2\pi}} \exp \left[-\frac{(r - \langle r \rangle)^2}{2\sigma^2} \right]. \quad (\text{C.1})$$

As mentioned above, another key assumption made within the context of Gaussian statistics of a freely jointed chain is concerned with the small extensions compared to the contour length $r \ll L$. If this condition is fulfilled, the probability $p(r)$ can be ob-

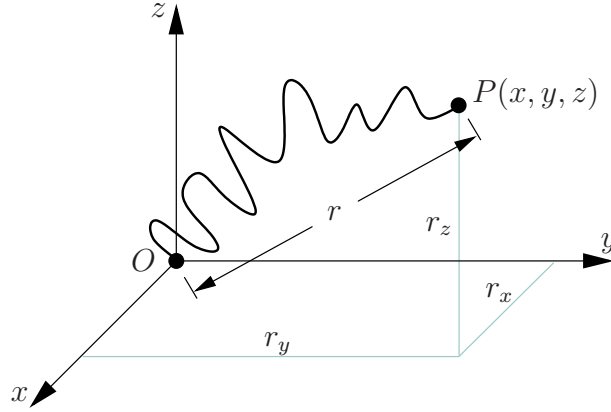


Figure C.1: The freely jointed chain with one end fixed at the origin O .

tained by multiplying the probability of joint events taking place independently, i.e. $p(r_x, r_y, r_z) = p(r_x)p(r_y)p(r_z)$. These separate events are none other than the projections r_x, r_y, r_z of the end-to-end distance r on the Cartesian axes, see Figure C.1. The distribution of each projection $p(r_i)$ for $i = x, y, z$ has then the following Gaussian form

$$p(r_i) = \frac{1}{\sigma_i \sqrt{2\pi}} \exp \left[-\frac{(r_i - \langle r_i \rangle)^2}{2\sigma_i^2} \right], \quad (\text{C.2})$$

as well. This approximation reduces the three-dimensional random walk problem to the one-dimensional one. Now, let l_i stand for the length projection of a module of the chain on the i -axis. Since any direction that a segment may sample is random, the probability density $p(l_i)$ is uniform. The normality condition $\int_{-l}^l p(l_i) dl_i = 1$ leads to $p(l_i) = 1/(2l)$. Then, the mean value $\langle l_i \rangle$ and the variance $\sigma_{l_i}^2 := \langle l_i^2 \rangle - \langle l_i \rangle^2$ can then be determined as

$$\langle l_i \rangle = \int_{-l}^l l_i p(l_i) dl_i = 0 \quad \text{and} \quad \sigma_{l_i}^2 = \int_{-l}^l l_i^2 p(l_i) dl_i = \frac{l^2}{3}. \quad (\text{C.3})$$

Finding the coordinate of a single chain of N bonds on i -axis is analogous to the problem of the one-dimensional random walk, see e.g. REIF [172], p.4. To this end, let n_1 and n_2 denote the number of steps in the respective directions satisfying $n_1 + n_2 = N$. If the probability of stepping in the positive direction p and the corresponding probability in the negative sense q are equal, i.e. $p = q = 1/2$, the problem is symmetric. We then have $\langle n_1 \rangle = N/2$ and $\sigma_{n_1} = \sqrt{N}/2$. According to the definition of variance $\sigma_{n_1}^2 := \langle n_1^2 \rangle - \langle n_1 \rangle^2$, we obtain $\langle n_1^2 \rangle = \sigma_{n_1}^2 + \langle n_1 \rangle^2 = N/4 + N^2/4$. The i -coordinate of the chain end, its mean value and standard deviation are computed by starting from relation $r_i = \sigma_{l_i}(2n_1 - N)$,

$$\langle r_i \rangle = \sigma_{l_i}(2\langle n_1 \rangle - N) = 0, \quad (\text{C.4})$$

$$\sigma_i^2 := \langle r_i^2 \rangle - \langle r_i \rangle^2 = \langle r_i^2 \rangle = \sigma_{l_i}^2 \cdot (4 \cdot \langle n_1 \rangle^2 - 4\langle n_1 \rangle \cdot N + N^2) = N \cdot \sigma_{l_i}^2, \quad (\text{C.5})$$

$$\rightsquigarrow \sigma_i = \sigma_{l_i} \sqrt{N} = \frac{l\sqrt{N}}{\sqrt{3}}. \quad (\text{C.6})$$

Insertion of these results into (C.2) yields

$$p(r_i) = \left(\frac{3}{2\pi r_0^2} \right)^{1/2} \exp \left[-\frac{3 r_i^2}{2 r_0^2} \right]. \quad (\text{C.7})$$

Since we assumed that all coordinates of the end point of the chain are independent from each other, multiplication rule yields

$$p(r_x, r_y, r_z) = \left(\frac{3}{2\pi r_0^2} \right)^{3/2} \exp \left[-\frac{3(r_x^2 + r_y^2 + r_z^2)}{2r_0^2} \right] = \left(\frac{3}{2\pi r_0^2} \right)^{3/2} \exp \left[-\frac{3r^2}{2r_0^2} \right]. \quad (\text{C.8})$$

According to the distribution density of r , given in (C.8), the mean value of r , coinciding with its most probable value, is zero. But if one considers the target analogy given in TRELOAR [196], p.52 where the distribution of the coordinates of the shots on a target is given by two dimensional Gaussian distribution. It would not be wrong to say that the most probable position is at $r = 0$ but the most probable distance of any shot is not zero. Since r does not have negative value physically, we can determine the second moment of r . Its square-root gives a realistic representative end-to-end distance for the unloaded state of a chain, which is denoted as $r_0 = l\sqrt{N}$. Use of the definition (3.10)₁ for the micro stretch in Section 3.2.1 in (C.8) yields

$$p(\lambda) = \left(\frac{3}{2\pi r_0^2} \right)^{3/2} \exp \left[-\frac{3}{2}\lambda^2 \right]. \quad (\text{C.9})$$

Having the probability distribution in terms of the stretch λ , the entropy of the Gaussian chain can readily be determined through Boltzmann's equation

$$\eta = k \ln p(\lambda) = \eta_0 - \frac{3}{2}k\lambda^2 \quad (\text{C.10})$$

where k denotes the Boltzmann constant. As mentioned in Chapter 1, it is established that the deformation of a rubber chain is chiefly governed by entropy changes. This is one of the celebrated features of rubber elasticity, commonly referred to as *entropic elasticity*. That is, internal energy e variations are merely governed by temperature changes. The Helmholtz free energy of the Gaussian chain under isothermal conditions is then obtained

$$\psi(\lambda) = -\theta\eta(\lambda) = \psi_0 + \frac{3}{2}k\theta\lambda^2, \quad (\text{C.11})$$

as given in (3.17). The force energy conjugate to the stretch then comes out to be a linear function of the stretch

$$F_{Gauss} := \partial_\lambda \psi(\lambda, \theta) = 3k\theta\lambda, \quad (\text{C.12})$$

proportional to temperature θ , as already given in (3.18). At this point, it is important to observe that the Gaussian force assumes a finite value as the stretch $\lambda = r/r_0$ approaches to its limiting value $\lambda = \sqrt{N}$ corresponding to the fully extended state of the chain $r = lN$, as depicted in Figure 3.2a. This is in contrast to the reality which suggest a divergent force response at this limiting case. It may also seem to odd that force (C.12) does not vanish at $\lambda = 1$. This is, however, only valid for a single chain. If the three-dimensional incompressible macroscopic response of a network considered, the stress-free undeformed configuration is readily available.

The Non-Gaussian Chain. A systematic derivation of thermodynamical quantities for the non-Gaussian chain can be achieved through one of the well-established ensemble theories of equilibrium statistical mechanics. Entropy, a key concept linking statistical mechanics to thermodynamics, has more clear interpretation in the statistical theory of

information as a measure of disorder. The Boltzmann equation $\eta = k \ln \Omega$ serves as a key equation of statistical mechanics, a version of which has already been used in (C.10) for the computation of entropy of a Gaussian chain. In statistical mechanics, a system of interest is macroscopically constraint to a priori prescribed set of external variables concerning one or some of the quantities such as energy, volume, temperature, pressure, number of constituents. For the prescribed macrostate, there are many accessible microstates Ω compatible with the prescribed macrostate. Each of these microstates may be virtually imagined as a “snap shot” of a system. Instead of trying to understand the behavior of each microstate of the constituents in detail, mean behavior of the overall system is aimed to be described. Probability methods are devised to understand the mean behavior of the system in equilibrium. An *ensemble* can be looked upon as a collection of all admissible microstates of a system. Depending on the severity of constraints imposed on a system, three fundamental types of ensembles, namely *microcanonical*, *canonical* and *grand canonical ensembles*, have been introduced. In *microcanonical ensemble*, the system is fully isolated; that is, no energy exchange is allowed. Thus, all accessible microstates of the system is forced to be compatible with the externally imposed constant energy state, say e . The *fundamental postulate* of statistical mechanics states that in an isolated system in macroscopic equilibrium, all accessible microstates are equally probable. This means, if the system has total $\Omega(e)$ microstates, the probability of finding a microstate with an energy $e_i \in [e, e + \delta e]$ is a priori set to $P_i = 1/\Omega$. Other states with larger or smaller amount of energies are a priori excluded, i.e. $P_i = 0$ for $e_i \notin [e, e + \delta e]$. This uniform probability is commonly referred to as the *microcanonical distribution*. All of the other classes of ensembles are actually based on the microcanonical ensemble. If a system under consideration is placed in a reservoir that is assumed to be much larger than the system, the union of the system and the reservoir then forms again the microcanonical ensemble. In *canonical ensemble*, the rigid system is located in a large heat reservoir so that its temperature, volume and number of constituents are kept constant but the energy exchange between the system and the heat reservoir is allowed. In *grand canonical ensemble*, on the other hand, external constraints are further relaxed such that the system is allowed to exchange constituents with the the reservoir beside energy. Selection of a particular class of ensemble depends upon the macro-constraints imposed on the real system under consideration.

In the forthcoming part, we consider the freely jointed chain as a system composed of fixed N number of segments and subjected to a constant tip force f at constant temperature. This system can be interpreted as an isothermal-isobaric version of the canonical ensemble, the so-called θ - p ensemble of statistical mechanics. In this case, the system of interest is considered to be located in a reservoir that keeps the temperature and pressure constant. The system is neither insulated nor rigid such that an energy exchange between the system and the reservoir in the form of both heat and work is allowed. Before going into details of the isothermal-isobaric ensemble, let us first consider the canonical (isothermal) ensemble in which only heat form of energy exchange is allowed. The probability of finding the system in a state with energy e_i in the canonical ensemble is described by the canonical distribution

$$p_i = \frac{1}{Z} \exp(-\beta e_i) \quad (\text{C.13})$$

where $\beta := 1/k\theta$ and Z denotes the *partition function* (“Zustandssumme”) defined as

$$Z(\theta) = \sum_i \exp(-\beta e_i). \quad (\text{C.14})$$

Once the partition function is computed, mean values of the thermodynamical quantities that shall be considered as almost fixed at thermodynamic limit can be computed, see DIU ET AL. [44]. We first consider the energy

$$e = \langle e \rangle = \sum_i e_i p_i = Z^{-1} \sum_i e_i \exp(-\beta e_i) = -\partial_\beta \ln Z. \quad (\text{C.15})$$

Multiplication of the mean energy e with $d\beta$ can be considered as the differential of $-\ln Z$, i.e. $ed\beta = -\partial_\beta \ln Z d\beta = -d(\ln Z)$. Through the product rule, the left hand side of this expression can be rewritten as $ed\beta = d(e\beta) - \beta de$. Since the system is rigid, the energy change de is solely due to the heat exchange, i.e. $de = dq = \theta d\eta$, and therefore $ed\beta = d(e\beta) - \beta \theta d\eta$. Use of this result in the expression for $-d(\ln Z)$ leads us to the mean value of entropy for the canonical ensemble

$$\eta = k(\ln Z + \beta e), \quad (\text{C.16})$$

and the average free energy through $\psi := e - \theta\eta$

$$\psi = -k\theta \ln Z. \quad (\text{C.17})$$

It should be noted that in the derivation of the expressions for the entropy (C.16) and the free energy (C.17), the integration constants are suppressed for brevity. The derivations carried out so far can readily be extended to a system of the isothermal-isobaric ensemble, see e.g. DIU ET AL. [44], p.501 and LULEI [124], p.43. Since the system of interest considered here is a polymer chain under constant tip force in lieu of a box of gas under constant pressure, hereafter we denote this ensemble as θ - F ensemble with F standing for the tip force. Analogous to (C.14), the partition function of θ - F ensemble characterized by the external variables temperature θ and force F

$$Z(\theta, F) = \int_{\mathcal{D}_r} \sum_i \exp(-\beta h_i(r)) dr. \quad (\text{C.18})$$

where the end-to-end distance r is an internal variable continuously changing within the domain \mathcal{D}_r and $h_i(r) := e_i(r) - Fr$ denotes enthalpy of the microstate (i) characterized by the energy state e_i and end-to-end distance r . Then, the probability of finding the system at energy $e_i(r)$ and the end-to-end distance r is given by

$$p_i(r) = \frac{1}{Z} \exp(-\beta h_i(r)). \quad (\text{C.19})$$

Analogous to the canonical energy (C.15), we determine the mean enthalpy h

$$h = -\partial_\beta \ln Z, \quad (\text{C.20})$$

and the average end-to-end distance r

$$r = \beta^{-1} \partial_F \ln Z \quad (\text{C.21})$$

of the $\theta-F$ ensemble. If steps analogous to the ones used for deriving (C.16) are followed by taking into account $dh = -rdF + \theta d\eta$, we obtain the expression for the entropy

$$\eta = k(\ln Z + \beta h) = k \ln Z + (e - Fr)/\theta \quad (\text{C.22})$$

and the free energy

$$\psi = -k\theta \ln Z + Fr, \quad (\text{C.23})$$

respectively. That is; once the partition function $Z(\theta, F)$ is computed, all thermodynamics quantities are readily determined through the relations (C.20)-(C.23).

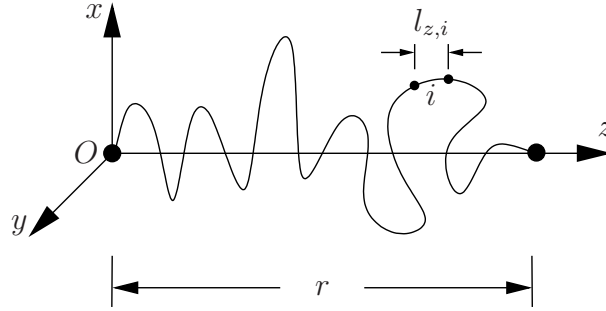


Figure C.2: Polymer chain lying on z -axis.

We are now ready to apply the above outlined formulation to the freely jointed chain. Let an idealized chain of freely rotating links lie on z -axis and be subjected to prescribed constant load F , see Figure C.2. A configuration of the chain is described through the set \mathbf{x} which contains the projection lengths of each module on the z -axis, i.e. $\mathbf{x} := \{l_{z,1}, l_{z,2}, \dots, l_{z,N}\}$ with each $l_{z,i} \in [-l; l]$ satisfying the condition

$$\mathcal{D} := \left\{ \mathbf{x} \mid \sum_{i=1}^N l_{z,i} = r(\mathbf{x}) \right\}. \quad (\text{C.24})$$

Since orientation of each segment is a priori uniform, probability density in all directions is $p(l_{z,i}) = \frac{1}{2l}$ and the accessible states of the chain are defined by equation (C.24). Since the direction of each module is assumed to be independent from others, the multiplication rule is utilized to compute an infinitesimal probability $dP(\mathbf{x})$ in equation

$$dP(\mathbf{x}) = dP(l_{z,1}) \cdot dP(l_{z,2}) \cdot \dots \cdot dP(l_{z,N}) = \left(\frac{1}{2l} \right)^N \prod_{i=1}^N dl_{z,i} \quad (\text{C.25})$$

Then the partition function of a freely jointed chain which deform under constant energy state can be written as

$$Z(\theta, F) = \int_{\mathcal{D}} \exp(\beta r(\mathbf{x})F) dP(\mathbf{x}). \quad (\text{C.26})$$

Incorporation of the results (C.24) and (C.25) in (C.26) then leads us to the following form

$$Z(\theta, F) = \left\{ \frac{1}{2l} \int_{-l}^l dl_z \cdot \exp(\beta Fl_z) \right\}^N = \left\{ \frac{\sinh \chi}{\chi} \right\}^N. \quad (\text{C.27})$$

with $\chi := \beta Fl$. Insertion of this result into (C.21) yields the expression for the end-to-end distance r

$$r = Nl\mathcal{L}(\chi) \quad (\text{C.28})$$

where $\mathcal{L}(\chi)$ denotes the well-known Langevin function defined as

$$\mathcal{L}(\chi) := \coth \chi - 1/\chi. \quad (\text{C.29})$$

In the present context, the conventional approximation is concerned with inversion of (C.28) for $\chi = \mathcal{L}^{-1}(\lambda_r)$ where $\lambda_r := r/Nl$. The error introduced through this approximation vanishes as the number of chain segments N approaches to infinity. For finite values of N , the treatment remains inexact, see FLORY [64] p.321. Having this result with $F = k\theta\mathcal{L}^{-1}(\lambda_r)/l$ at hand, the free energy function can readily be obtained through (C.23)

$$\psi(\lambda_r) = k\theta N \left(\lambda_r \mathcal{L}^{-1}(\lambda_r) + \ln \frac{\mathcal{L}^{-1}(\lambda_r)}{\sinh \mathcal{L}^{-1}(\lambda_r)} \right). \quad (\text{C.30})$$

as already been introduced in (3.19).

References

- [1] *ARAMIS User Manual. Deformation measurement using the grating method.* GOM mbH, Braunschweig.
- [2] AKSEL, N.; HÜBNER, C. [1996]: *The Influence of Dewetting in Filled Elastomers on the Changes of Their Mechanical Properties.* Archive of Applied Mechanics, 66: 231–241.
- [3] ANAND, L.; AMES, N. M. [2006]: *On Modeling the Micro-Indentation Response of an Amorphous Polymer.* International Journal of Plasticity, 22: 1123–1170.
- [4] ANAND, L.; GURTIN, M. E. [2003]: *A Theory of Amorphous Solids Undergoing Large Deformations, with Application to Polymeric Glasses.* International Journal of Solids and Structures, 40: 1465–1487.
- [5] ARGON, A. S. [1973]: *A Theory for the Low-Temperature Plastic Deformation of Glassy Polymers.* The Philosophical Magazine, 28: 839–865.
- [6] ARGON, A. S.; BESSONOV, M. I. [1977]: *Plastic Deformation in Polyimides, with New Implications on the Theory of Plastic Deformation of Glassy Polymers.* Philosophical Magazine, 35: 917–933.
- [7] ARRUDA, E. M.; BOYCE, M. C. [1993]: *Evolution of Plastic Anisotropy in Amorphous Polymers During Finite Straining.* International Journal of Plasticity, 9: 697–720.
- [8] ARRUDA, E. M.; BOYCE, M. C. [1993]: *A Three-Dimensional Constitutive Model for the Large Stretch Behavior of Rubber Elastic Materials.* Journal of the Mechanics and Physics of Solids, 41: 389–412.
- [9] ARRUDA, E. M.; BOYCE, M. C.; JAYACHANDRAN, R. [1995]: *Effects of Strain Rate, Temperature and Thermomechanical Coupling on the Finite Strain Deformation of Glassy Polymers.* Mechanics of Materials, 19: 193–212.
- [10] BAŽANT, Z. P.; OH, B. H. [1986]: *Efficient Numerical Integration on the Surface of a Sphere.* Zeitschrift für angewandte Mathematik und Mechanik, 66: 37–49.
- [11] BEATTY, M. F.; KRISHNASWAMY, S. [2000]: *The Mullis Effect in Equibiaxial Deformation.* Journal of Applied Mathematics and Physics (ZAMP), 51: 984–1015.
- [12] BEATTY, M. F.; KRISHNASWAMY, S. [2000]: *A Theory of Stree-Softening in Incompressible Isotropic Materials.* Journal of the Mechanics and Physics of Solids, 48: 1931–1965.
- [13] BERGMANN, D.; RITTER, R. [1999]: *3D Deformation Measurement in Small Areas Based on Grating Method and Photogrammetry.* In *GOM User Meeting.*
- [14] BERGSTRÖM, J. S.; BOYCE, M. C. [1998]: *Constitutive Modeling of the Large Strain Time-Dependent behavior of Elastomers.* Journal of the Mechanics and Physics of Solids, 46: 931–954.
- [15] BERGSTRÖM, J. S.; BOYCE, M. C. [1999]: *Mechanical Behavior of Particle Filled Elastomers.* Rubber Chemistry and Technology, 72: 633–656.
- [16] BERGSTRÖM, J. S.; BOYCE, M. C. [2000]: *Large Strain Time-Dependent Behavior of Filled Elastomers.*

- [17] BERNSTEIN, B.; KEARSLEY, E. A.; ZAPAS, L. J. [1963]: *A Study of Stress Relaxation with Finite Strain*. Transactions of the Society of Rheology, 7: 391–4110.
- [18] BIOT, M. A. [1965]: *Mechanics of Incremental Deformations*. John Wiley & Sons, Inc., New York.
- [19] BIRD, R. B.; HASSAGER, O.; ARMSTRONG, R. C.; CURTISS, C. F. [1977]: *Dynamics of Polymeric Liquids Vol.2 Kinetic Theory*. John Wiley & Sons, Inc., New York.
- [20] BOUASSE, H.; CARRIÈRE, Z. [1903]: *Courbes de traction du caoutchouc vulcanisé*. Annales de la Faculté des Sciences de l'Université de Toulouse, 5: 257–283.
- [21] BOWDEN, P. B. [1973]: *Introduction*. In HAWARD, R. N. (Editor): *The Physics of Glassy Polymers*, Chapter 5, pp. 279–339. Applied Science Publishers Ltd, London, 1st Edition.
- [22] BOWDEN, P. B.; JUKES, J. A. [1972]: *The Plastic Flow of Isotropic Polymers*. Journal of Materials Science, 7: 52–63.
- [23] BOWDEN, P. B.; RAHA, S. [1970]: *The formation of Micro Shear Bands in Polystyrene and Polymethylmethacrylate*. The Philosophical Magazine, 22: 463–482.
- [24] BOYCE, M. C. [1996]: *Direct Comparison of the Gent and the Arruda–Boyce Constitutive Models of Rubber Elasticity*. Rubber Chemistry and Technology, 69: 781–785.
- [25] BOYCE, M. C.; ARRUDA, E. M. [2000]: *Constitutive Models of Rubber Elasticity: A Review*. Rubber Chemistry and Technology, 73: 504–523.
- [26] BOYCE, M. C.; ARRUDA, E. M.; JAYACHANDRAN, R. [1994]: *The Large Strain Compression, Tension, and Simple Shear of Polycarbonate*. Polymer Engineering and Science, 34: 716–725.
- [27] BOYCE, M. C.; HAWARD, R. N. [1997]: *The Post–Yield Deformation of Glassy Polymers*. In HAWARD, R. N.; YOUNG, R. J. (Editors): *The Physics of Glassy Polymers*, Chapter 5, pp. 213–293. Chapman & Hall, London, 2nd Edition.
- [28] BOYCE, M. C.; PARKS, D. M.; ARGON, A. S. [1988]: *Large Inelastic Deformation of Glassy Polymers. Part I: Rate Dependent Constitutive Model*. Mechanics of Materials, 7: 15–33.
- [29] BOYCE, M. C.; WEBER, G. G.; PARKS, D. M. [1989]: *On the Kinematics of Finite Strain Plasticity*. Journal of the Mechanics and Physics of Solids, 37: 647–665.
- [30] BRUHNS, O. T.; XIAO, H.; MEYERS, A. [2001]: *Constitutive Inequalities for an Isotropic Elastic Strain Energy Function Based on Hencky's Logarithmic Strain Tensor*. Proceedings of the Royal Society London A, 457: 2207–2226.
- [31] BUECHE, F. [1960]: *Molecular Basis for the Mullins Effect*. Journal of Applied Polymer Science, 4: 107–114.
- [32] BUECHE, F. [1961]: *Mullins Effect and Rubber–Filler Interaction*. Journal of Applied Polymer Science, 5: 271–281.
- [33] CHADWICK, P. [1999]: *Continuum Mechanics*. Dover Publications, Inc., Mineola.

- [34] COHEN, A. [1991]: *A Padé Approximant to the Inverse Langevin Function*. *Rheological Acta*, 30: 270–273.
- [35] COLEMAN, B.; GURTIN, M. E. [1967]: *Thermodynamics with Internal State Variables*. *The Journal of Chemical Physics*, 47: 597–613.
- [36] COLEMAN, B.; NOLL, W. [1961]: *Foundations of Linear Viscoelasticity*. *Reviews of Modern Physics*, 33: 239–249.
- [37] COLEMAN, B. D.; NOLL, W. [1963]: *The Thermodynamics of Elastic Materials with Heat Conduction and Viscosity*. *Archive for Rational Mechanics and Analysis*, 13: 167–178.
- [38] CRIST, B. [1997]: *Yield Processes in Glassy Polymers*. In HAWARD, R. N.; YOUNG, R. J. (Editors): *The Physics of Glassy Polymers*, Chapter 4, pp. 155–212. Chapman & Hall, London, 2nd Edition.
- [39] DANNENBERG, E. M. [1974]: *The Effects of Surface Chemical Interactions on the Properties of Filler-Reinforced Rubbers*. *Rubber Chemistry and Technology*, 48: 410–444.
- [40] DEAM, R. T.; EDWARDS, S. F. [1976]: *The Theory of Rubber Elasticity*. *Philosophical Transactions of the Royal Society London A*, 280: 317–353.
- [41] DE GENNES, P. G. [1971]: *Reptation of a Polymer Chain in the Presence of Fixed Obstacles*. *The Journal of Chemical Physics*, 55: 572–579.
- [42] DE GROOT, S.; MAZUR, P. [1984]: *Non-Equilibrium Thermodynamics*. Dover.
- [43] DE SOUZA NETO, E. A.; PERIĆ, D.; OWEN, D. R. J. [1994]: *A Phenomenological Three-Dimensional Rate-Independent Continuum Damage Model for Highly Filled Polymers: Formulation and Computational Aspects*. *Journal of the Mechanics and Physics of Solids*, 42: 1533–1550.
- [44] DIU, B.; GUTHMANN, C.; LEDERER, D.; ROULET, B. [1994]: *Grundlagen der Statistischen Physik*. Walter de Gruyter, Berlin.
- [45] DOI, M.; EDWARDS, S. F. [1986]: *The Theory of Polymer Dynamics*. Clarendon Press, Oxford.
- [46] DORFMANN, A.; OGDEN, R. W. [2003]: *A Pseudo-Elastic Model for Loading, Partial Unloading and Reloading of Particle-Reinforced Rubber*. *International Journal of Solids and Structures*, 40: 2699–2714.
- [47] DORFMANN, A.; OGDEN, R. W. [2004]: *A Constitutive Model for the Mullins Effect with Permanent Set in Particle-Reinforced Rubber*. *International Journal of Solids and Structures*, 41: 1855–1878.
- [48] DOYLE, T. C.; ERICKSEN, J. L. [1956]: *Nonlinear Elasticity*. In DRYDEN, H. L.; KÁRMÁN, T. VON (Editors): *Advances in Applied Mechanics*, Vol. 4, pp. 53–116. Academic Press, New York.
- [49] DROZDOV, A. D. [1996]: *Finite Elasticity and Viscoelasticity: A Course in the Nonlinear Mechanics of Solids*. World Scientific Publishing Co., Singapore.
- [50] DROZDOV, A. D.; DORFMANN, A. [2001]: *Stress-Strain Relations in Finite Viscoelastoplasticity of Rigid-Rod Networks: Applications to the Mullins Effect*. *Continuum Mechanics and Thermodynamics*, 13: 183–205.

- [51] DROZDOV, A. D.; DORFMANN, A. [2002]: *Finite Viscoelasticity of Filled Rubbers: The Effects of Pre-loading and Thermal Recovery*. Continuum Mechanics and Thermodynamics, 14: 337–361.
- [52] DUPAIX, R. B.; BOYCE, M. C. [2005]: *Finite Strain Behavior of Poly(ethylene terephthalate) (PET) and Poly(ethylene terephthalate)-glycol (PETG)*. Polymer, 46: 4827–4838.
- [53] EDWARDS, S. F.; VILGIS, T. A. [1988]: *The Tube Model Theory of Rubber Elasticity*. Reports on Progress in Physics, 51: 243–297.
- [54] ERINGEN, A. C. [1962]: *Nonlinear Theory of Continuous Media*. McGraw-Hill Book Company, Inc., New York.
- [55] ERMAN, B. [2004]: *Molecular Aspects of Rubber Elasticity*. In SACCOMANDI, G.; OGDEN, R. W. (Editors): *Mechanics and Thermomechanics of Rubberlike Solids*, Chapter 2, pp. 63–89. Springer, Wien.
- [56] ERMAN, B.; FLORY, P. J. [1978]: *Theory of Elasticity of Polymer Networks. II. The effect of geometric constraints on junctions*. The Journal of Chemical Physics, 68: 5363–5369.
- [57] EYRING, H. J. [1936]: *Viscosity, Plasticity, and Diffusion as Examples of Absolute Reaction Rates*. The Journal of Chemical Physics, 4: 283–291.
- [58] FERRY, J. D. [1980]: *Viscoelastic Properties of Polymers*. John Wiley & Sons, Inc., New York.
- [59] FINDLEY, W. N.; LAI, J. S.; ONARAN, K. [1989]: *Creep and Relaxation of Non-linear Viscoelastic Materials*. Dover Publication. Reprint of a 1976 North-Holland.
- [60] FLORY, P. J. [1953]: *Principles of Polymer Chemistry*. Cornell University Press, Ithaca.
- [61] FLORY, P. J. [1961]: *Thermodynamic Relations for High Elastic Materials*. Transactions of the Faraday Society, 57: 829–838.
- [62] FLORY, P. J. [1976]: *Statistical Thermodynamics of Random Networks*. Proceedings of the Royal Society London A, 351: 351–380.
- [63] FLORY, P. J. [1977]: *Theory of Elasticity of Polymer Networks. The effect of local constraints on junctions*. The Journal of Chemical Physics, 66: 5720–5729.
- [64] FLORY, P. J. [1989]: *Statistical Mechanics of Chain Molecules*. Clarendon Press, Oxford.
- [65] FLORY, P. J.; ERMAN, B. [1982]: *Theory of Elasticity of Polymer Networks. 3. Macromolecules*, 15: 800–806.
- [66] FLORY, P. J.; REHNER, J. J. [1943]: *Statistical Mechanics of Cross-Linked Polymer Networks: I. Rubberlike Elasticity*. The Journal of Chemical Physics, 11: 512–520.
- [67] FURUKAWA, J. [1955]: *A Kinetic Interpretation of the Rheological Behavior of High Polymers*. Journal of Polymer Science, 15: 193–202.
- [68] GENT, A. N. [1996]: *A New Constitutive Relation for Rubber*. Rubber Chemistry and Technology, 69: 59–61.

- [69] GÖKTEPE, S.; MIEHE, C. [2005]: *A Micro–Macro Approach to Rubber–Like Materials. Part III: The Micro–Sphere Model of Anisotropic Mullins–Type Damage*. *Journal of the Mechanics and Physics of Solids*, 53: 2259–2283.
- [70] GOVAERT, L. E.; TIMMERMANS, P. H. M.; BREKELMANS, W. A. M. [2000]: *The Influence of Intrinsic Strain Softening on Strain Localization in Polycarbonate: Modeling and Experimental Validation*. *Journal of Engineering Materials and Technology*, 122: 177–185.
- [71] GOVINDJEE, S. [1997]: *An Evaluation of Strain Amplification Concepts via Monte Carlo Simulations of an Ideal Composite*. *Rubber Chemistry and Technology*, 70: 25–37.
- [72] GOVINDJEE, S.; SIMÓ, J. C. [1991]: *A Micro–Mechanically Based Continuum Damage Model for Carbon Black–Filled Rubbers Incorporating Mullins’ Effect*. *Journal of the Mechanics and Physics of Solids*, 39: 87–112.
- [73] GOVINDJEE, S.; SIMÓ, J. C. [1992]: *Mullins’ Effect and the Strain Amplitude Dependence of the Storage Modulus*. *International Journal of Solids and Structures*, 29: 1737–1751.
- [74] GOVINDJEE, S.; SIMÓ, J. C. [1992]: *Transition from Micro–Mechanics to Computationally Efficient Phenomenology: Carbon Black–Filled Rubbers Incorporating Mullins’ Effect*. *Journal of the Mechanics and Physics of Solids*, 40: 213–233.
- [75] GREEN, A.; NAGHDI, P. [1965]: *A General Theory of an Elastic–Plastic Continuum*. *Archive for Rational Mechanics and Analysis*, 18: 251–281.
- [76] GREEN, M. S.; TOBOLSKY, A. V. [1946]: *A New Approach to the Theory of Relaxing Polymeric Media*. *The Journal of Chemical Physics*, 14: 80–92.
- [77] G’SELL, C.; HIVER, J. M.; DAHOUN, A.; SOUAHI, A. [1992]: *Video–Controlled Tensile Testing of Polymers and Metals Beyond the Necking Point*. *Journal of Materials Science*, 27: 5031–5039.
- [78] G’SELL, C.; JONAS, J. J. [1979]: *Determination of the Plastic Behaviour of Solid Polymers at Constant True Strain Rate*. *Journal of Materials Science*, 14: 583–591.
- [79] GURTIN, M. E.; FRANCIS, E. C. [1981]: *Simple Rate–Independent Model for Damage*. *Journal of Spacecraft and Rockets*, 18: 285–286.
- [80] HAMED, G. L.; HATFIELD, S. [1989]: *On the Role of Bound Rubber in Carbon–Black Reinforcement*. *Rubber Chemistry and Technology*, 62: 143–156.
- [81] HARWOOD, J. A. C.; MULLINS, L.; R., P. A. [1965]: *Stress Softening in Natural Rubber Vulcanizates. Part II. Stress Softening Effects in Pure Gum and Filler Loaded Rubbers*. *Journal of Applied Polymer Science*, 9: 3011–3021.
- [82] HARWOOD, J. A. C.; PAYNE, A. R. [1966]: *Stress Softening in Natural Rubber Vulcanizates. Part III. Carbon Black–Filled Vulcanizates*. *Journal of Applied Polymer Science*, 10: 315–324.
- [83] HARWOOD, J. A. C.; PAYNE, A. R. [1966]: *Stress Softening in Natural Rubber Vulcanizates. Part IV. Unfilled Vulcanizates*. *Journal of Applied Polymer Science*, 10: 1203–1211.

- [84] HASAN, O. A.; BOYCE, M. C. [1995]: *A Constitutive Model for the Nonlinear Viscoelastic Viscoplastic Behavior of Glassy Polymers*. *Polymer Engineering and Science*, 35: 331–344.
- [85] HASAN, O. A.; BOYCE, M. C.; LI, X. S.; BERKO, S. [1993]: *An Investigation of the Yield and Postyield Behavior and Corresponding Structure of Poly(methyl methacrylate)*. *Journal of Polymer Science*, 31: 185–197.
- [86] HAUPT, P. [1993]: *On the Mathematical Modelling of Material Behavior in Continuum Mechanics*. *Acta Mechanica*, 100: 129–154.
- [87] HAUPT, P. [2002]: *Continuum Mechanics and Theory of Materials*. Springer-Verlag, Berlin, Heidelberg, 2. Edition.
- [88] HAUPT, P.; SEDLAN, K. [2001]: *Viscoplasticity of Elastomeric Materials: Experimental Facts and Constitutive Modelling*. *Archive of Applied Mechanics*, 71: 89–109.
- [89] HAWARD, R. N.; MANN, J. [1964]: *Reinforced Thermoplastics*. *Proceedings of the Royal Society London A*, 282: 120–134.
- [90] HAWARD, R. N.; MURPHY, B. M.; WHITE, E. F. T. [1971]: *Relationship between Compressive Yield and Tensile Behavior in Glassy Thermoplastics*. *Journal of Polymer Science: Part A-2*, 9: 801–814.
- [91] HAWARD, R. N.; THACKRAY, G. [1968]: *The Use of a Mathematical Model to Describe Isothermal Stress–Strain Curves in Glassy Thermoplastics*. *Proceedings of the Royal Society London A*, 302: 453–472.
- [92] HEINRICH, G.; KALISKE, M. [1997]: *Theoretical and Numerical Formulation of a Molecular Based Constitutive Tube–Model of Rubber Elasticity*. *Computational and Theoretical Polymer Science*, 7: 227–241.
- [93] HEINRICH, G.; STRAUBE, E. [1983]: *On the Strength and Deformation Dependence of the Tube–Like Topological Constraints of Polymer Networks, Melts and Concentrated Solutions, I. The polymer network case*. *Acta Polymerica*, 34: 589–594.
- [94] HEINRICH, G.; STRAUBE, E. [1984]: *On the Strength and Deformation Dependence of the Tube–Like Topological Constraints of Polymer Networks, Melts and Concentrated Solutions, I. Polymer melts and concentrated solutions*. *Acta Polymerica*, 35: 115–119.
- [95] HEINRICH, G.; STRAUBE, E.; HELMIS, G. [1988]: *Rubber Elasticity of Polymer Networks: Theories*. *Advances in Polymer Science*, 85: 33–87.
- [96] HOLT, W. L. [1932]: *Behavior of Rubber Under Repeated Stresses*. *Rubber Chemistry and Technology*, 5: 79–89.
- [97] HOLZAPFEL, G. A.; SIMÓ, J. C. [1996]: *A New Viscoelastic Constitutive Model for Continuous Media at Finite Thermomechanical Changes*. *International Journal of Solids and Structures*, 33: 3019–3034.
- [98] HOPE, P. S.; WARD, I. M.; GIBSON, A. G. [1980]: *The Hydrostatic Extrusion Polymethylmethacrylate*. *Journal of Materials Science*, 15: 2207–2220.
- [99] JAMES, A. G.; GREEN, A. [1975]: *Strain Energy Functions of Rubber. II. The Characterization of Filled Vulcanizates*. *Journal of Applied Polymer Science*, 19: 2319–2330.

- [100] JAMES, H. M.; GREEN, A.; SIMPSON, G. M. [1975]: *Strain Energy Functions of Rubber. I. Characterization of Gum Vulcanizates*. Journal of Applied Polymer Science, 19: 2033–2058.
- [101] JAMES, H. M.; GUTH, E. [1943]: *Theory of Elastic Properties of Rubber*. The Journal of Chemical Physics, 11: 455–481.
- [102] JONES, D. F.; TRELOAR, L. R. G. [1975]: *The Properties of Rubber in Pure Homogeneous Strain*. Journal of Physics D: Applied Physics, 8: 1285–1304.
- [103] KACHANOV, L. M. [1986]: *Introduction to Continuous Damage Mechanics*. Martinus Nijhoff Publishers, Dordrecht, Netherlands.
- [104] KALISKE, M.; HEINRICH, G. [1999]: *An Extended Tube–Model for Rubber Elasticity: Statistical–Mechanical Theory and Finite Element Implementation*. Rubber Chemistry and Technology, 72: 602–632.
- [105] KALISKE, M.; NASDALA, L.; ROTHERT, H. [2001]: *On Damage Modelling for Elastic and Viscoelastic Materials at Large Strain*. Computers and Structures, 79: 2133–2141.
- [106] KALISKE, M.; ROTHERT, H. [1997]: *Formulation and Implementation of Three–Dimensional Viscoelasticity at Small and Finite Strains*. Computational Mechanics, 19: 228–239.
- [107] KAWABATA, S.; MATSUDA, M.; TEI, K.; KAWAI, H. [1981]: *Experimental Survey of the Strain Energy Density Function of Isoprene Rubber Vulcanizate*. Macromolecules, 14: 154–162.
- [108] KAYE, A. [1962]: *Non–Newtonian Flow in Incompressible Fluids*. Technical Report 134, College of Aeronautics, Cranfield CoA.
- [109] KECK, J.; MIEHE, C. [1997]: *An Eulerian Overstress–Type Viscoplastic Constitutive Model in Spectral Form. Formulation and Numerical Implementation*. In *Computational Plasticity; Fundamentals and Applications*, Vol. 1, pp. 997–1003.
- [110] KLÜPPEL, M.; SCHRAMM, J. [1999]: *An advanced micro–mechanical model of hyperelasticity and stress softening of reinforced rubbers*. In DORFMANN, A.; MUHR, A. (Editors): *Constitutive Models for Rubber*, pp. 211–218. Balkema Publications, Lisse.
- [111] KRÖNER, E. [1960]: *Allgemeine Kontinuumstheorie der Versetzungen und Eigenspannungen*. Archive for Rational Mechanics and Analysis, 4: 273–334.
- [112] KUHN, W. [1934]: *Über die Gestalt fadenförmiger Moleküle in Lösungen*. Kolloid-Zeitschrift, 68: 2–15.
- [113] KUHN, W. [1936]: *Beziehungen zwischen Molekülgröße, statistischer Molekülgestalt und elastischen Eigenschaften hochpolymerer Stoffe*. Kolloid-Zeitschrift, 76: 258–271.
- [114] KUHN, W.; GRÜN, F. [1942]: *Beziehungen zwischen elastischen Konstanten und Dehnungsdoppelbrechung hochelastischer Stoffe*. Kolloid-Zeitschrift, 101: 248–271.
- [115] LEE, E. H. [1969]: *Elastic–Plastic Deformation at Finite Strain*. ASME Journal of Applied Mechanics, 36: 1–6.
- [116] LEMAITRE, J. [1996]: *A Course on Damage Mechanics*. Springer–Verlag, Berlin Heidelberg, 2nd Edition.

- [117] LI, J. C. M.; GILMAN, J. J. [1970]: *Disclination Loops in Polymers*. Journal of Applied Physics, 41: 4248–4256.
- [118] LION, A. [1996]: *A Constitutive Model for Carbon Black Filled Rubber. Experimental Investigations and Mathematical Representations*. Continuum Mechanics and Thermodynamics, 8: 153–169.
- [119] LION, A. [1997]: *On the Large Deformation Behaviour of Reinforced Rubber at Different Temperatures*. Journal of the Mechanics and Physics of Solids, 45: 1805–1834.
- [120] LODGE, A. S. [1956]: *A Network Theory of Flow Birefringence and Stress in Concentrated Polymer Solutions*. Transactions of the Faraday Society, 52: 120–130.
- [121] LOVE, A. E. H. [1944]: *A Treatise on the Mathematical Theory of Elasticity*. Dover, New York, 2nd Edition.
- [122] LUBLINER, J. [1985]: *A Model of Rubber Viscoelasticity*. Mechanics Research Communications, 12: 93–99.
- [123] LU, J.; RAVI-CHANDAR, K. [1999]: *Inelastic Deformation and Localization Phenomena in Polycarbonate Under Tension*. International Journal of Solids and Structures, 36: 391–425.
- [124] LULEI, F. [2002]: *Mikromechanisch motivierte Modelle zur Beschreibung finiter Deformationen gummiartiger Polymere: physikalische Modellbildung und numerische Simulation*. Dissertationsschrift 02-I-09, Institut für Mechanik (Bauwesen), Lehrstuhl I, Universität Stuttgart.
- [125] LULEI, F.; MIEHE, C. [2001]: *A physically-based constitutive model for the finite viscoelastic deformations in rubbery polymers based on a directly evaluated micro-macro transition*. In BESDO, D.; SCHUSTER, R.; IHLEMANN, J. (Editors): *Constitutive Models for Rubber II*, pp. 117–125. Balkema Publications, Lisse.
- [126] MANDEL, J. [1972]: *Plasticité Classique et Viscoplasticité*. Springer-Verlag, Berlin.
- [127] MARCKMANN, G.; VERRON, E. [2006]: *Comparison of Hyperelastic Models for Rubberlike Materials*. Rubber Chemistry and Technology, 79: 835–858.
- [128] MARCKMANN, G.; VERRON, E.; GORNET, L.; CHAGNON, G.; CHARRIER, P.; FORT, P. [2002]: *A Theory of Network Alteration for the Mullins Effect*. Journal of the Mechanics and Physics of Solids, 50: 2011–2028.
- [129] MARK, J. E.; ERMAN, B. [1988]: *Rubberlike Elasticity A Molecular Primer*. John Wiley & Sons Inc., New York.
- [130] MARRUCCI, G. [1996]: *Dynamics of Entanglements: A Nonlinear Model Consistent with the Cox-Merz Rule*. Journal of Non-Newtonian Fluid Mechanics, 62: 279–289.
- [131] MARSDEN, J. E.; HUGHES, T. J. R. [1983]: *Mathematical Foundations of Elasticity*. Prentice-Hall, Englewood Cliffs, New Jersey.
- [132] MARSHALL, I.; THOMPSON, A. B. [1954]: *The Cold Drawing of High Polymers*. Proceedings of the Royal Society London A, 221: 541–557.
- [133] MAUGIN, G. A. [1999]: *The Thermomechanics of Nonlinear Irreversible Behaviors. An Introduction*. World Scientific Publishing Co. Pte. Ltd.

- [134] MEDALIA, A. I. [1978]: *Effect of Carbon Black on Dynamic Properties of Rubber Vulcanizates*. Rubber Chemistry and Technology, 51: 437–523.
- [135] MÉNDEZ, J. [2004]: *Finite Elastic and Inelastic Behavior of Rubbery Polymers: Experiments and Modeling*. Master Thesis 04-I-02, Institut für Mechanik (Bauwesen), Lehrstuhl I, Universität Stuttgart.
- [136] MÉNDEZ, J.; GÖKTEPE, S.; MIEHE, C. [2006]: *Experiments and Identifications for Finite Polymer Inelasticity*. Proceedings in Applied Mathematics and Mechanics PAMM, 6: 401–402.
- [137] MIEHE, C. [1994]: *Aspects of the Formulation and Finite Element Implementation of Large Strain Isotropic Elasticity*. International Journal for Numerical Methods in Engineering, 37: 1981–2004.
- [138] MIEHE, C. [1994]: *Computation of Isotropic Tensor Functions*. Communications in Applied Numerical Methods, 9: 889–896.
- [139] MIEHE, C. [1995]: *Discontinuous and Continuous Damage Evolution in Ogden-Type Large-Strain Elastic Materials*. European Journal of Mechanics A / Solids, 14: 697–720.
- [140] MIEHE, C. [1996]: *Numerical Computation of Algorithmic (Consistent) Tangent Moduli in Large-Strain Computational Inelasticity*. Computer Methods in Applied Mechanics and Engineering, 134: 223–240.
- [141] MIEHE, C. [1998]: *A Constitutive Frame of Elastoplasticity at Large Strains Based on the Notion of a Plastic Metric*. International Journal of Solids and Structures, 35: 3859–3897.
- [142] MIEHE, C. [1998]: *A Formulation of Finite Elastoplasticity Based on Dual Co- and Contra-variant Eigenvector Triads Normalized with Respect to a Plastic Metric*. Computer Methods in Applied Mechanics and Engineering, 159: 223–260.
- [143] MIEHE, C. [2001]: *Geometrical Methods of Nonlinear Continuum Thermomechanics*. Lecture Notes, University of Stuttgart.
- [144] MIEHE, C. [2003]: *Computational Micro-To-Macro Transitions for Discretized Micro-Structures of Heterogeneous Materials at Finite Strains Based on the Minimization of Averaged Incremental Energy*. Computer Methods in Applied Mechanics and Engineering, 192: 559–591.
- [145] MIEHE, C. [2006]: *Theoretical and Computational Mechanics of Materials*. Lecture Notes, University of Stuttgart.
- [146] MIEHE, C.; APEL, N. [2004]: *Anisotropic Elastic-Plastic Analysis of Shells at Large Strains. A Comparison of Multiplicative and Additive Approaches to Enhanced Finite Element Design and Constitutive Modelling*. International Journal for Numerical Methods in Engineering, 61: 2067–2113.
- [147] MIEHE, C.; APEL, N.; LAMBRECHT, M. [2002]: *Anisotropic Additive Plasticity in the Logarithmic Strain Space: Modular Kinematic Formulation and Implementation Based on Incremental Minimization Principles for Standard Materials*. Computer Methods in Applied Mechanics and Engineering, 191: 5383–5425.
- [148] MIEHE, C.; GÖKTEPE, S. [2005]: *A Micro-Macro Approach to Rubber-Like Materials. Part II: The Micro-Sphere Model of Finite Rubber Viscoelasticity*. Journal of the Mechanics and Physics of Solids, 53: 2231–2258.

- [149] MIEHE, C.; GÖKTEPE, S.; LULEI, F. [2004]: *A Micro–Macro Approach to Rubber–Like Materials. Part I: The Non–Affine Micro–Sphere Model of Rubber Elasticity*. Journal of the Mechanics and Physics of Solids, 52: 2617–2660.
- [150] MIEHE, C.; KECK, J. [2000]: *Superimposed Finite Elastic–Viscoelastic–Plastoelastic Stress Response with Damage in Filled Rubbery Polymers. Experiments, Modelling and Algorithmic Implementation*. Journal of the Mechanics and Physics of Solids, 48: 323–365.
- [151] MIEHE, C.; LAMBRECHT, M. [2001]: *Algorithms for Computation of Stresses and Elastic Moduli in Terms of Seth–Hill’s Family of Generalized Strain Tensors*. Communications in Numerical Methods in Engineering, 17: 337–353.
- [152] MIEHE, C.; SCHOTTE, J.; LAMBRECHT, M. [2002]: *Homogenization of Inelastic Solid Materials at Finite Strains Based on Incremental Minimization Principles. Application to the Texture Analysis of Polycrystals*. Journal of the Mechanics and Physics of Solids, 50: 2123–2167.
- [153] MOONEY, M. [1940]: *A Theory of Large Elastic Deformation*. Journal of Applied Physics, 11: 582–592.
- [154] MORMAN, K. N. [1986]: *The Generalized Strain Measure with Application to Non-homogeneous Deformations in Rubber-like Solids*. Journal of Applied Mechanics, 53: 726–728.
- [155] MULLINS, L. [1948]: *Effect of Stretching on the Properties of Rubber*. Rubber Chemistry and Technology, 21: 281–300.
- [156] MULLINS, L. [1969]: *Softening of Rubber by Deformation*. Rubber Chemistry and Technology, 42: 339–362.
- [157] MULLINS, L.; TOBIN, N. R. [1957]: *Theoretical Model for the Elastic Behavior of Filler–Reinforced Vulcanized Rubbers*. Rubber Chemistry and Technology, 30: 555–571.
- [158] MULLINS, L.; TOBIN, N. R. [1965]: *Stress Softening Rubber Vulcanizates. Part I. Use of a Strain Amplification Factor to Describe the Elastic Behavior of Filler–Reinforced Vulcanized Rubber*. Journal of Applied Polymer Science, 9: 2993–3009.
- [159] NAGHDI, P. [1990]: *A Critical Review of the State of Finite Plasticity*. Journal of Applied Mathematics and Physics (ZAMP), 41: 315–394.
- [160] OGDEN, R.W. [1972]: *Large Deformation Isotropic Elasticity: on the Correlation of Theory and Experiment for Incompressible Rubberlike Solids*. Proceedings of the Royal Society London A, 326: 565–584.
- [161] OGDEN, R. W. [1984]: *Non-Linear Elastic Deformations*. Ellis Horwood, Chichester.
- [162] OGDEN, R. W.; ROXBURG, D. G. [1999]: *A Pseudo–Elastoc Model for the Mullins Effect in Filled Rubber*. Proceedings of the Royal Society London A, 455: 2861–2877.
- [163] PAPADOPOULOS, P.; LU, J. [1998]: *A General Framework for the Numerical Solution of Problems in Finite Elasto–plasticity*. Computer Methods in Applied Mechanics and Engineering, 159: 1–18.

- [164] PAPADOPOULOS, P.; LU, J. [2001]: *On the Formulation and Numerical Solution of Problems in Anisotropic Finite Plasticity*. Computer Methods in Applied Mechanics and Engineering, 190: 4889–4910.
- [165] PETERS, E. A. J. F. [2000]: *Polymers in Flow. Modelling and Simulation*. Ph.D. Thesis, Delft University of Technology.
- [166] PONTE CASTAÑEDA, P.; SUQUET, P. [1998]: *Nonlinear Composites*. Advances in Applied Mechanics, 34: 171–303.
- [167] RABINOWITZ, S.; WARD, I. M.; PARRY, J. S. C. [1970]: *The Effect of Hydrostatic Pressure on the Shear Yield Behaviour of Polymers*. Journal of Materials Science, 5: 29–39.
- [168] RAHA, S.; BOWDEN, P. B. [1972]: *Birefringence of Plastically Deformed Poly(methyl methacrylate)*. Polymer, 13: 174–183.
- [169] RAJAGOPAL, K. R.; WINEMAN, A. S. [1992]: *A Constitutive Equation for Non-linear Solids Which Undergo Deformation Induced Microstructural Changes*. International Journal of Plasticity, 8: 385–395.
- [170] REESE, S. [2003]: *A Micromechanically Motivated Material Model for the Thermo-Viscoelastic Material Behaviour of Rubber-Like Polymers*. International Journal of Plasticity, 19: 909–940.
- [171] REESE, S.; GOVINDJEE, S. [1998]: *A Theory of Finite Viscoplasticity and Numerical Aspects*. International Journal of Solids and Structures, 35: 3455–3482.
- [172] REIF, F. [1965]: *Fundamentals of Statistical and Thermal Physics*. McGraw-Hill, Inc.
- [173] RIGBI, Z. [1980]: *Reinforcement of Rubber by Carbon Black*. Advances in Polymer Science, 36: 21–68.
- [174] RITTER, R. [1989]: *Rasterverfahren*. In ROHRBACH, C. (Editor): *Handbuch für Experimentelle Spannungsanalyse*, Chapter D 2.4, pp. 279–299. VDI-Verlag.
- [175] RIVLIN, R. S.; SAUNDERS, D. W. [1950]: *Large Elastic Deformations of Isotropic Materials VII. Experiments on the Deformation of Rubber*. Proceedings of the Royal Society London A, 243: 251–288.
- [176] ROBERTSON, R. E. [1966]: *Theory for the Plasticity of Glassy Polymers*. The Journal of Chemical Physics, 44: 3950–3956.
- [177] RONCA, G.; ALLEGRA, G. [1975]: *An Approach to Rubber Elasticity with Internal Constraints*. The Journal of Chemical Physics, 63: 4990–4997.
- [178] ROUSE, P. E. [1953]: *A Theory of the Linear Viscoelastic Properties of Dilute Solutions of Colling Polymers*. The Journal of Chemical Physics, 21: 1272–1280.
- [179] SCHEDAY, G. [2003]: *Theorie und Numerik der Parameteridentifikation von Materialmodellen der finiten Elastizität und Inelastizität auf der Grundlage optischer Feldmeßmethoden*. Dissertationsschrift 03-I-11, Institut für Mechanik (Bauwesen), Lehrstuhl I, Universität Stuttgart.
- [180] SCOTT, K. W.; STEIN, R. S. [1953]: *A Molecular Theory of Stress Relaxation in Polymeric Media*. The Journal of Chemical Physics, 21: 1281–1286.

- [181] SIDOROFF, F. [1974]: *Un modèle viscoélastique non linéaire avec configuration intermédiaire*. Journal de Mécanique, 13: 679–713.
- [182] SILHAVÝ, M. [1997]: *The Mechanics and Thermodynamics of Continuous Media*. Springer, Berlin.
- [183] SIMÓ, J. C. [1987]: *On A Fully Three-Dimensional Finite-Strain Viscoelastic Damage Model: Formulation and Computational Aspects*. Computer Methods in Applied Mechanics and Engineering, 60: 153–173.
- [184] SIMO, J. C.; MARSDEN, J. [1984]: *On the Rotated Stress Tensor and the Material Version of the Doyle-Ericksen Formula*. Archive for Rational Mechanics and Analysis, 86: 213–231.
- [185] SIMÓ, J. C.; TAYLOR, R. L. [1991]: *Quasi-Incompressible Finite Elasticity in Principal Stretches. Continuum Basis and Numerical Algorithms*. Computer Methods in Applied Mechanics and Engineering, 85: 273–310.
- [186] SIMO, J. C.; TAYLOR, R. L.; PISTER, K. S. [1985]: *Variational and Projection Methods for the Volume Constraint in Finite Deformation Plasticity*. Computer Methods in Applied Mechanics and Engineering, 51: 177–208.
- [187] SPITZIG, W. A.; RICHMOND, O. [1979]: *Effect of Hydrostatic Pressure on the Deformation Behavior Polyethylene and Polycarbonate in Tension and in Compression*. Polymer Engineering and Science, 19: 1129–1139.
- [188] STRAUBE, E.; URBAN, V.; PYCKHOUT-HINZEN, W.; RICHTER, D. [1994]: *SANS Investigations of Topological Constraints and Microscopic Deformations in Rubbrelastic Networks*. Macromolecules, 27: 7681–7688.
- [189] STRAUBE, E.; URBAN, V.; PYCKHOUT-HINZEN, W.; RICHTER, D.; GLINKA, C. J. [1995]: *Small-Angle Neutron Scattering Investigation of Topological Constraints and Tube Deformation in Networks*. Physical Review Letters, 74: 4464–4467.
- [190] TANAKA, F.; EDWARDS, S. F. [1992]: *Viscoelastic Properties of Physically Crosslinked Networks Part 3. Time-Dependent Phenomena*. Journal of Non-Newtonian Fluid Mechanics, 43: 289–309.
- [191] TANNER, R. I. [1985]: *Engineering Rheology*. Oxford University Press, Revised Edition.
- [192] TOMITA, Y.; TANAKA, S. [1995]: *Prediction of Deformation Behavior of Glassy Polymers Based on Molecular Chain Network Model*. International Journal of Solids and Structures, 32: 3423–3434.
- [193] TRELOAR, L. R. G. [1944]: *Stress-Strain Data for Vulcanised Rubber Under Various Types of Deformation*. Transactions of the Faraday Society, 40: 59–70.
- [194] TRELOAR, L. R. G. [1946]: *The Elasticity of a Network of Long-Chain Molecules. - III*. Transactions of the Faraday Society, 42: 83–94.
- [195] TRELOAR, L. R. G. [1946]: *The Photoelastic Properties of Short-Chain Molecular Networks*. Transactions of the Faraday Society, 50: 881–896.
- [196] TRELOAR, L. R. G. [1975]: *The Physics of Rubber Elasticity*. Clarendon Press, Oxford, 3rd Edition.

- [197] TRELOAR, L. R. G.; RIDING, G. [1979]: *A Non-Gaussian Theory of Rubber in Biaxial Strain. I. Mechanical Properties*. Proceedings of the Royal Society London A, 369: 261–280.
- [198] TRUESDELL, C.; NOLL, W. [1965]: *The Non-linear Field Theories of Mechanics*. In FLÜGGE, S. (Editor): *Encyclopedia of Physics III/3*, Vol. III/3. Springer-Verlag, Berlin.
- [199] VAN DEN BOGERT, P. A. J.; DE BORST, R. [1994]: *On the Behavior of Rubberlike Materials in Compression and Shear*. Archive of Applied Mechanics, 64: 136–146.
- [200] VILGIS, T. A.; ERMAN, B. [1993]: *Comparison of the Constrained Junction and the Slip-Link Models of Rubber Elasticity*. Macromolecules, 26: 6657–6659.
- [201] VINCENT, P. I. [1960]: *The Necking and Cold-Drawing of Rigid Plastics*. Polymer, 1: 7–19.
- [202] VOLKENSTEIN, M. V. [1963]: *Configurational Statistics of Polymer Chains*. Interscience Publishers, New York. (Translated from the Russian edition (1958) by S. N. Timasheff and M. J. Timasheff).
- [203] WANG, M. C.; GUTH, E. [1952]: *Statistical Theory of Networks of Non-Gaussian Flexible Chains*. The Journal of Chemical Physics, 20: 1144–1157.
- [204] WIENTJES, R. H. W.; JONGSCHAAP, R. J. J.; DUIJS, M. H. G.; MELLEMA, J. [1999]: *A New Transient Network Model for Associative Polymer Networks*. Journal of Rheology, 43: 375–391.
- [205] WINTER, D. [1993]: *Optische Verschiebungsmessung nach dem Objektrasterprinzip mit Hilfe eines flächenorientierten Ansatzes*. Ph.D. Thesis, Technische Universität Carolo-Wilhelmina zu Braunschweig.
- [206] WU, P. D.; VAN DER GIESSEN, E. [1993]: *On Improved Network Models for Rubber Elasticity and Their Applications to Orientation Hardening in Glassy Polymers*. Journal of the Mechanics and Physics of Solids, 41: 427–456.
- [207] WU, P. D.; VAN DER GIESSEN, E. [1994]: *Analysis of Shear Band Propagation in Amorphous Glassy Polymers*. International Journal of Solids and Structures, 31: 1493–1517.
- [208] WU, P. D.; VAN DER GIESSEN, E. [1995]: *On Neck Propagation in Amorphous Glassy Polymers Under Plane Strain Tension*. International Journal of Plasticity, 11: 211–235.
- [209] XIAO, H.; BRUHNS, O. T.; MEYERS, A. [2006]: *Elastoplasticity Beyond Small Deformations*. Acta Mechanica, 182: 31–111.
- [210] YEOH, O. H. [1993]: *Some Forms of the Strain Energy Function for Rubber*. Rubber Chemistry and Technology, 66: 754–771.
- [211] ZECHA, H. [2005]: *Zur Beschreibung des viskoelastischen Verhaltens von Elastomeren bei finiten Verzerrungen: Experimente, Modellbildung und Simulationen*. Dissertationsschrift 05-I-15, Institut für Mechanik (Bauwesen), Lehrstuhl I, Universität Stuttgart.
- [212] ZIMM, B. H. [1956]: *Dynamics of Polymer Molecules in Dilute Solution: Viscoelasticity, Flow Birefringence and Dielectric Loss*. The Journal of Chemical Physics, 24: 269–278.

Curriculum Vitae

Personal Data

Name	Serdar Göktepe
Date of Birth	June 21, 1977
Place of Birth	Fethiye, Turkey
Parents	Serpil and Nail Göktepe
Siblings	Serap Şimşek
Marital Status	Single
Nationality	Turkish

School Education

1983-1988	Central Atatürk Primary School, Fethiye
1988-1991	Fethiye Central Secondary School, Fethiye
1991-1994	Bursa A.O.S. Science High School, Bursa

University Education

1994-1999	Undergraduate Studies of Civil Engineering, Middle East Technical University, Ankara
1999-2000	Graduate Studies of Civil Engineering, Middle East Technical University, Ankara
2000-2002	M.Sc. in Computational Mechanics of Materials and Structures (COMMAS), University of Stuttgart

Professional Occupation

1999-2000	Teaching Assistant, Structural Mechanics Laboratory, Middle East Technical University, Ankara
2002-2007	Research Associate, Institute of Applied Mechanics, Civil Engineering, University of Stuttgart

In dieser Schriftenreihe bisher erschienene Berichte:

- I-1(1996) *Theoretische und algorithmische Konzepte zur phänomenologischen Beschreibung anisotropen Materialverhaltens*, J. Schröder, Dissertation, 1996.
- I-2(1996) *Zur Theorie und Numerik finiter elastoplastischer Deformationen von Schalen-tragwerken*, B. Seifert, Dissertation, 1996.
- I-3(1996) *Zur Modellierung des künstlichen Infrarot-Dichroismus in Polymerfolien bei großen Verformungen*, J. Buhler, Dissertation, 1996.
- I-4(1998) *Verfahren zur Ermittlung der Erdbebenlasten mit Berücksichtigung des stochastischen Charakters des Bebens*, S. Zhang, Dissertation, 1998.
- I-5(1998) *Zur Beschreibung finiter Deformationen von Polymeren: Experimente, Modellbildung, Parameteridentifikation und Finite-Elemente- Formulierung*, J. Keck, Dissertation, 1998.
- I-6(1999) *Berechnungsverfahren instationär erregter Systeme im Frequenzbereich*, A. Jaworek, Dissertation, 1999.
- I-7(2000) *Homogenisierungsmethoden der nichtlinearen Kontinuumsmechanik unter Beachtung von Stabilitätsproblemen*, J. Schröder, Habilitation, 2000.
- I-8(2002) *Theorie und Numerik von Materialinstabilitäten elastoplastischer Festkörper auf der Grundlage inkrementeller Variationsformulierungen*, M. Lambrecht, Dissertation, 2002.
- I-9(2002) *Mikromechanisch motivierte Modelle zur Beschreibung finiter Deformationen gummiartiger Polymere: physikalische Modellbildung und numerische Simulation*, F. Lulei, Dissertation, 2002.
- I-10(2003) *Adaptive Finite-Elemente-Berechnungen der nichtlinearen Festkörpermechanik bei kleinen und großen Verzerrungen*, A. Koch, Dissertation, 2003.
- I-11(2003) *Theorie und Numerik der Parameteridentifikation von Materialmodellen der finiten Elastizität und Inelastizität auf der Grundlage optischer Feldmeßmethoden*, G. Scheday, Dissertation, 2003.
- I-12(2004) *Approaches to the Description of Anisotropic Material Behaviour at Finite Elastic and Plastic Deformations, Theory and Numerics*, N. Apel, Dissertation, 2004.
- I-13(2004) *Temperaturabhängige Beschreibung visko-elasto-plastischer Deformationen kurzglasfaserverstärkter Thermoplaste: Modellbildung, Numerik und Experimente*, S. Rieger, Dissertation, 2004.
- I-14(2005) *Zur Parameteridentifikation komplexer Materialmodelle auf der Basis realer und virtueller Testdaten*, A. Rieger, Dissertation, 2005.
- I-15(2005) *Viskoelastisches Verhalten von Elastomeren bei finiten Verzerrungen: Experimente, Modellierung und Simulationen*, H. Zecha, Dissertation, 2005.

- I-16(2005) *Mehrskalenmodelle in der Festkörpermechanik und Kopplung von Mehrgittermethoden mit Homogenisierungsverfahren*, C.G. Bayreuther, Dissertation, 2005.
- I-17(2005) *Static and Dynamic Homogenization Analyses of Discrete Granular and Atomistic Structures on Different Time and Length Scales*, J. Dettmar, Dissertation, 2005.
- I-18(2006) *Incompatibility and Instability Based Size Effects in Crystals and Composites at Finite Elastoplastic Strains*, M. Becker, Dissertation, 2006.
- I-19(2007) *Aspects of Energy Minimization in Solid Mechanics: Evolution of Inelastic Microstructures and Crack Propagation*, E. Gürses, Dissertation, 2007.
- I-20(2007) *Micro-Macro Approaches to Rubbery and Glassy Polymers: Predictive Micromechanically-Based Models and Simulations*, S. Göktepe, Dissertation, 2007.